# Systems Performance Analysis for Autonomous Spacecraft Navigation within Satellite Constellations using Intersatellite Optical Communications Links

by
Peter Grenfell
B.S., University of California at Berkeley (2017)
S.M., Massachusetts Institute of Technology (2020)
Submitted to the Department of Aeronautics and Astronautics
in partial fulfillment of the requirements for the degree of
Doctor of Philosophy in Aeronautics and Astronautics
at the
MASSACHUSETTS INSTITUTE OF TECHNOLOGY
February 2024


Author .....
Department of Aeronautics and Astronautics
January 12, 2024

Certified by .....
Kerri Cahoy
Professor of Aeronautics and Astronautics

Certified by .....
Olivier De Weck
Professor of Astronautics and Engineering Systems

Certified by .....
Simone D'Amico
Associate Professor of Aeronautics and Astronautics

Certified by .....
Michael Paluszek
President and Founder, Princeton Satellite Systems

Accepted by .....
Jonathan P. How
R. C. Maclaurin Professor of Aeronautics and Astronautics Chair,
Graduate Program Committee

THIS PAGE INTENTIONALLY LEFT BLANK

# Systems Performance Analysis for Autonomous Spacecraft Navigation within Satellite Constellations using Intersatellite Optical Communications Links

by

Peter Grenfell

Submitted to the Department of Aeronautics and Astronautics
on January 12, 2024, in partial fulfillment of the
requirements for the degree of
Doctor of Philosophy in Aeronautics and Astronautics

## Abstract

Free-space optical communications is an advanced technology for high data rate communications that has experienced rapid development for space applications over the last couple decades, due to the increasing need for bandwidth with modern sensing and information technologies. Lasercom has advantages over radio frequency (RF) systems, with the primary advantage being better scalability of terminal data rates versus Size, Weight, and Power (SWaP) constraints. A lasercom terminal already has the necessary hardware for optical intersatellite link (OISL) measurements, since it is the same hardware that is needed for communications. Intersatellite measurements can be used to improve the observability of satellite orbits in applications like satellite communications constellations. We will perform a systems analysis of the OISL measurement technology to better understand how measurement errors are related to the hardware design. We analyze relativistic effects when modeling the intersatellite light propagation. We expand on previous constellation analyses, in particular navigation via OISLs within LEO mega-constellations like Starlink, Earth navigation constellations like the Global Positioning System (GPS), and notional Lunar & Mars constellations. We estimate the achievable performance in these applications and show that baseline OISL navigation performance is on the order of 0.1-10 m and 0.1-10 mm/s, depending on the application configuration. This is comparable to existing state-of-the-art non-autonomous navigation methods like GPS and radio ground tracking and at least one order of magnitude better than existing autonomous navigation methods such as optical navigation. Lasercom crosslinks not only enable increased throughput in satellite communications constellations, but they can also be used to enable collectively-autonomous, high-precision navigation.

Thesis Supervisor: Kerri Cahoy
Title: Professor of Aeronautics and Astronautics

Thesis Supervisor: Olivier De Weck
Title: Professor of Astronautics and Engineering Systems

Thesis Supervisor: Simone D'Amico
Title: Associate Professor of Aeronautics and Astronautics

Thesis Supervisor: Michael Paluszek
Title: President and Founder, Princeton Satellite Systems

# Acknowledgments

This thesis is dedicated to all of my family and friends, who have supported me throughout this long journey. Thank you to my parents for their love and support. This accomplishment would not have been possible without them. Thank you to my sister and brother-in-law for their love and encouragement. Thank you to my partner, who supported and encouraged me throughout this long process. Thank you to my aunts, uncles, and cousins. Thank you to my friends at home in Maryland, in California, and at MIT. Thank you to my advisor, Kerri Cahoy, who mentored me, supported me in my research goals, and gave me the opportunity to complete my graduate education at MIT. Thank you to my colleagues in MIT STAR Lab for mentorship and camaraderie. Thank you to my colleagues on the CLICK mission team, including those at MIT STAR Lab, at the University of Florida PSSL, and at NASA Ames Research Center. Thank you to the sponsors at NASA Ames Research Center of the CLICK mission, which supported my graduate research assistantship at MIT.

*Disclaimer: The views and opinions expressed in this work are solely those of the author and do not necessarily reflect the views of NASA, MIT, the University of Florida, or other associated parties.*

THIS PAGE INTENTIONALLY LEFT BLANK

# Contents

THIS PAGE INTENTIONALLY LEFT BLANK

# List of Figures

THIS PAGE INTENTIONALLY LEFT BLANK

# List of Tables

THIS PAGE INTENTIONALLY LEFT BLANK

# Nomenclature

$(x_c, y_c)$ Centroid coordinates in pixels of an optical signal spot referred to the sensor coordinates

$\boldsymbol{\rho}$ Intersatellite relative position vector in meters with respect to the host satellite referred to inertial coordinates

$\Delta x$ Oscillator phase deviation (seconds)

$\hat{\mathbf{x}}$ Estimated system state

$\mathbf{x}$ True system state

$\Omega$ Right-Ascension of the Ascending Node (RAAN) in degrees

$\omega_p$ Argument of Periapsis in degrees

$\phi$ Intersatellite elevation bearing angle in radians referred to inertial coordinates

$\psi$ Generalized (unwrapped and normalized) phase of periodic signal

$\rho$ Intersatellite range (m)

$\rho_{a,ud}$ Apparent intersatellite range in meters as measured by two-way TOF

$\sigma_q$ Satellite Process Noise Standard Deviation (RMS of acceleration components ($m/s^2$))

$\sigma_r$ Satellite Position Uncertainty Standard Deviation (norm of position components (m))

$\sigma_v$ Satellite Velocity Uncertainty Standard Deviation (norm of velocity components (mm/s))

$\sigma_x$ Oscillator phase jitter (seconds)

$\sigma_y$ Oscillator Allan deviation

$\tau_{a,ud}$ Two-way time of flight in seconds (uplink and downlink only)

$\theta$ Intersatellite azimuth bearing angle in radians referred to inertial coordinates

$c$ Speed of light (m/s)

$J_k$ System state estimate error Fisher information matrix at time $t_k$

$l_{CN(P)}^{99}$ $\log_{10}(\mathrm{CN}(P_k))$ $99^{\mathrm{th}}$ Percentile for CRLB or EKF response

$N_d$ Integrated Doppler count

$P_{\mathrm{rx}}$ Received power at a sensor (W)

$P_{\mathrm{tx}}$ Transmitted power at a transmitter (e.g. laser power (W))

$P_k$ System state estimate error covariance matrix at time $t_k$

$P_n$ Total noise power at a sensor (W)

$Q$ System process noise matrix

$R_A^B$ Matrix representation of coordinate rotation from frame A to frame B

$T_s$ PPM slot period (seconds)

$t_s$ Effective settling time in seconds of a CRLB or EKF response

CN Condition Number

CRLB Cramer-Rao Lower Bound

DSN Deep Space Network

EIRP Effective Isotropic Radiated Power

EKF Extended Kalman Filter

ELF Elliptical Lunar Frozen Orbit: line of apsides librating in the polar region with lifetime in excess of ten years

FOV Field of View

GEO Geosynchronous Earth Orbit

LEO Low Earth Orbit

LVLH Local-Vertical-Local-Horizontal Frame

MEO Medium Earth Orbit

MOC Mission Operations Center

NEA Noise Equivalent Angle

NEES Normalized Estimation Error Squared

OISL Optical Intersatellite Link

PAT Pointing, Acquisition, and Tracking

PLL Phase Locked Loop

PPM Pulse-Position Modulation

RF Radio Frequency

RMS Root Mean Squared

SF Slope Factor

SNR Signal-to-Noise Ratio

SOA State-of-the-Art

TLE Two-Line Elements

TOF Time-of-Flight ($\tau$)

TT&C Telemetry, Tracking, & Command

WD-PX-SY Satellite number Y in plane X in a Walker-Delta Constellation

# Chapter 1

# Introduction

Spacecraft navigation is a critical element of spacecraft operations. Non-autonomous navigation methods have ground operators and computers in-the-loop. For semi-autonomous methods in Earth orbit, the spacecraft automatically uses terrestrial data sources in real-time such as GPS. Autonomous methods are independent of real-time terrestrial data sources. Conventional autonomous navigation methods have been limited to methods that can be implemented with a single satellite (e.g., terrain-relative optical navigation). This will be hereafter referred to as "individual-autonomy". Autonomous navigation methods that require two or more satellites, in particular methods that use measurements derived from inter-satellite links (ISLs), will be referred to as "collective-autonomy". Individually-autonomous navigation methods are still not as precise as conventional ground-operations approaches (see Fig. 1-1). However, collectively-autonomous ISL-based navigation methods are competitive with conventional non-autonomous approaches like radio ground tracking and may be the highest accuracy navigation methods for deep space applications (see Fig. 1-1).

Given recent technology advances, it is possible to use groups of smaller spacecraft to achieve missions that have previously been the domain of large, individual spacecraft [1]. There are increased efforts in further developing satellite communications networks, both in Earth orbit and in deep space. Optical communications crosslinks are already being implemented in the LEO Starlink constellation to improve data routing performance and reduce latency [2]. ISL-based navigation can be

used to establish a level of collective autonomy. Furthermore, Optical ISLs (OISLs) have improved performance relative to radio ISLs, both in ranging and in angles measurements. OISLs should be considered by mission planners for future collectively-autonomous, high-precision navigation within satellite constellations.

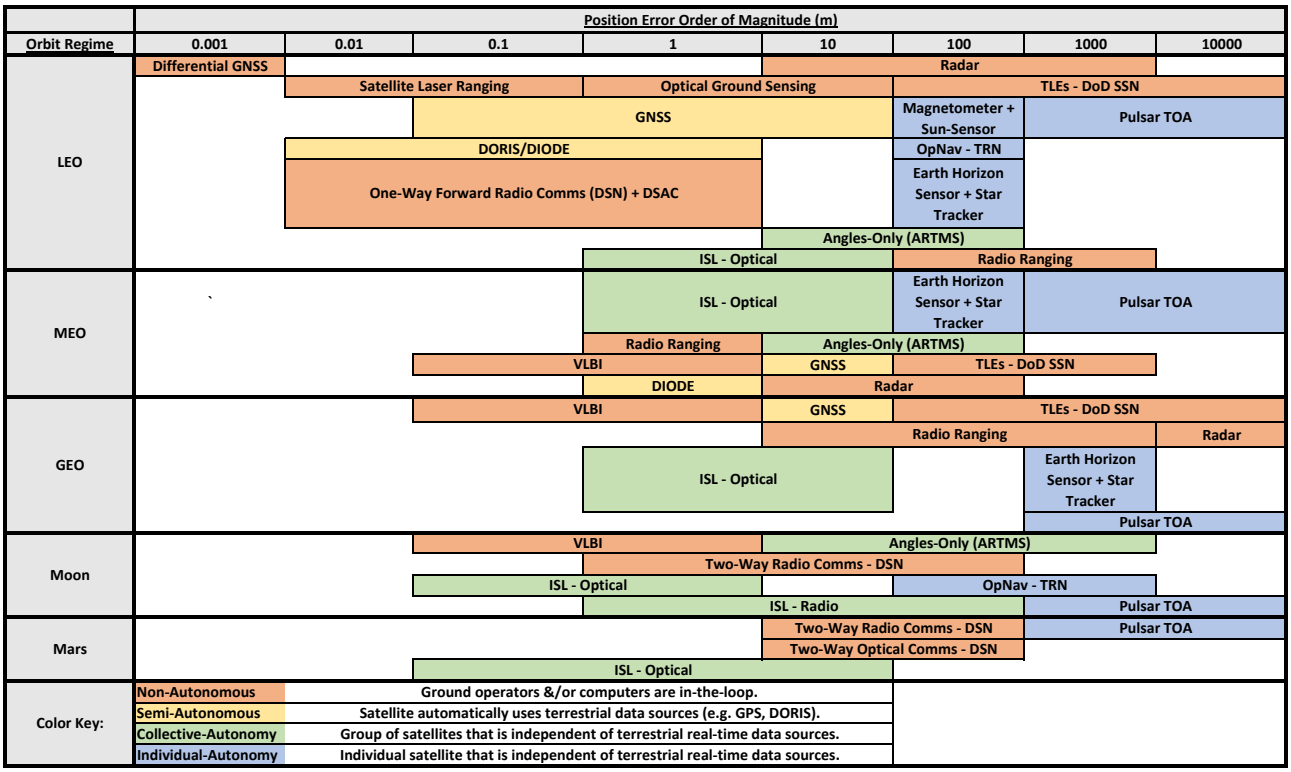


Figure 1-1: Summary of Absolute Orbit Determination Methods. OISL findings are based on simulations from this work. Others are from the following references: Differential GNSS [3]; Radar [4, 5, 6]; SLR [3]; Optical Ground Sensing [6]; TLEs [7, 8, 9]; DSN [10, 11, 12, 13, 14, 15]; Radio Ranging [16, 17, 18, 19, 20]; VLBI [21]; GNSS [22, 23, 24, 25, 26, 27]; DORIS/DIODE [28, 29, 30]; OpNav - TRN [31, 32]; Magnetometer + Sun Sensor [33]; Earth Horizon Sensor + Star Tracker [34]; Angles-Only (ARTMS) [35, 36]; Pulsar TOA [37]; ISL - Radio [38, 39, 40, 41].

## 1.1 Literature Review

Laser communications (lasercom) has advantages over radio frequency (RF) systems, with the primary advantage being better scalability of terminal data rates versus Size, Weight, and Power (SWaP) [42, 43, 44]. Lasercom is being considered for telecommunications and Earth observing satellites in civil, commercial, and defense space

applications. Lasercom links have been demonstrated numerous times, and there are plans to incorporate the technology into Earth constellations and next generation deep space exploration missions [45, 46, 47, 2]. Both NASA's planned deep space missions and commercial Earth orbiting mega-constellations will benefit from increased autonomy for navigation and stationkeeping to help mitigate risk and cost [46, 48]. Precision positioning, navigation, and timing (PNT) capability that is independent of the Global Positioning System (GPS) is necessary for improving the resilience of military assets [49]. Laser communications is already being considered as an alternative or supplement to existing RF systems for highly secure, jam-resistant, and high-data-rate military communications [50]. Optical wavelengths are not as affected by plasma scintillation in the ionosphere, which affects some RF wavelengths [51]. Also, RF wavelengths are subject to FCC licensing and regulation; whereas, optical wavelengths currently are not [52]. However, high-powered ground uplink lasers do require approval from the FAA and Laser Clearing House, in addition to operational safety procedures and engineering [52]. Also, optical wavelengths are absorbed by clouds, and atmospheric turbulence causes scintillation effects, so optical links to the ground are limited by weather [44]. This limitation can be mitigated by geographic diversity of optical ground stations [44].

Navigation using OISLs can be straightforwardly incorporated into missions that already intend to use OISLs for high data rate communications over long distances, such as hundreds to thousands of kilometers or more. The lasercom terminal already has the necessary hardware for OISL navigation measurements since it is the same hardware that is needed for communications, so adding the navigation capability does not require any significant changes to the system design [51, 67]. In particular, range is derived from the measured phase shift of the signal that occurs during free-space propagation [67]. The lasercom system also requires a pointing, acquisition, and tracking (PAT) system to precisely point its laser(s) and acquire and track the laser(s) from the partner terminal. This system measures the bearing angles of the line of sight between the two terminals, which can be combined with the inertial attitude measured by a star tracker to derive the bearing angles with regard to inertial space

Table 1.1: Selection of Satellite Laser Communications Technology Demonstration Missions. $P_{\text{Tx}}$ is the transmit laser power, and $\theta_{\text{FWHM}}$ is the transmit laser Full-Width Half-Maximum (FWHM) beam divergence angle. Note that for the intersatellite links, the launch year is the most recent launch year if multiple launches were involved. (*): Link not yet demonstrated.

| Launch Year | Mission: Satellite(s) | $P_{\text{Tx}}$ (mW) | Data Rate (Mbps) | $\theta_{\text{FWHM}}$ ($\mu$rad) | Ref. |
|---|---|---|---|---|---|
| | Links to Ground Stations | | | | |
| 2013 | LLCD: LADEE (Lunar) | 500 | 622 | 15 | [53] |
| 2014 | SOTA: SOCRATES (LEO) | 22 | 10 | 223 | [54] |
| 2016 | OSIRIS: BiROS (LEO) | 1000 | 1000 | 200 | [55] |
| 2017 | OCSD: Aerocube C (LEO) | 2000 | 200 | 873 | [56] |
| 2019 | VSOTA: RISESAT (LEO) | 80 | 0.1 | 1300 | [57] |
| 2022 | TBIRD (LEO) | 1000 | 200000 | 130 | [58, 59] |
| 2022 | CLICK: A (LEO) | 200 | 10 | 1300 | [60] |
| 2023 | DSOC: Psyche (en route to Asteroid Belt) | 4000 | 100 | 7.5 | [61, 62] |
| | Intersatellite Links | | | | |
| 1998 | SILEX: SPOT-4 to ARTEMIS (LEO-GEO) | 70 | 50 | 4 | [55] |
| 2001 | SILEX: ARTEMIS to SPOT-4 (LEO-GEO) | 35 | 2 | 7 | [63, 64] |
| 2002 | DLR-LCT: TerraSAR-X, NFIRE (LEO-LEO) | 1000 | 5625 | 9 | [64, 65] |
| 2005 | OICETS: OICETS to ARTEMIS (LEO-GEO) | 100 | 50 | 7 | [63, 64] |
| 2012 | EDRS: Sentinel 1A, Alphasat (LEO-GEO) | 5000 | 2800 | 8 | [64] |
| 2023 | LCRD: ISS, STPSat-6 (LEO-GEO) | 3000 | 1200 | 16 | [45, 66] |
| 2024* | CLICK: B, C (LEO-LEO) | 200 | 20 | 70 | [60] |

(see Figure 1-2). The combination of range and inertial bearing angles measurements give a complete description of the inertial relative position vector, and can therefore be used to estimate the absolute orbits of both spacecraft involved in the link with a high degree of precision [68, 32, 69].

An application of navigation using OISLs is for space communications infrastructure such as Earth communications constellations and deep space communications networks (e.g. Lunar Network and Mars Comms Relays). The OISL navigation capability could be used for autonomous stationkeeping, which has a typical requirement on the order of $10^2$ m [70]. OISL navigation could also be used to aid in time transfer for clock synchronization, with a typical requirement on the order of $10^1$ m and $10^1$ m/s [71]. OISL navigation could also be used to augment the capabilities of existing terrestrial navigation constellations (e.g. GPS or Galileo [72]) or to develop novel

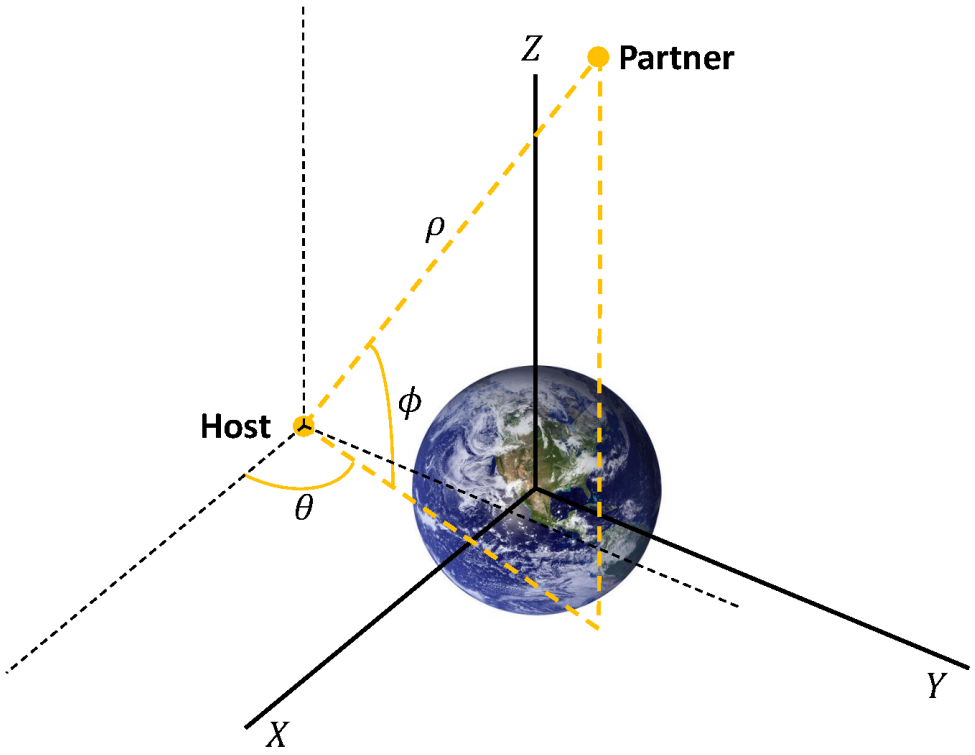


Figure 1-2: Depiction of the geometric range ($\rho$) and inertial bearings angles ($\theta, \phi$) of the partner satellite relative to the host satellite. The bearings angles are defined with respect to the inertial frame of the central body, which is depicted in Cartesian coordinates as $(X, Y, Z)$. The dotted lines represent the inertial reference frame translated to the position of the host satellite. This geometric picture is only an approximation, since light propagation between the two satellites is subject to relativistic effects. Developing a detailed, realistic measurement model will be the subject of Chapter 3.

deep space navigation constellations. For example, a network of spacecraft around the Moon with synchronized clocks would be able to provide Positioning, Navigation, and Timing (PNT) services for users, including other satellites and ground receivers. The network would form a "Space Clock", which would be synchronized with Earth time as needed, like GPS time [71].

The Cislunar Autonomous Positioning System (CAPS) has been developed in order to provide a provide a PNT service from the Artemis Lunar Gateway's near rectilinear halo orbit (NRHO) via two-way RF links to lunar users [41]. Lasercom links would provide higher accuracy range measurements in addition to precise angles measurements that improve the observability of the orbits [32]. The gateway service

could be augmented by additional satellites in a Lunar constellation equipped with lasercom terminals. For example, in proposed Lunar Network (LunaNet) concept [47], satellites placed in lunar orbit could provide additional network nodes for enhanced Lunar mission operations (see Figure 1-3). As the number of users increases both on the Lunar surface and in-orbit, the LunaNet constellation will offset demand on the Gateway's limited resources and fill-in its service outage periods. Further details on the LunaNet constellation can be found in Chapter 4.

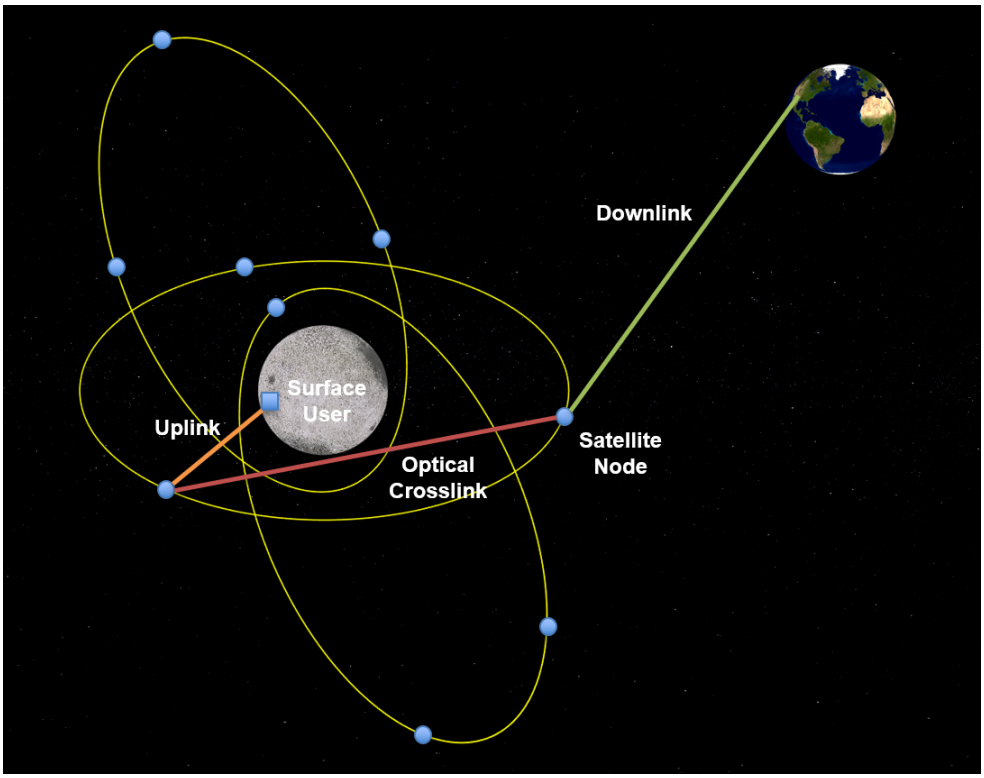


Figure 1-3: Example lunar communications relay via a Lunar Network constellation with optical intersatellite links. The uplinks and downlinks may also be optical depending on the mission design.

Navigation with intersatellite links can be applied to any mission with multiple satellites. Navigation using intersatellite measurements has received a substantial amount of attention over the years. One of the earliest papers that mentions the use of intersatellite laser communications is Yong et al. in 1982 [73], which perform covariance analysis that shows that the orbits could be observed from the intersatellite range and bearings measurements. The observability of the absolute orbits of

two satellites using relative position vector measurements within a Newtonian central body gravity model was proven by Markley in 1984 [32]. The relative position vector can be parameterized into range and spherical angles relative to the inertial coordinate system, called the inertial bearing angles. The signal Doppler shift can be measured to determine the range-rate as well. The Doppler and range measurements are effectively interchangable for problem observability, since they are not independent [74]. The choice of which one to use is determined by the available sensor technology that gives better performance. The combination of range/Doppler and bearings represents a relative position vector measurement. Many applications use RF range/Doppler-only or optical angles-only measurements. The range/Doppler-only case has been studied extensively [75, 40, 41, 76, 77]. Only a subset of the absolute orbit states (semi-major axis, eccentricity, and true anomaly) are observable within the Newtonian gravity model if only range/Doppler measurements are available; however, given perturbation forces and *a priori* information, the symmetries that prevent full state observability are broken [40]. The angles-only case has been studied extensively in the context of passive optical measurements for satellite formation flying [35, 36, 78, 79]. The angles-only case also has limited observability in the Newtonian gravity case, but with perturbations and optimized orbit geometries, the absolute orbits can be observed from angles-only measurements [36].

Psiaki extended Markley's analysis of the full relative position vector measurement case in 1999, performing observability analysis with J2 perturbations, assuming a retro-reflector LIDAR system with a camera [69]. Psiaki showed that the gravitational field components could be estimated using RF ranging and imaging a beacon with a camera, which would benefit gravitational science missions like GRAIL and GRACE [80]. Using range and angle sensors for navigation has been studied in various ways, mainly focusing on the J2 perturbations case and typically assuming RF ranging and a camera for bearings measurements [81, 82, 83, 84, 85]. Dave performed extensive analysis of the J2 perturbations case, assuming intersatellite laser communications, including Walker Delta type Earth constellations and notional Mars constellations [68].

Typically, measurement models are idealized geometric models with noise and biases added [68]. In this work, we perform systems analysis of the lasercom terminal to better understand how the measurement errors are related to the hardware design. We are also interested in the relativistic effects when modeling the light propagation in order to reduce systematic modeling errors in estimation. We will also investigate the effects of high order perturbing forces, which are often ignored in the literature. We will also expand on the constellation analysis conducted by previous authors by investigating new mega-constellations like Starlink as well as notional lunar and Mars constellations.

## 1.2 Thesis Contributions and Organization

The contributions of this dissertation are organized into three chapters. In Chapter 2, we perform a systematic observability analysis, using idealized OISL measurement models. We also analyze the sensitivity of orbit determination performance with respect to orbital geometries and to measurement parameters, and assess the impact of non-observable configurations for satellite constellations. In Chapter 3, we develop higher fidelity OISL measurement models that capture key system parameters and include relativistic effects. We develop the analytical relationships between optical communications system parameters (e.g. data rate) and OISL measurement capabilities. We analyze the sensitivity of the measurement model to the optical communications system design parameters. In Chapter 4, we conduct OISL navigation system performance analyses using high fidelity OISL measurement models for Earth, the Moon, and Mars constellation case studies using Cramer-Rao Lower Bound (CRLB) and Monte Carlo Kalman Filter simulations. We assess the effects of perturbations on performance for realistic force models with higher fidelity than $J_2$ gravity. We show how different crosslink configurations in the constellation network impact the system performance.

# Chapter 2

# Orbit Observability from OISLs

Orbit determination using OISL measurements can be modeled as a hybrid continuous-discrete system of the following form:

$$\dot{\mathbf{x}}(t) = \mathbf{f}(\mathbf{x}(t), \mathbf{u}(t), t) + G_\nu(t)\boldsymbol{\nu}(t) \tag{2.1a}$$

$$\mathbf{y}_k = \mathbf{h}(\mathbf{x}_k, \mathbf{w}_k) \tag{2.1b}$$

where $\mathbf{x}^T = [\mathbf{x}_s^T, \mathbf{p}^T]$, $\mathbf{x}_s \in \mathbb{R}^n$ is the set of satellite state vectors, $\mathbf{p} \in \mathbb{R}^p$ is a vector of additional parameters that are to be estimated, such as coefficients in the force model or measurement biases, $\boldsymbol{\nu}(t)$ is the process noise, $\mathbf{y}_k = \mathbf{y}(t_k) \in \mathbb{R}^q$ is the set of OISL measurements, $\mathbf{w}_k$ is the discrete measurement noise process, and $\mathbf{u} \in \mathbb{R}^r$ represents thrust from spacecraft manuevers. In this work, we are interested cases where all the satellites are orbiting a single, large celestial body like the Earth, the Moon, or Mars. We do not consider other scenarios in this work, such as flying around asteroids or interplanetary trajectories but leave these scenarios for future work. The orbital

dynamics of the satellites is:

$$\mathbf{x}_s^T = [\mathbf{x}_{s,0}^T, ..., \mathbf{x}_{s,N-1}^T] = [\mathbf{r}_0^T, \mathbf{v}_0^T, ..., \mathbf{r}_{N-1}^T, \mathbf{v}_{N-1}^T] \tag{2.2a}$$

$$\text{where for } i \in \{0, ..., N-1\} \tag{2.2b}$$

$$\dot{\mathbf{r}}_i(t) = \mathbf{v}_i(t) \tag{2.2c}$$

$$\dot{\mathbf{v}}_i(t) = -\frac{\mu}{\|\mathbf{r}_i(t)\|^3}\mathbf{r}_i(t) + \hat{\mathbf{a}}_p(t, \mathbf{r}_i(t), \mathbf{v}_i(t)) + \tilde{\mathbf{a}}_p(t) \tag{2.2d}$$

where the first acceleration term is Newtonian two-body gravity, $\hat{\mathbf{a}}_p$ are modeled perturbing accelerations, and $\tilde{\mathbf{a}}_p$ is the dynamics modeling error due to deliberate simplification and/or limitations in *a priori* knowledge. The dynamics modeling error is what is modeled as process noise for each spacecraft state. The spacecraft position and velocity vector components are Cartesian elements with respect to the local pseudo-inertial frame. For example, if the spacecraft are orbiting the Earth, then an Earth-Centered Inertial (ECI) frame is used, such as the Geocentric Celestial Reference Frame (GCRF) or the J2000 frame. There are $N$ spacecraft orbits to be estimated. The orbit determination algorithm is processed on-board the "host" spacecraft, which is state $\mathbf{x}_0$. There are $N-1$ partner spacecraft, indexed as $\{1, .., N-1\}$. All measurements are taken by the host spacecraft, so they are all relative to the host. Not all partner spacecraft are measured at each point in time. Depending on the technology capabilities, the host will be able to link with at most $M$ partners at a time. The simplest configuration is $M = 1$, one partner at a time. Note that this is a distributed estimation problem: each spacecraft independently estimates its state and the states of its partners on-board and in real-time. We do not assume any real-time transfer of state estimation information between the spacecraft or any centralized processing on the ground. The measurement vector for a particular time will be:

$$\mathbf{y}^T(t) = [\mathbf{y}_{i_1}^T(t), ..., \mathbf{y}_{i_m}^T(t)];\ \{i_1, ..., i_m\} \subset \{1, ..., N-1\},\ m \leq M \tag{2.3}$$

Simultaneous measurements are assumed to be taken using independently operating lasercom terminals with distinct hardware, so the noise vector can be similarly constructed:

$$\mathbf{w}_k^T = [\mathbf{w}_{k,i_1}^T, ..., \mathbf{w}_{k,i_m}^T] \tag{2.4}$$

where each of the $\mathbf{w}_{k,i} \in \mathbb{R}^l$ are independent noise vectors associated with each terminal. Some estimation algorithms, such as the extended Kalman filter, require the evaluation of the measurement gradient with respect to the state:

$$H = \frac{\partial \mathbf{h}}{\partial \mathbf{x}} = \begin{bmatrix} \frac{\partial \mathbf{h}_{i_1}}{\partial \mathbf{x}_s} & \frac{\partial \mathbf{h}_{i_1}}{\partial \mathbf{p}} \\ ... & ... \\ \frac{\partial \mathbf{h}_{i_m}}{\partial \mathbf{x}_s} & \frac{\partial \mathbf{h}_{i_m}}{\partial \mathbf{p}} \end{bmatrix} = \begin{bmatrix} H_{s,i_1} & H_{p,i_1} \\ ... & ... \\ H_{s,i_m} & H_{p,i_m} \end{bmatrix} \tag{2.5}$$

The gradient of the $i^{\text{th}}$ partner measurement with respect to the satellite states is:

$$H_{s,i} = \frac{\partial \mathbf{h}_i}{\partial \mathbf{x}_s} = \left[ \frac{\partial \mathbf{h}_i}{\partial \mathbf{x}_0}, \mathbf{0}_{q\times 6(i-1)}, \frac{\partial \mathbf{h}_i}{\partial \mathbf{x}_i}, \mathbf{0}_{q\times 6(N-i)} \right] \tag{2.6}$$

where $q = \dim(\mathbf{y}_k)$. The EKF is also formulated with an additive noise model, so the measurement model is expanded to first order in the noise argument as follows:

$$\mathbf{h}(\mathbf{x}_k, \mathbf{w}_k) \approx \mathbf{h}(\mathbf{x}_k, \mathbf{0}) + G_k \mathbf{w}_k \tag{2.7}$$

where

$$G_k = \frac{\partial \mathbf{h}}{\partial \mathbf{w}_k} = \begin{bmatrix} \frac{\partial \mathbf{h}_{i_1}}{\partial \mathbf{w}_k} \\ ... \\ \frac{\partial \mathbf{h}_{i_m}}{\partial \mathbf{w}_k} \end{bmatrix} \tag{2.8}$$

The gradient of the $i^{\text{th}}$ partner measurement with respect to the noise vector is:

$$\frac{\partial \mathbf{h}_i}{\partial \mathbf{w}_k} = \left[ \mathbf{0}_{q\times li}, \frac{\partial \mathbf{h}_i}{\partial \mathbf{w}_{k,i}}, \mathbf{0}_{q\times l(m-i-1)} \right] \tag{2.9}$$

where $l = \dim(\mathbf{w}_{k,i})$. $G_k$ is a block diagonal matrix with diagonal blocks given by:

$$G_{k,ii} = \frac{\partial \mathbf{h}_i}{\partial \mathbf{w}_{k,i}} \tag{2.10}$$

Since the measurements are independent, the covariance of the measurement noise vector $R_{\mathbf{w},k} = \mathbb{E}[\mathbf{w}_k \mathbf{w}_k^T]$ is also a block diagonal matrix, with diagonal blocks given by $R_{\mathbf{w},k,ii} = R_{k,i} = \mathbb{E}[\mathbf{w}_{k,i} \mathbf{w}_{k,i}^T]$. Therefore, the estimated covariance used by the EKF $\tilde{R}_k = G_k R_{\mathbf{w},k} G_k^T$ is a also block diagonal matrix, with diagonal blocks given by $\tilde{R}_{k,ii} = G_{k,ii} R_{k,i} G_{k,ii}^T$. Due to the block structures of both the covariance and the gradient $H$, simultaneous measurements can be processed by the EKF algorithm sequentially (one partner at a time), rather than concatenating them and processing them all in one step. Sequential processing reduces memory overhead for the algorithm.

## 2.1 Extended Kalman Filter

In general, the continuous-discrete Extended Kalman Filter (EKF) is formulated as follows [86]:

$$\hat{\mathbf{x}}(t_0) = \hat{\mathbf{x}}_0, P_0 = E[\tilde{\mathbf{x}}(t_0)\tilde{\mathbf{x}}^T(t_0)] \tag{2.11a}$$

$$K_k = P_k^- H_k^T (H_k P_k^- H_k^T + R_k)^{-1} \tag{2.11b}$$

$$H_k = \frac{\partial \mathbf{h}}{\partial \mathbf{x}}(\mathbf{x}_k^-) \tag{2.11c}$$

$$\hat{\mathbf{x}}_k^+ = \hat{\mathbf{x}}_k^- + K_k(\mathbf{y}_k - h(\mathbf{x}_k^-)) \tag{2.11d}$$

$$P_k^+ = (I - K_k H_k) P_k^- \tag{2.11e}$$

$$\dot{\hat{\mathbf{x}}}(t) = \mathbf{f}(\hat{\mathbf{x}}(t), \mathbf{u}(t), t) \tag{2.11f}$$

$$\dot{P}(t) = F(t)P(t) + P(t)F^T(t) + Q(t) \tag{2.11g}$$

$$F(t) = \frac{\partial \mathbf{f}}{\partial \mathbf{x}}(\mathbf{x}(t), \mathbf{u}(t), t) \tag{2.11h}$$

where $\hat{\mathbf{x}}_k^- = E[\mathbf{x}|\mathbf{y}_1, ..., \mathbf{y_{k-1}}]$ is the *a priori* state estimate, $\hat{\mathbf{x}}_k^+ = E[\mathbf{x}|\mathbf{y}_1, ..., \mathbf{y_k}]$ is the *a posteriori* state estimate, $\tilde{\mathbf{x}} = \hat{\mathbf{x}} - \mathbf{x}$ is the state estimate error, $P_k^- = E[\tilde{\mathbf{x}}_k^- \tilde{\mathbf{x}}_k^{-T}]$

is the *a priori* error covariance, $P_k^+ = E[\tilde{\mathbf{x}}_k^+ \tilde{\mathbf{x}}_k^{+T}]$ is the *a posteriori* error covariance, and $K_k \in R^{n \times m}$ is the Kalman gain. The process noise is modeled as an unbiased Gaussian white noise process: $\boldsymbol{\nu}(t) \sim N(\mathbf{0}, Q(t))$. Generally speaking, orbital dynamics modeling error exhibits non-random periodic behavior and biases. However, we will show in Chapter 4 that the EKF's unbiased Gaussian white noise model can be used successfully for orbital dynamics modeling error for OISL navigation. Equation 2.11a is the filter initialization step. Equations 2.11b-2.11e are called the correction or measurement-update step, which generate the *a posteriori* estimates. Equations 2.11f-2.11h give the state and covariance dynamics, which are the basis for the prediction or time-update step that generates the *a priori* estimates. These steps can be organized at a high level into the structure given in Algorithm 1. $\Gamma_{k,k-1}$ is defined

**Algorithm 1** Extended Kalman Filter Algorithm Structure

$[\hat{\mathbf{x}}_0^-, P_0^-] = \text{initialize}()$
**while** online **do**
  **return** $[\hat{\mathbf{x}}_k^+, P_k^+] = \text{correction}(\hat{\mathbf{x}}_k^-, P_k^-, \mathbf{y}_k)$
  $[\hat{\mathbf{x}}_{k+1}^-, P_{k+1}^-] = \text{prediction}(\hat{\mathbf{x}}_k^+, P_k^+)$
**end while**

using the state transition matrix [87]:

$$\Gamma_{k,k-1} = \Gamma(t_k, t_{k-1}) = \int_{t_{k-1}}^{t_k} \Phi(t_k, \tau) G_\nu(\tau) d\tau \tag{2.12}$$

In our case, $G_\nu = I$. There are other estimation algorithms such as the Iterated EKF (IEKF), the Unscented Kalman Filter (UKF), and the Particle Filter (PF). In Chapter 4, we will analyze the performance of the EKF for multiple case studies of OISL navigation within satellite constellations and show that an EKF with adaptive noise modeling is sufficient for performance close to the Cramer-Rao Lower Bound (CRLB) limit. Therefore, implementing one of these alternative, more computationally expensive algorithms will at best only have marginally better performance for OISL navigation in satellite constellations. This is why we limit our focus to the EKF in this work.

## 2.2 Filter Initialization

At the beginning of the spacecraft's mission or during a cold start reset, the navigation algorithm must be initialized using *a priori* information on the states of each spacecraft to be estimated, along with estimated uncertainties. Otherwise, the previous on-board estimate can be used. For the current analysis, we will assume that this information is relayed to the spacecraft via contact with the mission operations center (MOC). The MOC is assumed to have orbit information for each spacecraft generated via conventional means. This information is also needed in order to initialize the lasercom crosslink pointing, acquisition, and tracking (PAT) process. Depending on the divergence angle of the beacon laser stage, the laser is either pointed directly along the estimated line of sight or scanned over an angular region of uncertainty around the estimated line of sight [43]. Once the acquisition sensor receives the beacon, then the remainder of the typically multi-stage PAT process can be completed to establish and maintain the link. Note that this initialization uncertainty along with the convergence time requirement on the scanning process (e.g. less than 30 seconds) is one of the factors that can determine the minimum link range for a lasercom crosslink. Other factors include sensor saturation limits and maximum slew rates. The initial *a priori* information that is assumed for the analyses in this work is based on conservative estimates of RMS errors from conventional RF TT&C links both to Earth-orbiting satellites [16, 17] and to deep space satellites using the DSN [10, 11, 12, 13, 14, 15]: 1 km in each position axis and 100 mm/s in each velocity axis 1-sigma with respect to body-centered inertial coordinates.

## 2.3 Idealized Geometric Measurements

The analyses carried out in the literature to date use idealized geometric measurement models of the range, range-rate, and/or bearings angles. In this section, we briefly cover the mathematics of the idealized geometric model, which we will use for observability analysis. The geometric measurements are a set of parameters that can be

derived from the relative position and velocity vectors between a partner spacecraft and the host spacecraft:

$$\boldsymbol{\rho}_i = \mathbf{r}_i - \mathbf{r}_0 = (x_i - x_0)\mathbf{E}_x + (y_i - y_0)\mathbf{E}_y + (z_i - z_0)\mathbf{E}_z \tag{2.13a}$$

$$\dot{\boldsymbol{\rho}}_i = \mathbf{v}_i - \mathbf{v}_0 = (\dot{x}_i - \dot{x}_0)\mathbf{E}_x + (\dot{y}_i - \dot{y}_0)\mathbf{E}_y + (\dot{z}_i - \dot{z}_0)\mathbf{E}_z \tag{2.13b}$$

where $\{\mathbf{E}_x, \mathbf{E}_y, \mathbf{E}_z\}$ forms an orthonormal basis for the local pseudo-inertial frame. These vectors can be parameterized in terms of range ($\rho$), bearings angles ($\theta, \phi$), range-rate ($\dot{\rho}$), and the angular rate vector ($\boldsymbol{\omega}$):

$$\boldsymbol{\rho}_i(\rho_i, \theta_i, \phi_i) = \rho_i \hat{\boldsymbol{\rho}}_i(\theta_i, \phi_i) \tag{2.14a}$$

$$\dot{\boldsymbol{\rho}}_i(\dot{\rho}_i, \theta_i, \phi_i, \boldsymbol{\omega}_i) = \dot{\rho}_i \hat{\boldsymbol{\rho}}_i(\theta_i, \phi_i) + \boldsymbol{\omega}_i \times \hat{\boldsymbol{\rho}}_i(\theta_i, \phi_i) \tag{2.14b}$$

$$\text{where } \hat{\boldsymbol{\rho}}_i(\theta_i, \phi_i) = \cos(\theta_i)\cos(\phi_i)\mathbf{E}_x + \sin(\theta_i)\cos(\phi_i)\mathbf{E}_y + \sin(\phi_i)\mathbf{E}_z \tag{2.14c}$$

The measurement taken with the $i^{\text{th}}$ partner is:

$$\mathbf{y}_i^T = [\rho_i, \theta_i, \phi_i, \dot{\rho}_i] + \mathbf{b}^T + \mathbf{w}_\mathbf{y}^T \tag{2.15a}$$

$$\rho_i = \|\mathbf{r}_i - \mathbf{r}_0\| \tag{2.15b}$$

$$\theta_i = \tan^{-1}\left(\frac{y_i - y_0}{x_i - x_0}\right) \in [0, 2\pi) \tag{2.15c}$$

$$\phi_i = \sin^{-1}\left(\frac{z_i - z_0}{\|\mathbf{r}_i - \mathbf{r}_0\|}\right) \in [-\pi/2, \pi/2] \tag{2.15d}$$

$$\dot{\rho}_i = (\mathbf{v}_i - \mathbf{v}_0) \cdot \frac{\mathbf{r}_i - \mathbf{r}_0}{\|\mathbf{r}_i - \mathbf{r}_0\|} \tag{2.15e}$$

where $\mathbf{b}$ is measurement bias, and $\mathbf{w}_i$ is measurement noise. The measurement noise is modeled as a Gaussian white noise process: $\mathbf{w}_i \sim N(0, R_i)$; $R_i = \text{diag}(\sigma_\rho^2, \sigma_\theta^2, \sigma_\phi^2, \sigma_{\dot{\rho}}^2)$. The noise covariance is modeled as fixed and the same for all partners. We will develop a more detailed measurement noise model in Chapter 3 and show that a Gaussian white noise model is a reasonable approximation for OISL measurement modeling. The measurement components can be re-parameterized in terms of the

relative position and velocity vectors as follows:

$$\rho_i = \|\boldsymbol{\rho}_i\| \tag{2.16a}$$

$$\theta_i = \tan^{-1}\left(\frac{\boldsymbol{\rho}_i \cdot \mathbf{E}_y}{\boldsymbol{\rho}_i \cdot \mathbf{E}_x}\right) \tag{2.16b}$$

$$\phi_i = \sin^{-1}(\hat{\boldsymbol{\rho}}_i \cdot \mathbf{E}_z) \tag{2.16c}$$

$$\dot{\rho}_i = \dot{\boldsymbol{\rho}}_i \cdot \hat{\boldsymbol{\rho}}_i \tag{2.16d}$$

The gradient expressions are given in Appendix A.

## 2.4 Analytical Observability

Although the general OISL navigation problem is not amenable to analytical observability analysis methods, there is a simplified form of the problem that is. This is the two satellite case using a Newtonian two-body gravitational model with relative position vector measurements. The observability results for this case were derived by Markley [32],and the results are summarized here for reference. The model is as follows:

$$\dot{\mathbf{x}} = \mathbf{f}(\mathbf{x}) = \begin{bmatrix} \dot{\mathbf{r}}_1 \\ \dot{\mathbf{v}}_1 \\ \dot{\mathbf{r}}_2 \\ \dot{\mathbf{v}}_2 \end{bmatrix} = \begin{bmatrix} \mathbf{v}_1 \\ -\frac{\mu}{\|\mathbf{r}_1\|^3}\mathbf{r}_1 \\ \mathbf{v}_2 \\ -\frac{\mu}{\|\mathbf{r}_2\|^3}\mathbf{r}_2 \end{bmatrix} \tag{2.17a}$$

$$\mathbf{y} = \boldsymbol{\rho}_{12} = \mathbf{r}_2 - \mathbf{r}_1 \tag{2.17b}$$

The linear observability matrix is defined as:

$$O_k^T(t) = [N_0^T(t), ..., N_{k-1}^T(t)] \tag{2.18a}$$

$$\text{where } N_0 = \frac{\partial \mathbf{y}}{\partial \mathbf{x}} \tag{2.18b}$$

$$\text{and } N_{i+1} = N_i \frac{\partial \mathbf{f}}{\partial \mathbf{x}} + \dot{N}_i \tag{2.18c}$$

The observability criterion is:

$$\exists t^* \in [t_0, t_1], \exists k \in \mathbb{N} \text{ such that } \text{rank}(O_k^T(t^*)) = \dim(\mathbf{x}). \tag{2.19}$$

The non-observability criterion is the inverse of the observability criterion:

$$\forall t^* \in [t_0, t_1], \forall k \in \mathbb{N} \text{ such that } \text{rank}(O_k^T(t^*)) < \dim(\mathbf{x}). \tag{2.20}$$

Markley demonstrated a recursive approach to generate the observability matrix and showed how substituting certain geometric constraints leads to non-observability. These are:

$$1)\ \|\mathbf{r}_1(t)\| = \|\mathbf{r}_2(t)\|\ \forall t \tag{2.21a}$$

$$\implies a_1(t) = a_2(t)\ \&\ e_1(t) = e_2(t)\ \forall t \tag{2.21b}$$

$$\text{and either 2-a or 2-b:} \tag{2.21c}$$

$$2\text{-a})\ \mathbf{h}_1(t) \times \mathbf{h}_2(t) = 0\ \forall t \tag{2.21d}$$

$$\implies \Omega_1(t) = \Omega_2(t)\ \&\ |i_2(t) - i_1(t)| \in \{0, \pi\}\ \forall t \tag{2.21e}$$

$$2\text{-b})\ (\mathbf{r}_1(t) \pm \mathbf{r}_2(t)) \times \mathbf{c} = 0\ \forall t \tag{2.21f}$$

$$\implies \left(|\Omega_2(t) - \Omega_1(t)| = \pi \text{ or } \frac{d}{dt}(i_2(t) - i_1(t)) = 0\right) \tag{2.21g}$$

$$\text{and } \omega_1(t) = \omega_2(t) \text{ and } M_1(t) = M_2(t)\ \forall t \tag{2.21h}$$

where $\mathbf{h} = \mathbf{r} \times \mathbf{v}$ is the orbit specific angular momentum vector, and $\mathbf{c}$ is an arbitrary constant vector. If (1) and ((2-a) or (2-b)), then the system is non-observable. Therefore, if not (1) or not ((2-a) and (2-b)), then the system is observable. (1) is true if the Keplerian shape parameters (semi-major axis and eccentricity) are the same for both satellites. (2-a) is true if the satellites share the same orbital plane. If (1) and (2-a), then the satellites share the same orbit. In this case, if the momentum axes are anti-aligned, the satellites are on a collision course. (2-b) is true if the satellite orbits only differ by an inclination offset or by an offset in RAAN of 180°. This is illustrated Figure 2-1. Note that that if (1) and the position vector difference is constant, the

satellites are on a collision course. The absolute orbit observability was be explained conceptually by Psiaki [69] by considering the system to be a gravity gradiometer, with the two spacecraft being the proof masses of two accelerometers. The second derivative of the relative position measurements is the relative acceleration, which is caused by the gravity gradient. The gravity gradient is a function of the absolute position of the midpoint between the two spacecraft. This is why a sequence of relative position measurements can be used to determine the absolute orbits of the two spacecraft.

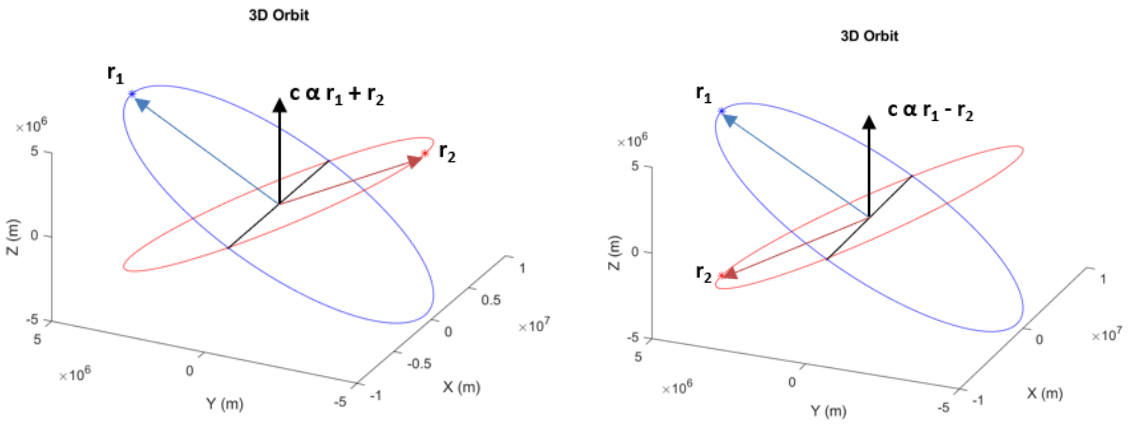


Figure 2-1: (2-b) Non-observable configurations where for (a) initial Kepler elements differ only by 180 deg in RAAN, and for (b) initial Kepler elements differ only in inclination.

## 2.5 Numerical Observability

For the general problem, numerical methods must be used to assess observability. One approach is to compute the condition number of observability Grammian [88]:

$$W = \sum_{k=0}^{M-1} \Phi^T(t_k, t_0) H_k^T H_k \Phi(t_k, t_0) \tag{2.22}$$

where $M$ is the number of measurements and $\Phi(t_k, t_0)$ is the system state transition matrix from the initial time $t_0$ to the $k^{\text{th}}$ measurement time $t_k$, which satisfies the

following differential equation:

$$\dot{\Phi}(t, t_0) = \frac{\partial \mathbf{f}(\mathbf{x}(t), \mathbf{u}(t), t)}{\partial \mathbf{x}} \Phi(t, t_0);\ \Phi(t_0, t_0) = I \tag{2.23}$$

If the condition number is sufficiently large, then the estimation problem is ill-conditioned and exhibits low observability. An upper bound on the condition number for the observability of orbit determination problems of the type we are interested in is $10^{16}$ [78]. An alternative approach is to directly estimate the information matrix via the Cramer-Rao lower bound (CRLB) of the state error covariance ($P_k$) of an estimator [89]:

$$P_k \geq P_k^* = J_k^{-1} \tag{2.24}$$

where $P_k^*$ is the CRLB for the error covariance, and $J_k$ is the Fisher information matrix, which can be computed recursively by:

$$J_k = (\Phi_{k,k-1}^{-1})^T J_{k-1} \Phi_{k,k-1}^{-1} + H_k^T \tilde{R}_k^{-1} H_k;\ J_0 = P_0^{-1} \tag{2.25}$$

where $P_0$ is the error covariance of the initial *a priori* state estimate. This is the information form of the EKF information matrix algorithm without process noise. Note that in this form, the CRLB can be initialized with zero information $J_0 = 0$. Also, the state transition matrix $\Phi_{k,k-1} = \Phi(t_k, t_{k-1})$ and the measurement gradient $H_k$ are evaluated using the true state $\mathbf{x}$. The linearized measurement noise is modeled as an unbiased Gaussian white noise process $G_k \mathbf{w}_k \sim N(\mathbf{0}, \tilde{R}_k = G_k R_{\mathbf{w},k} G_k^T)$. For the purposes of lower bounding the error, the measurement bias is taken to be zero. The CRLB recursion can also be computed using the covariance matrix $P_k^*$:

$$P_k^* = (I - K_k H_k)(\Phi_{k,k-1} P_{k-1}^* \Phi_{k,k-1}^T);\ P_0^* = P_0 \tag{2.26a}$$

$$K_k = P_k^* H_k^T (\tilde{R}_k + H_k P_k^* H_k^T)^{-1} \tag{2.26b}$$

where $K_k$ is the Kalman gain matrix. This recursion is straightforward to derive from Equation 2.25 and the matrix inversion lemma. It is the standard EKF covariance

algorithm without process noise, evaluated at the true state. To compute the CRLB with process noise, the algorithm is modified as:

$$P_k^* = (I - K_k H_k)(\Phi_{k,k-1} P_{k-1}^* \Phi_{k,k-1}^T + Q_k);\ P_0^* = P_0 \tag{2.27}$$

The process noise $\boldsymbol{\nu}$ can be modeled as an unbiased Gaussian white noise process with auto-correlation $\mathbb{E}[\boldsymbol{\nu}(t)\boldsymbol{\nu}(\tau)^T] = Q(t)\delta(t-\tau)$. The discrete sample covariance $Q_k$ is [87]:

$$Q_k = \int_{t_{k-1}}^{t_k} \Phi(t,\tau) G_\nu(\tau) Q(\tau) G_\nu^T(\tau) \Phi^T(t,\tau) d\tau \tag{2.28}$$

Alternatively, the process noise can be modeled as an unbiased Gaussian white noise sequence with auto-correlation $\mathbb{E}[\boldsymbol{\nu}(t_i)\boldsymbol{\nu}(t_j)^T] = Q(t_k)\delta_{ij}$ where $\delta_{ij}$ is the Kronecker delta. The discrete sample covariance $Q_k$ is then [87]:

$$Q_k = \Gamma_{k,k-1} Q(t_k) \Gamma_{k,k-1}^T \tag{2.29a}$$

$$\Gamma_{k,k-1} = \int_{t_{k-1}}^{t_k} \Phi(t_k,\tau) G_\nu(\tau) d\tau \tag{2.29b}$$

This is the model that we use.

The noise values used for the following analyses are shown in Table 2.1. They are based on systems analysis in Chapter 3. These noise values are static for simplicity in the observability analysis. These are conservative range and range-rate values based on a low-rate 40 Mbps crosslink at long range. As described in detail in Chapter 3, the range and range-rate noise values generally scale with range and inversely with data rate. We compute dynamic noise values as a function of intersatellite range for the performance analysis in Chapter 4. The angles value is from the peak error value for either azimuth ($\theta$) or elevation ($\phi$) (they are roughly the same but azimuth is slightly higher). The angles noise model is based on a pointing-acquisition and tracking system and attitude determination system noise analysis. For this analysis, the measurements are unbiased ($\mathbf{b} = \mathbf{0}$). The process noise is chosen based on values from the literature [78] and simulations of the process noise sensitivity. We choose a low process noise value: high force model accuracy. We conduct detailed process noise

analysis for less accurate force models in Chapter 4. Since we are using the covariance algorithm, we cannot initialize with zero information, we can set the initial covariance to very large values. The covariance is initialized as as diagonal matrix with position and velocity component errors as in Table 2.1: the first three diagonal elements for each satellite are $(100 \text{ km})^2$, and the last three diagonal elements are $(100 \text{ m/s})^2$. The initial errors would be less if initialized using radio TT&C tracking, but we are interested in observability rather than performance in this chapter, so we introduce large errors to make sure that the covariance doesn't assume an unrealistic local minimum due to good initialization.

Table 2.1: General Parameters Used for Observability Simulations

| CRLB Algorithm | Covariance Form |
|---|---|
| Initial Position Component Std. Dev. | 100 km |
| Initial Velocity Component Std. Dev. | 100 m/s |
| Acceleration Process Noise ($\sigma_a = \sigma_q$) | $\sqrt{10^{-15}} \approx 3.16 \times 10^{-8}$ m/s$^2$ |
| Range Noise ($\sigma_\rho$) | 1 cm |
| Bearings Noise ($\sigma_\theta = \sigma_\phi$) | 11 $\mu$rad (2.26 arcsec) |
| Range-Rate Noise ($\sigma_{\dot{\rho}}$) | 0.2 mm/s |
| Measurement Bias ($\mathbf{b}$) | $\mathbf{0}$ |

The observability metrics we use are derived from $P_k^*$. The first is the condition number, which is the ratio of the largest singular value to the smallest. Note that since $P_k^* = J_k^{-1}$: $\text{CN}(J_k) = \text{CN}(P_k^*)$. In addition, we examine the elements of the diagonal of $P_k^*$ for each satellite. Let $P_{ii,k}^*$ be the diagonal block of $P_k^*$ associated with the $i^{th}$ satellite. Then the position uncertainty ($\sigma_{r,i}$) and velocity uncertainty ($\sigma_{v,i}$) metrics are defined as:

$$\sigma_{r,i,k} \equiv \sqrt{\sigma_{x,i,k}^2 + \sigma_{y,i,k}^2 + \sigma_{z,i,k}^2} \tag{2.30a}$$

$$\sigma_{v,i,k} \equiv \sqrt{\sigma_{v_x,i,k}^2 + \sigma_{v_y,i,k}^2 + \sigma_{v_z,i}^2} \tag{2.30b}$$

$$\text{where } [\sigma_{x,i,k}^2, \sigma_{y,i,k}^2, \sigma_{z,i,k}^2, \sigma_{v_x,i,k}^2, \sigma_{v_y,i,k}^2, \sigma_{v_z,i,k}^2] = \text{diag}(P_{ii,k}^*) \tag{2.30c}$$

Note that $\sigma_{r,i,k}/\sqrt{3} = \text{RMS}(\sigma_{x,i,k}, \sigma_{y,i,k}, \sigma_{z,i,k})$ and $\sigma_{v,i}/\sqrt{3} = \text{RMS}(\sigma_{v_x,i,k}, \sigma_{v_y,i,k}, \sigma_{v_z,i,k})$. Statistics for these metrics over the simulation interval $[t_0, t_f]$ are computed over the

time interval $[t_s, t_f]$, where $t_s$ is the the settling time. Data over $[t_0, t_s)$ are excluded because the algorithm has not yet converged. We define the effective settling time $t_s$ as the time after which the value of the largest singular value ($\sigma_P^{\max}$) of the system covariance matrix ($P_k^*$) is within one order of magnitude of its final value at $t_f$. This definition is chosen simply to exclude the initial transient behavior. Values for the settling time are given along with the other metrics when they are presented.

$$t_s : \forall t > t_s \ \& \ t <= t_f, \ |\log_{10}(\sigma_P^{\max}(t_f) - \sigma_P^{\max}(t))| < 1 \tag{2.31}$$

It is useful to smooth the $\sigma_P^{\max}(t)$ timeseries using a moving maximum filter to mitigate the effects of oscillating solutions, which occur when the problem is weakly observable.

## 2.6 Measurement Configurations

In this section, we compare the observability of different subsets of the three measurement types: range, Doppler, and bearings. Navigation using intersatellite range and Doppler measurements has been studied extensively in the context of radio measurements [41, 38, 39]. It is a known result that using only range and/or Doppler intersatellite measurements requires perturbations and *a priori* knowledge to eliminate symmetries in the Newtonian force model that cause the problem to become unobservable [41]. For that reason, we will use a LEO-LEO link example since the perturbations from the higher order asymmetries in the gravitational field are sufficient for observability [41]. The initialization will be with high uncertainty (100 km and 100 m/s) to show how the observability is affected by the measurement configuration and presence of perturbations. The simulation duration is 1 day with 10 second measurement sampling. The three different force models used are Newtonian gravity without perturbations, Newtonian gravity with the inclusion of the J2 aspheric gravitational potential term (degree 2 x order 0), and lastly the inclusion of the aspheric potential terms up to $24^{\text{th}}$ degree and order (24x24). The process noise is held fixed for each so that the results focus on the effects of the perturbations on the problem

observability rather than the accuracy of the force model. The results are summarized in Table 2.2.

Table 2.2: Observability for Subsets of Measurement Types. Note: $l^{99}_{CN(P)}$ is the 99$^{\text{th}}$ percentile of the condition number of the covariance matrix, and $\sigma_{r,rms}$ (m) and $\sigma_{v,rms}$ (mm/s) are the RMS position and velocity uncertainties for both satellites. The cells are colored red (unobservable), yellow (observable with high uncertainty), and green (observable with low uncertainty).

| Config. | Newtonian | | | J2 | | | Aspheric 24x24 | | |
|---|---|---|---|---|---|---|---|---|---|
| | $l^{99}_{CN(P)}$ | $\sigma_{r,rms}$ | $\sigma_{v,rms}$ | $l^{99}_{CN(P)}$ | $\sigma_{r,rms}$ | $\sigma_{v,rms}$ | $l^{99}_{CN(P)}$ | $\sigma_{r,rms}$ | $\sigma_{v,rms}$ |
| $\rho$ | 18.13 | $8 \cdot 10^4$ | $9 \cdot 10^4$ | 18.14 | $6 \cdot 10^4$ | $7 \cdot 10^4$ | 10.16 | 30.36 | 33.21 |
| $\dot{\rho}$ | 17.81 | $8 \cdot 10^4$ | $9 \cdot 10^4$ | 15.67 | $5 \cdot 10^4$ | $5 \cdot 10^4$ | 10.52 | 114.29 | 123.13 |
| $(\rho, \dot{\rho})$ | 18.66 | $8 \cdot 10^4$ | $9 \cdot 10^4$ | 18.12 | $5 \cdot 10^4$ | $5 \cdot 10^4$ | 10.34 | 31.60 | 34.13 |
| $(\theta, \phi)$ | 14.33 | $5 \cdot 10^4$ | $5 \cdot 10^4$ | 13.07 | $8 \cdot 10^3$ | $8 \cdot 10^3$ | 12.54 | $6 \cdot 10^3$ | $6 \cdot 10^3$ |
| $(\rho, \theta, \phi)$ | 7.70 | 2.34 | 2.57 | 7.41 | 1.93 | 2.11 | 7.41 | 1.93 | 2.11 |
| $(\theta, \phi, \dot{\rho})$ | 7.03 | 2.35 | 2.58 | 7.00 | 2.29 | 2.50 | 6.99 | 2.29 | 2.50 |
| $(\rho, \theta, \phi, \dot{\rho})$ | 7.70 | 2.34 | 2.57 | 7.41 | 1.93 | 2.11 | 7.41 | 1.93 | 2.11 |

As expected, the range-only, Doppler-only, and range-Doppler cases are all unobservable for the Newtonian and J2 cases: the log condition number metric is relatively high (should be less than 16), and the position and velocity uncertainties are similar to the initial uncertainty ($10^5$ m and $10^5$ mm/s). With the perturbation effects of the 24x24 gravity field, these cases become observable. The bearings-only case with Newtonian gravity is marginally better than unobservable (log condition number is 14.33). However, with J2 or 24x24 perturbations, observability improves to a few kilometers uncertainty, but does not reach the precision of the range or Doppler cases. The uncertainty would improve somewhat if the initialization error was smaller. On the other hand, there is a significantly better observability for the range-bearings, Doppler-bearings, and range-Doppler-bearings cases. They all exhibit low condition numbers and low position and velocity uncertainties (on par with GPS tracking in LEO). The system also becomes much less sensitive to perturbations with these configurations. These configurations all exhibit similar performance and are mostly insensitive to the effects of perturbations. It appears from the results that the range and Doppler measurements are redundant, since there is no change in observability between the range-bearings and range-Doppler-bearings. In fact, these measurement

types are not independent: a Doppler range-rate measurement is equivalent to taking the difference of two range measurements and dividing by the time interval (in the limit of small time intervals, this is the time derivative). It is known that combining these measurements does not theoretically improve performance [74, 38]. Whichever of the two (range or Doppler) has the lower effective measurement error will dominate the estimation performance. In this case of LEO-LEO OISLs, the range measurement has the lower effective measurement error, though only by a small amount (about 0.3 m and 0.4 mm/s). Turan compared the two for cislunar intersatellite radio measurements and also found that range measurements were more effective for navigation [38]. On the other hand, ground-based radio tracking systems like the Deep Space Network (DSN) have historically relied highly accurate Doppler measurements [74, 90]. In summary, given that the default hardware for optical communications terminals has the capability for range/Doppler and bearings measurements, they have a substantial technological advantage over past systems, which would require combinations of radio range/Doppler and radio-phase or optical angles sensors to have the same level of observability for absolute orbit determination using intersatellite measurements.

## 2.7 Navigation within Satellite Constellations

In a single-shell satellite constellation following the typical Walker Delta or Walker Star configuration, the satellites are designed to be in circular orbits with the same orbital radius and inclination. The configuration is defined by $i : N_s/N_p/f$ where $i$ is the inclination of the planes, $N_s$ is the total number of satellites, $N_p$ is the number of planes, and $f$ is a phasing parameter that determines the relative mean anomaly between neighboring satellites in adjacent planes [91]. For a Walker Delta constellation, the ascending nodes of the planes are spaced evenly over 360°. In a Walker Star constellation, the ascending nodes of the planes are spaced evenly over 180°. We are interested in constellations that feature inter-satellite links. For example, the Iridium NEXT LEO constellation (Walker-Star 86.4° : 66/6/2) has Ka-band radio

intersatellite links. Optical intersatellite links are planned for the Starlink phase one LEO constellation (Walker-Delta 53° : 1584/22/17 [92]) in the latest versions of its satellites [2, 68]. The inter-connectivity design in the constellation is a careful trade

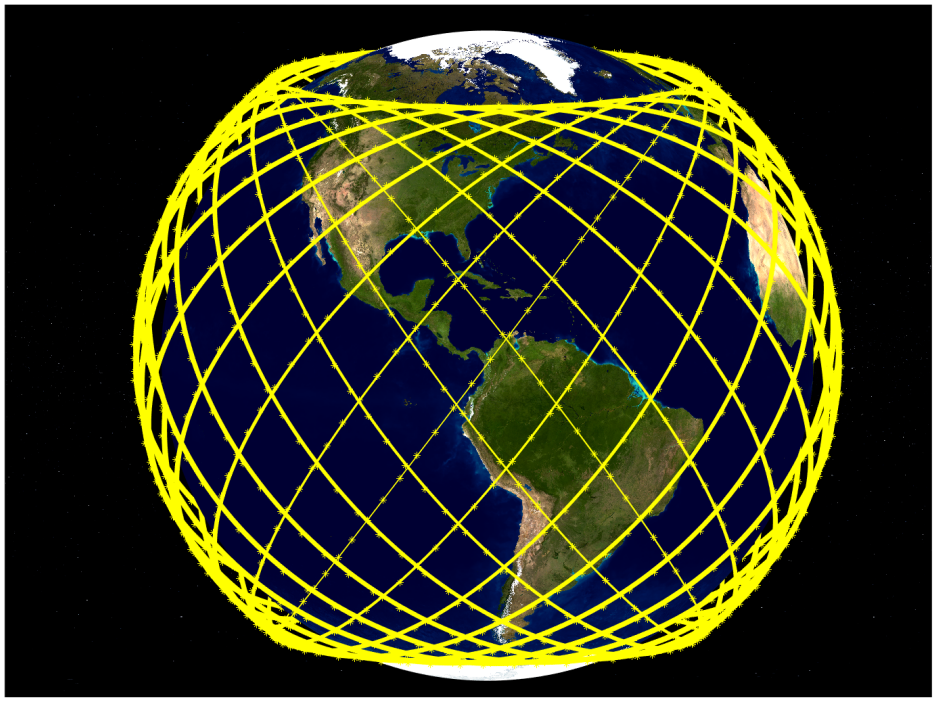

Figure 2-2: Starlink Constellation (Phase 1) (Walker-Delta 53° : 1584/22/17 model [92] rendered using MATLAB R2023b in the local inertial frame)

between satellite design complexity and the mission objectives, such as low-latency global data routing. For a LEO communications constellation like Starlink or Iridium, the satellites are designed to support up to four intersatellite links: two to the co-planar satellites ahead and behind the host and one for a satellite in each of the two adjacent planes [2, 91]. For example, see Figure 4-1. Note that adjacent planes are the planes that are incrementally offset in RAAN, not the intersecting planes, which can also have nearby satellites, but since they are crossing the orbital plane of the host, their relative velocity is high which is difficult to design terminals for. Hence the host is only communicating with satellites that are moving with it (e.g. if the host is ascending/descending in latitude, so are its four partners). For a Walker-Star, this only includes satellites on the same "side" of the constellation (half the constel-

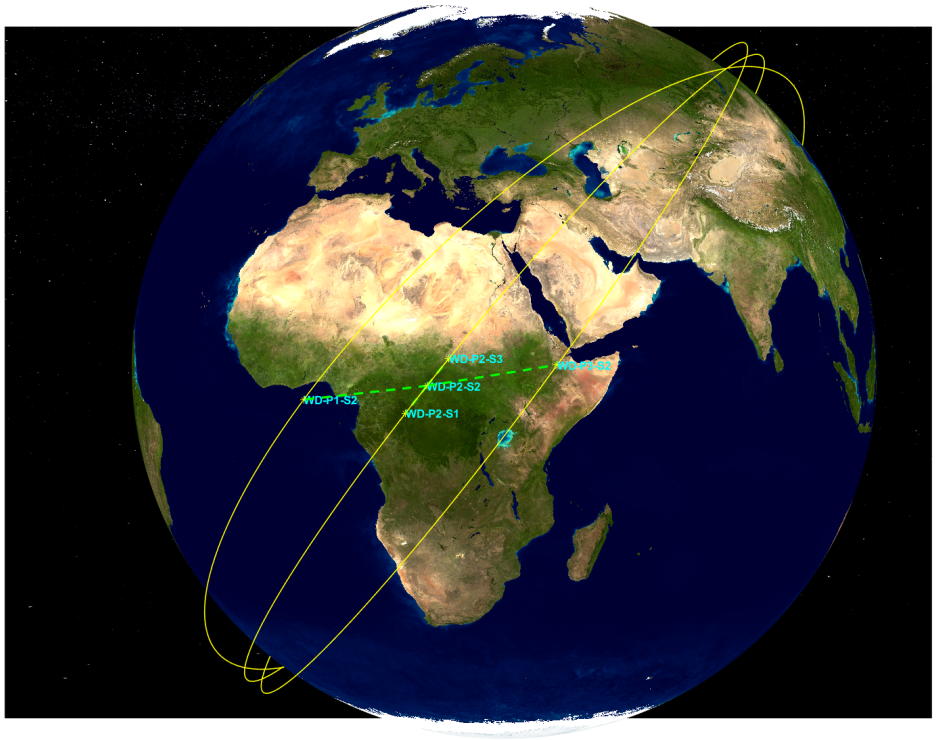


Figure 2-3: LEO Constellation Example Scenario: Starlink satellite with four simultaneous link partners. The host satellite is in the second plane and the second slot (WD-P2-S2). The co-orbital partners are WD-P2-S1 and WD-P2-S3. The partners in the same slots in the adjacent planes are WD-P1-S2 and WD-P3-S2. See Table 2.3 for the orbital elements.

lation is ascending in latitude, and the other half is descending). This means that the satellites on the seam of the Walker Star only have three connections. Theoretically, with perfect station keeping, the co-planar links in these examples would be unobservable according to the Newtonian gravity analysis. In reality, the satellites do not exactly satisfy the unobservability criterion, so the co-planar links are observable, but the performance may be degraded depending on the magnitude of the offsets in the orbital elements from the unobservable configuration. We will show later that given small offsets from the unobservable configuration, the problem becomes observable: the configuration behaves like a singularity condition (we will sometimes refer to these configurations as singular configurations). Regardless, the cross-planar links are observable according to the Newtonian gravity analysis since they are offset by $\Delta\Omega \neq 180°$. Assuming the co-planar satellites do satisfy the unobservability criterion

such that they are not practically observable, we will show that including even one observable link makes the entire system observable. This is true because if the host's absolute orbit is observable, then relative position measurements (range and inertial bearings) to any other satellite give its absolute orbit also. This is a general feature of this problem: if the set of states to be estimated includes at least one observable pair of satellite orbits, then all of the other satellites' orbits will be observable.

We present CRLB results for the LEO Starlink crosslink example to illustrate our discussion so far. For practical analysis, a single satellite from the constellation is selected as the host, and its partners are selected based on typical connectivity for the constellation as in Figure 2-3. Note that all simulations in this work are run using custom code written in MATLAB (version R2023b), with all basic orbital mechanics subroutines being handled via the Orekit library (version 11.3) [93, 94]. The initial orbital elements for each of the satellites are given in Table 2.3. First, we consider the

Table 2.3: Initial orbit elements for Starlink satellites selected for analysis from Walker-Delta Constellation 53° : 1584/22/17 [92]. The ($a$,$e$,$i$,$\omega_p$) coordinates are based on TLE data for STARLINK-1515 from June 2022.

| Satellite | $a$ (km) | $e$ | $i$ (deg) | $\Omega$ (deg) | $\omega_p$ (deg) | $M$ (deg) |
|---|---|---|---|---|---|---|
| WD-P2-S2 (Host) | 6925.4 | $1.43 \times 10^{-4}$ | 53.06 | 16.36 | 78.60 | 8.86 |
| WD-P1-S2 | 6925.4 | $1.43 \times 10^{-4}$ | 53.06 | 0 | 78.60 | 5.00 |
| WD-P2-S1 | 6925.4 | $1.43 \times 10^{-4}$ | 53.06 | 16.36 | 78.60 | 3.86 |
| WD-P2-S3 | 6925.4 | $1.43 \times 10^{-4}$ | 53.06 | 16.36 | 78.60 | 13.86 |
| WD-P3-S2 | 6925.4 | $1.43 \times 10^{-4}$ | 53.06 | 32.73 | 78.60 | 12.72 |

observability of different link types. The results are summarized in Table 2.4. The co-orbital link with perfect station keeping is a singular configuration for the problem as predicted analytically. However, in reality, there is imperfect station keeping. For example, the station keeping error for the Starlink constellation is on average 370 m in position and 0.52 m/s in velocity (1-sigma) [95]. Of the six Keplerian elements, only offsets to $(a, e, \Omega, \omega_p)$ can restore observability in the co-orbital case. A pure offset to the inclination or the mean anomaly is still a singular configuration; though these can have an effect in combination with offsets to the other elements, which we will see later. Since this orbit is near-circular, offsets to the argument of perigee have little

effect, so the main offsets to consider are to $(a, e, \Omega)$. Using the jacobian coordinate transformation for WD-P2-S2, the 1-sigma station keeping errors in these elements are approximately 695 m, $8.4 \times 10^{-5}$, and $2.8 \times 10^{-3}$ degrees, respectively. We will analyze the observability sensitivity near singular configurations in more depth in Section 2.8. Also, we will only consider static offsets to the initial conditions. In reality, station keeping is a dynamic process, with periodic correction manuevers taking place over time; however, simulating this long term behavior is beyond the scope of this work, so we only include the offset at the initial condition of the simulations and do not include manuevers during the short duration of the simulation. The result when applying these 1-sigma errors as offsets to the orbit of the partner satellite, such as $(\delta a, \delta e, \delta\Omega) = (695\text{m}, 8.4 \times 10^{-5}, 2.8 \times 10^{-3}\text{deg})$, is that the problem becomes observable and converges, although the predicted CRLB uncertainty after 24 hours is higher than the other configurations (see Table 2.4). Lastly, we ran additional

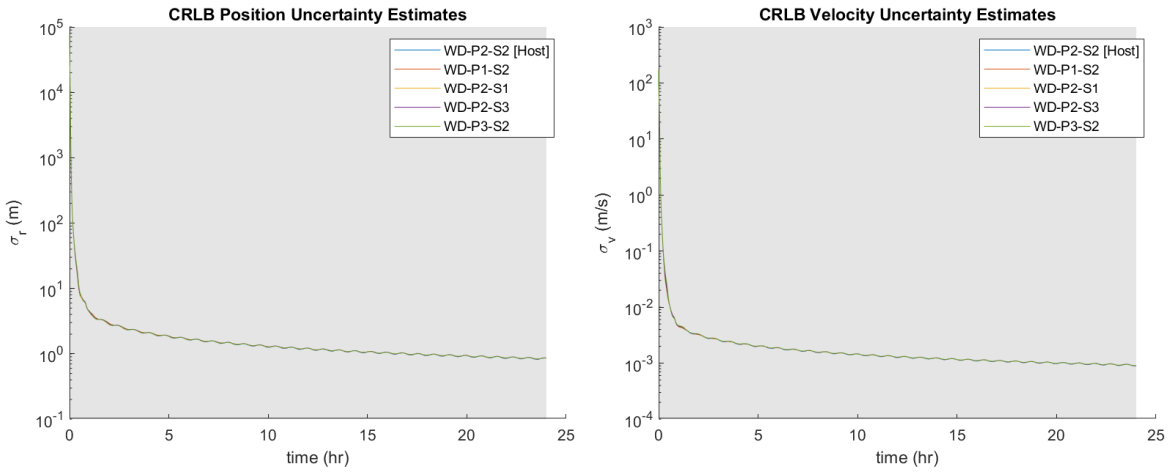


Figure 2-4: (a) Position and (b) velocity uncertainties for Four-Way Link using Newtonian gravity model. Note that the grey background indicates that measurements are continuously available at the simulation measurement period (white background would indicate a measurement outage).

analysis with a reference truth force model, holding the process noise constant to see how the additional variation in the orbital elements from perturbations affects the problem observability. The Earth's gravity model is 100 x 100 with solid and ocean tides and is based on the EIGEN-6S coefficients. Additional gravitational perturbations include third body accelerations from the Sun, Moon, and all of the planets, in

Table 2.4: LEO Constellation Example Results using Newtonian gravity. Unless otherwise noted, there is no station keeping error applied to constellation initial conditions. This analysis uses range and bearings measurements. For a co-orbital Link (WD-P2-S2 & WD-P2-S3) with zero station keeping error: $\log_{10}(\mathrm{CN}(P_k))$ $99^{\mathrm{th}}$ Percentile $\equiv l^{99}_{CN(P)} = 16.79$ (this is unobservable, as expected).

| Satellite | $\sigma_r$ (m) | | | $\sigma_v$ (mm/s) | | |
|---|---|---|---|---|---|---|
| | Min | RMS | Max | Min | RMS | Max |
| Co-Orbital Link with moderate station keeping error: $t_s = 5.30$ hrs, $l^{99}_{CN(P)} = 9.81$ | | | | | | |
| WD-P2-S2 | 15.17 | 27.13 | 47.34 | 16.72 | 29.65 | 50.51 |
| WD-P2-S3 | 15.17 | 27.13 | 47.34 | 16.71 | 29.65 | 50.50 |
| Cross-Planar Link (Adjacent Planes): $t_s = 2.82$ hrs, $l^{99}_{CN(P)} = 7.70$ | | | | | | |
| WD-P2-S2 | 1.50 | 2.35 | 4.43 | 1.64 | 2.57 | 4.82 |
| WD-P3-S2 | 1.50 | 2.34 | 4.33 | 1.63 | 2.57 | 4.89 |
| Cross-Planar & Co-planar Link: $t_s = 2.83$ hrs, $l^{99}_{CN(P)} = 7.68$ | | | | | | |
| WD-P2-S2 | 1.16 | 1.85 | 3.37 | 1.26 | 2.02 | 3.84 |
| WD-P2-S3 | 1.17 | 1.85 | 3.38 | 1.27 | 2.02 | 3.85 |
| WD-P3-S2 | 1.19 | 1.86 | 3.39 | 1.29 | 2.04 | 3.86 |
| Four-Way Link: $t_s = 2.90$ hrs, $l^{99}_{CN(P)} = 7.74$ | | | | | | |
| WD-P2-S2 | 0.82 | 1.30 | 2.36 | 0.89 | 1.42 | 2.70 |
| WD-P1-S2 | 0.84 | 1.31 | 2.39 | 0.91 | 1.43 | 2.69 |
| WD-P2-S1 | 0.83 | 1.31 | 2.38 | 0.90 | 1.43 | 2.72 |
| WD-P2-S3 | 0.83 | 1.31 | 2.37 | 0.90 | 1.43 | 2.72 |
| WD-P3-S2 | 0.83 | 1.30 | 2.36 | 0.91 | 1.43 | 2.72 |

addition to relativistic corrections. The non-gravitational forces are solar radiation pressure and atmospheric drag. The drag model is NRLMSISE00, and the spacecraft parameters are modeled based on an estimated Starlink satellite mass of 250 kg and 30 $\mathrm{m}^2$ solar panel area (sun-pointing) [96, 97]. The epoch time is chosen to be during a recent period of high solar activity (2015-05-15 21:48:10.000 UTC) to demonstrate the potential worst case effects of solar radiation pressure and drag. The statistics for each of the metrics are summarized in Table 2.5. For the co-orbital case with stationkeeping error in Table 2.5, the CRLB RMS position and velocity uncertainties are about three times less than the Newtonian case shown in Table 2.4. However, for the cross-planar link, the position and velocity uncertainties for the "truth" force model are only slightly lower than the Newtonian force model (less than 0.5 m and 0.5 mm/s difference). The additional perturbations vary the orbital elements further,

which helps improve observability for the co-orbital case; however, the cross-planar case already has high observability, so the additional perturbations have little effect. The main take away from these results is that once a non-singular configuration link is established, any additional satellite orbits are observable, even if those satellites are in singular configurations. The non-observable configurations behave like singularities: small offsets from these configurations restore observability. We will analyze sensitivity to these offsets in Section 2.8. Once a baseline non-singular configuration link is established (e.g. cross-planar between adjacent satellites), the predicted position and velocity uncertainty only slightly improves when adding additional links. In other words, there are diminishing returns to multiple access link configurations. The observability of the problem is not highly sensitive to the effects of perturbing forces. We will explore these results in greater depth and with other constellation configurations in Chapter 4, where we will also include higher fidelity measurement models with varying measurement noise. In the remainder of this chapter, we will vary the main governing parameters of the problem to analyze how this impacts observability.

Table 2.5: LEO Crosslink example results with high fidelity force model.

| Satellite | $\sigma_r$ (m) | | | $\sigma_v$ (mm/s) | | |
|---|---|---|---|---|---|---|
| | Min | RMS | Max | Min | RMS | Max |
| Co-Orbital Link with moderate station keeping error: $t_s = 3.68$ hr, $l^{99}_{CN(P)} = 8.83$ | | | | | | |
| WD-P2-S2 | 5.26 | 8.67 | 15.98 | 5.70 | 9.32 | 17.04 |
| WD-P2-S3 | 5.27 | 8.67 | 15.99 | 5.70 | 9.32 | 17.06 |
| Cross-Planar Link (Adjacent Planes): $t_s = 3.70$ hr. $\log_{10}(\mathrm{CN}(J_k))$ $99^{\text{th}}$ Percentile: 7.41 | | | | | | |
| WD-P2-S2 | 1.20 | 1.94 | 3.44 | 1.31 | 2.11 | 3.91 |
| WD-P3-S2 | 1.21 | 1.93 | 3.45 | 1.31 | 2.12 | 3.92 |

## 2.8 Sensitivity to Non-Observable Configurations

In order to determine the impact of the Newtonian non-observable configurations on constellation design, we simulated crosslink scenarios with small offsets in $a$, $e$, and

$\Omega$ from the non-observable configuration (where all of these offsets are zero). We ran the sensitivity analysis first with a LEO host satellite and then with a MEO host satellite (see Table 2.6). For the LEO host satellite case, Figures 2-5 & 2-6 give the

Table 2.6: Initial orbit elements for host satellites for observability sensitivity analyses. The coordinates are based on TLE data for the STARLINK-1515 (LEO) from June 2022 and for the GPS satellite USA319 (MEO) from July 2022.

| Satellite | $a$ (km) | $e$ | $i$ (deg) | $\Omega$ (deg) | $\omega_p$ (deg) | $M$ (deg) |
|---|---|---|---|---|---|---|
| LEO Host | 6925.4 | $1.43 \times 10^{-4}$ | 53.06 | 321.62 | 78.60 | 40.90 |
| MEO Host | 26559.6 | $5.41 \times 10^{-3}$ | 55.20 | 29.95 | 188.27 | 180.98 |

observability metrics over a range of positive offsets. For this analysis, the median after settling of the root-sum-square of the position/velocity uncertainty metric for both satellites is used (median($\sqrt{\sigma_{r,0,k}^2 + \sigma_{r,1,k}^2}$)). The observability metrics behave symmetrically for negative offsets in $a$ and $\Omega$, so these are not shown. The simulation is run for 7 days with a measurement period of 5 minutes. Four different force models relevant for a LEO host satellite are used to show the effect (if any) of introducing perturbations. The same is done with a MEO host satellite since the third body forces and solar radiation pressure are more important at that altitude than for the LEO case, where higher order central body potential terms and atmospheric drag are more important. The condition number results are shown in Figure 2-5. The limit on the condition number for observability is about $10^{16}$, so the LEO problem is observable according to this criterion for approximately $\Delta a \geq 1$ m, $\Delta e \geq 1.5 \times 10^{-6}$, and $\Delta\Omega \geq 1.5 \times 10^{-4}$ degrees for all of the tested perturbations. The corresponding offset requirements for the MEO problem are slightly higher, at approximately $\Delta a \geq 32$ m, $\Delta e \geq 3.2 \times 10^{-6}$, and $\Delta\Omega \geq 6.8 \times 10^{-4}$ degrees for all of the tested perturbations. The non-observable configuration clearly behave like singularities, with only small offsets required to restore observability. It is notable that the perturbations do not significantly improve observability of the problem near the singular points; the required offsets are the same for the different force models. This is consistent with our previous results. As shown in Section 2.7, if the reference configuration is singular (e.g., a co-orbital pair of satellites) moderate station keeping error will

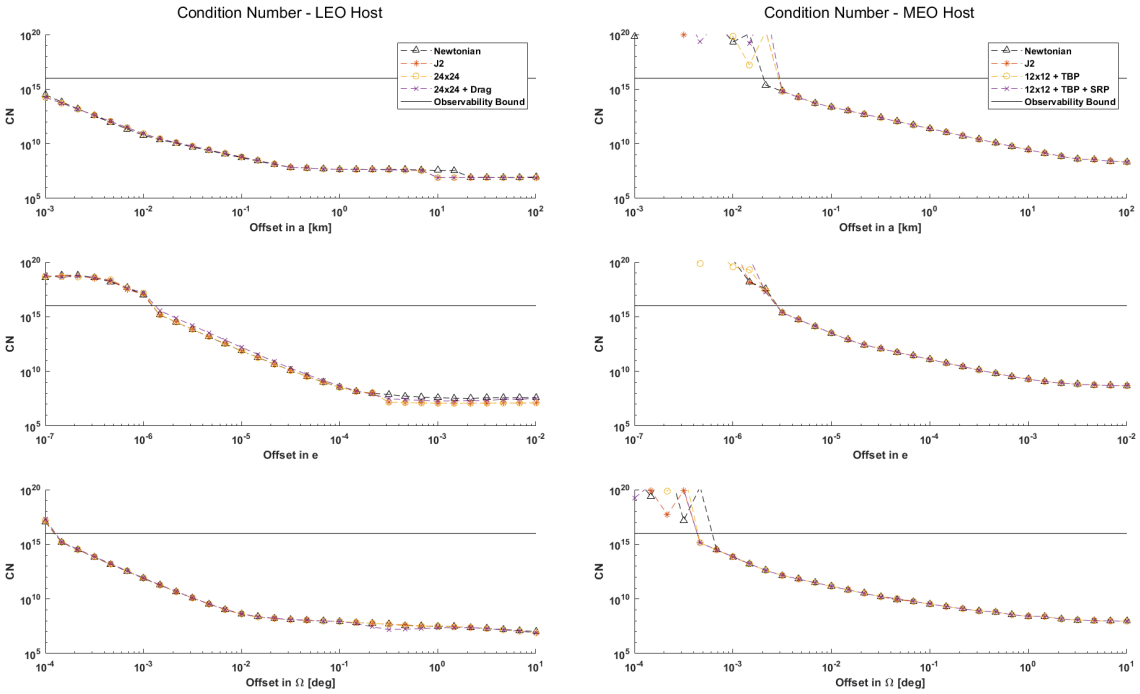


Figure 2-5: Sensitivity of covariance condition number near Newtonian non-observable configurations for (a) LEO and (b) MEO host satellite (see Table 2.6).

result in offsets that are greater than these observability thresholds. However, the observability is still degraded in such close proximity to the singular configurations, as can be seen in Figures 2-6 and 2-7 for LEO and MEO crosslinks, respectively. The baseline cross-plane link (adjacent planes) for this duration and measurement period for the Newtonian gravity force model has RMS position and velocity uncertainties of about 5 m and 5.5 mm/s for the LEO case and 28 m and 4 mm/s for the MEO case. There are diminishing returns to increasing the offsets: the observability metrics exhibit asymptotic behavior over the small offset ranges shown here. For the LEO host, the position and velocity uncertainties settle to less than 20 m and 20 mm/s at approximately $\Delta a \geq 681$ m, $\Delta e \geq 3.2 \times 10^{-4}$, or $\Delta\Omega \geq 6.8 \times 10^{-2}$ degrees. For the MEO host, the position and velocity uncertainties settle to less than 60 m and 10 mm/s at approximately $\Delta a \geq 46.42$ km, $\Delta e \geq 1.5 \times 10^{-3}$, or $\Delta\Omega \geq 1$ degree. Note that these settled uncertainties decrease for higher frequency measurements and are also lower if combinations of offsets are present. It is apparent that links that are held

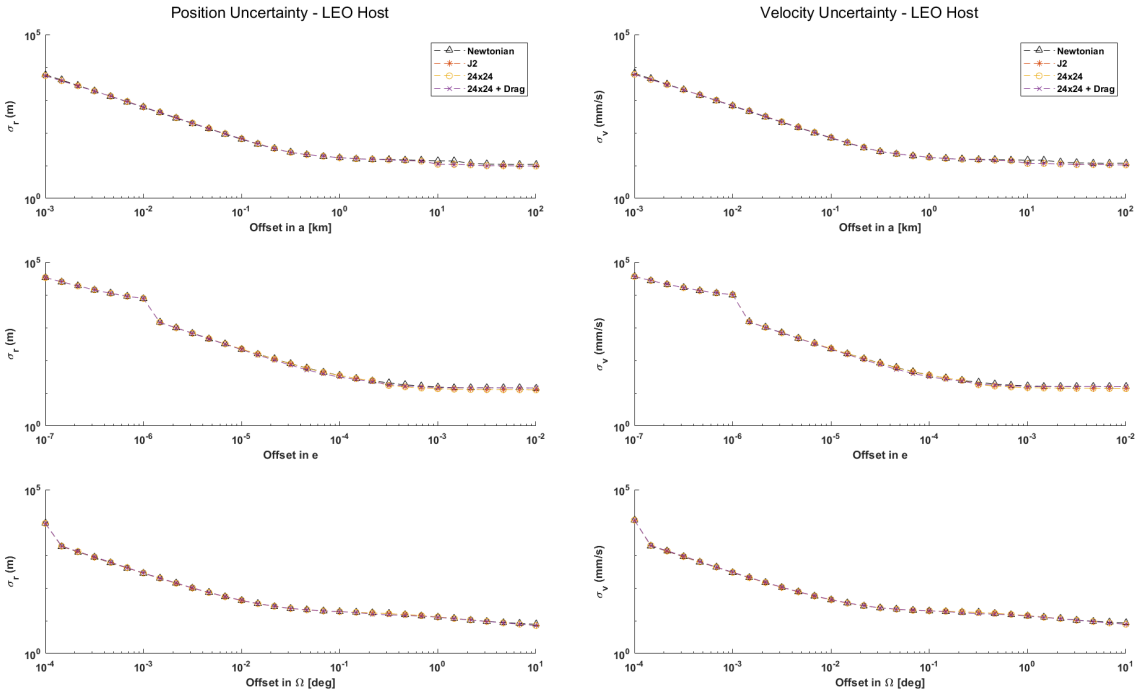


Figure 2-6: Sensitivity of position and velocity uncertainties near Newtonian non-observable configurations for a LEO host satellite (see Table 2.6).

near a singular configuration with high station keeping accuracy will have sub-optimal observability, even with the effects of perturbations. This needs to be taken into account for any missions that have singular link configurations. For example, a string of pearls configuration would nominally only have co-orbital links, so when periodic station keeping manuevers occur that bring the two satellites closer to the singular configuration, the orbit determination error will increase. If the OISL navigation is being used for autonomous station keeping, then the increase in orbit uncertainty as the satellites get closer to the singular configuration would prevent the satellites from achieving that configuration. Further analysis of the effects of station keeping over long time horizons is future work. These potential issues vanish for constellations with non-singular links (e.g. links between different satellite planes). As we will see in Section 2.9, there are only small variations in observability once a sufficient offset requirement from the singular configuration is met.

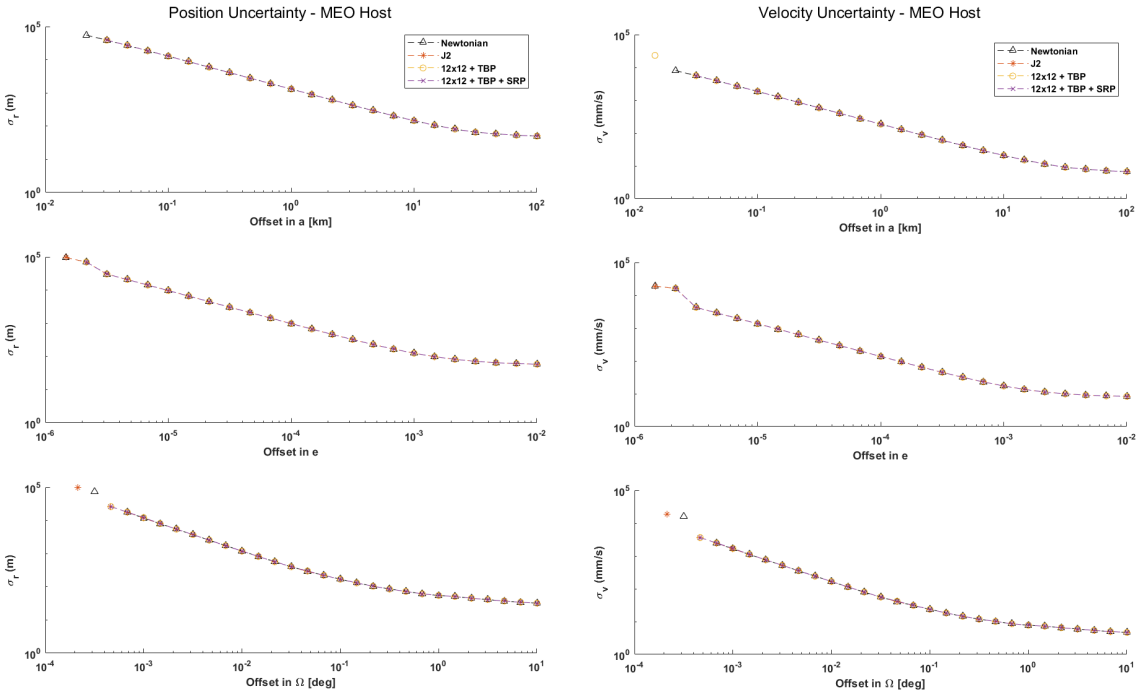


Figure 2-7: Sensitivity of position and velocity uncertainties near Newtonian non-observable configurations for a MEO host satellite (see Table 2.6). Note that for some of the small perturbation cases (e.g., $\Delta\Omega \sim 10^{-4}$ degrees), the condition number is much higher than the observability bound, so the CRLB uncertainty metrics diverge and are therefore not plotted.

## 2.9 Survey over Orbital Geometries

In this section, we vary the relative orbital elements by large values to see if the observability changes significantly for different types of orbital geometries. The simulation duration is 10 days, the measurement period is 5 minutes, and access is unconstrained so as not to confound the geometry sensitivity results with access limitations. The offsets in the other elements are zero. In case all the elements would be the same, an offset of $\Delta M = 0.1°$ is used to represent the singular point. When applying offsets to $i$ or $M$, a fixed offset is also applied to $M$ or $\Omega$, respectively (otherwise, the system would be singular). The results show that all three unobservability criteria over a

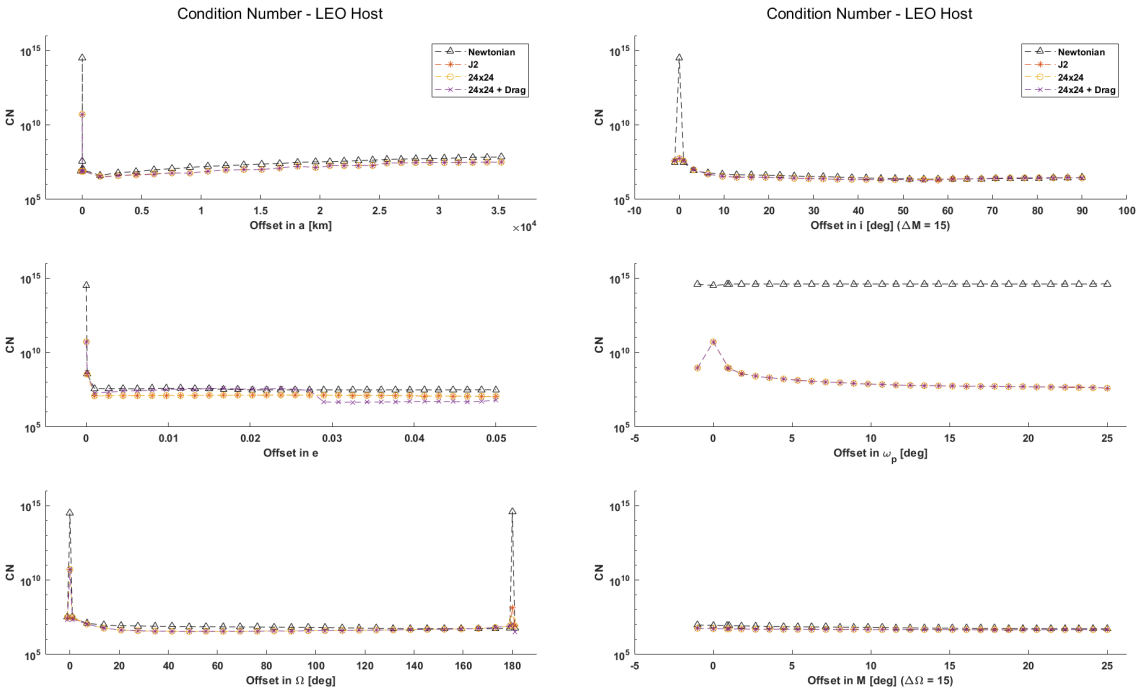


Figure 2-8: Condition numbers for varying relative initial orbital elements with various perturbing forces and LEO host satellite (see Table 2.6).

large range of offsets behave like singularities. Away from the singularities, there are small changes to observability metrics with varying offsets in $a$, $e$, $i$, and $\omega_p$. For all of the test cases, additional perturbations beyond J2 have negligible impact on the observability metrics.

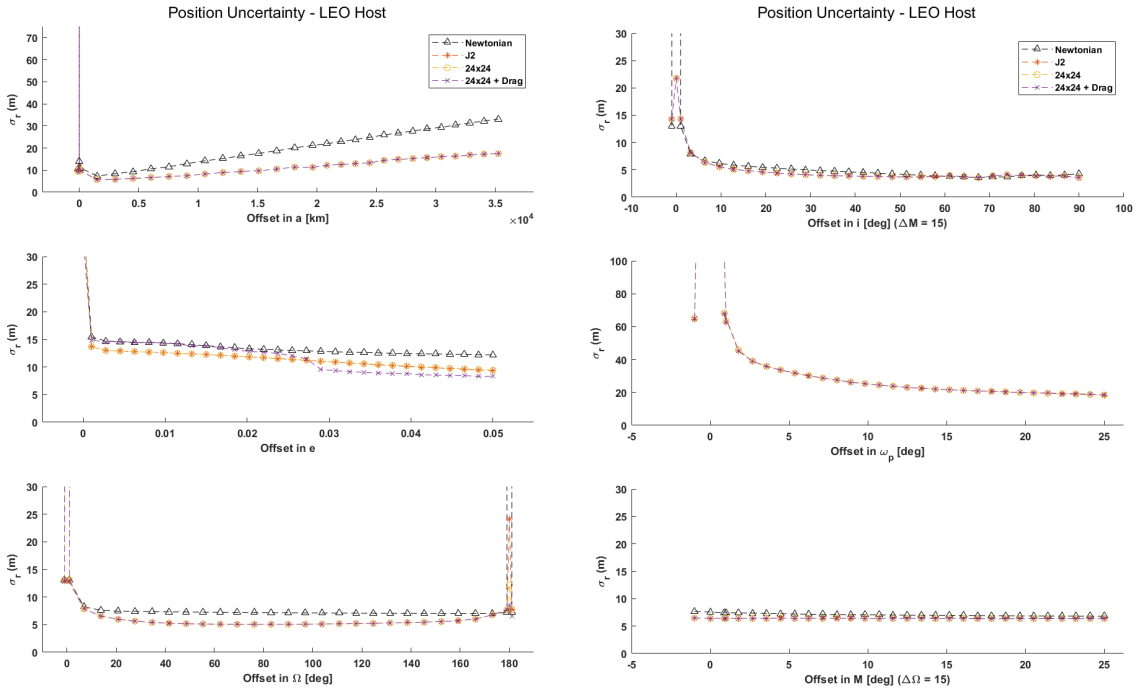


Figure 2-9: Position Uncertainties for varying relative initial orbital elements with various perturbing forces and LEO host satellite (see Table 2.6).

For the case of a LEO host satellite, Figures 2-8 and 2-9 show the variation in the condition number and CRLB position uncertainty, respectively, when varying one of the partner satellite's orbital elements. The CRLB velocity uncertainty can be found in Appendix B.1: Figure B-1. For the Newtonian force model, there is improved position and velocity uncertainties for LEO partners relative to higher altitude partners (about 20 m and 10 mm/s). With the addition of perturbations, the LEO partners have only about a 10 m reduction in position uncertainty and a slightly higher velocity uncertainty (about 1 mm/s) compared to the higher altitude partners. The eccentricity offsets for LEO orbits are limited to 0.05 because higher eccentricities would cause the orbit to impact the Earth. Over this small range of eccentricy offsets, there is little change in observability, with small improvements from the effects of perturbations. Overall, once sufficient separation from the singular point is achieved at an offset of about 5° in any of the angular elements ($i$, $\Omega$, $\omega_p$, $M$), the observability metrics are insensitive to additional increases in the offsets. The effect of the perturbations is to

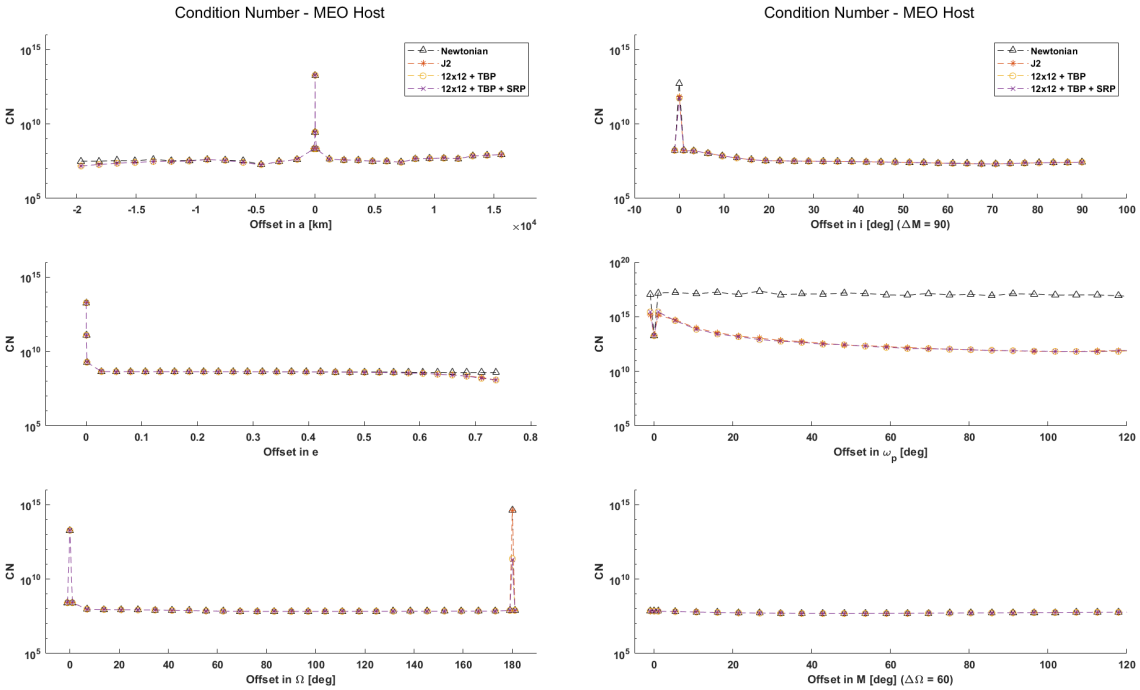


Figure 2-10: Condition numbers for varying relative initial orbital elements with various perturbing forces and MEO host satellite (see Table 2.6).

improve observability by a small amount. Lastly, offsets in the argument of perigee have a diminished effect in this example because the orbit is near-circular. We will look at some highly eccentric orbits when we study a lunar constellation example in Chapter 4.

For the case of a MEO host satellite, Figures 2-10 and 2-11 show the variation in the condition number and CRLB position uncertainty, respectively, when varying one of the partner satellite's orbital elements. The CRLB velocity uncertainty can be found in Appendix B.1: Figure B-2. There is a slight improvement in position uncertainty for lower altitude partners relative to higher alititude partners (about 10 m), and vice-versa for velocity uncertainty (about 10 mm/s). Also, the position uncertainty is slightly lower for eccentricity offsets between 0.1-0.2, and the velocity uncertainty is insensitive to eccentricity offsets. The observability metrics are mostly insensitive to offsets in $\Omega$ or $M$ once sufficient separation from the singular point is achieved at about 5°. The observability improves slightly with increasing inclination

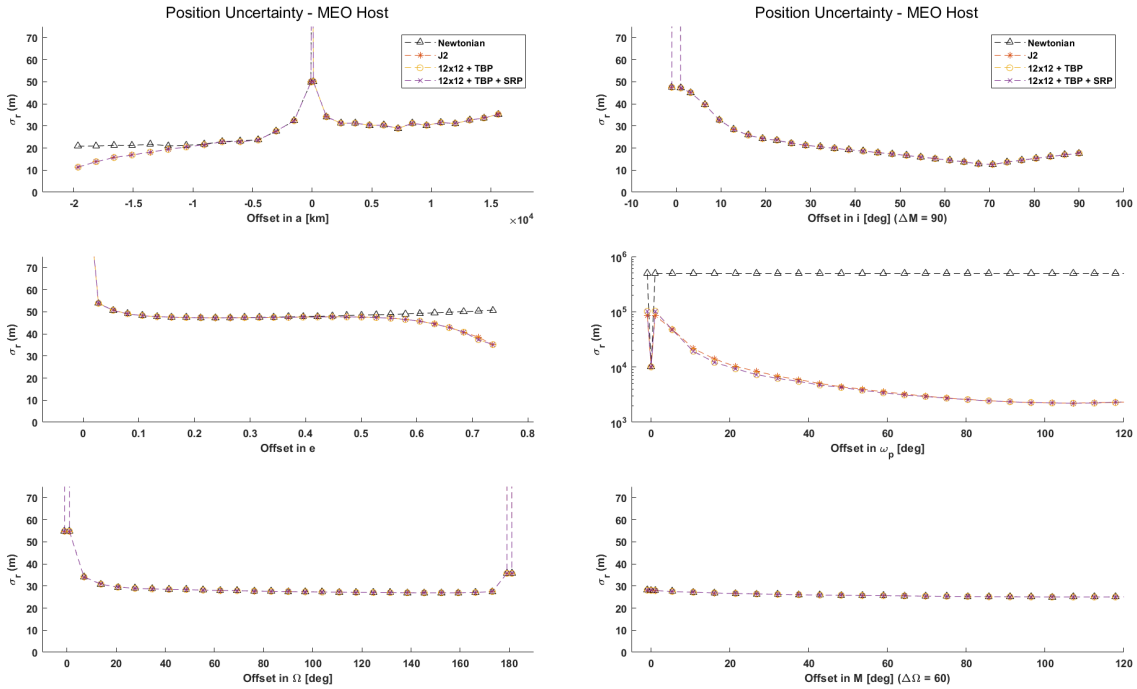


Figure 2-11: Position Uncertainties for varying relative initial orbital elements with various perturbing forces and MEO host satellite (see Table 2.6).

offset up to about $\Delta i = 70^\circ$ (about 15 m better than lower inclinations), after which the observability starts to degrade slightly. Offsets in the argument of perigee do improve the condition number to a technically observable level (less than $\sim 10^{16}$) if at least the J2 perturbation is present; however, since the orbits are near-circular, they have much less impact than offsets in $(a, e, \Omega)$. The uncertainty in the position and velocity is still high for pure offsets in the argument of perigee. The variation in semi-major axis shows improved observability relative to the Newtonian case for lower altitude partners if the J2 perturbation is added. Similarly, for eccentricity offsets greater than 0.5, the J2 perturbation improves observability. Including the J2 perturbation improves observability for all argument of perigee offsets. The results for the inclination, RAAN, and mean anomaly offsets are insensitive to perturbations.

## 2.10 Sensitivity to Filter Parameters

We now turn to the observability sensitivity to filter parameters (e.g., measurement oise standard deviations). We study a baseline Starlink crosslink (WD-P2-S2 to WD-P3-S2) from Section 2.7 as the reference case (see Table 2.3 for the initial orbital elements). Figure 2-12 shows the variation in the position uncertainty metric with

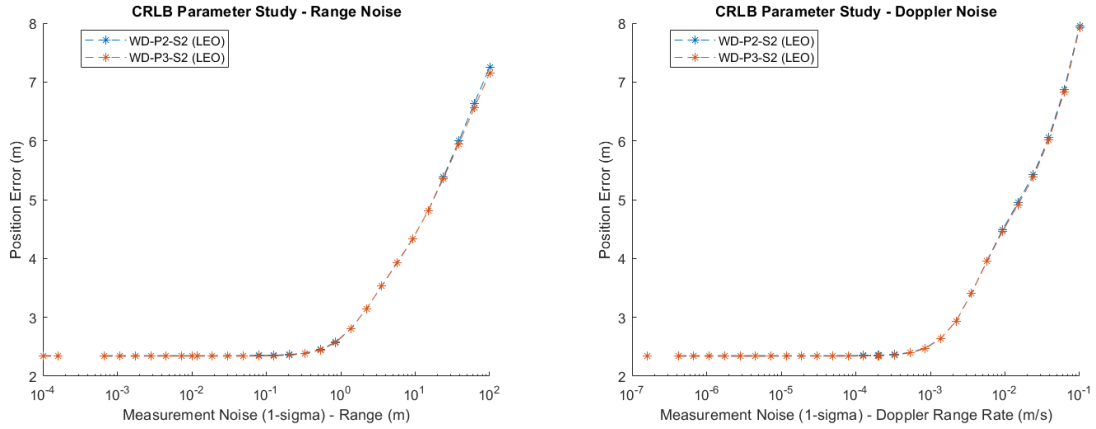


Figure 2-12: Variation in RMS position uncertainty with range and range-rate noise. Note that since the range and Doppler measurements are redundant, for range noise variation, the measurement configuration is range-bearings; and, for range-rate noise variation, the measurement configuration is Doppler-bearings.

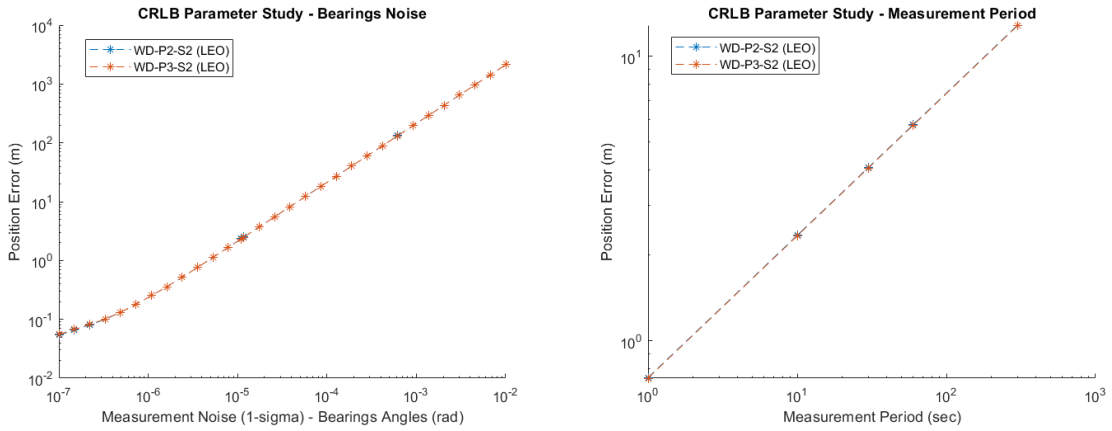


Figure 2-13: Variation in RMS position uncertainty with (a) bearings noise on both az and el for range-bearings configuration and (b) measurement period for range-bearings configuration.

varying range and range-rate noise values (1-sigma), and Figure 2-13 (a) is the corresponding chart when varying both bearing noise values simultaneously. The velocity

uncertainties have the same behavior as the position uncertainties, and the corresponding plots are in Appendix B.2. For the variation in range uncertainty, only the range and bearings measurements are used, and likewise for the variation in Doppler range-rate uncertainty (only Doppler and bearings measurements are used). This is because the range and Doppler measurements are redundant, and if both were included, varying one would have very little effect on the observability. Note that this redundancy could actually be useful in practice if the designer wants to make the system more insensitive to variations in range/Doppler measurement performance. What is clear from these charts is that when varying only one of the two major measurement types (range/Doppler or bearings), there is a point of diminishing returns to decreasing the measurement error where one of the two measurement types dominates the uncertainty. We say that this measurement type has a higher "effective error" than the other measurement type. With our reference 1-sigma values of $10^{-2}$ m range uncertainty, $2 \times 10^{-4}$ m/s Doppler range-rate uncertainty, and $1.1 \times 10^{-5}$ rad bearings uncertainty, the points of diminishing returns for the LEO baseline cross-planar example are approximately $5 \times 10^{-1}$ m range, $5 \times 10^{-4}$ m/s Doppler, and $1 \times 10^{-7}$ rad. So for the reference error values, the uncertainty is bearing angles dominated, and further improvements to the range/Doppler error do not improve observability further.

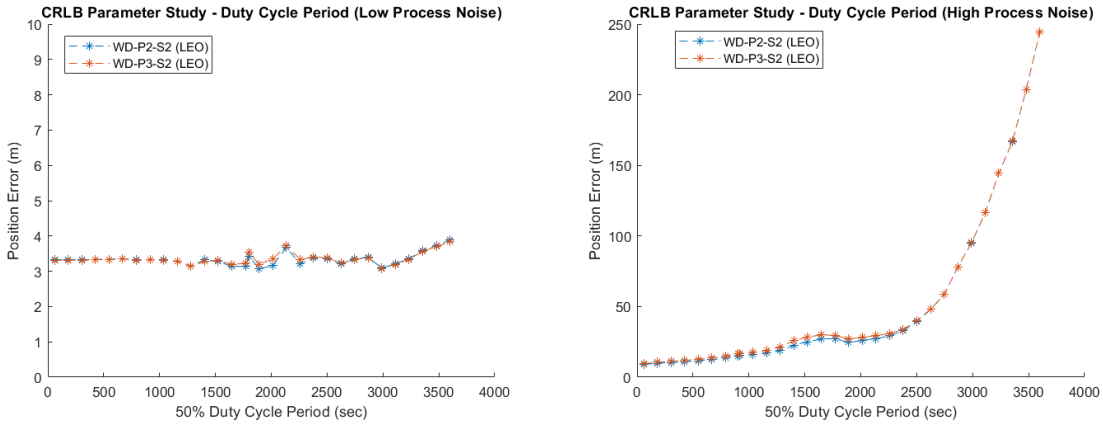


Figure 2-14: Variation in RMS position uncertainty with period for a 50% on/off link duty cycle with (a) $\sigma_q = 3.16 \times 10^{-8}$ m/s$^2$ and (b) $\sigma_q = 3.99 \times 10^{-6}$ m/s$^2$.

Figure 2-13 (b) shows the variation in the position uncertainty metric with the

measurement period. The relationship closely follows the following power law approximation: $\sigma_{r,\text{rms}} \approx 0.7397\sqrt{T_y}$ (units are seconds for $T_y$ and meters for $\sigma_{r,\text{rms}}$). Generally, increasing the measurement frequency (reducing the measurement period) improves observability. The maximum measurement frequency is limited by star tracker measurement frequency (typically 1-5 Hz [98]). We discuss the frequencies of the measurements in Chapter 3. To assess the effect of measurement outages, we duty cycle the link at 50% on/off and vary the duty cycle period. Figure 2-14 (a) shows the position uncertainty with the reference process noise value ($\sigma_q = 3.16 \times 10^{-8}$ m/s$^2$), and Figure 2-14 (b) shows the position uncertainty with a higher process noise value ($\sigma_q = 3.99 \times 10^{-6}$ m/s$^2$).

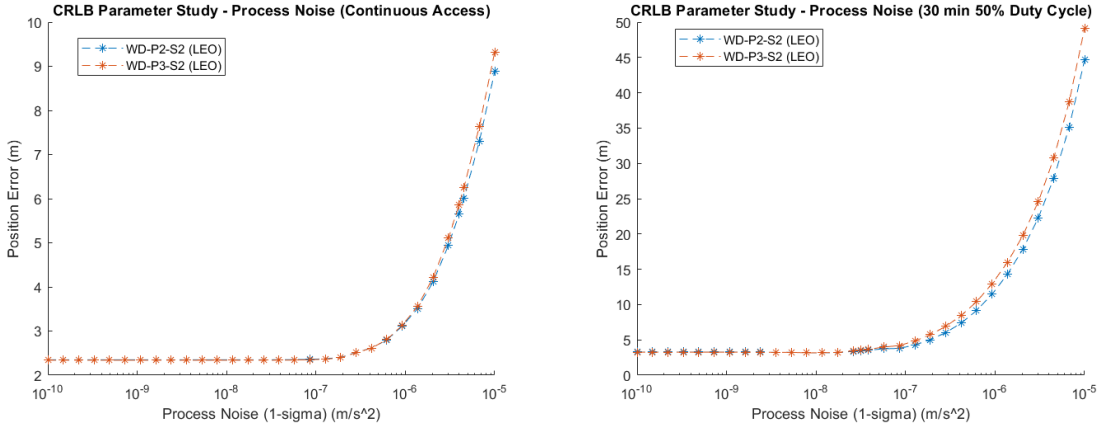


Figure 2-15: Variation in RMS position uncertainty with process noise for (a) continous link access and (b) a 50% link duty cycle with a 30 minute period.

The higher process noise value is derived from an analysis of force model error using a 24 x 24 gravity field model for this orbit, which is discussed in detail in Chapter 4 along with the rest of the process noise analysis results. For case (a) with low process noise, the outage periods do not significantly effect the observability; however, for case (b) with higher process noise, the position uncertainty increases roughly linearly up to about 30 m at about 1500 seconds, then it begins to increase exponentially. This is because for links with long outage periods, a high accuracy force model is needed to propagate the orbit accurately over long outage periods. We analyze what force models are needed for different orbit regimes in Chapter 4.

We vary the process noise to see how it impacts the uncertainty. The results for

the default continous link access (apart from sun-keep out) shown in Figure 2-15 (a), and the results for a 50% link duty cycle with a 30 minute period are shown in Figure 2-15 (b). In both cases, there is a point of diminishing returns where reducing the process noise further has negligible impact on the position uncertainty. For continuous measurements, this is at approximately $\sigma_q = 2 \times 10^{-7}$ m/s$^2$, which is near our reference process noise value for this section. This is not a coincidence; we picked the reference value for the analysis in these sections in part because of this result, in addition to it being used in the literature [78]. For the case with 30 minute outages, the point of diminishing returns is at about $\sigma_q = 3 \times 10^{-8}$ m/s$^2$. As we show in Chapter 4, for this LEO orbit (Table 2.3), this level of process noise would require a high fidelity force model (e.g., 100 x 100 gravity field with drag, third body perturbations, solar radiation pressure, etc). This would be computationally expensive. In addition, to compute the drag and solar radiation pressure terms accurately requires data from external sources like solar activity and the Earth's magnetic field activity, as well as the attitude, geometry, and mass properties of the host satellite and its partners. Although this information could be disseminated over the communications network, it would complicate the systems design and likely require oversight from ground operators. Practically, the level of process noise for the LEO case will be higher than the point of diminishing returns. We will explore this important facet of the problem in depth for Earth, Lunar, and Mars orbits in Chapter 4.

## 2.11 Chapter Summary

First, we compared the observability of different subsets of the three measurement types: range, Doppler, and bearings. The range and Doppler measurements are essentially equivalent in terms of observability, and whichever one has a lower effective measurement error will dominate the estimate, and using both measurements is redundant in most cases. Using only range, Doppler, or bearings is only a partial measurement of the relative position vector, so it is well known that in such a scenario, the absolute orbit is only partially observable in the Newtonian gravity case, and the observability improves with force model perturbations that remove symmetries from the force model.

A lasercom terminal is able to measure the full relative position vector (range and bearings or Doppler and bearings), which makes the absolute orbit fully observable for most orbital configurations. The two-satellite problem is known to be unobservable in the Newtonian gravity case if the two satellites have the same shape parameters $(a, e)$ and either: share the same orbital plane, are only offset in inclination, or are only offset in RAAN by 180°. In principle this would rule out intersatellite links between satellites that share the same orbit, which is the most common of the three cases to arise in practice. However, we have shown that the unobservability criteria behave like singularies, and small offsets from these configurations due to imperfect station keeping and perturbing forces restore observability. The effects of perturbing forces do not significantly impact observability, unlike the single measurement cases (e.g. range-only). We showed that if the host satellite has multiple link partners, only one pair of satellites in the estimation problem needs to be observable, since once the host satellite's absolute orbit is known, any other satellite's orbit is observable using the relative position measurements provided by the lasercom terminal.

We assessed the sensitivity of the the problem observability to measurement parameters. In particular, we showed that decreasing the measurement period improved observability proportionally to the square-root of the measurement period. We also showed that either the range/Doppler or the bearings measurement determines lower

bound on observability, depending on which one has a lower effective error. In our example, the range had a lower effective error, so the problem was most sensitive to errors in the angular measurement. We will explore the measurements in depth in the next chapter.

We analyzed the effects of process noise for both continuous link access and duty cycled link access cases. We showed that the problem is less sensitive to process noise if continuous links are available, as would be expected. We also showed that the problem has low sensitivity to short outage periods if the process noise is sufficiently low (e.g., $\sigma_q \leq 2 \times 10^{-7}$ m/s$^2$ for a LEO orbit with continuous measurements). There are diminishing returns to decreasing process noise. In the next chapter, we perform systems analyses of the lasercom measurement technology to develop higher fidelity measurement models.

# Chapter 3

# OISL Measurement Systems

In this chapter, systems analysis for optical intersatellite link measurements will be performed. This will provide more accurate measurement models than the geometric model to form the basis for a system that can be fielded. It will also relate the measurements to physical system parameters, which will allow the subsequent analyses to not only rely on existing capabilities, but to inform systems design choices for technology development going into the future.

## 3.1 Systems Analysis for Range Measurements

Ranging methodologies used with radio measurements include sequential ranging (tone-based), pseudorandom-noise (PN) code ranging, combined Gaussian minimum-shift keying, and telemetry ranging [99]. Examples of periodic signals used for radio ranging include sinusoidal carrier or sub-carrier tones, PN sequences (e.g. periodic bit stream), and telemetry frames (frame boundaries are delimited by synchronization markers) [99]. Telemetry-based methods are the most straightforward approaches to ranging using a laser communications terminal, since all of the required hardware is already present in order to perform communications. An architecture for optical telemetry ranging has been developed by Net and Hamkins that does not require clock synchronization between the terminals and does not impede data flow: ranging and communications can occur simultaneously with less than 0.005% bandwidth

impact for data rates of at least 5.4 Mbps [99]. The basis for ranging measurements

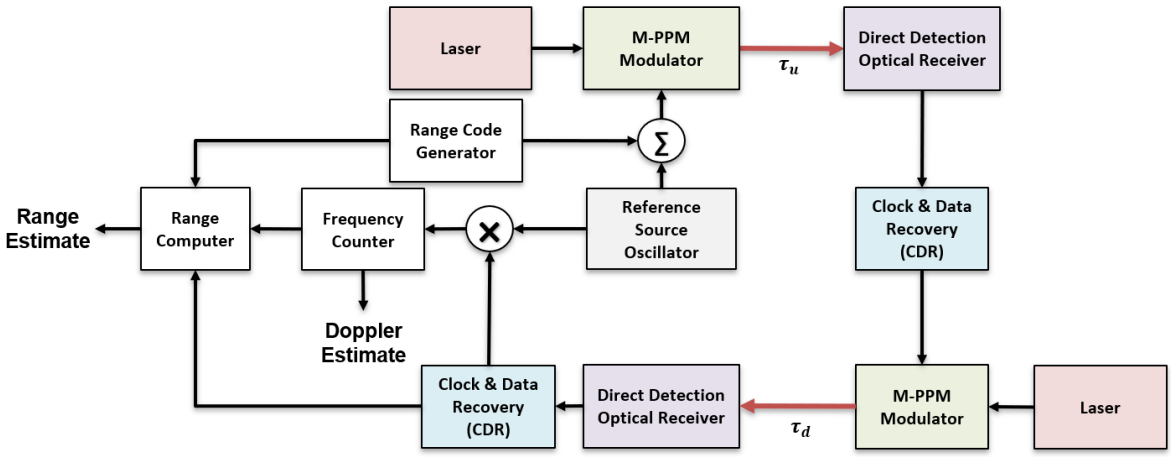


Figure 3-1: System diagram for two-way intersatellite ranging and Doppler measurements with direct detection pulse-position modulation [51, 100].

using electromagnetic signals is determining the time that it takes for light to travel between two observers, called the time of flight. For two-way ranging, the measured time of flight ($\tau$) is

$$\tau = t_R - t_T \tag{3.1a}$$

$$= (t_T + \tau_u^{\text{tx}} + \tau_u + \tau_u^{\text{rx}} + \tau_d^{\text{tx}} + \tau_d + \tau_d^{\text{rx}}) - t_T \tag{3.1b}$$

$$= \tau_{ud} + \tau_c \tag{3.1c}$$

$$\tau_{ud} = \tau_u + \tau_d \tag{3.1d}$$

$$\tau_c = \tau_u^{\text{tx}} + \tau_u^{\text{rx}} + \tau_d^{\text{tx}} + \tau_d^{\text{rx}} \tag{3.1e}$$

$$\rho_{a,ud} = \frac{c}{2}\tau_{ud} = \frac{c}{2}(\tau - \tau_c) \tag{3.1f}$$

where $\rho_{a,ud}$ is the apparent range between the observers, $\tau_u$ and $\tau_d$ are respectively the uplink and downlink times of flight, $\tau_{ud}$ is the two-way time of flight (not including any hardware delays), $t_T$ is the recorded transmit time, $t_R$ is the recorded receive time, and $\tau_c$ represents the cumulative sum of the hardware delays inherent in the link (uplink transmit $\tau_u^{\text{tx}}$, uplink receive $\tau_u^{\text{rx}}$, downlink transmit $\tau_d^{\text{tx}}$, and downlink receive $\tau_d^{\text{rx}}$). The apparent range $\rho_{a,ud}$ is not equal to the instananeous geometric

range at the recorded measurement time $\rho(t_R)$. The model for $\rho_{a,ud}$ as a function of the system state at $t_R$ is derived in Section 3.1.5. Hardware delays are determined via calibration. For intersatellite communications, the "uplink" ($u$) is the initial transmission from the host satellite to the partner satellite, and the "downlink" ($d$) is the response transmission from partner satellite to the host satellite.

The ranging systems that we will be discussing rely on that fact that for any transmitted periodic signal, the time of flight between transmitter and receiver introduces a phase delay which can be measured. Some clarifying notation is in order: let $s(t)$ be some periodic signal with period $T$. Its phase ($\theta$) can in general be defined as the argument of the first complex coefficient of its Fourier series expansion [101].

$$\theta(t) = 2\pi \frac{t - t_0}{T} \bmod 2\pi, t \geq t_0 \tag{3.2}$$

where $t_0$ is the arbitrary cycle start time. It is useful to perform a mathematical operation to normalize and unwrap the phase such that it is monotonically increasing rather than cyclical [99].

$$\psi(t) = \text{unwrap}\left(\frac{\theta(t)}{2\pi}\right) = \frac{t - t_0}{T} = N(t) + \phi(t) \tag{3.3}$$

$\psi$ is called the generalized phase, and $N$ and $\phi$ are its integer and fractional parts. Note that the integer part may be subdivided into multiple components. The transmitter records the outgoing signal phase ($\psi_T$) and its time derivative ($\dot{\psi}_T$). By the fundamental theorem of calculus,

$$\int_{t_T}^{t_R} \dot{\psi}_T(t)dt = \psi_T(t_R) - \psi_T(t_T) \tag{3.4}$$

For a given receive time ($t_R$) measured by the host, Equation 3.4 is solved for the initial transmission time ($t_T$) after inferring the initial transmission phase ($\psi_T(t_T)$) from a phase measurement at one of the receivers in the link. In general, the transmission frequency $f_T(t) = \dot{\psi}_T(t)$ is a function of time due to Doppler pre-compensation applied the uplink and frequency noise, so the equation is solved for $t_T$ via numerical meth-

ods. In conventional ranging, this phase measurement occurs at the host's receiver ($\psi_R(t_R)$). By virtue of the design of the conventional ranging system, $\psi_R(t_R) = \psi_T(t_T)$ [101]. In telemetry ranging, the phase measurement occurs at the partner's receiver ($\psi_P(t_P)$) at time $t_P = t_R - \tau_d$, and this data is then sent back to the host over the telemetry stream. The host uses this data and the fact that $\psi_P(t_P) = \psi_T(t_T)$ to solve equation 3.4 [101, 99]. While we used the continuous-time representation of phase, in general the phase measurements can be discrete samples. For a discussion of the discrete-time case, see [99].

The transmission frequency can be expressed as:

$$\dot{\psi}_T(t) = f_T(t) = (1 + \beta(t))(1 + y(t))f_{T,0} \approx (1 + \beta(t) + y(t))f_{T,0} \tag{3.5}$$

where $\beta = \dot{\rho}/c$ determines the Doppler pre-compensation shift, $y$ is the normalized frequency deviation due to noise, and $f_{T,0}$ is the reference signal frequency. The approximation is valid because $\beta \ll 1$ and $y \ll 1$. For example, in a worst case LEO-LEO link, the relative speed $|\dot{\rho}| \approx 15$ km/s, which corresponds to $|\beta| \approx 5 \times 10^{-5}$. Also, the transmitter is designed with a highly stable frequency source such that the Allan deviation (measure of the average frequency deviation) is on the order of $10^{-10}$ or smaller [102]. The phase shift integral over the two-way time interval $\tau = t_R - t_T$ is:

$$\int_{t_T}^{t_R} \dot{\psi}_T(t)dt = \int_{t_T}^{t_R} (1 + \beta(t) + y(t))f_{T,0}dt \tag{3.6a}$$

$$= f_{T,0}\left(\tau + \int_{t_R-\tau}^{t_R} \beta(t)dt + \int_{t_R-\tau}^{t_R} y(t)dt\right) \tag{3.6b}$$

$$= f_{T,0}\left(\tau + \tau\bar{\beta}(t_R, \tau) + \tau\bar{y}(t_R, \tau)\right) \tag{3.6c}$$

$$= f_{T,0}(\tau + \Delta\tau_\beta(t_R, \tau) + \Delta x(t_R, \tau)) \tag{3.6d}$$

where $\bar{f}_T(t_R, \tau)$ is the average frequency, $\bar{\beta}(t_R, \tau)$ and $\bar{y}(t_R, \tau)$ are average frequency deviations over the two-way interval $\tau$, and $\Delta\tau_\beta$ and $\Delta x$ are biases due to Doppler pre-compensation and transmitter oscillator phase deviations over the two-way interval.

Using Eq. 3.4, the two-way time of flight is then:

$$\tau_{ud} = \frac{1}{f_{T,0}}(\psi_T(t_R) - \tilde{\psi}) - (\Delta\tau_\beta + \Delta x + \tau_c) \tag{3.7}$$

where $\tilde{\psi} = \psi_T(t_T) = \{\psi_P(t_P) \text{ or } \psi_R(t_R)\}$, for telemetry (P) or conventional (R) ranging, respectively. The measured values for each of these terms are $\hat{t}_R = t_R + \delta t_R$, $\hat{\tilde{\psi}} = \tilde{\psi} + \delta\tilde{\psi}$, and $\hat{\tau}_c = \tau_c + \delta\tau_c$. $\delta t_R$ and $\delta\tilde{\psi}$ are random noise terms, and $\delta\tau_c$ is residual bias due to the system hardware delay calibration error. Moving forward, we assume that either the Doppler pre-compensation bias is known, or that there is no Doppler pre-compensation (as per the CCSDS 141.10-O-1 laser communications standard [103]). The oscillator phase deviation $\Delta x$ is treated as an unknown random noise term. The two-way time of flight calculated from the measurements can therefore be expressed as:

$$\begin{aligned}
\hat{\tau}_{ud} &= \frac{1}{f_{T,0}}(\psi_T(\hat{t}_R) - \hat{\tilde{\psi}}) - (\Delta\tau_\beta + \hat{\tau}_c) && \text{(3.8a)}\\
&= \frac{1}{f_{T,0}}(\psi_T(t_R + \delta t_R) - (\tilde{\psi} + \delta\tilde{\psi})) - (\Delta\tau_\beta + \tau_c + \delta\tau_c) && \text{(3.8b)}\\
&= \frac{1}{f_{T,0}}(\psi_T(t_R) + \bar{f}_T(t_R, \delta t_R)\delta t_R - \tilde{\psi} - \delta\tilde{\psi}) - (\Delta\tau_\beta + \tau_c) - \delta\tau_c && \text{(3.8c)}\\
&= \tau_{ud} + \frac{\bar{f}_T(t_R, \delta t_R)}{f_{T,0}}\delta t_R - \frac{1}{f_{T,0}}\delta\tilde{\psi} + \Delta x - \delta\tau_c && \text{(3.8d)}
\end{aligned}$$

Further examining the receive time noise term ($\delta t_R$),

$$\begin{aligned}
\frac{\bar{f}_T(t_R, \delta t_R)}{f_{T,0}}\delta t_R &= (1 + \bar{\beta}(t_R, \delta t_R) + \bar{y}(t_R, \delta t_R))\delta t_R && \text{(3.9a)}\\
&= \delta t_R + \bar{\beta}(t_R, \delta t_R)\delta t_R + \bar{y}(t_R, \delta t_R)\delta t_R && \text{(3.9b)}\\
&\approx \delta t_R && \text{(3.9c)}
\end{aligned}$$

where the quadratic error terms $\bar{\beta}\delta t_R$ and $\bar{y}\delta t_R$ are negligible. The two-way time of flight model is then:

$$\hat{\tau}_{ud} = \tau_{ud} - \delta\tau_c + \Delta x + \delta t_R - T_0\delta\tilde{\psi} \tag{3.10}$$

$T_0 = 1/f_{T,0}$ is the transmitted signal period. The apparent range can therefore be modeled with a biased additive noise model:

$$\hat{\rho}_{a,ud} = \rho_{a,ud} + \delta\rho_b + \delta\rho_n \tag{3.11a}$$

$$\rho_{a,ud} = \frac{c}{2}\tau_{ud} \tag{3.11b}$$

$$\delta\rho_b = -\frac{c}{2}\delta\tau_c \tag{3.11c}$$

$$\delta\rho_n = \frac{c}{2}\delta t_n = \frac{c}{2}(\Delta x + \delta t_R - T_0\delta\tilde{\psi}) \tag{3.11d}$$

where $\delta\rho_b$ is the bias error, and where the noise $\delta\rho_n$ can be seen to be a linear combination of $\delta t_R$ & $\delta\tilde{\psi}$. In practice, the bias error is from the residual of a calibration process, and may be significant enough that it must be estimated or considered by EKF: the bias is appended to the state as an additional parameter to be estimated. For simplicity, we assume the calibration process is sufficiently accurate that the bias is negligible relative to the noise, and we model $\delta\rho_b = 0$. Estimating significant biases is relegated to future work. In Section 3.1.1, we determine models for the noise terms $\Delta x$, $\delta t_R$, and $\delta\tilde{\psi}$.

### 3.1.1 Modeling Optical Communications Ranging Noise

A common direct-detection optical communications modulation format is Pulse-Position-Modulation (PPM) [102]. In this format, the telemetry frames are subdivided into symbols, which are further subdivided into slots of time $T_s$. The number of slots per symbol is the PPM order ($M$). Information is encoded by emitting a pulse during one of the symbol slots. In general, there may be some slots that are left empty at the end of each symbol, called the inter-symbol guard time $T_g = GT_s$, to allow the laser to build up energy to emit a pulse. The symbol period is therefore $T_{\text{sym}} = (M+G)T_s$. The communications data rate is $R_b = R_e\log_2(M)/T_{\text{sym}}$ (bits/s), where $R_e$ is the error correction code rate [102, 104]. Time can be normalized into units of slots $u \equiv t/T_s$.

The generalized phase measurement is [99, 105]:

$$\psi = N_{\text{frame}} U_{\text{frame}} + N_{\text{sym}} M + \phi = N_{\text{frame}} U_{\text{frame}} + s + \epsilon \tag{3.12}$$

where $U_{\text{frame}} = T_{\text{frame}}/T_s$ is the normalized frame period, and $\phi$ is the phase of the pulse relative to the symbol start time. This is illustrated for a two-way ranging scheme in Figure 3-2. The frame count is known because the frame ID numbers are

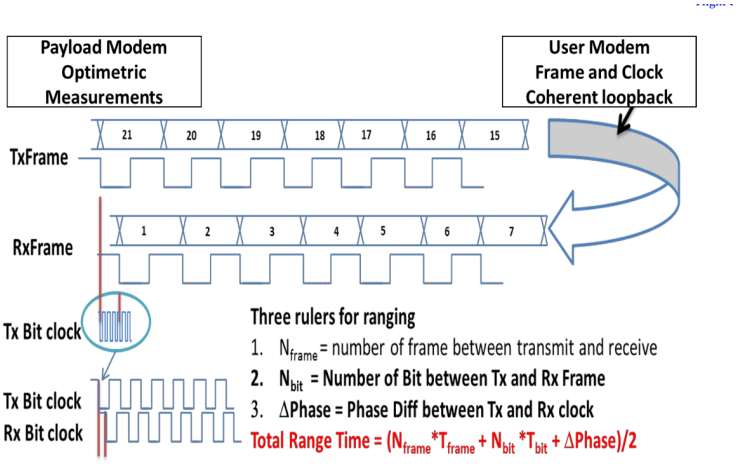


Figure 3-2: Two-way ranging for direct-detection optical communications link via data clock. Image credit: Yang et al. [51].

encoded in the frame headers, and the frames are time tagged using the attached synchronization marker (ASM) [99]. The slot clock is recovered from the received signal, which is used to count the number of slots that have elapsed ($s$) since the ASM [99]. The slot tracking loop is used to determine the fraction of slot elapsed ($\epsilon$) since the end of the last slot [99]. For a fixed-length encoding scheme, $s$ is sized such that the range ambiguity can be resolved within a single frame [99]. We assume no errors in frame or symbol counting, so the generalized phase error is equal to the relative phase error:

$$\delta\psi = \delta\phi \tag{3.13}$$

The phase error can be modeled as a function of the communications system parameters. The received optical signal is converted into a photocurrent using an ideal photodetector, with sufficient bandwidth that individual photon arrival times may

be observed. The measured photocurrent is thresholded and triggers a sampling of a clock, which produces photon arrival timestamps ($\hat{t}$) [104]:

$$\hat{t} = \frac{\Psi(t+\delta)}{2\pi f_c} = t + \delta + x(t+\delta) \tag{3.14}$$

where $t$ is the true arrival time, $\Psi$ is the clock phase, $f_c$ is the nominal clock frequency, $\delta \sim N(0, \sigma_\delta^2)$ is the detector jitter (which randomly offsets the arrival times), and $x(t+\delta)$ is the clock oscillator phase noise. The clock oscillator phase noise is modeled as a band-limited Gaussian random process with a power-law power spectral density $S_x(f)$. Values of $S_x(f)$ are specified by empirical data over a frequency band $[f_0, f_h = 2f_c]$. The RMS phase jitter in seconds can be calculated by [106]:

$$\sigma_x = \frac{1}{2\pi f_c}\sqrt{2\int_{f_0}^{f_h} S_x(f)df} \tag{3.15}$$

The phase jitter can be approximated using broadband white noise [106]:

$$\sigma_x \approx \frac{1}{2\pi f_c}\sqrt{2(f_h - f_0)S_x(f_h)} \tag{3.16}$$

For example, for the Symmetricom 9961 TXCO [107]: $10\log_{10}(S_x(f_h)) = -150$ dBc/Hz, $f_c = 125$ MHz, $f_0 = 10$ Hz, $\sigma_x \approx 1$ ps. Moving forward, we approximate the clock phase jitter as a Gaussian distribution $x(t+\delta) \sim N(0, \sigma_x^2)$. In practice, the noise characteristics of the clock should be determined empirically during ground testing to verify that any error associated with this approximation has a negligible effect on the filter performance. The timing model can then be written as:

$$\hat{t} = t + \eta \tag{3.17a}$$

$$\eta \sim N(0, \sigma_\eta^2 = \sigma_\delta^2 + \sigma_x^2) \tag{3.17b}$$

The normalized timing model is:

$$\hat{u} = u + \nu \tag{3.18a}$$

$$\nu \sim N(0, \sigma_\nu^2 = (\sigma_\eta / T_s)^2) \tag{3.18b}$$

The normalized photon arrival time ($u$) for a PPM signal can be modeled as an inhomogeneous Poisson process with rate function [108, 104]:

$$\Lambda(u) = T_s q_e i(T_s u) = n_s \left( \sum_{k=-\infty}^{\infty} g(u - kM - \phi) \right) + n_b \tag{3.19}$$

where $q_e$ is the electron charge, $i(t)$ is the photocurrent, $n_s$ is the mean number of signal photons per pulse, $n_b$ is the mean number of noise photons per slot (e.g. thermal and dark noise), and $g(u)$ is the normalized pulse shape. Pulses are assumed to be non-overlapping. The pulse shape can be modeled as a generalized Gaussian [104]:

$$g(u) = \frac{p}{2a\Gamma(1/p)} \exp(-|u/a|^p) \tag{3.20}$$

where $a$ is the $1/e$ pulse width, and $p$ is the decay rate of the pulse tail. A standard Gaussian has $p = 2$, and the pulse becomes more square as $p$ increases. The observed arrival ($\hat{u}$) rate function is the convolution [104]:

$$\hat{\Lambda}(u) = (f_\nu * \Lambda)(u) \tag{3.21}$$

where $f_\nu$ is the Gaussian pdf of $N(0, \sigma_\nu^2)$. Moving forward, we model the pulse shape as Gaussian ($p = 2$):

$$g(u) = \frac{1}{\sqrt{2\pi\sigma_a^2}} \exp\left( -\frac{u^2}{2\sigma_a^2} \right) \tag{3.22}$$

where $\sigma_a = a/\sqrt{2}$. The observed arrival rate function can then be analytically calculated.

$$\hat{\Lambda}(u) = f_\nu(u) * \Lambda(u) \tag{3.23a}$$

$$= f_\nu(u) * \left( n_s \left( \sum_{k=-\infty}^{\infty} g(u - kM - \phi) \right) + n_b \right) \tag{3.23b}$$

$$= n_s \left( \sum_{k=-\infty}^{\infty} f_\nu(u) * g(u - kM - \phi) \right) + f_\nu(u) * n_b \tag{3.23c}$$

$$= n_s \left( \sum_{k=-\infty}^{\infty} \hat{g}(u - kM - \phi) \right) + n_b \tag{3.23d}$$

where $\hat{g}(u)$ is a Gaussian function with variance $\sigma_{\hat{a}}^2 = \sigma_a^2 + \sigma_\nu^2$, and $\hat{a} = \sigma_{\hat{a}}\sqrt{2}$.

For a given set of observations $S_{\hat{u}} = \{\hat{u}_1, ..., \hat{u}_N\}$ of $K$ pulses over an integration time of $U_i = T_i/T_s = KM$, the maximum likelihood estimate (MLE) of some parameter vector $\boldsymbol{\theta}$ is:

$$\hat{\boldsymbol{\theta}}_{\text{MLE}} = \arg\max_{\boldsymbol{\theta}} \log\, p(S_{\hat{u}}, N; \boldsymbol{\theta}) \tag{3.24}$$

where the likelihood function $p(S_{\hat{u}}, N; \boldsymbol{\theta})$ is the conditional joint probability density of the set of observations. We assume that the observed pulses are not overlapping: $M > \hat{a}$. The log-likelihood function is [104, 109]:

$$L(\boldsymbol{\theta}) = \log\, p(S_{\hat{u}}, N; \boldsymbol{\theta}) = \begin{cases} -\int_{U_i} \hat{\Lambda}(u; \boldsymbol{\theta}) du + \sum_{i=0}^{N-1} \log\, \hat{\Lambda}(u_i; \boldsymbol{\theta}), \text{ for } N > 0 \\ -\int_{U_i} \hat{\Lambda}(u; \boldsymbol{\theta}) du, \text{ for } N = 0 \end{cases} \tag{3.25}$$

In general, the Cramer-Rao inequality for an MLE is:

$$\text{Cov}[\hat{\boldsymbol{\theta}}_{\text{MLE}}] \geq I(\boldsymbol{\theta})^{-1} \tag{3.26}$$

where $I(\boldsymbol{\theta})$ is the Fisher information matrix:

$$I(\boldsymbol{\theta}) = -\mathbb{E}\left[\frac{\partial^2 L(\boldsymbol{\theta})}{\partial \boldsymbol{\theta}^2}\right] \tag{3.27}$$

The MLE is asymptotically efficient, which means that in the limit of large sample size $N$, the covariance approaches the Cramer-Rao Lower Bound ($I(\boldsymbol{\theta})^{-1}$). The MLE is also asymptotically normal: the distribution of $\hat{\boldsymbol{\theta}}_{\text{MLE}}$ converges to $N(\bar{\boldsymbol{\theta}}, I(\boldsymbol{\theta})^{-1})$, where $\bar{\boldsymbol{\theta}}$ is are the true parameter values. For the phase estimate: $\hat{\phi} = \bar{\phi} + \delta\phi$, with $\delta\phi \sim N(0, \sigma_\phi^2)$. Given that $\delta\psi = \delta\phi$, $\delta\psi \sim N(0, \sigma_\psi^2)$. The phase error variance is [104]:

$$\sigma_\psi^2 = \sigma_\phi^2 = \frac{\sigma_{\hat{a}}^2}{\xi K n_s} \tag{3.28a}$$

$$\xi = \frac{1}{\sigma_{\hat{a}}^2}\int_{-M/2}^{M/2} \frac{u^2 \hat{g}(u)^2}{\hat{g}(u) + n_b/n_s} du \tag{3.28b}$$

The parameter terms can be re-expressed as:

$$n_s = \frac{P_{\text{rx}} M T_s}{E_{\text{ph}}} \tag{3.29a}$$

$$n_b = \frac{P_n T_s}{E_{\text{ph}}} \tag{3.29b}$$

$$K = \frac{T_i}{M T_s} \tag{3.29c}$$

$$\sigma_{\hat{a}}^2 = \frac{a^2}{2} + \frac{\sigma_\delta^2 + \sigma_x^2}{T_s^2} \tag{3.29d}$$

where $P_{\text{rx}}$ is the average received optical power, $P_n$ is the average noise power, and $E_{\text{ph}} = hc/\lambda$ is the energy per photon. The signal-to-noise ratio (SNR) is defined in terms of the peak-power ($P_{\text{rx,pk}} = g(0) M P_{\text{rx}} = M P_{\text{rx}}/\sqrt{\pi a^2}$):

$$\text{SNR} \equiv \frac{P_{\text{rx,pk}}}{P_n} = \frac{M P_{\text{rx}}}{P_n \sqrt{\pi a^2}} = \frac{n_s}{n_b \sqrt{\pi a^2}} \tag{3.30}$$

Making the substitutions:

$$\sigma_\psi^2 = \frac{E_{\text{ph}}}{\xi P_{\text{rx}} T_i}\left(\frac{a^2}{2} + \frac{\sigma_\delta^2 + \sigma_x^2}{T_s^2}\right) \tag{3.31a}$$

$$\xi = \frac{1}{\sigma_{\hat{a}}^2}\int_{-M/2}^{M/2} \frac{u^2 \hat{g}(u)^2}{\hat{g}(u) + (\text{SNR}\sqrt{\pi a^2})^{-1}} du \tag{3.31b}$$

Note that for large SNR, $\xi \approx 1$.

Next, we turn to the received frame arrival time measurement error $\delta t_R$. Under the serially concatenated PPM (SCPPM) architecture, the receiver relies on the detection of an attached synchronization marker (ASM) as part of the synchronization-marked transfer frame (SMTF) [99, 110]. This process uses symbol timing information from the receiver symbol tracking loop [111]. The theoretical performance is determined by evaluating the error bound on symbol synchronization [105]. We assume a direct detection PPM system; therefore, the purpose of the synchronization system is to recover the slot timing, from which frame and word synchronizations can be achieved using a coding technique [112]. In practice, a phase-locked loop (PLL) with a pre-processing filter may be used, which has a normalized timing error variance [112]:

$$\mathbb{E}[\delta u_{\text{PLL}}^2] = \zeta F_d \mathbb{E}[\delta u_{\text{ELG}}^2] = \frac{\zeta F_d B_L T_{\text{sym}}}{(2\pi)^2 n_s} \tag{3.32}$$

where $B_L$ is the tracking loop bandwidth, $\zeta$ is a dimensionless parameter that depends on the pulse shape and the preprocessing filter transfer function, and $F_d$ is the detector's excess noise factor. Substituting our previous expression for $n_s$,

$$\sigma_L^2 \equiv \mathbb{E}[\delta u_{\text{PLL}}^2] = \frac{\zeta F_d B_L T_{\text{sym}}}{(2\pi)^2}\left(\frac{E_{\text{ph}}}{P_{\text{rx}} T_{\text{sym}}}\right) = \left(\frac{\zeta F_d B_L}{4\pi^2}\right)\frac{E_{\text{ph}}}{P_{\text{rx}}} \tag{3.33}$$

We use this to model the frame arrival timing error variance $\sigma_R^2 = \mathbb{E}[\delta t_R^2] = T_s^2 \sigma_L^2$.

We address the oscillator phase noise term $\Delta x$. For the crosslinks of interest in this work, the range is on the order of $10^3$ to $10^5$ km, which yields a two-way time of flight $\tau \approx \tau_{ud} \approx 2\rho/c$ on the order of $10^{-3}$ to $10^0$ seconds, where we assume $\tau_c < 10^{-3}$ seconds. Moving forward, we assume the use of a clock that has an approximately

white noise spectrum over this range of relevant sample times. The oscillator phase deviation $\Delta x$ is then modeled as a Gaussian white noise process [102, 13, 113]:

$$\Delta x(t_R, \tau) = x(t_R) - x(t_R - \tau) \sim N(0, \sigma^2_{\Delta x}(\tau)) \tag{3.34a}$$

$$\sigma_{\Delta x}(\tau) \approx \sqrt{2}\tau\sigma_y(\tau) \tag{3.34b}$$

where $\sigma_y(\tau)$ is the Allan deviation with a sample time of $\tau$. The approximation ignores linear phase drift, which is negligible over the time of flight range of interest [13]. Moving forward, we assume that the clock's Allan variance can be modeled as inversely proportional to the sample time [102, 114]:

$$\sigma_y(\tau) \approx \frac{k_y}{\sqrt{\tau}} \approx \frac{k_y}{\sqrt{2\rho/c}} \tag{3.35}$$

where $k_y \approx \sigma_y(1 \text{ sec})$.

Combining the above results, the component ranging noise terms are modeled as independent white Gaussian noise processes; therefore, the total ranging noise is also modeled as a white Gaussian noise process:

$$\delta\rho_n = \frac{c}{2}(\Delta x + \delta t_R - T_s\delta\psi) \sim N(0, \sigma^2_\rho) \tag{3.36a}$$

$$\sigma^2_\rho = \mathbb{E}[\delta\rho^2_n] = \left(\frac{c}{2}\right)^2 (\sigma^2_{\Delta x} + \sigma^2_R + T^2_s\sigma^2_\psi) \tag{3.36b}$$

$$\sigma_\rho = \sqrt{\sigma^2_{\rho,x} + \sigma^2_{\rho,\psi}} \tag{3.36c}$$

$$\sigma_{\rho,\psi} \equiv \frac{c}{2}\sqrt{\sigma^2_R + T^2_s\sigma^2_\psi} = \frac{cT_s}{2}\sqrt{\sigma^2_L + \sigma^2_\psi} \tag{3.36d}$$

$$\sigma_{\rho,x} \equiv \frac{c}{2}\sigma_{\Delta x}(\tau) = \frac{c}{\sqrt{2}}\tau\sigma_y(\tau) \approx k_y\sqrt{c\rho} \tag{3.36e}$$

where $\sigma_R = T_s\sigma_L$. The photodetection phase noise is:

$$\sigma_{\rho,\psi} = \frac{cT_s}{2}\sqrt{\frac{E_{\text{ph}}}{P_{\text{rx}}}\left(\frac{\zeta F_d B_L}{4\pi^2} + \left(\frac{a^2}{2} + \frac{\sigma^2_\delta + \sigma^2_x}{T^2_s}\right)\frac{1}{\xi T_i}\right)} \tag{3.37a}$$

In Section 3.1.2, we look at modeling the received power $P_{\text{rx}}$ using the optical link equation.

### 3.1.2 The Optical Link Equation

The optical link equation models the received power as a function of the optical transmitter and receiver properties and the optical path:

$$P_{\text{rx}} = P_{\text{tx}} G_{\text{tx}} G_{\text{rx}} L_{\text{path}} L_{\text{ptg}} L_{\text{tx}} L_{\text{rx}} L_{\text{atm}} \tag{3.38}$$

where $P_{\text{rx}}$ is the power to the receiver sensor in Watts, $P_{\text{tx}}$ is the power from the laser source in Watts, $G_{\text{tx}}$ is the transmitter gain, $G_{\text{rx}}$ is the receiver gain, $L_{\text{path}}$ is the path loss, $L_{\text{ptg}}$ is the pointing loss, $L_{\text{tx}}$ and $L_{\text{rx}}$ are the transmitter and receiver optical implementation losses, and $L_{\text{atm}}$ is the atmospheric loss. The gain and loss terms are all dimensionless with $L \leq 1$ for all loss terms. Simple equations can be given for some of them as follows [43, 44, 23, 104]:

$$G_{\text{tx}} = \begin{cases} \left(\frac{\pi D_{\text{tx}}}{\lambda}\right)^2 \frac{2}{\alpha_t} \left(\exp(-\alpha_t^2) - \exp(-\alpha_t^2 \gamma_t^2)\right)^2 & \text{(central-obscuration)} \\ \frac{32}{\theta_{1/e^2}^2} & \text{(untruncated and unobscured)} \end{cases} \tag{3.39a}$$

$$G_{\text{rx}} = \left(\frac{\pi D_{\text{rx}}}{\lambda}\right)^2 (1 - \gamma_r^2) \tag{3.39b}$$

$$L_{\text{path}} = \left(\frac{\lambda}{4\pi\rho}\right)^2 \tag{3.39c}$$

$$L_{\text{ptg}} = \exp\left(-8\left(\frac{\delta\theta}{\theta_{1/e^2}}\right)^2\right) \tag{3.39d}$$

where $\lambda$ is the laser wavelength, $D_{\text{tx}}$ is the diameter of the receiver aperture, $\alpha_t = D_{\text{tx}}/(2w) = \pi D_{\text{tx}} \theta_{1/e^2}/(4\lambda)$ is the aperture to beam width ($w$) ratio, $\gamma_t = B_{\text{tx}}/D_{\text{tx}}$ is the transmitter obscuration ratio, $D_{\text{rx}}$ is the diameter of the receiver aperture, $\gamma_t = B_{\text{rx}}/D_{\text{rx}}$ is the receiver obscuration diameter ($B_{\text{rx}}$) to aperture diameter ratio, $\delta\theta$ is the pointing error angle relative to the true line of sight between the terminals, and $\theta_{1/e^2}$ is the laser $1/e^2$ full-width beam divergence angle. More detailed statistical modeling of the pointing loss can be found in [23, 43, 115]. $L_{\text{atm}}$ is based on atmospheric modeling of absorption and scattering of the laser wavelength and is a function of distance that the beam travels within the atmosphere. For our analyses, we will

not consider crosslinks that pass through a significant portion of the atmosphere. Therefore, we model $L_{\text{atm}} = 1$ ($L_{\text{atm,dB}} = 0$ dB). Note that link terms are often specified in decibels (dB): $X_{\text{dB}} \equiv 10\log_{10}(X)$.

### 3.1.3 Received Power Requirement for Laser Communications

For the purposes of this work, the lasercom system's minimum received average power requirement $P_{\text{rx-req}}$ is assumed to be optimized such that the received power at the maximum operational range ($\rho_{\max}$) and at the worst allowed pointing loss ($L_{\text{ptg-req}}$) exceeds the minimum required power level for communications at the by some margin factor.

$$P_{\text{rx-req}} = P_{\text{tx}} G_{\text{tx}} G_{\text{rx}} L_{\text{path}}(\rho_{\max}) L_{\text{ptg-req}} L_{\text{tx}} L_{\text{rx}} \tag{3.40a}$$

$$(P_{\text{tx}} G_{\text{tx}} G_{\text{rx}} L_{\text{tx}} L_{\text{rx}})_{\text{req}} = \frac{P_{\text{rx-req}}}{L_{\text{path}}(\rho_{\max}) L_{\text{ptg-req}}} \tag{3.40b}$$

$$\text{therefore:} \tag{3.40c}$$

$$P_{\text{rx}} = P_{\text{rx-req}} \frac{L_{\text{path}}(\rho)}{L_{\text{path}}(\rho_{\max})} \frac{L_{\text{ptg}}}{L_{\text{ptg-req}}} \tag{3.40d}$$

$$= P_{\text{rx-req}} \left( \frac{\rho_{\max}}{\rho} \right)^2 \frac{L_{\text{ptg}}}{L_{\text{ptg-req}}} \tag{3.40e}$$

Equation 3.40b represents a constraint on the system parameters that make up the product on the left-hand side. Given additional size, weight, and power (SWaP) constraints as well as reasonable assumptions on the hardware implementation losses ($L_{\text{tx}} L_{\text{rx}}$), it is possible to bound the values of the transmit power $P_{\text{tx}}$, the receiver aperture size $D_{\text{tx}}$, and the transmit gain $G_{\text{tx}}$. If the transmitter aperture design is untruncated and unobscured, the transmit gain value directly determines the transmitter beam divergence $\theta_{1/e^2}$. angle. Otherwise, the divergence angle, transmitter aperture size, and obscuration ratio are traded-off using the terminal's size and weight constraints. The pointing loss is a random variable, so the pointing requirement is specified as: $\mathbb{P}[|L_{\text{ptg,dB}}| \leq |L_{\text{ptg-req,dB}}|] = \mathbb{P}[L_{\text{ptg}} \geq L_{\text{ptg-req}}] = p$. This implies that

with probability $p$ (e.g. $p = 99.99\%$):

$$P_{\text{rx}} \geq P_{\text{rx-req}} \left( \frac{\rho_{\max}}{\rho} \right)^2 \tag{3.41}$$

The maximum achievable data rate for a given set of communications parameters is called the channel capacity ($C$). Determining the capacity of a Poisson M-PPM channel with noise requires evaluating the relative entropy functions of the signal and noise, which do not have an exact analytical solution. However, the solution may be approximated as [115, 116]:

$$C(P_{\text{rx}}) \approx \frac{P_{\text{rx}}^2}{E_{\text{ph}} \ln(2)} \left( \frac{P_{\text{rx}}^2 M T_s}{E_{\text{ph}} \ln(M)} + \frac{P_{\text{rx}}}{\ln(M)} + \frac{2P_{\text{n}}}{M-1} \right)^{-1} \tag{3.42}$$

where $P_n$ is the detected noise power. This approximation is accurate to within 20% error for $0.25 \leq R_e \leq 0.75$ [115]. The minimum required power to close a link for a given data bit rate requirement $R_b$ satisfies the following inequality [116]:

$$C(P_{\text{rx-min}}) \geq R_b = R_e \frac{\log_2 M}{M T_s} \tag{3.43}$$

The minimum received power therefore satisfies:

$$\frac{(1-R_e) P_{\text{rx-min}}^2}{R_b E_{\text{ph}} \ln(2)} - \frac{P_{\text{rx-min}}}{\ln(M)} - \frac{2P_n}{M-1} \geq 0 \tag{3.44}$$

Note that $P_n$ is a function of of the received power due to shot noise. The required power must exceed this minimum power by some margin factor ($m$):

$$P_{\text{rx-req}} \geq m P_{\text{rx-min}} \tag{3.45}$$

where $m$ is the margin factor that accounts for detector jitter loss $m_{\text{jitter,dB}}$, detector quantum efficiency $m_{\eta,\text{dB}}$, $m_{\text{imp,dB}}$ implementation efficiency, code efficiency, and any additional factor of safety:

$$m_{\text{dB}} = m_{\text{jitter,dB}} + m_{\eta,\text{dB}} + m_{\text{imp,dB}} + m_{\text{code,dB}} + m_{\text{FOS,dB}} \tag{3.46}$$

For example, the code efficiency margin is the increase in signal power required to achieve a particular bit error rate (BER), which depends on the coding scheme. For example, for a BER $\sim 10^{-5}$, $m_{\text{code,dB}}$: SCPPM $\sim$ 0.5-1 dB, Reed-Solomon $\sim$ 2.5-3.0 dB, and uncoded $\sim$ 5 dB [115]. Moving forward, we assume SCPPM with $m_{\text{code,dB}} = 1$ dB and $R_e = 2/3$ [117].

The noise power $P_n$ is modeled as shot noise ($\sigma_{shot}$) from an Avalanche-Photodiode-Detector (APD) and thermal noise from the pre-amplifier ($\sigma_{amp}$), typically a transimpedence amplifier (TIA). The shot noise includes detected power from the signal ($P_{\text{rx}}$) and background ($P_b$) as well as dark current ($i_{d,m}$). These are defined as: [44, 120]:

$$P_n = \sigma_n/(M_d R_d) \tag{3.47a}$$

$$\sigma_n = \sqrt{\sigma_{shot}^2 + \sigma_{amp}^2} \tag{3.47b}$$

$$\sigma_{shot}^2 = 2F_d M_d^2 B_e q_e (i_{d,m} + R_d(P_{rx} + P_b)) \tag{3.47c}$$

$$\sigma_{amp}^2 = (4k_B T/R_{amp}) F_{amp} B_e = i_{amp}^2 B_e \tag{3.47d}$$

$$P_b = I_b w_\lambda \Omega_d A_{\text{rx}} \eta_d L_{\text{rx}} \tag{3.47e}$$

where $q_e$ is the electron charge, $k_B$ is Boltzmann's constant, $T$ is the temperature, $F_{amp}$ is the amplifier excess noise factor, $\Omega_d$ is the solid angle of the detector's field of view, and $A_{\text{rx}}$ is the receiver aperture area. Additional terms are defined in Table 3.43, and example link and receiver parameter values are given that will be used in all subsequent analyses. Example transmitter parameter values needed to close a link for short and long range crosslink scenarios are shown in Table 3.2. Example values of $P_{\text{rx-req}}$ and $P_{\text{peak-req}}$ that have been computed using the parameter values in Table 3.43 are shown in Figure 3-3. Note that for a given data rate, the required power decreases as the PPM order increases. Moving forward, our default design PPM order will be PPM-16.

Table 3.1: Example Optical Communications System Parameters. Note that values without a citation are computed from the other parameters. For example, the data rate, PPM order, and ECC rate determine the slot width as per Equation 3.43.

| | | |
|---|---|---|
| Communications Link Parameters | | |
| $R_b$ | Data Rate Requirement | 622 Mbps [118] |
| $M$ | Design PPM Order | 16 [118] |
| $R_e$ | Error Correction Code Rate | 1/2 [118] |
| $T_s$ | Slot Width | 0.2 ns |
| $a$ | Normalized Pulse Width | 1/2 [104] |
| $B_L T_s$ | Normalized PLL Bandwidth | 0.01 [112] |
| $\lambda$ | Optical Carrier Wavelength | 1550 nm [118] |
| $P_{\text{rx-min}}$ | Channel Avg Rx Power Requirement | $-95.40$ dBW |
| $m$ | Total Required Margin | 11.49 dB |
| $P_{\text{rx-req}}$ | Avg Rx Power Requirement | $-83.91$ dBW |
| $P_{\text{pk-req}}$ | Peak Rx Power Requirement | $-71.35$ dBW |
| Receiver Optics | | |
| $D_{\text{rx}}$ | Aperture Diameter | 10 cm [118] |
| $L_{\text{rx,dB}}$ | Receiver Loss | $-1.5$ dB [119] |
| $w_\lambda$ | Bandpass Filter Width | 0.2 nm [115] |
| $\text{FOV}_d$ | Detector Field-of-View | 1 mrad [119] |
| InGaAs Avalanche Photodiode Detector (APD) | | |
| $\eta_d$ | Quantum Efficiency | 0.8 [120] |
| $R_d$ | Responsivity | 1 $A/W$ [120] |
| $M_d$ | Gain | 10 [120] |
| $F_d$ | Excess Noise Factor | 3.5 [120] |
| $D_d$ | Sensor Diameter | 200 $\mu$m [120] |
| $B_e$ | Filter Bandwidth | 500 MHz [120] |
| $i_{d,m}$ | Unmultiplied Dark Current | 2.5 nA [120] |
| $i_{amp}$ | TIA Input-Referred Noise Density | 2.1 $pA/\sqrt{\text{Hz}}$ [120] |
| $\sigma_\delta$ | Detector Jitter | 240 ps [115] |
| Background and Total Noise | | |
| $I_b$ | Background Radiance (Stars) at 1550 nm | $4 \times 10^{-7}$ W/(m$^2$sr$\mu$m) [43] |
| $P_b$ | Background Noise Power | $-178.5$ dBW |
| $P_n$ | Avg Noise Power at $P_{\text{rx-req}}$ | $-82.94$ dBW |
| Atomic Clock | | |
| $\sigma_y(1 \text{ sec})$ | Allan Deviation ($\tau = 1$ sec) | $3 \times 10^{-11}$ [121] |
| $\sigma_x$ | Clock Jitter | 12.17 ps [121] |

Table 3.2: Example Transmitter Parameters (Assuming $L_{\text{tx}} = L_{\text{rx}}$). The cited ranges are not comprehensive for all orbits and will vary depending on the exact configuration. These examples simply show that the divergence angles and transmitter powers needed to close a link using the receiver parameters in Table 3.1 are reasonable since they are similar to the parameters for existing terminals (see Table 1.1). LLO stands for Low Lunar Orbit. LNRHO stands for Lunar Near Rectilinear Halo Orbit, which is type of orbit being studied for NASA's Lunar Gateway and other missions [10].

| | | |
|---|---|---|
| LEO-LEO: $\rho_{\max} = 2300$ km | | |
| $\text{EIRP}_{\text{req}}$ | Required EIRP | 81.36 dBW |
| $\theta_{1/e^2}$ | Divergence Angle | 150 $\mu$rad |
| $P_{\text{tx}}$ | Transmitter Avg Power | 96.2 mW |
| LEO-MEO: $\rho_{\max} = 33466$ km | | |
| $\text{EIRP}_{\text{req}}$ | Required EIRP | 104.6 dBW |
| $\theta_{1/e^2}$ | Divergence Angle | 15 $\mu$rad |
| $P_{\text{tx}}$ | Transmitter Avg Power | 204 mW |
| LEO-GEO: $\rho_{\max} = 49139$ km | | |
| $\text{EIRP}_{\text{req}}$ | Required EIRP | 108.0 dBW |
| $\theta_{1/e^2}$ | Divergence Angle | 15 $\mu$rad |
| $P_{\text{tx}}$ | Transmitter Avg Power | 439 mW |
| LLO-LNRHO: $\rho_{\max} = 73525$ km | | |
| $\text{EIRP}_{\text{req}}$ | Required EIRP | 111.5 dBW |
| $\theta_{1/e^2}$ | Divergence Angle | 15 $\mu$rad |
| $P_{\text{tx}}$ | Transmitter Avg Power | 983 mW |

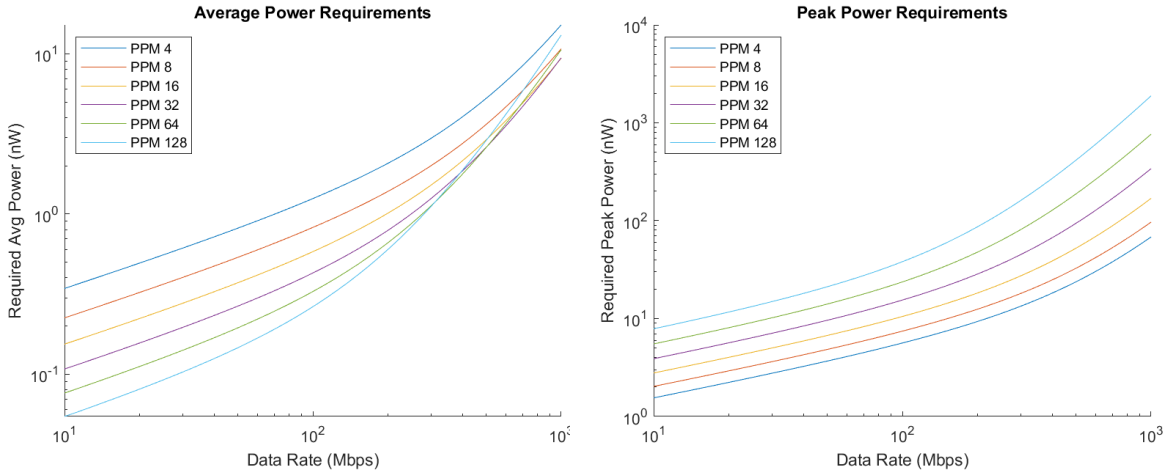


Figure 3-3: (a) Example required average power values ($P_{\text{rx-req}}$) at different data rates and PPM orders. (b) Example required peak power values ($P_{\text{rx-req}}$) at different data rates and PPM orders.

### 3.1.4 Range Measurement Noise Sensitivity Analysis

Values for the ranging error (1-sigma) are computed while varying individual system parameters in Table 3.1. In Figure 3-4, the required data rate is varied from 10 Mbps to 1.244 Gbps. Changing the data rate has a large impact on the ranging error because it directly affects the slot width and the required power. In particular, there are three distinct regions where different elements of the ranging error model dominate. In the low data rate (∼10-20 Mbps) regime, the detector error dominates, which makes sense since in this low power photon-counting regime, the detector jitter has a large impact. For moderate data rates (∼20-100 Mbps), the synchronization error dominates. For high data rates (∼100-1000 Mbps), the clock error dominates, which makes sense since the ultimate limit on performance is error due to timing stability. In Figure 3-5,

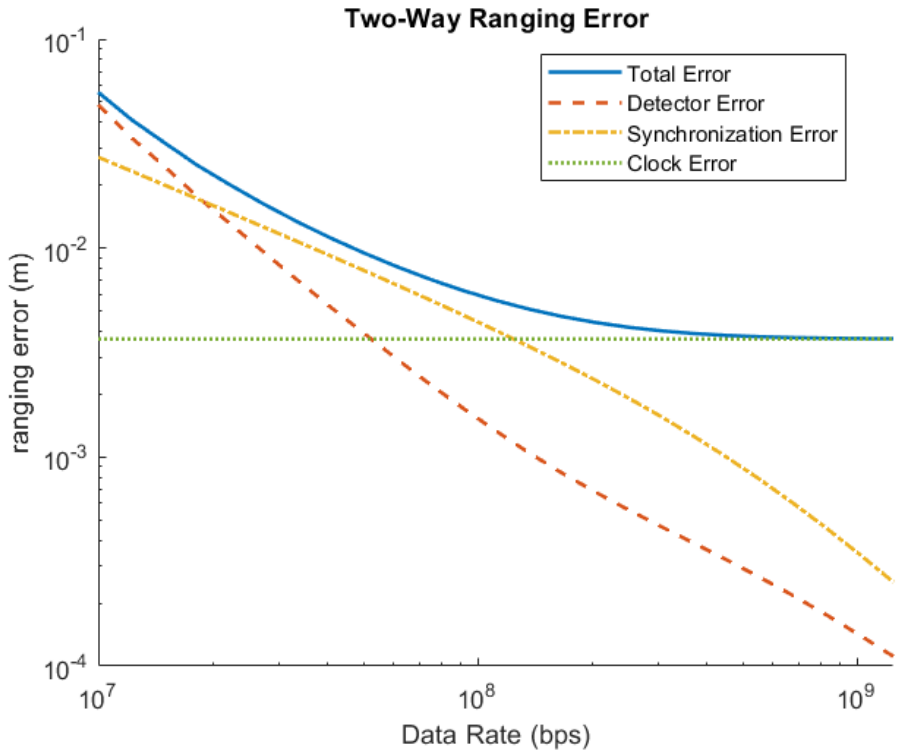


Figure 3-4: Sensitivity of range error to data rate.

the maximum design range is varied. Since the default data rate is 622 Mbps, the range error is highly sensitive to clock errors, which grow with distance due to the increasing time of flight. For sufficiently short links (∼2000 km or less), the time of

flight is small enough that the clock error is less than the synchronization error. In

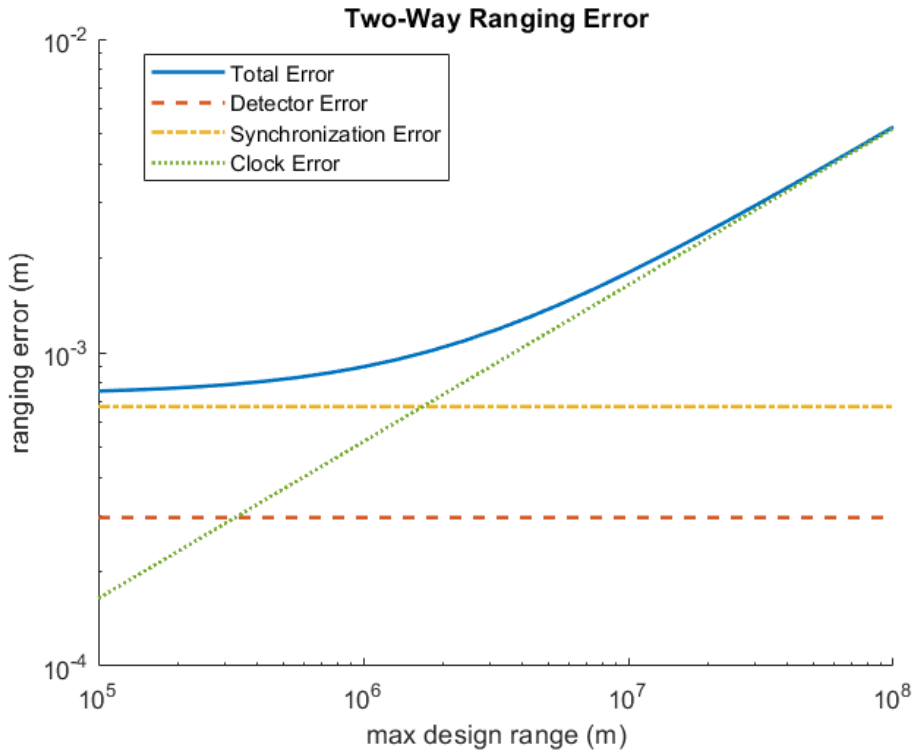


Figure 3-5: Sensitivity of range error to maximum design range.

Figure 3-6, the normalized range (range divided by maximum design range) is varied. Since the default data rate is 622 Mbps, the range error is dominated by the clock error term, which decreases with range because of the decreasing time of flight. The other error terms also decrease with range because of the increasing received power. This behavior of decreasing error with normalized range is true for all data rates. In Section 3.1.5, we turn to modeling the apparent range as a function of the spacecraft states.

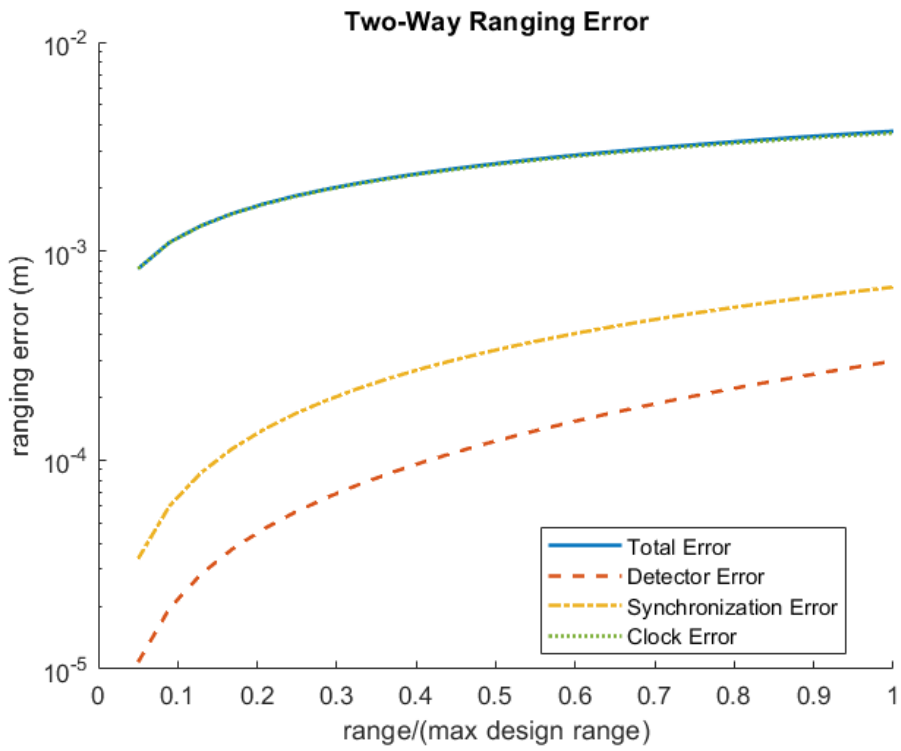


Figure 3-6: Sensitivity of range error to normalized range.

### 3.1.5 Modeling Apparent Range

For estimation, we need a model of the apparent range that is a function of the satellite state vectors at the time of measurement. Due to the motion of the satellites, in combination with relativistic effects, the apparent range determined from the time of flight is offset from the instantaneous geometric range between the satellites. In general relativity, the path that photons take in spacetime is a geodesic curve governed by the metric tensor field. For practical computational modeling of the time of flight, an approximate model is used. The error requirement for this approximate model is that it is sufficiently accurate such that the systematic model error is is negligible compared to the measurement noise floor. The noise levels for the lasercom ranging systems of primary interest in this work ($10^{-3}$ to $10^{-1}$ m) are on the order of several picoseconds to a few hundred picoseconds, so we aim for sub-picosecond level ($10^{-4}$ m) accuracy in modeling the time of flight. In this section, we follow the analysis of the GRACE and GRACE follow-on missions described by Yan et al. [122]. The

one-way photon path from the transmitter to the receiver is approximated as a line in space:

$$\mathbf{r}_{\mathrm{ph}}(\lambda) = \mathbf{r}_{\mathrm{tx}}(t_{\mathrm{tx}}) + \lambda(\mathbf{r}_{\mathrm{rx}}(t_{\mathrm{rx}}) - \mathbf{r}_{\mathrm{tx}}(t_{\mathrm{tx}}));\ \lambda \in [0,1] \tag{3.48}$$

where $t_{\mathrm{rx}}$ is the time of photon reception, $t_{\mathrm{tx}} = t_{\mathrm{rx}} - \tau$ is the time of photon transmission, $\tau$ is the one-way time of flight, and $\mathbf{r}_{\mathrm{rx}}$ and $\mathbf{r}_{\mathrm{tx}}$ are the position functions of the receiver and transmitter, respectively. Relativistic light bending effects are negligible for our purposes, and are therefore not included in this analysis [122]. The one-way time of flight ($\tau$) can be expressed as:

$$\tau = \tau_{\mathrm{GEO}} + \Delta\tau_{\mathrm{SR}} + \Delta\tau_{\mathrm{GR}} \tag{3.49}$$

where $\tau_{\mathrm{GEO}}$ is the time of flight if transmitter was stationary (corresponds to the geometric range), and $\Delta\tau_{\mathrm{SR}}$ & $\Delta\tau_{\mathrm{GR}}$ are the corrections due to special relativity and general relativity, respectively. $\tau_{\mathrm{GEO}}$ can be expressed in terms of the transmitter and receiver positions:

$$\tau_{\mathrm{GEO}} = \frac{\rho(t_{\mathrm{rx}})}{c} = \frac{1}{c}\left\|\mathbf{r}_{\mathrm{rx}}(t_{\mathrm{rx}}) - \mathbf{r}_{\mathrm{tx}}(t_{\mathrm{rx}})\right\| \tag{3.50}$$

$\tau_{\mathrm{SR}} = \tau_{\mathrm{GEO}} + \Delta\tau_{\mathrm{SR}}$ is the time of flight including the effect of the motion of the transmitter. It is defined as:

$$\tau_{\mathrm{SR}} = \frac{1}{c}\left\|\mathbf{r}_{\mathrm{rx}}(t_{\mathrm{rx}}) - \mathbf{r}_{\mathrm{tx}}(t_{\mathrm{tx}})\right\| \tag{3.51}$$

The correction due to general relativity can be expanded as:

$$\Delta\tau_{GR} = \Delta\tau_{\mathrm{PM}} + \Delta\tau_{\mathrm{HM}} + \Delta\tau_{\mathrm{SM}} \tag{3.52}$$

$\Delta\tau_{\mathrm{PM}}$ is the correction due to the primary moment of the central body's gravitational field (also called the Shapiro delay).

$$\Delta\tau_{\mathrm{PM}} = \frac{2\mu}{c^3}\ln\left(\frac{\|\mathbf{r}_{\mathrm{rx}}(t_{\mathrm{rx}})\| + \|\mathbf{r}_{\mathrm{tx}}(t_{\mathrm{tx}})\| + \|\mathbf{r}_{\mathrm{rx}}(t_{\mathrm{rx}}) - \mathbf{r}_{\mathrm{tx}}(t_{\mathrm{tx}})\|}{\|\mathbf{r}_{\mathrm{rx}}(t_{\mathrm{rx}})\| + \|\mathbf{r}_{\mathrm{tx}}(t_{\mathrm{tx}})\| - \|\mathbf{r}_{\mathrm{rx}}(t_{\mathrm{rx}}) - \mathbf{r}_{\mathrm{tx}}(t_{\mathrm{tx}})\|}\right) \tag{3.53}$$

$\Delta\tau_{\mathrm{HM}}$ is the correction due to higher moments of the central body's gravitational field and third-body perturbing potentials, and $\Delta\tau_{\mathrm{SM}}$ is the correction due to the central body's spin moment. Expressions for these can be found in [122]. Importantly, all of the GR correction terms are functions of $\mathbf{r}_{\mathrm{tx}}(t_{\mathrm{tx}})$ and $\mathbf{r}_{\mathrm{rx}}(t_{\mathrm{rx}})$. Putting these results together, the one-way time of flight can be implicitly defined as

$$\tau = f_\tau(\mathbf{r}_{\mathrm{rx}}(t_{\mathrm{rx}}), \mathbf{r}_{\mathrm{tx}}(t_{\mathrm{rx}} - \tau)) \tag{3.54a}$$

$$= \frac{1}{c} \left\| \mathbf{r}_{\mathrm{rx}}(t_{\mathrm{rx}}) - \mathbf{r}_{\mathrm{tx}}(t_{\mathrm{rx}} - \tau) \right\| + \Delta\tau_{GR}(\mathbf{r}_{\mathrm{rx}}(t_{\mathrm{rx}}), \mathbf{r}_{\mathrm{tx}}(t_{\mathrm{rx}} - \tau)) \tag{3.54b}$$

This equation can be iteratively solved:

$$\tau_{i+1} = f_\tau(\mathbf{r}_{\mathrm{rx}}(t_{\mathrm{rx}}), \mathbf{r}_{\mathrm{tx}}(t_{\mathrm{rx}} - \tau_i)); \; \tau_0 = 0 \tag{3.55}$$

Note that since the position vectors of orbiting satellites have magnitudes on the order of $10^6$ m, the precision of this algorithm in 64-bit (double) floating point arithmetic is on the order of $10^{-6}$ ps, which is sufficient for our purposes. If higher accuracy is needed, the iterative algorithm can be expanded for the first few terms into a closed-form analytical solution [122]. The time of flight was computed for a worst-case LEO-to-LEO crosslink (relative speed $\sim$ 15 km/s), a worst-case LEO-to-GEO crosslink (relative speed $\sim$ 7.4 km/s), and a worst-case LLO-to-LNRHO crosslink (relative speed $\sim$ 1.6 km/s). The results are summarized in Table 3.3 and show that in order to achieve picosecond accuracy, a time of flight model that includes $\Delta\tau_{\mathrm{SR}}$ and $\Delta\tau_{\mathrm{PM}}$ is needed. The other correction terms are negligible. For the Earth orbits, $\Delta\tau_{\mathrm{HM}}$ was calculated using a J2 approximation for the aspheric perturbing potential and the third-body perturbing potentials for the Moon and the Sun. For the Lunar orbits, $\Delta\tau_{\mathrm{HM}}$ was calculated using a J2 approximation for the aspheric perturbing potential and the third-body perturbing potentials for the Earth and the Sun. Refining the potential to higher accuracy by using higher order aspheric terms is unnecessary, since this term is negligible for our purposes. Therefore, the model

Table 3.3: Time of Flight Calculation Examples

| | LEO-Tx to LEO-Rx | LEO-Tx to GEO-Rx | LLO-Tx to LNRHO-Rx |
|---|---|---|---|
| $\tau_{\text{GEO}}$ | $\sim 3.59$ ms | $\sim 143.98$ ms | $\sim 239.37$ ms |
| $\lvert\Delta\tau_{\text{SR}}\rvert$ | $\sim 90.56$ ns | $\sim 3538.59$ ns | $\sim 1321.73$ ns |
| $\lvert\Delta\tau_{\text{PM}}\rvert$ | $\sim 4.58$ ps | $\sim 81.02$ ps | $\sim 1.61$ ps |
| $\lvert\Delta\tau_{\text{HM}}\rvert$ | $\sim 2 \times 10^{-3}$ ps | $\sim 15 \times 10^{-3}$ ps | $\sim 37 \times 10^{-3}$ ps |
| $\lvert\Delta\tau_{\text{SM}}\rvert$ | $\sim 4 \times 10^{-7}$ ps | $\sim 1 \times 10^{-5}$ ps | $\sim 2 \times 10^{-18}$ ps |
| LEO-LEO Rx: $a = 6960.6$ km, $e = 0.0017$, $i = 98.08°$ $\Omega = 109.65°$, $\omega_p = 334.37°$, $M = 207.49°$ | | | |
| LEO-LEO Tx: $a = 6960.6$ km, $e = 0.0017$, $i = 81.92°$ $\Omega = 289.65°$, $\omega_p = 334.37°$, $M = 32.49°$ | | | |
| LEO-GEO Rx: $a = 42165.2$ km, $e = 0.0003$, $i = 11.7°$ $\Omega = 42.13°$, $\omega_p = 313.01°$, $M = 230.48°$ | | | |
| LEO-GEO Tx: $a = 6960.6$ km, $e = 0.0003$, $i = 101.7°$ $\Omega = 42.13°$, $\omega_p = 313.01°$, $M = 320.48°$ | | | |
| LLO-LNRHO Rx: $a = 37788$ km, $e = 0.898$, $i = 90°$ $\Omega = 0°$, $\omega_p = 90°$, $M = 180°$ | | | |
| LLO-LNRHO Tx: $a = 1788$ km, $e = 0$, $i = 89.8°$ $\Omega = 0°$, $\omega_p = 270°$, $M = 90°$ | | | |

we will use for one-way time of flight is:

$$\tau = \tilde{f}_\tau(\mathbf{r}_{\text{rx}}(t_{\text{rx}}), \mathbf{r}_{\text{tx}}(t_{\text{rx}} - \tau)) \tag{3.56a}$$

$$= \frac{1}{c} \left\| \mathbf{r}_{\text{rx}}(t_{\text{rx}}) - \mathbf{r}_{\text{tx}}(t_{\text{rx}} - \tau) \right\| + \Delta\tau_{PM}(\mathbf{r}_{\text{rx}}(t_{\text{rx}}), \mathbf{r}_{\text{tx}}(t_{\text{rx}} - \tau)) \tag{3.56b}$$

For two-way ranging,

$$\tau_d = \tilde{f}_\tau(\mathbf{r}_0(t'), \mathbf{r}_i(t' - \tau_d)) \tag{3.57a}$$

$$\tau_u = \tilde{f}_\tau(\mathbf{r}_i(t''), \mathbf{r}_0(t'' - \tau_u)) \tag{3.57b}$$

$$t' = t_R - \tau_d^{\text{rx}} \tag{3.57c}$$

$$t'' = t' - \tau_d - \tau_u^{\text{rx}} - \tau_d^{\text{tx}} \tag{3.57d}$$

where the recorded measurement time is $t_R$. The time of flight $\tau_d$ is determined first. Once $\tau_d$ is known, $t''$ can be determined, and then $\tau_u$ can be found. Using a kinematic constant acceleration approximation, the time shifted position vectors can be written

in terms of the spacecraft states at $t_R$:

$$\mathbf{r}_0(t') \approx \mathbf{r}_0(t_R) - \mathbf{v}_0(t_R)\tau_d^{\text{rx}} + \frac{1}{2}\mathbf{a}_0(t_R)(\tau_d^{\text{rx}})^2 \tag{3.58a}$$

$$\mathbf{r}_i(t' - \tau_d) \approx \mathbf{r}_i(t_R) - \mathbf{v}_i(t_R)(\tau_d^{\text{rx}} + \tau_d) + \frac{1}{2}\mathbf{a}_i(t_R)(\tau_d^{\text{rx}} + \tau_d)^2 \tag{3.58b}$$

$$\mathbf{r}_i(t'') \approx \mathbf{r}_i(t_R) - \mathbf{v}_i(t_R)(\tau_c'' + \tau_d) + \frac{1}{2}\mathbf{a}_i(t_R)(\tau_c'' + \tau_d)^2 \tag{3.58c}$$

$$\mathbf{r}_0(t'' - \tau_u) \approx \mathbf{r}_0(t_R) - \mathbf{v}_0(t_R)(\tau_c'' + \tau_d + \tau_u) + \frac{1}{2}\mathbf{a}_0(t_R)(\tau_c'' + \tau_d + \tau_u)^2 \tag{3.58d}$$

where $\tau_c'' = \tau_u^{\text{rx}} + \tau_d^{\text{tx}} + \tau_d^{\text{rx}}$. Using these approximations in combination with a Newtonian gravity approximation ($\mathbf{a} \approx -\mu\mathbf{r}/\left\|\mathbf{r}\right\|^3$) instead of integrating the full force model has a negligible impact on error. For the LEO-LEO case, error $\sim 2 \times 10^{-3}$ ps, and for the LEO-GEO case, error $\sim 0.2$ ps. To improve computational speed, we can limit the iterative process to the minimum number of iterations required to achieve picosecond accuracy. Using the approximate model described so far (with 1 $\mu$s for each hardware delay) two-way TOF errors for different numbers of iterations were calculated for the same LEO-LEO and LEO-GEO cases. The results are shown in Table 3.4. Three iterations is sufficient to achieve picosecond or better accuracy. With

Table 3.4: Two-Way Time of Flight Calculation Convergence

| Iterations | $\tau_{ud}$ Error: LEO-LEO | $\tau_{ud}$ Error: LEO-GEO |
|---|---|---|
| 1 | $\sim 180.47$ ns | $\sim 3537.29$ ns |
| 2 | $\sim 4.54$ ps | $\sim 84.45$ ps |
| 3 | $\sim 5.11 \times 10^{-3}$ ps | $\sim 0.48$ ps |

3 iterations, perfectly calibrated hardware delays up to 10 ms each have negligible impact. Calibration errors for each of the hardware delays up to about 10 ns have a negligible impact. Measurement model gradients can be found in Appendix A.

## 3.2 Systems Analysis for Range-Rate Measurements

The Doppler effect changes the signal frequency and period:

$$\frac{f_{\text{rx}}}{f_{\text{tx}}} = \frac{T_{\text{tx}}}{T_{\text{rx}}} = \gamma(1-\beta) \approx 1-\beta \tag{3.59}$$

where $\beta = \dot{\rho}/c$, and $\gamma = 1/\sqrt{1-\beta^2} \approx 1$, since $\dot{\rho} \ll c$. The Doppler shift for a one-way link is the change in the signal frequency:

$$\Delta f = f_{\text{rx}} - f_{\text{tx}} = -\frac{\dot{\rho}}{c} f_{\text{tx}} \tag{3.60}$$

For an ideal two-way link, the transponder synchronizes the outgoing ("downlink") signal frequency with the incoming ("uplink") signal frequency ($f_{\text{rx,u}} = f_{\text{tx,d}}$), so the two-way Doppler shift is:

$$\begin{aligned}
\Delta f_{ud} &= f_{\text{rx,d}} - f_{\text{tx,u}} && \text{(3.61a)}\\
&= (f_{\text{rx,d}} - f_{\text{tx,d}}) + (f_{\text{rx,u}} - f_{\text{tx,u}}) - (f_{\text{rx,u}} - f_{\text{tx,d}}) && \text{(3.61b)}\\
&= \Delta f_d + \Delta f_u && \text{(3.61c)}\\
&= -\frac{\dot{\rho}}{c} f_{\text{tx,d}} - \frac{\dot{\rho}}{c} f_{\text{tx,u}} && \text{(3.61d)}\\
&= -\frac{\dot{\rho}}{c}(f_{\text{tx,u}} + \Delta f_u) - \frac{\dot{\rho}}{c} f_{\text{tx,u}} && \text{(3.61e)}\\
&= -\frac{\dot{\rho}}{c}\left(f_{\text{tx,u}} - \frac{\dot{\rho}}{c} f_{\text{tx,u}}\right) - \frac{\dot{\rho}}{c} f_{\text{tx,u}} && \text{(3.61f)}\\
&= \left(-\frac{2\dot{\rho}}{c} + \left(\frac{\dot{\rho}}{c}\right)^2\right) f_{\text{tx,u}} && \text{(3.61g)}\\
&\approx -\frac{2\dot{\rho}}{c} f_{\text{tx,u}} && \text{(3.61h)}
\end{aligned}$$

where in the last line, the quadratic term is dropped since $\dot{\rho} \ll c$. Hence, the ideal two-way Doppler shift is twice the one-way Doppler shift and is proportional to the range-rate.

In practice, what is measured is the integrated Doppler count ($N_d$) over the time

interval between receive times ($I = \{t_{R_1}, t_{R_2}\} = \{t - T_I, t\}$) [74, 87]:

$$N_d(t) \equiv -\int_{t-T_I}^{t} \Delta f_{ud}(t)dt = \int_{t-T_I}^{t} f_T(t) - f_R(t)dt \tag{3.62}$$

where $f_T = f_{tx,u}$, $f_R = f_{rx,d}$, $t_{R_1}$ and $t_{R_2}$ are signal receive times at the host terminal, and $T_I$ is the integration time. The signal frequency is the derivative of the phase ($f_T = \dot{\psi}_T$ and $f_R = \dot{\psi}_R$). Therefore,

$$\begin{aligned}
N_d &= \int_{t_{R_1}}^{t_{R_2}} \dot{\psi}_T(t) - \dot{\psi}_R(t)dt && \text{(3.63a)}\\
&= \int_{t_{R_1}}^{t_{R_2}} \dot{\psi}_T(t)dt - \int_{t_{R_1}}^{t_{R_2}} \dot{\psi}_R(t)dt && \text{(3.63b)}\\
&= (\psi_T(t_{R_2}) - \psi_T(t_{R_1})) - (\psi_R(t_{R_2}) - \psi_R(t_{R_1})) && \text{(3.63c)}\\
&= (\psi_T(t_{R_2}) - \psi_T(t_{R_1})) - (\psi_T(t_{T_2}) - \psi_T(t_{T_1})) && \text{(3.63d)}\\
&= (\psi_T(t_{R_2}) - \psi_T(t_{T_2})) - (\psi_T(t_{R_1}) - \psi_T(t_{T_1})) && \text{(3.63e)}\\
&= n_d + \Delta n_\beta + \Delta n_y && \text{(3.63f)}
\end{aligned}$$

where $n_d = f_{T,0}(\tau_2 - \tau_1)$ is the nominal, unbiased Doppler count, and $\Delta n_\beta$ and $\Delta n_y$ are biases due to frequency deviations from Doppler pre-compensation and transmitter reference frequency noise, respectively. Applying the two-way time of flight definitions:

$$n_d = f_{T,0}(\tau_{ud_2} + \tau_c - \tau_{ud_1} - \tau_c) = f_{T,0}(\tau_{ud_2} - \tau_{ud_1}) = \frac{2f_{T,0}}{c}(\rho_{a,ud_2} - \rho_{a,ud_1}) \tag{3.64}$$

Hence, the unbiased Doppler count is proportional to the change in the apparent range over the integration time interval, it is independent of the two-way ranging hardware delay $\tau_c$. Dividing by the integration time gives a measure of the average apparent range-rate:

$$\frac{n_d}{T_I} = \frac{2f_{T,0}}{c}\frac{\rho_{a,ud}(t_{R_2}) - \rho_{a,ud}(t_{R_1})}{t_{R_2} - t_{R_1}} = \frac{2f_{T,0}}{c}\frac{1}{T_I}\int_{t_{R_2}-T_I}^{t_{R_2}} \dot{\rho}_{a,ud}(t)dt = \frac{2f_{T,0}}{c}\bar{\dot{\rho}}_{a,ud}(t_{R_2}, T_I) \tag{3.65}$$

The Doppler observable is not the instantaneous geometric range-rate ($\dot{\rho}$); rather, it is the average apparent range-rate ($\bar{\dot{\rho}}_{a,ud}$):

$$\bar{\dot{\rho}}_{a,ud}(t, T_I) = \frac{c}{2f_{T,0}T_I} n_d(t) = \frac{1}{T_I}(\rho_{a,ud}(t) - \rho_{a,ud}(t - T_I)) \tag{3.66}$$

Moving forward, we assume that either the Doppler pre-compensation bias $\Delta n_\beta$ is known, or that there is no Doppler pre-compensation (as per CCSDS 141.10-O-1 laser communications standard [103]). The measurement model is then:

$$\hat{\bar{\dot{\rho}}}_{a,ud} = \frac{c}{2f_{T,0}T_I}(n_d + \delta n_d + \Delta n_y) \tag{3.67a}$$

$$= \bar{\dot{\rho}}_{a,ud} + \delta\bar{\dot{\rho}}_\psi + \delta\bar{\dot{\rho}}_y \tag{3.67b}$$

$$\delta\bar{\dot{\rho}}_\psi \equiv \frac{c}{2f_{T,0}T_I}\delta n_d \tag{3.67c}$$

$$\delta\bar{\dot{\rho}}_y \equiv \frac{c}{2f_{T,0}T_I}\Delta n_y \tag{3.67d}$$

The optical communications Doppler noise is composed of photodetection phase noise and oscillator frequency noise [100]. In Section 3.2.1, we turn to modeling these noise terms.

### 3.2.1 Modeling Optical Communications Doppler Noise

We model the addition of error in the measured Doppler count due to photodetection noise as:

$$\hat{N}_d = N_d + \delta n_d \tag{3.68a}$$

$$= \psi_T(t_{R_2} + \delta t_{R_2}) - (\psi_R(t_{R_2}) + \delta\psi_{R_2}) - (\psi_T(t_{R_1} + \delta t_{R_1}) - (\psi_R(t_{T_1}) + \delta\psi_{R_1})) \tag{3.68b}$$

$$\delta n_d = (\bar{f}(t_{R_2}, \delta t_{R_2})\delta t_{R_2} - \delta\psi_{R_2}) - (\bar{f}(t_{R_1}, \delta t_{R_1})\delta t_{R_1} - \delta\psi_{R_1}) \tag{3.68c}$$

$$\approx (f_{T,0}\delta t_{R_2} - \delta\psi_{R_2}) - (f_{T,0}\delta t_{R_1} - \delta\psi_{R_1}) \tag{3.68d}$$

$$\delta\bar{\dot{\rho}}_\psi = \frac{c}{2f_{T,0}T_I}\delta n_d \tag{3.68e}$$

$$\approx \frac{c}{2T_I}((\delta t_{R_2} - T_s\delta\psi_{R_2}) - (\delta t_{R_1} - T_s\delta\psi_{R_1})) \sim N(0, \sigma_{\dot{\rho},\psi}) \tag{3.68f}$$

$$(\delta t_R(t) - T_s\delta\psi(t)) \sim N(0, \sigma^2_{\rho,\psi}(t)) \rightarrow \sigma_{\dot{\rho},\psi} = \frac{1}{T_I}\sqrt{\sigma^2_{\rho,\psi}(t) + \sigma^2_{\rho,\psi}(t - T_I)} \tag{3.68g}$$

where the same approximations are made as in the ranging noise section. Also, as before, the apparent range phase noise is modeled a white Gaussian random process. The apparent range-rate phase noise from can be modeled using the apparent range phase noise, under ideal conditions. Alternative modeling approaches include using phase transfer functions for the closed-loop system, which can include contributions from thermal and quantum noise; however, we assume sufficient SNR such that these effects are negligible [100]. Next, we model the Doppler count bias due to frequency deviation noise as:

$$\Delta n_y = f_{T,0}\int_{t_{R_2}-T_I}^{t_{R_2}} y(t)dt = f_{T,0}T_I\bar{y}(t_{R_2}, T_I) \tag{3.69}$$

Integration over the count time interval filters out frequencies higher than $1/T_I$, and the transfer function $1/\epsilon = \tau_{ud}/T_I$ is applied to lower frequencies [123]. The integration time $T_I$ is on the order of $10^1$ to $10^2$ seconds [100, 123]. Typical oscillators exhibit rapidly decreasing Allan variance up to a sample time of about $10^0$ seconds for high performance crystal oscillators (OCXO) and up to $10^3$ seconds or more for

atomic clocks (e.g. cesium, rubidium) [102, 124]. For OCXOs, the Allan variance is stable for sample times from $10^0$ to $10^2$ seconds [102, 124]. Moving forward, we assume the use of an atomic clock, which has a white noise spectrum when sampled at the integration time [125]. The frequency deviation factor is therefore modeled as [123]:

$$\bar{y}(t_{R_2}, T_I) \sim N(0, \sigma_y^2(T_I)/\epsilon^2) \tag{3.70}$$

where $\sigma_y^2$ is the Allan deviation of the reference clock. The Doppler range-rate error due to frequency instability is then:

$$\delta\bar{\dot{\rho}}_y = \frac{c}{2}\bar{y}(t_{R_2}, T_I) \sim N(0, \sigma_{\dot{\rho},y}^2) \tag{3.71a}$$

$$\sigma_{\dot{\rho},y} = \frac{c\tau_{ud}}{2T_I}\sigma_y(T_I) \approx \frac{\rho}{T_I}\sigma_y(T_I) \approx \frac{\rho k_y}{T_I^{3/2}} \tag{3.71b}$$

In this context, the difference between the apparent range and the geometric range is negligible. Finally, the overall apparent range-rate error model is:

$$\delta\bar{\dot{\rho}} = \delta\bar{\dot{\rho}}_\psi + \delta\bar{\dot{\rho}}_y \sim N(0, \sigma_{\dot{\rho}}^2) \tag{3.72a}$$

$$\sigma_{\dot{\rho}}(t) = \sqrt{\sigma_{\dot{\rho},y}^2(t) + \sigma_{\dot{\rho},\psi}^2(t)} \tag{3.72b}$$

$$= \sqrt{\left(\frac{\rho(t)}{T_I}\right)^2 \sigma_y^2(T_I) + \frac{\sigma_{\rho,\psi}^2(t) + \sigma_{\rho,\psi}^2(t - T_I)}{T_I^2}} \tag{3.72c}$$

### 3.2.2 Doppler Measurement Noise Sensitivity to Systems Parameters

Values for the range-rate error (1-sigma) are computed while varying individual system parameters in Table 3.1. In Figure 3-7, the required data rate is varied from 10 Mbps to 1.244 Gbps. The phase detection error comes from the ranging synchronization and detector error, which both decrease with data rate (see Figure 3-4). The phase detection error dominates the range-rate error over all the data rates for the given integration time of 60 seconds. In Figure 3-8, the integration time ($T_I$) is varied from 1 to 1000 seconds. The error decreases with increasing integration time. It is

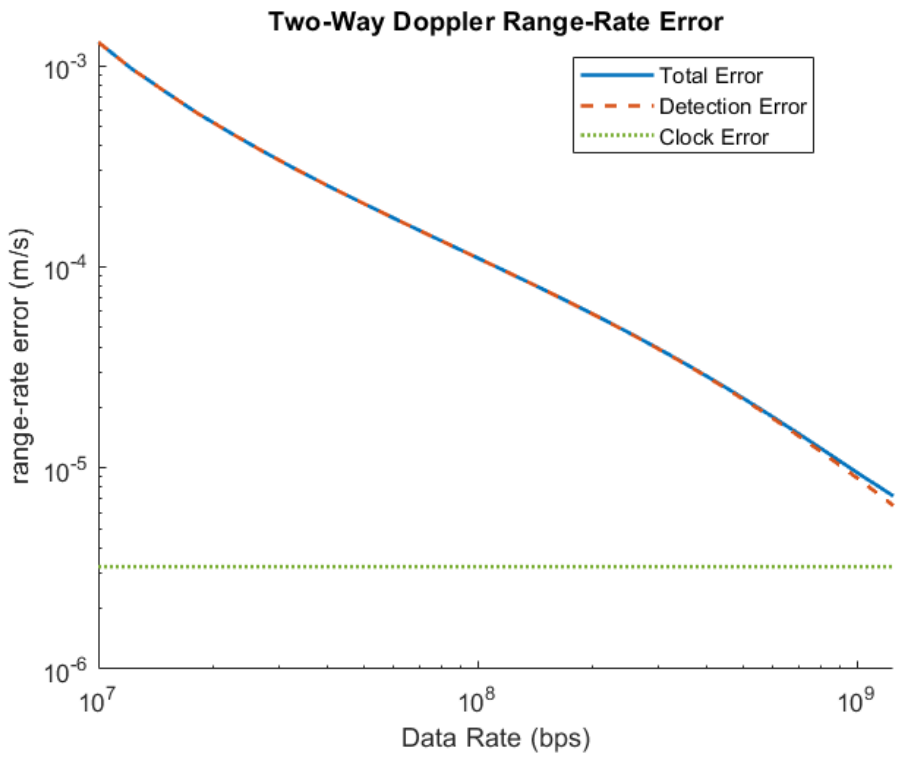


Figure 3-7: Sensitivity of range-rate error to data rate.

notable that for short integration times (∼1-3 seconds), the clock error dominates, whereas for longer integration times, the detection error dominates. Note that different clocks will have different Allan deviation profiles. In this case, the atomic clock is characterized by white noise and decreasing Allan deviation for sample times less than 1000 seconds. Also note that, in practice, the integration time is limited by the crosslink duration, which depends on the orbits of the two spacecraft. In some cases (e.g., a LEO-LEO flyby scenario), the link may only be a few minutes. In Figure 3-8, the normalized range (range divided by maximum design range) is varied. As was the case for range error, the range-rate error decreases with decreasing range. The clock error decreases because of the decreasing time of flight, and the detection error decreases because of the increasing received power. In Section 3.2.3, we turn to modeling the apparent range-rate.

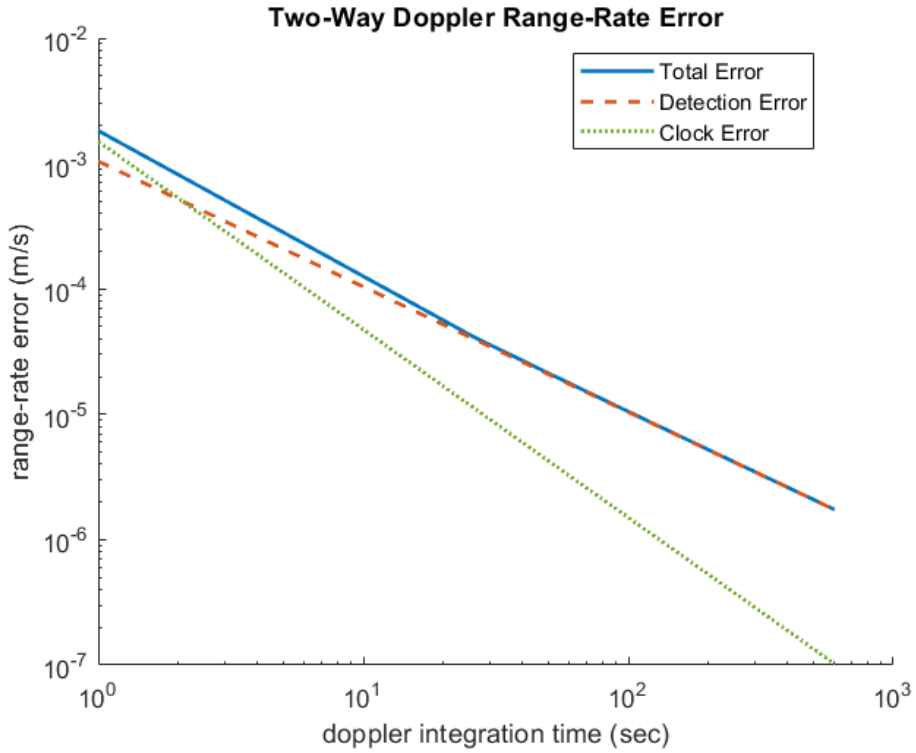


Figure 3-8: Sensitivity of range-rate error to Doppler integration time ($T_I$).

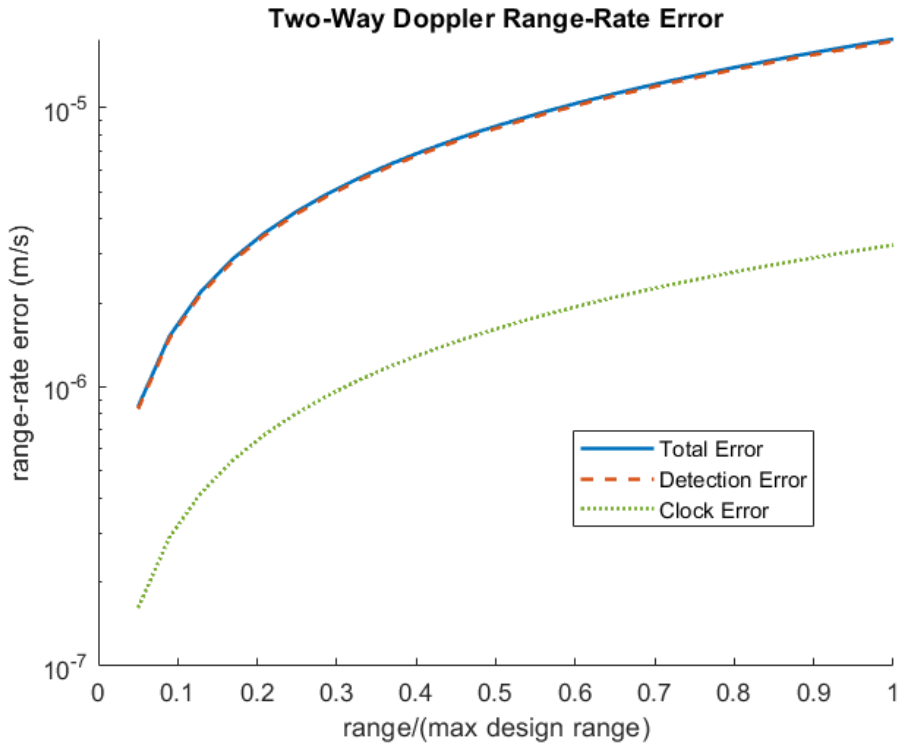


Figure 3-9: Sensitivity of range-rate error to range.

### 3.2.3 Modeling Average Apparent Range-Rate

The average apparent range-rate is based on the difference in the apparent range, which in turn is dependent on the differenced time of flight:

$$\bar{\dot{\rho}}_{a,ud}(t,T_I) = \frac{1}{T_I}(\rho_{a,ud}(t) - \rho_{a,ud}(t-T_I)) \tag{3.73a}$$

$$= \frac{c}{2T_I}(\tau_{ud}(t) - \tau_{ud}(t-T_I)) \tag{3.73b}$$

$$= \frac{c}{2T_I}\left((\tau_u(t) - \tau_u(t-T_I)) + (\tau_d(t) - \tau_d(t-T_I))\right) \tag{3.73c}$$

As before, the one-way time of flight is determined by an iterative method using approximations. The differenced one-way time of flight is:

$$\Delta\tau(t,T_I) = \tau(t) - \tau(t-T_I) \tag{3.74a}$$

$$= \Delta\tau_{\mathrm{GEO}}(t,T_I) + (\Delta\tau_{\mathrm{SR}}(t) - \Delta\tau_{\mathrm{SR}}(t-T_I)) + (\Delta\tau_{\mathrm{GR}}(t) - \Delta\tau_{\mathrm{GR}}(t-T_I)) \tag{3.74b}$$

The contributions of the differential TOF corrections are computed for three example cases in Table 3.5. The differential TOF corrections grow with the relative speed: the highest errors are for the $\sim$ 15 km/s LEO-LEO case, and the lowest errors are for the $\sim$ 1.6 km/s LLO-LNRHO case. As was the case for ranging, only the Shapiro correction from the GR terms is needed to achieve sub-picosecond level errors in general. It is possible entirely eliminate the GR correction term for sufficiently small relative velocity, as in in the LLO-LNRHO case. Table 3.6 shows how the number of TOF algorithm iterations is related to the two-way differential time of flight accuracy, using the same TOF approximation as for ranging (SR and PM corrections). As was the case for ranging, three iterations is sufficient for sub-picosecond level performance.

Table 3.5: Differenced Time of Flight Calculation Examples ($T_I = 60$ sec)

| | LEO-Tx to LEO-Rx | LEO-Tx to GEO-Rx | LLO-Tx to LNRHO-Rx |
|---|---|---|---|
| $\Delta\tau_{\text{GEO}}$ | $\sim 3.01$ ms | $\sim 1.46$ ms | $\sim 0.33$ ms |
| $\lvert\Delta\tau_{\text{SR},t} - \Delta\tau_{\text{SR},t-T_I}\rvert$ | $\sim 74.79$ ns | $\sim 22.35$ ns | $\sim 2.09$ ns |
| $\lvert\Delta\tau_{\text{PM},t} - \Delta\tau_{\text{PM},t-T_I}\rvert$ | $\sim 3.88$ ps | $\sim 2.40$ ps | $\sim 2.12 \times 10^{-2}$ ps |
| $\lvert\Delta\tau_{\text{HM},t} - \Delta\tau_{\text{HM},t-T_I}\rvert$ | $\sim 1.7 \times 10^{-3}$ ps | $\sim 2.3 \times 10^{-3}$ ps | $\sim 1 \times 10^{-6}$ ps |
| $\lvert\Delta\tau_{\text{SM},t} - \Delta\tau_{\text{SM},t-T_I}\rvert$ | $\sim 4 \times 10^{-7}$ ps | $\sim 3 \times 10^{-7}$ ps | $\sim 1 \times 10^{-14}$ ps |
| LEO-LEO Rx: $a = 6960.6$ km, $e = 0.0017$, $i = 98.08°$ $\Omega = 109.65°$, $\omega_p = 334.37°$, $M = 207.49°$ | | | |
| LEO-LEO Tx: $a = 6960.6$ km, $e = 0.0017$, $i = 81.92°$ $\Omega = 289.65°$, $\omega_p = 334.37°$, $M = 32.49°$ | | | |
| LEO-GEO Rx: $a = 42165.2$ km, $e = 0.0003$, $i = 11.7°$ $\Omega = 42.13°$, $\omega_p = 313.01°$, $M = 230.48°$ | | | |
| LEO-GEO Tx: $a = 6960.6$ km, $e = 0.0003$, $i = 101.7°$ $\Omega = 42.13°$, $\omega_p = 313.01°$, $M = 320.48°$ | | | |
| LLO-LNRHO Rx: $a = 37788$ km, $e = 0.898$, $i = 90°$ $\Omega = 0°$, $\omega_p = 90°$, $M = 180°$ | | | |
| LLO-LNRHO Tx: $a = 1788$ km, $e = 0$, $i = 89.8°$ $\Omega = 0°$, $\omega_p = 270°$, $M = 90°$ | | | |

Table 3.6: Two-Way Differential Time of Flight Calculation Convergence ($T_I = 60$ sec)

| Iterations | $\Delta\tau_{ud}$ Error: LEO-LEO | $\Delta\tau_{ud}$ Error: LEO-GEO |
|---|---|---|
| 1 | $\sim 149.14$ ns | $\sim 23.42$ ns |
| 2 | $\sim 3.69$ ps | $\sim 1.77$ ps |
| 3 | $\sim 5.7 \times 10^{-3}$ ps | $\sim 0.19$ ps |

## 3.3 Comparison to Radio ISL Measurements

At a high level, inter-satellite links using radio communications can measure the same observables: range, range-rate, and bearings as optical inter-satellite links. The benefit of OISLs is that for a given set of SWaP constraints, optical can achieve a higher data rate and more accurate measurements. Unlike lasercom, where angle measurements are essential to the functioning of the communications system, angle measurements for radio communications are optional and require additional hardware [38]. As in the optical case, radio range measurements are also based on the measurement of the time-of-flight induced phase shift of the modulated signal, and

range-rate measurements are also based on the integrated Doppler count [38]. These can be non-coherent or coherent, where again coherent systems are more complex. Following Moision et al. [109], we model the RF ranging estimates as being derived from the demodulated ranging clock of a residual carrier signal:

$$y(t) = A\cos(2\pi f_r t - \phi) + n(t) \tag{3.75}$$

where $A = \sqrt{2P_{\text{rx}}}$ is the received signal amplitude, $f_r$ is the ranging clock frequency, $\phi$ is the phase, and $n(t)$ is additive white Gaussian noise with power spectral density $S_n(f) = N_0/2$ over $f \in [-B, B]$ and zero elsewhere ($N_0$ is the noise spectral density (W/Hz), and $B$ is the signal bandwidth). For two-way, telemetry-based radio ranging, the same high-level model as OISLs applies [111]:

$$\delta\rho_n = \frac{c}{2}(\Delta x + \delta t_R - T_r\delta\psi) \sim N(0, \sigma_\rho^2) \tag{3.76a}$$

$$\sigma_\rho^2 = \mathbb{E}[\delta\rho_n^2] = \left(\frac{c}{2}\right)^2 (\sigma_{\Delta x}^2 + \sigma_R^2 + T_r^2\sigma_\psi^2) \tag{3.76b}$$

$$\sigma_\rho = \sqrt{\sigma_{\rho,x}^2 + \sigma_{\rho,\psi}^2} \tag{3.76c}$$

$$\sigma_{\rho,\psi} \equiv \frac{c}{2}\sqrt{\sigma_R^2 + T_r^2\sigma_\psi^2} \tag{3.76d}$$

$$\sigma_{\rho,x} \equiv \frac{c}{2}\sigma_{\Delta x}(\tau) = \frac{c}{\sqrt{2}}\tau\sigma_y(\tau) \approx k_y\sqrt{c\rho} \tag{3.76e}$$

$$\delta\bar{\dot{\rho}} = \delta\bar{\dot{\rho}}_\psi + \delta\bar{\dot{\rho}}_y \sim N(0, \sigma_{\dot{\rho}}^2) \tag{3.76f}$$

$$\sigma_{\dot{\rho}}(t) = \sqrt{\sigma_{\dot{\rho},y}^2(t) + \sigma_{\dot{\rho},\psi}^2(t)} \tag{3.76g}$$

$$= \sqrt{\left(\frac{\rho(t)}{T_I}\right)^2 \sigma_y^2(T_I) + \frac{\sigma_{\rho,\psi}^2(t) + \sigma_{\rho,\psi}^2(t - T_I)}{T_I^2}} \tag{3.76h}$$

where $T_r = 1/f_r$ is the the ranging clock period. For simplicity, we ignore Doppler (pre-compensation) effects on the ranging clock frequency, since they do not appreciably impact performance [111]. The noise due to synchronization $\sigma_R$ and due to phase measurements $\sigma_\psi$ take a different form since the signal modulation format is

different. The CRLB for the generalized phase measurement noise variance is [109]:

$$\sigma_\psi^2 = \frac{\sigma_\phi^2}{(2\pi)^2} = \frac{1}{4\pi^2}\left(\frac{2}{(P_{\rm rx}/N_0)T_i}\right) \tag{3.77}$$

where $S = P_{\rm rx}/(BN_0)$ is the signal-to-noise ratio, and $T_i$ is the phase measurement integration time. The symbol tracking timing noise standard deviation for simple BPSK and QPSK integrate and dump receivers is [111]:

$$\sigma_R^2 = \frac{2wB_{\rm sym}T_r^3}{\eta_{\rm sym}(E_s/N_0)} = \frac{4wB_{\rm sym}T_r^2}{\eta_{\rm sym}(P_{\rm rx}/N_0)} \tag{3.78}$$

where $E_s/N_0 = (P_{\rm rx}/2)/(f_r N_0) = SB/(2f_r)$ is the code symbol-to-noise ratio, $B_{\rm sym}$ is the symbol loop bandwidth, $w$ is the loop window fraction, and $\eta_{\rm sym}$ is the loop squaring loss [111]:

$$\eta_{\rm sym} = \frac{\left[\text{erf}(\sqrt{E_s/N_0}) - \frac{w}{2}\sqrt{\frac{E_s/N_0}{\pi}}\exp(-E_s/N_0)\right]^2}{1 + \frac{wE_s/N_0}{2} - \frac{w}{2}\left[\frac{\exp(-E_s/N_0)}{\sqrt{\pi}} + \sqrt{E_s/N_0}\,\text{erf}(\sqrt{E_s/N_0})\right]^2} \tag{3.79}$$

For high SNR ($E_s/N_0 \gg 1$), $\eta_{\rm sym} \approx 1$. The combined noise error standard deviation is therefore:

$$\sigma_{\rho,\psi} = \frac{c}{2}\sqrt{\frac{4wB_{\rm sym}T_r^2}{\eta_{\rm sym}(P_{\rm rx}/N_0)} + \frac{T_r^2}{4\pi^2}\left(\frac{2}{(P_{\rm rx}/N_0)T_i}\right)} = \frac{cT_r}{2}\sqrt{\frac{1}{(P_{\rm rx}/N_0)}\left(\frac{4wB_{\rm sym}}{\eta_{\rm sym}} + \frac{1}{2\pi^2 T_i}\right)} \tag{3.80}$$

A comparison of ranging noise for typical parameter values is shown in Figure 3-10. The RF ranging noise is limited by phase detection errors up to an integration time of about 10 msec, at which point the sychronization error dominates. The atomic clock error is negligible for the RF system, whereas it dominates our reference 622 Mbps lasercom system over all ranging integration times.

One approach to measuring bearings angles requires three receiving antennas separated by a baseline distance ($b$). The relative time-of-flight between the antennas

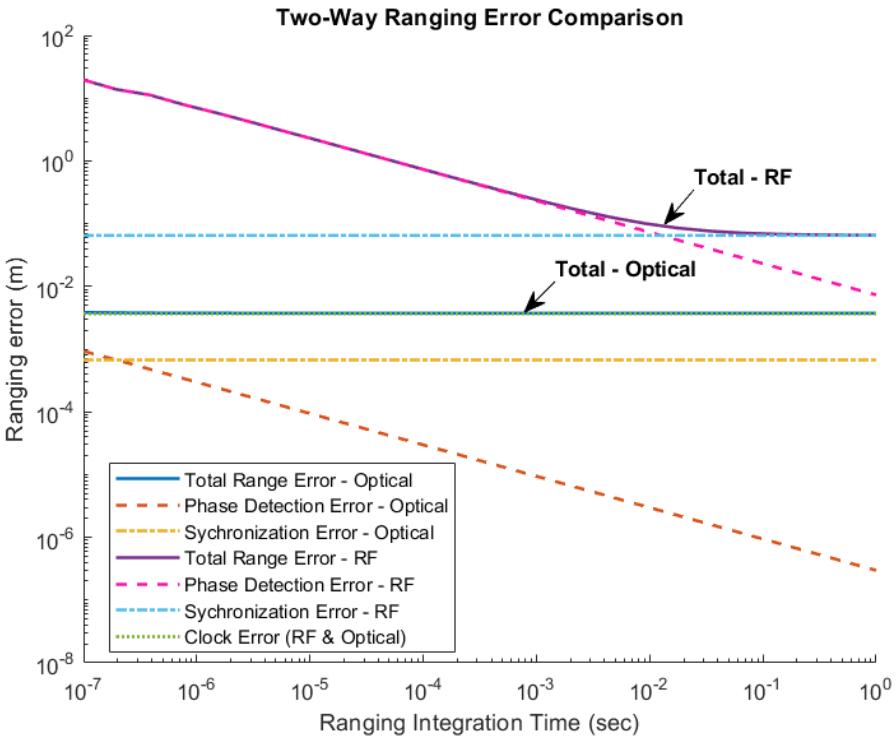


Figure 3-10: Comparison of Optical to RF Ranging over ranging integration times.

($\Delta\tau$) can be used to calculate the angle of incidence ($\theta$) [38]:

$$\Delta\tau = \tau_2 - \tau_1 = \frac{b}{c}\cos(\theta) \tag{3.81}$$

The variance in this measurement is directly related to the variance in the phase measurement [38]:

$$\sigma_\theta^2 = -\frac{1}{2}\ln\left(1 - 2\left(\frac{\sigma_\rho}{b}\right)^2\right) \tag{3.82}$$

In order for this approach to work, the baseline must be larger than the ranging error: $b > \sqrt{2}\sigma_\rho$. For a typical RF ranging error of 1 m, this requires a baseline of 1.4 m, which is only possible for very large spacecraft or spacecraft with deployables. Therefore, we do not consider radio angles measurements further. Some system architectures may use a combination of optical and radio measurements (i.e. optical angles and RF range and/or Doppler). It should be noted that at the long ranges of interest in this work (i.e. $10^3$ to $10^5$ km), an intersatellite optical sensing system

with a reasonable aperture size would need to utilize laser beacons, so the analysis in the next section on angles measurements would apply. In Section 3.4, we consider systems analysis for bearings measurements.

## 3.4 Systems Analysis for Bearings Measurements

The sensor that provides bearings measurements is part of the Pointing, Acquisition, and Tracking (PAT) subsystem of the lasercom payload. The PAT system can use cameras and/or quadrant photodiode devices like QPINs or QAPDs (quadcells). Both cameras and quadcells centroid an optical signal that is focused on their sensor area. The centroid noise is a combination of intrinsic electronics noise (e.g. dark current, pre-amp, readout, fixed pattern), any signal from background stray light, and jitter from mechanical vibrations.

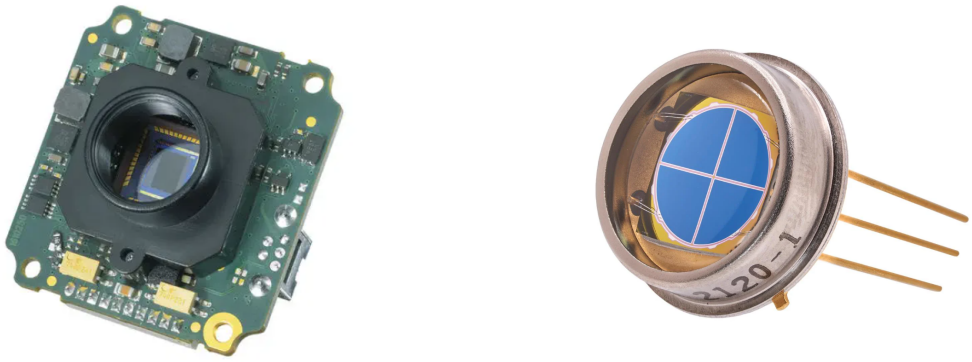

Figure 3-11: Example camera [126] and quadcell [127] sensors.

A sensor pixel/quadrant signal value is modeled with additive noise [43]:

$$A[i,j] = a[i,j] + n[i,j] \tag{3.83}$$

The centroid of an array of sensor signal values is as follows:

$$x_c = \frac{\sum_i \left( i \sum_j A[i,j] \right)}{\sum_i \sum_j A[i,j]} \tag{3.84a}$$

$$y_c = \frac{\sum_i \left( j \sum_j A[i,j] \right)}{\sum_i \sum_j A[i,j]} \tag{3.84b}$$

For sufficient SNR values (e.g. SNR $> 10$):

$$\sum_i \sum_j A[i,j] \approx \sum_i \sum_j a[i,j] \equiv \Sigma_a \tag{3.85}$$

The centroid equations then can be simplified into additive noise models:

$$x_c = \bar{x}_c + n_{x,c} \tag{3.86a}$$

$$y_c = \bar{y}_c + n_{y,c} \tag{3.86b}$$

$$\bar{x}_c = \frac{\sum_i \left( i \sum_j a[i,j] \right)}{\Sigma_a},\ n_{x,c} = \frac{\sum_i \left( i \sum_j n[i,j] \right)}{\Sigma_a} \tag{3.86c}$$

$$\bar{y}_c = \frac{\sum_i \left( j \sum_j a[i,j] \right)}{\Sigma_a},\ n_{y,c} = \frac{\sum_i \left( j \sum_j n[i,j] \right)}{\Sigma_a} \tag{3.86d}$$

In PAT systems analysis, the pixel/quadrant noise values are assumed zero-mean, independent, and identically distributed.

$$\mathbb{E}[n[i,j]] = 0 \tag{3.87a}$$

$$\mathrm{Var}[n[i,j]] = \sigma_n^2 \tag{3.87b}$$

The resulting mean and variance values for the centroid noise model are [43]:

$$\mathbb{E}[n_{x,c}] = \mathbb{E}[n_{y,c}] = 0 \tag{3.88a}$$

$$\sigma_{c,n}^2 = \mathrm{Var}[n_{x,c}] = \mathrm{Var}[n_{y,c}] = \frac{2N\sigma_n^2}{\Sigma_a^2} = \frac{1}{\mathrm{SNR}_e} \text{ (N x N centroid)} \tag{3.88b}$$

where $\mathrm{SNR}_e$ is the electrical signal-to-noise ratio. The noise equivalent angle (NEA)

is defined as [43]:

$$\sigma_{A,n} = \frac{\sigma_{c,n}}{\mathrm{SF}} = \frac{1}{\mathrm{SF}\sqrt{\mathrm{SNR}_e}} \tag{3.89}$$

where SF is the slope factor, which converts the centroid units into an angle.

$$\mathrm{SF} = \begin{cases} 1/(\mathrm{IFOV}) = f/w \text{ (Camera)} \\ k_s/\theta_s = k_s f/D_s \text{ (Quadcell, on-axis)} \end{cases} \tag{3.90}$$

where for the camera, the IFOV is the pixel FOV, and $w$ is the pixel pitch. For the quadcell, $k_s$ is the spot shape factor, $\theta_s$ is the spot angular diameter, $f$ is the effective focal length of the focusing optics, and $D_s$ is the spot diameter. Note that in general, the slope factor of a quadcell is a function of the spot shape, position, and the gap between the quadrants. Some shape factors are: Airy Diffraction Limited $k_s = 4.14$; Gaussian $k_s = 1.56$; Uniform $k_s = 1.27$ [43]. For best performance, the spot size should be on the order of the quadrant gap $g$. This is typically optimized to minimize power lost in the gap while also minimizing the spot size. There may be additional jitter noise ($\sigma_{c,j} = \sigma_{A,j}/\mathrm{SF}$) that is induced by structural vibrations from the terminal aperture pointing system (gimbal and/or reaction wheels). For PAT systems analysis, these noise terms are modeled as Gaussian distributed, so the total angular noise is:

$$\sigma_A = \sqrt{\sigma_{A,n}^2 + \sigma_{A,j}^2} \tag{3.91}$$

Given an optical transfer function, the centroid coordinates can be related to the intersatellite relative position vector in the sensor frame. Note that the optical transfer function may be sensitive to large temperature variations. The optical transfer

function is formulated in homogeneous coordinates $(x', y')$:

$$x' \equiv \frac{\boldsymbol{\rho}_{a,d}^S \cdot \mathbf{e}_x^S}{\boldsymbol{\rho}_{a,d}^S \cdot \mathbf{e}_z^S} = \frac{\hat{\boldsymbol{\rho}}_{a,d}^S \cdot \mathbf{e}_x^S}{\hat{\boldsymbol{\rho}}_{a,d}^S \cdot \mathbf{e}_z^S} \tag{3.92a}$$

$$y' \equiv \frac{\boldsymbol{\rho}_{a,d}^S \cdot \mathbf{e}_y^S}{\boldsymbol{\rho}_{a,d}^S \cdot \mathbf{e}_z^S} = \frac{\hat{\boldsymbol{\rho}}_{a,d}^S \cdot \mathbf{e}_y^S}{\hat{\boldsymbol{\rho}}_{a,d}^S \cdot \mathbf{e}_z^S} \tag{3.92b}$$

$$\mathbf{u}' \equiv \begin{bmatrix} x' \\ y' \\ 1 \end{bmatrix} = \frac{1}{\boldsymbol{\rho}_{a,d}^S \cdot \mathbf{e}_z^S} \boldsymbol{\rho}_{a,d}^S = \frac{1}{\hat{\boldsymbol{\rho}}_{a,d}^S \cdot \mathbf{e}_z^S} \hat{\boldsymbol{\rho}}_{a,d}^S \tag{3.92c}$$

Note the following useful equation follows from Eq. 3.92c:

$$\hat{\boldsymbol{\rho}}_{a,d}^S = \frac{\boldsymbol{\rho}_{a,d}^S}{\left\|\boldsymbol{\rho}_{a,d}^S\right\|} = \frac{\mathbf{u}'}{\|\mathbf{u}'\|} \tag{3.93}$$

where $\boldsymbol{\rho}_{a,d}^S$ is the apparent relative position of the beaconing/transmitting partner satellite with respect to the receiving host satellite in the sensor frame (S), which has the orthonormal basis $\{\mathbf{e}_x^S, \mathbf{e}_y^S, \mathbf{e}_z^S\}$ where the z-axis is the optical axis. For lasercom systems, the bearing angles measurement is accurate enough ($\sim 10^1 \mu$rad) that the time of flight needs to be taken into account. This effect is also important for laser pointing: the laser is pointed slightly ahead of the current target position to help minimize pointing losses. This time of flight pre-compensation bias is called the point-ahead angle. Typically, a dedicated fine steering mirror called a point ahead mirror (PAM) is implemented in the optical design to achieve this.

The optical transfer function is the following [128, 129]:

$$\begin{bmatrix} \bar{x}_c \\ \bar{y}_c \\ 1 \end{bmatrix} = K \begin{bmatrix} g_x(x') \\ g_y(y') \\ 1 \end{bmatrix} = K\mathbf{g}(\mathbf{u}') \tag{3.94}$$

where $K$ is the camera intrinsic matrix, which depends on the optical system model.

The simplest optical transfer function is the ideal pinhole camera model [129]:

$$K = \begin{bmatrix} -f/w & 0 & c_x \\ 0 & -f/w & c_y \\ 0 & 0 & 0 \end{bmatrix} \tag{3.95a}$$

$$g_x(x') = x' \tag{3.95b}$$

$$g_y(y') = y' \tag{3.95c}$$

where $(c_x, c_y)$ are the pixel coordinates of the image plane principal point (the center of the frame). Here we assume a camera model, but the slope factor could be replaced with a quadcell model. A model with additional parameters to account for optical distortions and sensor nonuniformities is [129]:

$$K = \begin{bmatrix} -f/w_x & s & c_x \\ 0 & -f/w_y & c_y \\ 0 & 0 & 0 \end{bmatrix} \tag{3.96a}$$

$$g_x(x') = f(r)x' + 2p_1x'y' + p_2(r^2 + 2x'^2) \tag{3.96b}$$

$$g_y(y') = f(r)y' + 2p_2x'y' + p_1(r^2 + 2y'^2) \tag{3.96c}$$

$$f(r) = \frac{1 + k_1r^2 + k_2r^4 + k_3r^6}{1 + k_4r^2 + k_5r^4 + k_6r^6},\ r = \sqrt{x'^2 + y'^2} \tag{3.96d}$$

where $s$ is the pixel skew, $w_x$ and $w_y$ are the pixel pitches in the x- and y-axes of the lens, $(k_1, k_2, k_3, k_4, k_5, k_6)$ are the radial distortion coefficients, and $(p_1, p_2)$ are the tangential distortion coefficients. These parameters are typically estimated via a calibration process. Note that we assume that the apparent direction vector in the sensor frame ($\boldsymbol{\rho}^S_{a,d}$) is fixed during the sensor sample time for each measurement. This means that the true centroid $(\bar{x}_c, \bar{y}_c)$ is static during the sample time, and any centroid motion is purely due to random jitter. In this work, we do not assume any measurements are available when the ranging/communications link is not closed. We also assume standard PAT system operations such that when the ranging/communications link is closed, the bearings sensor is actively stabilized with respect to the apparent signal

direction. This is accomplished via closed-loop tracking using the centroid measurements. The assumption that any centroid motion during the sample time is purely due to random jitter is valid if the centroid measurement frequency is significantly higher than the closed-loop tracking bandwidth ($\sim 10^0$ to $10^1$ Hz for typical gimbal or body pointing). Hence, there is negligible streaking/smearing of the detected optical signal during the sample time. This is true for the high SNR regime that we assume the system is operating in, where the centroid measurement frequency is high ($\sim 10^3$ to $10^6$ Hz).

The rotation relating the sensor frame (S) to the terminal body frame (B) comes from the mechanical design of the system. It can be measured on the ground ($\hat{R}_B^S$); however, there will be some uncertainty in the alignment due to temperature fluctuations in the space environment and potential shifts incurred during launch due to shock and vibration.

$$\hat{\boldsymbol{\rho}}_{a,d}^S = R_B^S \hat{\boldsymbol{\rho}}_{a,d}^B = R(\delta \mathbf{q}_B^S) \hat{R}_B^S \hat{\boldsymbol{\rho}}_{a,d}^B \tag{3.97}$$

where $\delta \mathbf{q}_B^S$ is the vector part of the error quaternion. The impact of temperature variation, shock, and vibration is dependent on the materials used and how the sensor is mounted relative to the star tracker. The expected variation in alignment can be estimated via analysis or ground environmental testing. If it is significant, the alignment variation can be estimated in space by including it as additional parameters in the state. A calibration using stars may also be possible depending on the optical design; typically narrow band filters are used to block background sources of light like stars.

The rotation relating the terminal body frame (B) to the inertial frame (I) is the terminal body attitude, which is generated by an attitude determination and control system (ADCS). If the terminal is gimballed, the ADCS is part of the gimbal control system (not the spacecraft's ADCS), and the "terminal body" is the optical head. An example of a gimballed terminal is MAScOT, which was developed for LCRD [58]. If the terminal is hard mounted to the spacecraft body, then terminal body frame is the spacecraft body frame, so the spacecraft's ADCS is used. An example of a hard

mounted terminal is the CLICK terminal [60]. A typical ADCS that is suitable for lasercom would include a star tracker for fine attitude measurements, with a precision gyroscope for attitude dynamic model replacement. A Multiplicative EKF (MEKF) would use these measurements to provide realtime terminal body attitude estimates ($\hat{R}_I^B$). The attitude estimation error ($\delta\mathbf{q}_I^B$) is another source of noise for bearing measurements.

$$\hat{\boldsymbol{\rho}}_{a,d}^B = R_I^B \hat{\boldsymbol{\rho}}_{a,d} = R(\delta\mathbf{q}_I^B)\hat{R}_I^B \hat{\boldsymbol{\rho}}_{a,d} \tag{3.98}$$

The combined rotation relating the sensor frame to the inertial frame is therefore:

$$\hat{\boldsymbol{\rho}}_{a,d}^S = R_I^S \hat{\boldsymbol{\rho}}_{a,d} = R_B^S R_I^B \hat{\boldsymbol{\rho}}_{a,d} = R(\delta\mathbf{q}_B^S)\hat{R}_B^S R(\delta\mathbf{q}_I^B)\hat{R}_I^B \hat{\boldsymbol{\rho}}_{a,d} \tag{3.99}$$

The apparent bearings are computed online ($\theta_C, \phi_C$) from the centroid measurement ($x_c, y_c$) and the estimated sensor attitude ($\hat{R}_I^S$). The Kalman Filter measurement model (i.e. $\mathbf{y} = \mathbf{h}(\mathbf{x})$) for the computed apparent bearings angles is:

$$\begin{bmatrix}\theta_C \\ \phi_C\end{bmatrix} = \mathbf{y}_{\theta_C,\phi_C}(x_c, y_c, \hat{R}_B^S, \hat{R}_I^B) = \mathbf{h}_{\theta_C,\phi_C}(\mathbf{x}_0, \mathbf{x}_i, \mathbf{n}_c, \delta\mathbf{q}_I^B; \delta\mathbf{q}_B^S) \tag{3.100a}$$

$$\theta_C = \tan^{-1}\left(\frac{\hat{\boldsymbol{\rho}}_C \cdot \mathbf{E}_y}{\hat{\boldsymbol{\rho}}_C \cdot \mathbf{E}_x}\right) \in [0, 2\pi) \tag{3.100b}$$

$$\phi_C = \sin^{-1}(\hat{\boldsymbol{\rho}}_C \cdot \mathbf{E}_z) \in [-\pi/2, \pi/2] \tag{3.100c}$$

$$\hat{\boldsymbol{\rho}}_C = (\hat{R}_I^S)^T \frac{\mathbf{u}'_C}{\|\mathbf{u}'_C\|} \tag{3.100d}$$

$$\hat{R}_I^S = \hat{R}_B^S \hat{R}_I^B = R^T(\delta\mathbf{q}_B^S) R_B^S R^T(\delta\mathbf{q}_I^B) R_I^B \tag{3.100e}$$

$$K\mathbf{g}(\mathbf{u}'_C) = \begin{bmatrix}x_c \\ y_c \\ 1\end{bmatrix} = K\mathbf{g}\left(\frac{1}{(R_I^S \hat{\boldsymbol{\rho}}_{a,d}(\mathbf{x}_0, \mathbf{x}_i)) \cdot \mathbf{e}_z^S} R_I^S \hat{\boldsymbol{\rho}}_{a,d}(\mathbf{x}_0, \mathbf{x}_i)\right) + \begin{bmatrix}\mathbf{n}_c \\ 0\end{bmatrix} \tag{3.100f}$$

where $\mathbf{n}_c^T = [n_{x,c}, n_{y,c}]$. Note that $\mathbf{h}_{\theta_C,\phi_C}$ is a non-additive, nonlinear function of the noise terms ($\mathbf{n}_c, \delta\mathbf{q}_I^B$). In practice, the sensor orientation bias $\delta\mathbf{q}_B^S$ is due to residuals from a calibration process. In practice, these residuals may be significant enough that they must be estimated or considered by the filter. For simplicity, we assume

the calibration process is sufficiently accurate that the bias is negligible relative to the noise, and we model $R(\delta\mathbf{q}_B^S) = I$. Estimating significant biases is relegated to future work. Also note that for a general optical transfer function, $\mathbf{u}'_C$ is calculated implicitly from $(x_c, y_c)$.

### 3.4.1 The Ideal Pinhole Camera Bearings Model

The idealized pinhole camera optical transfer function enables $(x'_C, y'_C)$ to be calculated explicitly from $(x_c, y_c)$.

$$\begin{bmatrix} x'_C \\ y'_C \end{bmatrix} = -\frac{1}{f/w}\left(\begin{bmatrix} x_c \\ y_c \end{bmatrix} - \mathbf{c}\right) \tag{3.101a}$$

$$= -\frac{1}{f/w}\left(\begin{bmatrix} \bar{x}_c \\ \bar{y}_c \end{bmatrix} + \mathbf{n}_c - \mathbf{c}\right) \tag{3.101b}$$

$$= -\frac{1}{f/w}\left(\left(-(f/w)\begin{bmatrix} x' \\ y' \end{bmatrix} + \mathbf{c}\right) + \mathbf{n}_c - \mathbf{c}\right) \tag{3.101c}$$

$$= \begin{bmatrix} x' \\ y' \end{bmatrix} - \frac{1}{f/w}\mathbf{n}_c \tag{3.101d}$$

$$= \begin{bmatrix} x' \\ y' \end{bmatrix} - \mathbf{n}_A \tag{3.101e}$$

where $\mathbf{n}_A = [n_{A,x}, n_{A,y}]$ are the equivalent angular noise values in each axis (both distributed as $N(0, \sigma_A^2)$). For the idealized pinhole camera, the calculated homogeneous coordinates have a linear additive noise model. They can be expressed in terms of the apparent relative position and the sensor attitude as:

$$\mathbf{u}'_C = \begin{bmatrix} (w/f)(c_x - x_c) \\ (w/f)(c_y - y_c) \\ 1 \end{bmatrix} = \frac{1}{(R_I^S \hat{\boldsymbol{\rho}}_{a,d}) \cdot \mathbf{e}_z^S} R_I^S \hat{\boldsymbol{\rho}}_{a,d} - \begin{bmatrix} \mathbf{n}_A \\ 0 \end{bmatrix} \tag{3.102}$$

The calculated bearings angles still have non-additive noise, so the noise covariance used in the CRLB and the EKF algorithms is computed via a linear approximation (for simplicity, we set the bias to zero).

$$\mathbf{h}_{\theta_C,\phi_C}(\mathbf{x}, \mathbf{n}_A, \delta\mathbf{q}_I^B) \approx \mathbf{h}_{\theta_C,\phi_C}(\mathbf{x}, \mathbf{n}_A = \mathbf{0}, \delta\mathbf{q}_I^B = \mathbf{0}) + G_C(\mathbf{x})\boldsymbol{\eta}_C \tag{3.103a}$$

$$G_C = \frac{\partial(\theta_C, \phi_C)}{\partial(\mathbf{n}_A, \delta\mathbf{q}_I^B)}(\mathbf{n}_A = \mathbf{0}, \delta\mathbf{q}_I^B = \mathbf{0}) \tag{3.103b}$$

$$\boldsymbol{\eta}_C = \begin{bmatrix} \mathbf{n}_A \\ \delta\mathbf{q}_I^B \end{bmatrix} \sim N(\mathbf{0}, R_C) \tag{3.103c}$$

$$G_C\boldsymbol{\eta}_C \sim N(\mathbf{0}, G_C R_C G_C^T) \tag{3.103d}$$

Note that the noise Jacobian $G_C$ is a function of the state. The noise Jacobian is:

$$\frac{\partial(\theta_C, \phi_C)}{\partial(\mathbf{n}_A, \delta\mathbf{q}_I^B)} = \begin{bmatrix} \frac{\partial\theta_C}{\partial\hat{\boldsymbol{\rho}}_C}\frac{\partial\hat{\boldsymbol{\rho}}_C}{\partial\mathbf{n}_A} & \frac{\partial\theta_C}{\partial\hat{\boldsymbol{\rho}}_C}\frac{\partial\hat{\boldsymbol{\rho}}_C}{\partial\delta\mathbf{q}_I^B} \\ \frac{\partial\phi_C}{\partial\hat{\boldsymbol{\rho}}_C}\frac{\partial\hat{\boldsymbol{\rho}}_C}{\partial\mathbf{n}_A} & \frac{\partial\phi_C}{\partial\hat{\boldsymbol{\rho}}_C}\frac{\partial\hat{\boldsymbol{\rho}}_C}{\partial\delta\mathbf{q}_I^B} \end{bmatrix} \tag{3.104a}$$

$$\frac{\partial\theta_C}{\partial\hat{\boldsymbol{\rho}}_C}(\mathbf{n}_A = \mathbf{0}, \delta\mathbf{q}_I^B = \mathbf{0}) = \frac{\hat{\rho}_{a,d}^x\mathbf{E}_y^T - \hat{\rho}_{a,d}^y\mathbf{E}_x^T}{(\hat{\rho}_{a,d}^x)^2 + (\hat{\rho}_{a,d}^y)^2} \tag{3.104b}$$

$$\frac{\partial\phi_C}{\partial\hat{\boldsymbol{\rho}}_C}(\mathbf{n}_A = \mathbf{0}, \delta\mathbf{q}_I^B = \mathbf{0}) = \frac{\mathbf{E}_z^T}{\sqrt{1 - (\hat{\rho}_{a,d}^z)^2}} \tag{3.104c}$$

$$\frac{\partial\hat{\boldsymbol{\rho}}_C}{\partial\mathbf{n}_A}(\mathbf{n}_A = \mathbf{0}, \delta\mathbf{q}_I^B = \mathbf{0}) = -((R_I^S\hat{\boldsymbol{\rho}}_{a,d}) \cdot \mathbf{e}_z^S)(I - \hat{\boldsymbol{\rho}}_{a,d}\hat{\boldsymbol{\rho}}_{a,d}^T)(R_I^S)^T \begin{bmatrix} I_{2\times2} \\ \mathbf{0}_{1\times2} \end{bmatrix} \tag{3.104d}$$

$$\frac{\partial\hat{\boldsymbol{\rho}}_C}{\partial\delta\mathbf{q}_I^B}(\mathbf{n}_A = \mathbf{0}, \delta\mathbf{q}_I^B = \mathbf{0}) = 2(R_I^B)^T(R_I^B\hat{\boldsymbol{\rho}}_{a,d})^\times \tag{3.104e}$$

$$\hat{\boldsymbol{\rho}}_C(\mathbf{n}_A = \mathbf{0}, \delta\mathbf{q}_I^B = \mathbf{0}) = \hat{\boldsymbol{\rho}}_{a,d} = [\hat{\rho}_{a,d}^x, \hat{\rho}_{a,d}^y, \hat{\rho}_{a,d}^z]^T \tag{3.104f}$$

### 3.4.2 Noise Equivalent Angular Error for Laser Tracking

The choice of tracking sensor depends on the pointing, acquisition, and tracking (PAT) system design. In general, the PAT system design will be multi-staged, where initial pointing uses a wide divergence beacon laser, and initial acquisition uses a wide FOV detector. These stages continue until the pointing accuracy is sufficient for the communications laser divergence and communications receiver FOV. The sensor used

for navigation measurements may in principle be any of the acquisition sensors used in the PAT stages, or a combination thereof. The acquisition sensors are preferred, since they measure the incoming signal without any interruption by steering mirrors, which would introduce additional uncertainty in the measurement. In general, if measurements from multiple acquisition sensors were available, they could be each used by the filtering algorithm, weighted by their respective uncertainties. For simplicity, we assume that the navigation algorithm only uses one of these sensors. We assume that it is an wide field of view, acquisition quadcell (QPIN) detector [130]. The main benefit of a quadcell detector over a camera is that it has higher bandwidth, so the beacon laser can be modulated in order to better isolate the received signal from background noise. We assume that the beacon laser is pulsed. Expressions for other forms of beacon modulation can be found in the literature [43]. The NEA is therefore [43]:

$$\sigma_A = \sqrt{\frac{1}{(\mathrm{SF})^2 \mathrm{SNR}_e} + \sigma_{A,j}^2} \tag{3.105a}$$

$$\mathrm{SNR}_e = \frac{I_{\mathrm{pk}}^2 (1 - 1/N_{\mathrm{ex}})^2}{4\left(\sigma_n^2 + q_e B_q I_{\mathrm{pk}} (1 + 1/N_{\mathrm{ex}})\right)} \tag{3.105b}$$

where $I_{\mathrm{pk}} = R_q P_{\mathrm{pk,bcn}}$ is the peak signal current, $R_q$ is the quadcell responsivity, $N_{\mathrm{ex}}$ is the modulated signal's extinction ratio, $B_q$ is the tracking loop bandwidth, and $\sigma_n$ is the signal-free noise in each quadrant.

$$\sigma_n = \sqrt{i_b^2 + i_d^2 + i_{\mathrm{amp}}^2} \tag{3.106a}$$

$$i_b^2 = 2 q_e B_q R_q P_b \tag{3.106b}$$

$$i_d^2 = 2 q_e B_q I_{d,q} \tag{3.106c}$$

$$i_{\mathrm{amp}}^2 = 4(\mathrm{NEI})^2 B_q \tag{3.106d}$$

where $I_{d,q}$ is the dark current, and NEI is the noise equivalent current density of the quadrant pre-amplifiers. We can flow down the required peak current from requirements on the probability of detection $p_d$ (e.g. 99.9%) and the probability of false

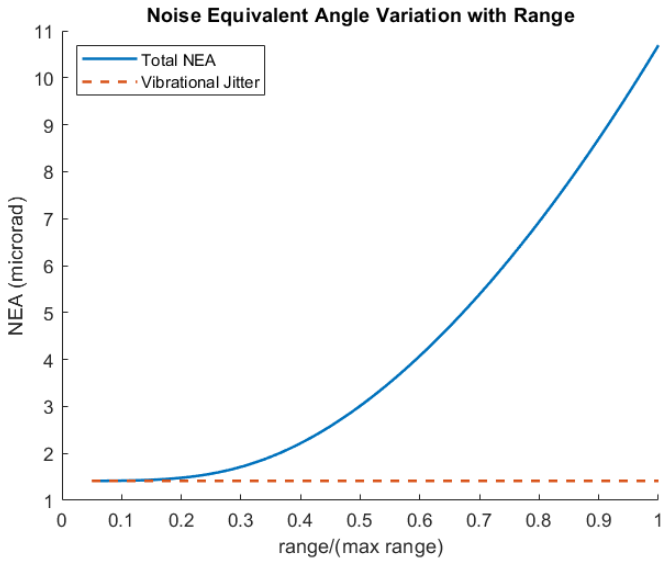


Figure 3-12: NEA variation with range relative to maximum design range (Equation 3.113). Parameters are in Table 3.8. Note that $r_n = 391.8$.

alarm $p_f$ (e.g., $10^{-6}$). Given Gaussian noise statistics, the peak signal requirement is [43]:

$$I_{\text{pk}} = K_1\sigma_n + K_2\sqrt{\sigma_n^2 + 2q_eB_qI_{\text{pk}}} \tag{3.107}$$

where $K_1$ and $K_2$ are defined by:

$$p_d = \frac{1}{\sqrt{2\pi}}\int_{-\infty}^{K_2} e^{(-x^2/2)}dx \tag{3.108a}$$

$$p_f = \frac{1}{\sqrt{2\pi}}\int_{K_1}^{\infty} e^{(-x^2/2)}dx \tag{3.108b}$$

$$\tag{3.108c}$$

For $p_d = 0.999$, $K_2 = 3.09023$, and for $p_f = 10^{-6}$, $K_1 = 4.75342$. The required peak signal current is:

$$I_{\text{pk-min}} = K_1\sigma_n + q_eB_qK_2^2 + \sqrt{(K_1\sigma_n + q_eB_qK_2^2)^2 + (K_2^2 - K_1^2)\sigma_n^2} \tag{3.109}$$

The peak current and power requirements with margin $m$ are:

$$I_{\text{pk-req}} = R_qP_{\text{pk-req}} = mI_{\text{pk-min}} \tag{3.110}$$

We again assume that the optical link is designed so that the minimum system performance is characterized by the power requirement at the maximum range. Values for the peak signal at other ranges are then:

$$I_{\text{pk}} = R_d P_{\text{pk}} = R_d P_{\text{pk-req}} \left( \frac{\rho_{\max}}{\rho} \right)^2 = I_{\text{pk-req}} \left( \frac{\rho_{\max}}{\rho} \right)^2 \tag{3.111}$$

The SNR is then related to the required SNR at the maximum range ($\text{SNR}_{e\text{-req}} = \text{SNR}_e(I_{\text{pk-req}})$) as:

$$\text{SNR}_e = \text{SNR}_{e\text{-req}} \left( \frac{\rho_{\max}}{\rho} \right)^4 \left( \frac{r_n + 1}{r_n + (\rho_{\max}/\rho)^2} \right) \tag{3.112}$$

where $r_n \equiv \sigma_n^2/(q_e B_q I_{\text{pk-req}}(1 + 1/N_{\text{ex}}))$. The noise equivalent angle is then:

$$\sigma_A = \sqrt{\frac{(\rho/\rho_{\max})^4}{(\text{SF})^2 \text{SNR}_{e\text{-req}}} \left( \frac{r_n + (\rho/\rho_{\max})^{-2}}{r_n + 1} \right) + \sigma_{A,j}^2} \tag{3.113}$$

The variation in NEA with range can be seen in Figure 3-12. Example beacon laser parameters are given in Table 3.7. The tracking system parameters we use are given in Table 3.8.

Table 3.7: Example Beacon Parameters (Assuming $L_{\text{tx}} = L_{\text{rx}}$)

| | | |
|---|---|---|
| LEO-LEO: $\rho_{\max} = 2300$ km | | |
| $\text{EIRP}_{\text{avg-req}}$ | Required Avg. EIRP | 57.01 dBW |
| $\theta_{1/e^2}$ | Divergence Angle | 6000 $\mu$rad |
| $P_{\text{tx}}$ | Transmitter Avg Power | 565 mW |
| LEO-MEO: $\rho_{\max} = 33466$ km | | |
| $\text{EIRP}_{\text{avg-req}}$ | Required Avg. EIRP | 80.26 dBW |
| $\theta_{1/e^2}$ | Divergence Angle | 300 $\mu$rad |
| $P_{\text{tx}}$ | Transmitter Avg Power | 299 mW |
| LEO-GEO: $\rho_{\max} = 49139$ km | | |
| $\text{EIRP}_{\text{avg-req}}$ | Required Avg. EIRP | 83.60 dBW |
| $\theta_{1/e^2}$ | Divergence Angle | 300 $\mu$rad |
| $P_{\text{tx}}$ | Transmitter Avg Power | 644 mW |
| LLO-LNRHO: $\rho_{\max} = 73525$ km | | |
| $\text{EIRP}_{\text{avg-req}}$ | Required Avg. EIRP | 87.10 dBW |
| $\theta_{1/e^2}$ | Divergence Angle | 250 $\mu$rad |
| $P_{\text{tx}}$ | Transmitter Avg Power | 1002 mW |

Table 3.8: Example Laser Beacon Tracking System Parameters. Note that values without a citation are computed from the other parameters. (*): For typical systems, the detector field of view ranges from ∼0.1°-10° [60, 54, 119], depending on the uncertainty area and if there is a scanning capability. We choose a FOV value within this range.

| | |
|---|---|
| Receiver Diameter | 10 cm [118] |
| Beacon Wavelength | 975 nm [131, 54] |
| Detector Field-of-View ($\text{FOV}_q$) | 1° (*) |
| Detector Width ($d$) | 3 mm [132] |
| Effective Focal Length ($f = d/\text{FOV}_q$) | 17.2 cm |
| Spot Shape Parameter ($k_s$) | 1.56 [43] |
| Detector Gap ($g$) | 10 $\mu$m [132] |
| Spot Diameter ($D_s = 2g$) | 20 $\mu$m |
| Spot Angular Diameter ($\theta_s = D_s/f$) | 116.4 $\mu$rad |
| Slope Factor ($\text{SF} = k_s/\theta_s$) | 13407 $\text{rad}^{-1}$ |
| Loop Bandwidth ($B_q$) | 1 kHz [119] |
| Responsivity ($R_q$) | 0.625 A/W [132] |
| Dark Current ($I_{d,q}$) | 0.6 nA [132] |
| NEI | $1.56 \times 10^{-14}$ A/$\sqrt{\text{Hz}}$ [132] |
| Background Radiance (Stars) at 975 nm | $1.6 \times 10^{-6}$ W/($\text{m}^2\text{sr}\mu\text{m}$) [43] |
| Receiver Loss | −1.5 dB [119] |
| Bandpass Filter Width | 0.2 nm [115] |
| Background Power ($P_b$) | -148.9 dBW |
| Extinction Ratio ($N_{\text{ex}}$) | 10 dB [43] |
| Signal-Free Noise Current ($\sigma_n$) | 1.08 nA |
| Probability of Detection ($p_d$) | 99.9% [43] |
| Probability of False-Alarm | $10^{-6}$ [43] |
| Minimum Peak Signal Current ($I_{\text{pk-min}}$) | 8.48 nA |
| Required Margin ($m$) | 3 dB |
| Required Peak Signal Current ($I_{\text{pk-req}}$) | 16.93 nA |
| Required Peak Signal Power | -105.7 dBW |
| Required $\text{SNR}_e$ | 16.9 dB |
| Detector NEA at Required SNR ($\sigma_{A,n}$) | 10.60 $\mu$rad |
| Vibrational Jitter ($\sigma_{A,j}$) | 1.4 $\mu$rad [119] |
| Total NEA at Maximum Range ($\sigma_A$) | 10.69 $\mu$rad |

### 3.4.3 Attitude Determination Errors

In this work, the attitude determination system is assumed to follow the typical practice of estimation using a multiplicative-extended Kalman filter (MEKF) with gyroscope and star-tracker measurements [133]. The star-tracker (ST) provides vector measurements of star directions that can be used to compute its attitude with respect to the inertial frame. The gyroscope is used in dynamics-replacement mode to integrate the attitude solution over time. The attitude solution drifts in-between star tracker measurements due to gyroscope noise. Example parameters are shown in Table 3.9. In Figure 3-13, the results of a Monte Carlo analysis with 1000 runs are

Table 3.9: Example Attitude Determination System Parameters [133]

| | |
|---|---|
| ST Angular Centroiding Error | 15 $\mu$rad (3.1 arcsec) |
| ST Measurement Rate | 1 Hz |
| ST FOV | 6° |
| Star Magnitude Threshold | 6 |
| Gyro Drift Noise Density | $3 \times 10^{-10}$rad/s$^2/\sqrt{\text{Hz}}$ |
| Gyro Angular Random Walk Noise Density | $7.27 \times 10^{-6}$rad/s$/\sqrt{\text{Hz}}$ |

shown for an MEKF using the parameters in Table 3.9. For further background on the MEKF algorithm, consult Markley and Crassidis [133]. The yaw axis is the star tracker's boresight axis, and the roll and pitch axes are the cross-boresight axes. It is noteable that the error in the boresight axis is significantly larger than the error in the cross-boresight axes. This is a well-known artifact of this attitude determination system, which can be mitigated by having two star trackers mounted orthogonal to each other and fusing their measurements.

The MEKF simulation is run assuming an equatorial LEO orbit, with the star tracker facing anti-nadir, which yields an average star availability of about 6 (with no outage periods). During a crosslink, the terminal attitude is typically essential knowledge for the PAT process, so we assume that the attitude is controlled to avoid star tracker outages (i.e. maintain a minimum sun keep out angle). We also assume the star field is uniformly distributed such that there is similar star availability across orbits and that the variation in attitude determination performance between orbits

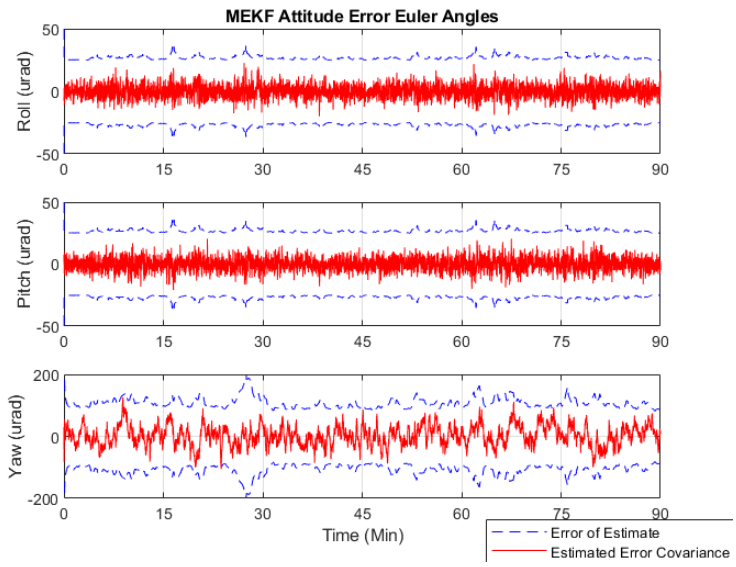


Figure 3-13: Example MEKF attitude determination errors. Roll (1-sigma): 5.22 $\mu$rad; Pitch (1-sigma): 5.31 $\mu$rad; Yaw (1-sigma): 32.82 $\mu$rad.

is negligible. For simplicity we assume that there are at least two star trackers such that the errors in all axes take on their minimum values. We will model the attitude determination error angle components in each axis equal to the average of the simulated roll and pitch errors: $\delta\theta_{AD} = 5.265$ $\mu$rad (1.086 asec). Note that: $\delta\mathbf{q}_{I,i}^{B} = \delta\theta_d/2$. In Section 3.4.4, we analyze the appropriate approximation to use for $\hat{\boldsymbol{\rho}}_{a,d}$.

### 3.4.4 Modeling Apparent Bearings

Following the same approach as in the previous discussion of apparent range, the apparent relative bearings of the signal at the recorded bearings measurement time $t_R$ are defined in general as:

$$\theta_{a,d}(t_R) = \tan^{-1}\left(\frac{\hat{\boldsymbol{\rho}}_{a,d}(t_R)\cdot\mathbf{E}_y}{\hat{\boldsymbol{\rho}}_{a,d}(t_R)\cdot\mathbf{E}_x}\right) \in [0, 2\pi) \tag{3.114a}$$

$$\phi_{a,d}(t_R) = \sin^{-1}(\hat{\boldsymbol{\rho}}_{a,d}(t_R)\cdot\mathbf{E}_z) \in [-\pi/2, \pi/2] \tag{3.114b}$$

$$\hat{\boldsymbol{\rho}}_{a,d}(t_R) = \frac{\boldsymbol{\rho}_{a,d}(t_R)}{\left\|\boldsymbol{\rho}_{a,d}(t_R)\right\|} \tag{3.114c}$$

$$\boldsymbol{\rho}_{a,d}(t_R) = \mathbf{r}_i(t' - \tau_d) - \mathbf{r}_0(t') \tag{3.114d}$$

$$\tau_d = f_\tau(\mathbf{r}_0(t'), \mathbf{r}_i(t' - \tau_d)) \tag{3.114e}$$

$$t' = t_R - \tau_d^{\text{rx}} \tag{3.114f}$$

where $\tau_d$ is the time of flight from the partner's laser transmitter to the host's sensor, and $\tau_d^{\text{rx}}$ is any hardware delay between the end of the detector integration time and $t_R$ (e.g., due to computational delays from image processing). Note that this is a one-way time of flight. This hardware delay is assumed to be known from system calibration. The noise level for apparent bearings measurements is on the order of $\sim 10^0$ to $10^1$ $\mu$rad. Therefore, approximation errors shall be $\leq 10^{-2}$ $\mu$rad. The corrections to the apparent bearings from each of the relativistic corrections are shown in Table 3.10. The orbit cases are modified from the previous ranging test cases to have a roughly balanced relative velocity split between range-rate and angular velocity. All corrections from general relativity are negligible relative to the noise. The angular time of flight correction from special relativity is significant relative to the noise; therefore, simply using the instantaneous geometric angles is insufficient.

Next, we consider the error in using a zero acceleration kinematic approximation for the time-shifted position vectors.

$$\mathbf{r}_0(t') \approx \mathbf{r}_0(t_R) - \mathbf{v}_0(t_R)\tau_d^{\text{rx}} \tag{3.115a}$$

$$\mathbf{r}_i(t' - \tau_d) \approx \mathbf{r}_i(t_R) - \mathbf{v}_i(t_R)(\tau_d^{\text{rx}} + \tau_d) \tag{3.115b}$$

For a hardware delay up to a conservative 0.1 sec, the error from using this approximation is negligible: less than 3 nrad in either $\theta_{a,d}$ or $\phi_{a,d}$ for both the LEO-LEO and LEO-GEO cases.

Table 3.10: Apparent Bearings Calculation Examples

| | LEO-Tx to LEO-Rx | LEO-Tx to GEO-Rx |
|---|---|---|
| $\theta_{a,d}^{\text{GEO}}$ | $\sim 1.935$ rad | $\sim 0.746$ rad |
| $\lvert\Delta\theta_{a,d}^{\text{SR}}\rvert$ | $\sim 19.25$ $\mu$rad | $\sim 11.73$ $\mu$rad |
| $\lvert\Delta\theta_{a,d}^{\text{PM}}\rvert$ | $\sim 2.62 \times 10^{-5}$ $\mu$rad | $\sim 5.44 \times 10^{-6}$ $\mu$rad |
| $\lvert\Delta\theta_{a,d}^{\text{HM}}\rvert$ | $< 1 \times 10^{-10}$ $\mu$rad | $< 1 \times 10^{-10}$ $\mu$rad |
| $\lvert\Delta\theta_{a,d}^{\text{SM}}\rvert$ | $< 1 \times 10^{-10}$ $\mu$rad | $< 1 \times 10^{-10}$ $\mu$rad |
| $\phi_{a,d}^{\text{GEO}}$ | $\sim -0.338$ rad | $\sim -0.074$ rad |
| $\lvert\Delta\phi_{a,d}^{\text{SR}}\rvert$ | $\sim 5.07$ $\mu$rad | $\sim 16.51$ $\mu$rad |
| $\lvert\Delta\phi_{a,d}^{\text{PM}}\rvert$ | $\sim 6.77 \times 10^{-6}$ $\mu$rad | $\sim 7.66 \times 10^{-6}$ $\mu$rad |
| $\lvert\Delta\phi_{a,d}^{\text{HM}}\rvert$ | $< 1 \times 10^{-10}$ $\mu$rad | $< 1 \times 10^{-10}$ $\mu$rad |
| $\lvert\Delta\phi_{a,d}^{\text{SM}}\rvert$ | $< 1 \times 10^{-10}$ $\mu$rad | $< 1 \times 10^{-10}$ $\mu$rad |
| LEO-LEO Rx: $a = 6960.6$ km, $e = 0.0017$, $i = 98.08°$ $\Omega = 109.65°$, $\omega_p = 334.37°$, $M = 252.49°$ | | |
| LEO-LEO Tx: $a = 6960.6$ km, $e = 0.0017$, $i = 82.08°$ $\Omega = 244.65°$, $\omega_p = 334.37°$, $M = 297.49°$ | | |
| LEO-GEO Rx: $a = 42165.2$ km, $e = 0.0003$, $i = 11.7°$ $\Omega = 42.13°$, $\omega_p = 313.01°$, $M = 230.48°$ | | |
| LEO-GEO Tx: $a = 6960.6$ km, $e = 0.0003$, $i = 56.7°$ $\Omega = 42.13°$, $\omega_p = 313.01°$, $M = 260.48°$ | | |

Lastly, we look at convergence of the iterative calculation algorithm, with the two approximations applied.

$$\tau_d^{i+1} = \frac{1}{c} \left\| \mathbf{r}_0(t') - \mathbf{r}_i(t' - \tau_d^i) \right\| ; \, \tau_d^0 = 0 \tag{3.116}$$

For a hardware delay up to a conservative 0.1 sec, the algorithm converges to less than 3 nrad error in either $\theta_{a,d}$ or $\phi_{a,d}$ for both the LEO-LEO and LEO-GEO cases after only one iteration. This means that the time of flight can be modeled as.

$$\tau_d \approx \tau_d^1 = \frac{1}{c} \left\| \mathbf{r}_0(t') - \mathbf{r}_i(t') \right\| = \frac{\rho(t')}{c} \tag{3.117}$$

Therefore, the apparent relative position can be modeled as

$$\boldsymbol{\rho}_{a,d}(t_R) \approx \mathbf{r}_i\left(t' - \frac{\rho(t')}{c}\right) - \mathbf{r}_0(t') \tag{3.118a}$$

$$\approx \mathbf{r}_i(t_R) - \mathbf{v}_i(t_R)\left(\tau_d^{\text{rx}} + \frac{\rho(t')}{c}\right) - (\mathbf{r}_0(t_R) - \mathbf{v}_0(t_R)\tau_d^{\text{rx}}) \tag{3.118b}$$

$$= \boldsymbol{\rho}(t') - \mathbf{v}_i(t_R)\frac{\|\boldsymbol{\rho}(t')\|}{c} \tag{3.118c}$$

$$\text{with } \boldsymbol{\rho}(t') = \boldsymbol{\rho}(t_R) - \dot{\boldsymbol{\rho}}(t_R)\tau_d^{\text{rx}} \tag{3.118d}$$

For both LEO-LEO and LEO-GEO cases, the uncertainty in the hardware delay calibration can be up to 10 $\mu$sec with negligible error in the apparent bearing angles. The measurement model gradients are given in Appendix A. As a final note, we can now assess the potential measurement frequency achievable given range/Doppler and bearings measurements. The range measurements are limited by the integration time, which is reasonably on the order of microseconds, so the range measurement frequency is on the order of hundreds of kHz to 1 MHz. The Doppler measurements are taken at the same rate; however, to get high accuracy, we must wait for the Doppler integration time to complete (e.g., 1 minute) before we start taking measurements. Next, the quadcell/camera measurements could be taken on the order of 1 kHz. Lastly, the star tracker measurements can be taken on the order of 1-5 Hz [98]. As far as complete range/Doppler+bearings measurements are concerned, the limiting sensor is the star tracker.

## 3.5 Chapter Summary

In this chapter, we performed systems analysis of the range, Doppler, and bearings measurements that can be generated using a laser communications system. We analyzed both the measurement error from the lasercom terminal design and the physical measurement model. For the ranging and Doppler error models, we focused on a full-duplex, direct-detection PPM laser communications system design with an atomic clock. We performed link analysis to show how there are potentially three regimes

of ranging error depending on the operational data rate: detector error dominated, synchronization error dominated, and clock error dominated. For a maximum design link range of 50,000 km, the regimes are approximately 10-20 Mbps, 20-100 Mbps, and $>$ 100 Mbps. For the high data rate (e.g. 622 Mbps - 1.244 Gbps), long link range systems that are planned for most future missions, the ranging and Doppler measurements will be clock error limited. In comparison, the RF ranging noise is mainly limited by phase detection errors. The atomic clock error is negligible for the RF system, whereas it dominates our reference 622 Mbps lasercom system over all ranging integration times. Shorter range links at high rates will be synchronization error dominated. At 622 Mbps, the transition point is a maximum design link range less than about 2000 km, which would be typical for a large constellation (e.g. Starlink). Given a terminal design for some maximum range, the ranging noise varies in real-time as the link range varies because of variable power received (due to path loss). Shorter range links will have higher received power and better ranging performance, in addition to higher communications data rate capacity. For the reference 622 Mbps link, the ranging error varies from about 1-5 mm (1-sigma) from 5000-50000 km.

The Doppler measurement gives the average range rate over an integration time. Given this model, the Doppler error is also dependent on the data rate. For our reference data rate of 622 Mbps with a Doppler integration time of 1 minute, the error from the detector/sychronization parts of the system dominate the error from the clock. The clock error only becomes the dominant error for short integration times (about 2 seconds in this case). Like the range error, the Doppler error also varies in real-time with the range because of the varying received power. For our reference link, it varies from about 1-20 microns/second (1-sigma) from 5,000-50,000 km. For the bearings error model, we showed how the noise in the calculated inertial bearings angles comes from both the lasercom terminal laser acquisition/tracking sensor (part of its PAT system), which gives angles relative to the sensor frame, and the star tracker that is used to determine the terminal's attitude with respect to the inertial frame. We analyzed a quadcell PAT sensor model and showed how the measurement noise depends on the SNR. For a given SNR requirement at the design max range, the

worst case error can be derived. The noise equivalent angle therefore decreased with range as the received power increases. The minimum NEA is limited by the residual effects of vibrational platform jitter (either the residuals from the damping/control system or the direct structural vibrations). Note that the sensor will also saturate at extremely short ranges (on the order of 10 km). Finally, the measurement frequency for complete range/Doppler and bearings measurements is limited by the star tracker to about 1-5 Hz, which is the lowest measurement frequency of all of the sensors (due to longer integration times needed to image stars).

We also analyzed the physical model for light propagation between the terminals, which is the basis for all of the measurements. The measured range for a two-way link is the apparent time of flight of light for the uplink combined with the downlink, along with any hardware delays. For the link configurations and measurement noise levels of interest (i.e., 1,000 to 100,000 km between satellites orbiting the same central body with mm to cm level noise), the TOF model needs to be better than about 1 picosecond. We showed that for this purpose, it is sufficient to model the TOF using special relativity with a single general relativistic correction: the Shapiro delay. The implicit, nonlinear equation that must be solved iteratively for the TOF can be truncated to 3 iterations with negligible error. The Doppler measurement is the integrated Doppler shift, which is mathematically equivalent to the average apparent range-rate over the integration time (plus noise). The average apparent range-rate is the difference of the apparent ranges at the endpoints of the integration interval divided by the integration time. This eliminates the hardware delay contribution. It also differences the relativistic effects; however, for sufficiently high relative velocities (e.g. a LEO-GEO relay), the Shapiro correction must still be taken into account for sufficiently accurate modeling. Again, the iterative solution to the differential TOF equation can be stopped at three iterations with negligible error. Lastly, the bearings measurement is actually of the apparent angles due to the time of flight of the signal. For typical noise levels, the apparent bearings can be calculated only using special relativity, and the iterative algorithm can be stopped at one iteration, so the time of flight can be approximated as the geometric range divided by the speed of

light, where any hardware delays should be taken into account when calculating the geometric range at the measurement time. Lastly, we have given expressions for the measurement gradients in Appendix A, which we will use along with the measurement model equations for the CRLB and Kalman Filter analysis in Chapter 4.

THIS PAGE INTENTIONALLY LEFT BLANK

# Chapter 4

# OISL Navigation Performance in Satellite Constellations

In this chapter, we apply the measurement models we have obtained to case studies of OISL-based navigation in satellite constellations around the Earth, the Moon, and Mars. We will use a baseline 622 Mbps link data rate, and the maximum link design range will vary depending on the application case. We will show how different types of orbital configurations lead to different measurement noise behavior due to variations in range and relative velocity. In Chapter 2, we showed that, away from exact singular configurations, the problem observability is not highly sensitive to the relative orbital configuration between link partners. However, the relative importance of the various perturbing forces is highly dependent on the orbits of each of the satellites. For example, aspheric gravitational field effects decrease with orbital altitude. The force model used determines the level of process noise in the estimator. In-between measurements, the estimator relies on the force model to propagate the orbit. The force model error causes the orbit estimate to diverge from the true orbit in-between measurements. The level of divergence depends on how accurate the force model approximation is. This is typical for any orbit determination problem, and the only mitigation is increasing the force model accuracy or the measurement frequency. For non-real time orbit determination, the estimates can be smoothed, which can also reduce the errors between measurements. Hence, the impact of process noise depends

on measurement availability, which depends on the orbits of the satellites along with any operational constraints.

In this chapter, we will assess the impacts of process noise and measurement availability for different satellite constellations. The measurement noise is also a function of the link geometry (the maximum design range and operational range), which will be incorporated into the simulations. The terminal design will be optimized to the maximum link range required for the typical intersatellite network connections. With conventional optical terminal designs, in order for constellations to quickly transfer data with low latency, multiple crosslink communications terminals are needed for data relays between satellites across the constellation. We will therefore also investigate the impact of links between the host satellite and more than one partner satellite, which would be the typical configuration in a high performance communications constellation. We do not assume any coordination between satellites in the constellation beyond establishing practical static or periodic links for the purposes of typical data routing in the communications network. In particular, we do not assume the existence of any centralized, ground-based planning algorithm that is optimizing for either communications data routing or for navigation. So the partners for any given host satellite are limited to a pre-defined list that is determined by mission planners prior to launch. Given that the observability is not highly sensitive to link geometry apart from the singular configurations, the best partners for links for OISL navigation are the nearby, non-coplanar satellites with the most link availability. Once maximum availability is achieved, there are diminishing returns for adding additional partners, so a dynamically optimized list of partners would not significantly improve performance beyond the static, single partner case with continuous access. Moreover, partners that have low availability are impractical to include since they would not contribute to the data routing capability of the network nor to the navigation objective.

Note that all of the case studies presented here are fictional link scenarios constructed to demonstrate the concepts and potential performance if the satellites were equipped with lasercom terminals designed as discussed in Chapter 3 (based on exist-

ing technology, but not any single existing design). The maximum design link ranges are chosen specifically for each example, as they would be in practice. Also, although the orbital elements used are based on actual TLEs, the simulation configurations do not correspond to any actual configuration of real satellites at a particular time in history. The simulation epoch time for all of the studies is chosen to be during a period of high solar activity (2015-05-15 21:48:10.000 UTC) to demonstrate the potential worst case effects of solar radiation pressure and drag.

## 4.1 Case Study: Starlink Constellation

The first case study is the Starlink constellation (phase one). As discussed in Chapter 2, the constellation is modeled as a Walker-Delta Constellation 53° : 1584/22/17 [92]. As before, a single satellite from the constellation is selected as the host, and its partners are selected based on typical connectivity for the constellation (see Figure 4-1). For a low-altitude communications constellation like Starlink, the satellites are

Table 4.1: Initial orbit elements for Starlink satellites selected for analysis from Walker-Delta Constellation 53° : 1584/22/17 [92]. The ($a$,$e$,$i$,$\omega_p$) coordinates are based on TLE data for STARLINK-1515 from June 2022.

| Satellite | $a$ (km) | $e$ | $i$ (deg) | $\Omega$ (deg) | $\omega_p$ (deg) | $M$ (deg) |
|---|---|---|---|---|---|---|
| WD-P2-S2 (Host) | 6925.4 | $1.43 \times 10^{-4}$ | 53.06 | 16.36 | 78.60 | 8.86 |
| WD-P1-S2 | 6925.4 | $1.43 \times 10^{-4}$ | 53.06 | 0 | 78.60 | 5.00 |
| WD-P2-S1 | 6925.4 | $1.43 \times 10^{-4}$ | 53.06 | 16.36 | 78.60 | 3.86 |
| WD-P2-S3 | 6925.4 | $1.43 \times 10^{-4}$ | 53.06 | 16.36 | 78.60 | 13.86 |
| WD-P3-S2 | 6925.4 | $1.43 \times 10^{-4}$ | 53.06 | 32.73 | 78.60 | 12.72 |
| WD-P10-S49 | 6925.4 | $1.43 \times 10^{-4}$ | 53.06 | 147.27 | 78.60 | 274.79 |
| WD-P12-S33 | 6925.4 | $1.43 \times 10^{-4}$ | 53.06 | 180 | 78.60 | 202.51 |
| WD-P16-S14 | 6925.4 | $1.43 \times 10^{-4}$ | 53.06 | 245.45 | 78.60 | 122.94 |

designed to support up to four intersatellite links: two to the co-planar satellites ahead and behind the host (WD-P2-S1 & WD-P2-S3) and one for a satellite in each of the two adjacent planes (WD-P3-S2 & WD-P1-S2) [2, 91]. Initially, the Starlink satellites were designed to have up to five intersatellite links, with the fifth terminal being allocated to links with crossing satellite planes (e.g. WD-P10-S49, WD-P12-

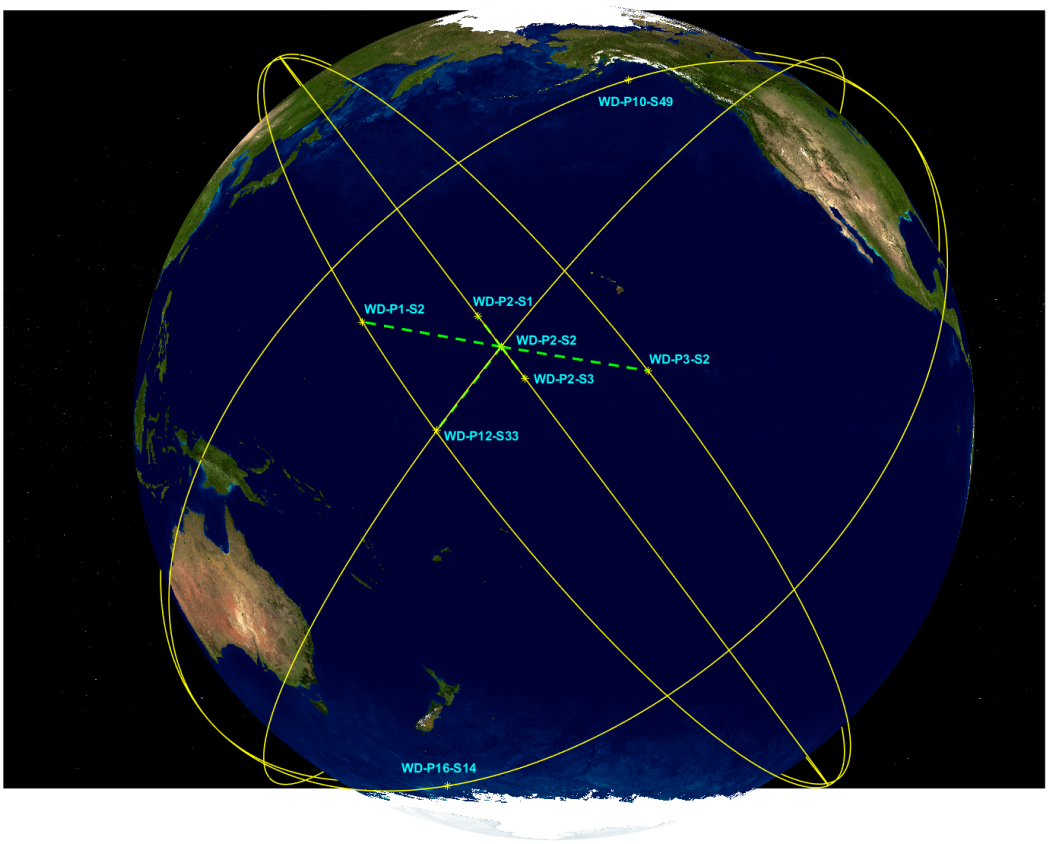


Figure 4-1: Selected satellites for Starlink constellation analysis. Host satellite (WD-P2-S2) and up to 5 partner satellites: 2 co-orbital partners (WD-P2-S1 & WD-P2-S3), 2 partners in adjacent planes in the same slots (WD-P1-S2 & WD-P3-S2), and one possible pre-planned partner in a crossing plane (WD-P10-S49, WD-P12-S33, or WD-P16-S24).

S33, WD-P16-S14), though this fifth terminal has subsequently been eliminated from the design [2]. The purpose of these crossing plane links is to rapidly transfer data from the ascending to descending satellites (or vice-versa) to reduce routing latency, rather than relaying the data with only co-moving satellites. We include this fifth terminal in some simulations to evaluate its impact on navigation performance. We also test with other subsets of the five possible links to show how different partners affect the result. 4-2.

Note that we do not include all crossing planes since the link durations for many of these crosslinks is relatively short. We selected three partners that have relatively long crosslink passes of about 5.8 to 6.7 minutes. We did not include satellites from

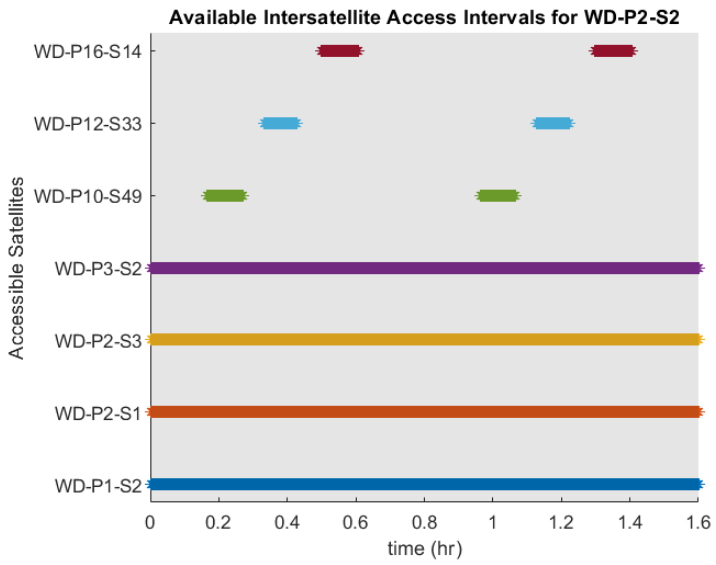


Figure 4-2: Link access for selected Starlink satellites with sun keep-out constraint of 10 degrees, maximum range of 2300 km, and maximum slew rate of 1 deg/sec. Note that the grey background color indicates when there is at least one link partner available. White background would indicate that there are no link partners available. In this case the entire background is grey since there is continuous access to the four neighbor satellites.

planes 11, 13, 14, and 15 because the host terminal would then spend too much time slewing rather than linking, which is not an efficient use of the fifth terminal (time spent slewing increases data routing latency). All of the other planes that are crossed, are crossed near the poles. For all simulations, we assume a gimbal-mounted lasercom terminal with a maximum slew rate of 1 deg/second, which is based on a terminal design from MIT Lincoln Laboratory for LCRD [134]. For the selected crossing plane satellites, the maximum slew rates are about 0.9 deg/s in azimuth and 0.063 deg/s in elevation relative to the host satellite's local-vertical-local-horizontal (LVLH) frame. We assume that the spacecraft body attitude rate is negligible relative to this frame (i.e., the spacecraft body is not slewing). Links to some spacecraft in the crossing planes can have short outages that occur in the middle of the pass due to the slew limit. We have selected the partners such that the slew rate does not cause outages during the passes. The required maximum design range to support the standard four-way link configuration is 2278.5 km, which we round up to 2300 km for the terminal maximum range requirement design parameter (note: the cross-planar

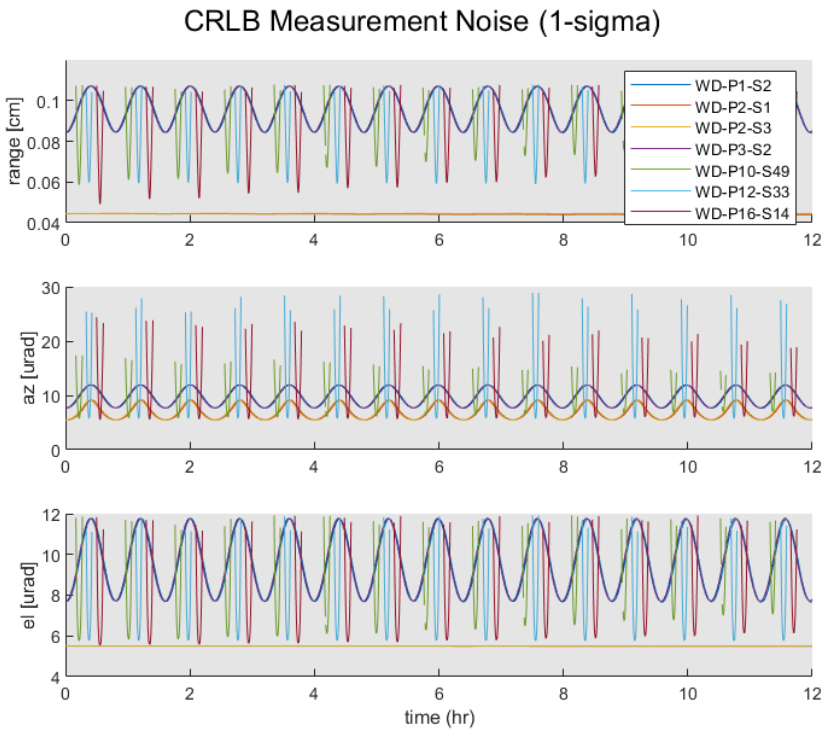


Figure 4-3: Measurement noise standard deviation values for all of the selected satellite links over the simulation duration.

links are longer than the co-planar links). We also impose a sun keep-out constraint along the link line-of-sight of 10 degrees (in both directions), which is based on the SILEX terminal design [135]. The link availability for one orbit for the selected satellites with these constraints is shown in Figure The measurement noise values computed as per our analysis for a 622 Mbps link with a quadcell and star tracker measurements in Chapter 3 are shown in Figure 4-3, and the summary statistics are given in Table 4.2. The measurement set used for the CRLB and EKF analyses to follow include range and bearings (no Doppler since range has a lower effective noise). Note that the measurement biases are not considered for the analysis, so the results assume sufficiently accurate measurement bias parameter calibration/estimation that the residual uncertainty is negligible. Analysis of the impact of measurement biases is future work.

Table 4.2: Measurement noise (1-sigma) model statistics for selected Starlink satellites. Host satellite is WD-P2-S2.

| Partner Satellite | Min | RMS | Max |
|---|---|---|---|
| Range [cm] | | | |
| WD-P1-S2 | 0.084 | 0.096 | 0.107 |
| WD-P2-S1 | 0.044 | 0.044 | 0.045 |
| WD-P2-S3 | 0.044 | 0.045 | 0.045 |
| WD-P3-S2 | 0.084 | 0.097 | 0.107 |
| WD-P10-S49 | 0.059 | 0.085 | 0.108 |
| WD-P12-S33 | 0.059 | 0.080 | 0.108 |
| WD-P16-S14 | 0.049 | 0.080 | 0.108 |
| Azimuth ($\theta$) [$\mu$rad] | | | |
| WD-P1-S2 | 7.657 | 9.846 | 11.931 |
| WD-P2-S1 | 5.498 | 7.085 | 9.147 |
| WD-P2-S3 | 5.502 | 7.088 | 9.147 |
| WD-P3-S2 | 7.698 | 9.877 | 11.937 |
| WD-P10-S49 | 5.750 | 9.872 | 17.344 |
| WD-P12-S33 | 5.761 | 14.007 | 28.868 |
| WD-P16-S14 | 5.551 | 12.166 | 24.399 |
| Elevation ($\phi$) [$\mu$rad] | | | |
| WD-P1-S2 | 7.657 | 9.757 | 11.770 |
| WD-P2-S1 | 5.498 | 5.500 | 5.503 |
| WD-P2-S3 | 5.502 | 5.502 | 5.503 |
| WD-P3-S2 | 7.698 | 9.786 | 11.775 |
| WD-P10-S49 | 5.750 | 8.183 | 11.920 |
| WD-P12-S33 | 5.756 | 7.716 | 11.916 |
| WD-P16-S14 | 5.549 | 7.746 | 11.911 |

### 4.1.1 Process Noise: Perturbing Accelerations

In this section, we assess the process noise from force model errors. The analysis of perturbing accelerations is shown in Table 4.3. They are graphed over time in Figure 4-4. The simulation duration is 12 hours, and the sampling period is 10 seconds. The shown acceleration values are the RMS of the norm of the accelerations due to each perturbation for both satellites over the entire simulation. The Earth's gravity model is based on the EIGEN-6S coefficients. The spacecraft parameters are the same as Chapter 2 (mass of 250 kg and 30 $m^2$ solar panel area). The panels are assumed pointed towards the sun, so the drag ram is area is modeled as approximately 64% of the solar area (this is the average forward ram area fraction of a flat sun-pointing

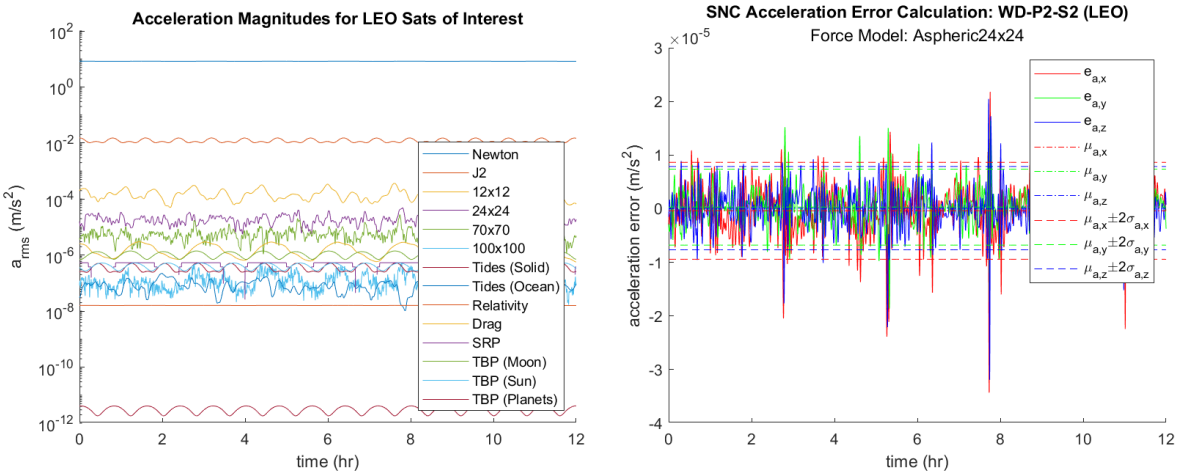


Figure 4-4: (a) RMS acceleration for both LEO satellites due to perturbations over simulation period. (b) Acceleration error and statistics for host satellite using a 24 x 24 gravity field model. Note that SNC refers to state noise compensation, which is a common way of estimating fixed Gaussian process noise parameters for the EKF.

plate in a circular orbit aligned with the ecliptic plane). The dominant perturbations come from the gravitational potential terms up to order and degree 70. The strongest perturbing effect after this is drag, which is closely followed by the third-body perturbing potential (TBP) from the Moon. The weakest perturbations are aspheric potential terms from order and degree 70 to 100, tidal gravitational potential effects

Table 4.3: LEO-LEO Perturbing Accelerations

| Acceleration | $a_{\text{rms}}$ (m/s$^2$) |
|---|---|
| Newtonian | 8.30 |
| $J_2$ | $1.21 \times 10^{-2}$ |
| 12 x 12 | $1.53 \times 10^{-4}$ |
| 24 x 24 | $2.14 \times 10^{-5}$ |
| 70 x 70 | $6.57 \times 10^{-6}$ |
| Drag (MSISE00) | $1.78 \times 10^{-6}$ |
| TBP: Moon | $1.08 \times 10^{-6}$ |
| SRP | $4.18 \times 10^{-7}$ |
| TBP: Sun | $4.16 \times 10^{-7}$ |
| Solid Tides | $3.60 \times 10^{-7}$ |
| 100 x 100 | $1.53 \times 10^{-7}$ |
| Ocean Tides | $9.23 \times 10^{-8}$ |
| Relativity | $1.59 \times 10^{-8}$ |
| TBP: Planets | $3.21 \times 10^{-12}$ |

(solid and ocean), the post-Newtonian relativistic gravitational correction [16], and third body perturbations from the planets (Mercury, Venus, Mars, Jupiter, Saturn, and Neptune). We do not include Earth albedo radiation pressure (it is not included in the Orekit 11.3 release); however, analysis in the literature shows that it is a weaker acceleration than ocean tides for LEO orbits [136], so it is negligible for our purposes. It should be noted that the non-gravitational forces (drag and solar radiation pressure) are challenging to model accurately in real-time onboard the spacecraft since they require regularly updated data on solar weather and the Earth's magnetic field, and they also require the host satellite to have knowledge of the mass and attitude of the partner satellites. Although this information could be disseminated to the host satellite via the communications network, it would simplify the design to avoid needing to model these forces. We therefore present four different models to show how process noise changes with the force model. The first three are truncated Earth gravity models, and the final one includes the drag force.

Table 4.4: LEO Cross-Planar Link (Adjacent Planes) Process Noise Analysis, where $\sigma_{a_p,\text{rms}}$ is the RMS over the 12 hour simulation duration of the magnitude of the perturbing acceleration, $|\frac{\mu_{a,p}}{\sigma_{a,p}}|_{\max}$ is the maximum ratio of the acceleration mean to the standard deviation (a measure of the model's bias error), $\sigma_{r,\text{rms}}$ and $\sigma_{v,\text{rms}}$ are the CRLB position and velocity uncertainties, and $t_s$ is the CRLB settling time (as defined in Chapter 2).

| Force Model | WD-P2-S2 | | | | |
|---|---|---|---|---|---|
| | $\sigma_{a_p,\text{rms}}$ ($\text{m/s}^2$) | $\lvert\frac{\mu_{a,p}}{\sigma_{a,p}}\rvert_{\max}$ | $\sigma_{r,\text{rms}}$ (m) | $\sigma_{v,\text{rms}}$ (mm/s) | $t_s$ (hr) |
| 12 x 12 | $1.31 \times 10^{-5}$ | 0.06 | 9.57 | 9.96 | 1.63 |
| 24 x 24 | $4.00 \times 10^{-6}$ | 0.09 | 5.28 | 5.50 | 1.73 |
| 70 x 70 | $1.23 \times 10^{-6}$ | 0.59 | 3.27 | 3.50 | 1.36 |
| 70 x 70 & Drag | $7.03 \times 10^{-7}$ | 0.43 | 3.01 | 3.25 | 1.36 |
| Force Model | WD-P3-S2 | | | | |
| | $\sigma_{a_p,\text{rms}}$ ($\text{m/s}^2$) | $\lvert\frac{\mu_{a,p}}{\sigma_{a,p}}\rvert_{\max}$ | $\sigma_{r,\text{rms}}$ (m) | $\sigma_{v,\text{rms}}$ (mm/s) | $t_s$ (hr) |
| 12 x 12 | $1.28 \times 10^{-5}$ | 0.02 | 10.06 | 10.31 | 1.63 |
| 24 x 24 | $3.98 \times 10^{-6}$ | 0.11 | 5.47 | 5.72 | 1.73 |
| 70 x 70 | $1.24 \times 10^{-6}$ | 0.31 | 3.29 | 3.56 | 1.36 |
| 70 x 70 & Drag | $7.35 \times 10^{-7}$ | 0.53 | 3.01 | 3.28 | 1.36 |

The process noise and corresponding CRLB statistics for the four different force

models are shown in Table 4.4 for an example crosslink between the host (WD-P2-S2) and one of its adjacent plane partners (WD-P3-S2). The RMS acceleration error is given along with the maximum ratio of the mean acceleration error to the RMS error. This gives an indication of the level of acceleration bias that in a typical EKF is ignored, so this ratio should ideally be small, though this bias can be estimated in an adaptive process noise scheme. The CRLB does not consider the effect of this bias, and the EKF simulation presented later ignores this bias. The reference truth force model includes all of the aforementioned perturbations with a 100 x 100 aspheric gravitational field and additionally includes the perturbation due to general relativity.

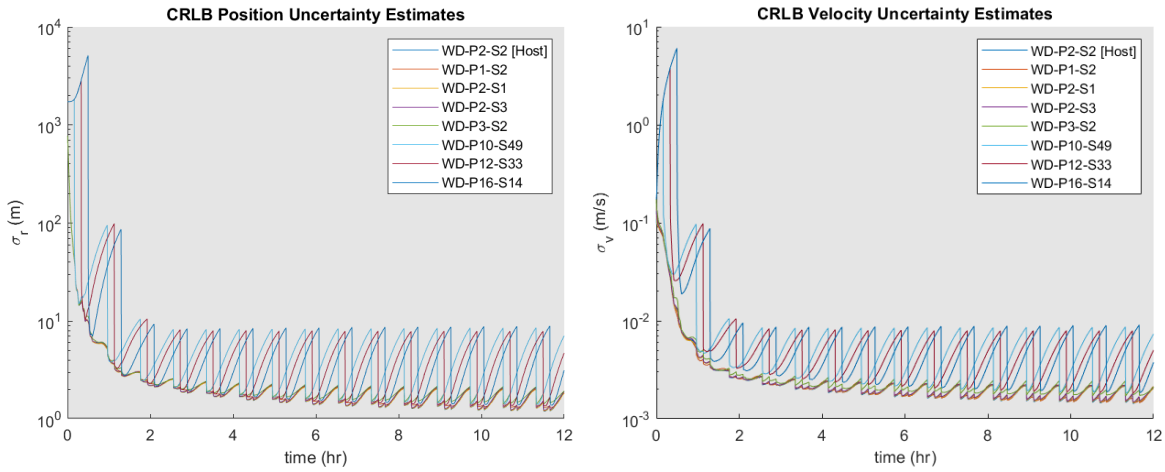


Figure 4-5: (a) Position and (b) velocity uncertainties for Starlink satellite for Four-Way Link and Crossing Planes scenario using 24 x 24 gravity field model.

The access constraints are as previously discussed in this section. Given a conservative maximum measurement rate of 1 Hz and a conservative margin for the computer processing time required to process the measurements onboard the spacecraft, we conservatively put the measurement frequency at 0.1 Hz (10 seconds) and note that running at higher frequencies would yield lower uncertainties (as previously shown in Chapter 2). For this example, the sun keep-out restriction does not have any outages (the minimum angle it reaches along the line of sight is about 14 degrees). In general, the effects of sun keep out will depend on beta angle, so they will vary for each link as the orbit slowly precesses. Having multiple options for link partners

helps to reduce the impact during periods where this constraint is overly restrictive. Lastly, it is important to note that all of the perturbing forces require knowledge of the absolute time (e.g. UTC time). For example, computing the aspheric Earth gravitation perturbations requires computing the rotational orientation of the Earth relative to the inertial frame (i.e., determining the ECI-to-ECEF coordinate frame rotation), which is computed using the absolute UTC time. Likewise, TBP requires determining the positions of the Sun and Moon from their known ephemerides, which requires knowledge of the absolute UTC time. For this analysis, the spacecraft is assumed to keep time sufficiently accurately (using its atomic clock) that additional force modeling error due to spacecraft clock error is negligible. Further investigation of this effect is future work. Increasing the gravitational force model accuracy from 12 x 12 to 24 x 24 reduces the CRLB position and velocity uncertainties by about 50% (an improvement of about 5 m and 5 mm/s). Increasing to 70 x 70 again reduces by about 40%, but this change is only about 2 m and 2 mm/s. Adding drag further reduces the error, but by less than 1 m and 1 mm/s. The settling times also reduce somewhat for higher accuracy models. Given these diminishing returns and the expectation of nearly continuous links for this configuration of satellites, we select the 24 x 24 gravitational field model for further analysis.

A CRLB analysis for different link configurations using the 24 x 24 gravity field model is given in Table 4.5. The co-orbital link with moderate station keeping error has poor convergence and higher uncertainty than the result in Chapter 2. This is due to the increased process noise, which means even greater offsets from the singular co-orbital configuration are needed for practical observability. We increase the station keeping offsets by an order of magnitude to show a case that is sufficiently far from the singular configuration for proper convergence, although the settled uncertainty is still relatively high. As we showed previously in Chapter 2, a sufficient condition for baseline observability performance is that the RAAN is offset by at least 5°, which is met by the cross-planar link to the adjacent satellite partner. This link to the adjacent plane gives uncertainties of about 5.3 m and and 5.6 mm/s. This is on-par with GPS tracking. Adding a co-planar link partner actually improves the uncertainties

Table 4.5: LEO Constellation Example CRLB Results using 24 x 24 gravity field model. Except for first two co-orbital cases, the orbital elements are exactly as defined in Table 4.1.

| Satellite | $\sigma_r$ (m) | | | $\sigma_v$ (mm/s) | | |
|---|---|---|---|---|---|---|
| | Min | RMS | Max | Min | RMS | Max |
| Co-Orbital Link with moderate station keeping error $(\delta a, \delta e, \delta\Omega) = (695\text{m}, 8.4 \times 10^{-5}, 2.8 \times 10^{-3}\text{deg})$: $t_s > 12$ hrs, $l^{99}_{CN(P)} = 13.09$ | | | | | | |
| WD-P2-S2 | 63.05 | 294.0 | 1225 | 68.83 | 315.4 | 776.0 |
| WD-P2-S3 | 63.05 | 294.1 | 1225 | 68.80 | 315.5 | 776.3 |
| Co-Orbital Link with high station keeping error (10 times higher than the moderate case): $t_s = 1.66$ hrs, $l^{99}_{CN(P)} = 11.34$ | | | | | | |
| WD-P2-S2 | 29.33 | 44.90 | 90.14 | 32.06 | 48.06 | 95.41 |
| WD-P2-S3 | 29.34 | 44.94 | 90.20 | 32.03 | 48.00 | 95.35 |
| Cross-Planar Link (Adjacent Planes): $t_s = 1.73$ hrs, $l^{99}_{CN(P)} = 8.56$ | | | | | | |
| WD-P2-S2 | 4.79 | 5.28 | 7.10 | 4.82 | 5.50 | 6.99 |
| WD-P3-S2 | 4.81 | 5.47 | 6.92 | 5.09 | 5.72 | 7.51 |
| Cross-Planar & Co-Orbital Link: $t_s = 1.58$ hrs, $l^{99}_{CN(P)} = 9.01$ | | | | | | |
| WD-P2-S2 | 3.49 | 3.97 | 6.32 | 3.60 | 4.15 | 6.03 |
| WD-P2-S3 | 3.53 | 4.01 | 6.38 | 3.58 | 4.12 | 6.02 |
| WD-P3-S2 | 3.61 | 4.17 | 6.24 | 3.75 | 4.35 | 5.94 |
| Four-Way Link: $t_s = 1.57$ hrs, $l^{99}_{CN(P)} = 9.06$ | | | | | | |
| WD-P2-S2 | 2.40 | 2.71 | 4.18 | 2.49 | 2.85 | 3.95 |
| WD-P1-S2 | 2.20 | 2.66 | 4.18 | 2.35 | 2.79 | 4.25 |
| WD-P2-S1 | 2.38 | 2.69 | 4.14 | 2.52 | 2.86 | 3.95 |
| WD-P2-S3 | 2.45 | 2.75 | 4.22 | 2.53 | 2.88 | 3.98 |
| WD-P3-S2 | 2.49 | 2.91 | 4.15 | 2.57 | 3.09 | 4.24 |
| Four-Way Link + Crossing Planes: $t_s = 4.29$ hrs, $l^{99}_{CN(P)} = 9.36$ | | | | | | |
| WD-P2-S2 | 1.20 | 1.59 | 2.20 | 1.44 | 1.82 | 2.34 |
| WD-P1-S2 | 1.31 | 1.63 | 2.22 | 1.46 | 1.84 | 2.37 |
| WD-P2-S1 | 1.21 | 1.59 | 2.18 | 1.46 | 1.83 | 2.35 |
| WD-P2-S3 | 1.23 | 1.63 | 2.25 | 1.48 | 1.87 | 2.38 |
| WD-P3-S2 | 1.42 | 1.76 | 2.29 | 1.71 | 2.03 | 2.59 |
| WD-P10-S49 | 1.41 | 4.63 | 8.57 | 1.83 | 4.97 | 8.66 |
| WD-P12-S33 | 1.37 | 4.40 | 8.03 | 1.82 | 4.67 | 8.12 |
| WD-P16-S14 | 1.39 | 4.74 | 8.94 | 1.85 | 5.09 | 9.06 |

slightly (by about 1 m and 1 mm/s), despite the co-planar partner being in a singular configuration. This again demonstrates only one fully observable link is needed for the entire system to be fully observable. Adding the remaining two partners in the

four-way Starlink configuration again slightly improves the uncertainties (by about 1 m and 1 mm/s). Adding the fifth terminal and links with the three selected crossing plane satellites once again slightly improves the uncertainties (to about 1.5 m and 1.5 mm/s). Also, it increases the settling time due to the outage periods of the crossing plane satellites, which also causes their uncertainties to be somewhat higher (about 4.5 m and 4.5 mm/s). Overall, the gains in performance from additional link partners beyond what is needed for continuous measurements in a non-singular configuration are relatively meager.

### 4.1.2 Monte Carlo Kalman Filtering Simulations

The simulation duration was 12 hours, and the measurement period was 10 seconds. The basic Kalman filter formulation used here assumes unbiased process noise, so the model selected for Monte Carlo simulations has a small value for the bias relative to the noise. The results are summarized in Table 4.6. Rather than manually tuning a fixed process noise standard deviation (i.e., State Noise Compensation (SNC) [87]) or the parameters of a variable process noise algorithm (e.g., Covariance Matching (CM), Adaptive SNC (ASNC), Dynamic Model Compensation (DMC), Adaptive DMC (ADMC) [137]), the process noise value is automatically tuned online using the Normalized Estimation Error Squared (NEES [138]) metric for feedback corrections to the process noise standard deviation at each measurement step. Hence, the results can be interpreted as the idealized performance of a Kalman filter utilizing an adaptive process noise algorithm (e.g., ASNC), which, if it was tuned properly, would yield similar results. This way, many different scenarios can be assessed without needing to laboriously tune the process noise parameters for each one. In practice, the parameters governing the process noise used in the EKF (either fixed noise or adaptive) would need to be tuned using extensive simulations, ideally including empirical orbit data from pathfinding missions. The details of this tuning process are not of interest in the current work, though it is important to consider that, in practice, an engineer (or team of engineers) would be dedicated to this task. The measurement noise covariance used by the Kalman filter is the same as the noise model used for the mea-

surement sample error. In reality, the filter would not have perfect knowledge of the measurement covariance, so it would either be set to the maximum anticipated value (e.g. the value at the maximum link range), or an adaptive measurement covariance algorithm would need to be implemented. The results here are representative of a filter with an idealized adaptive measurement covariance algorithm.

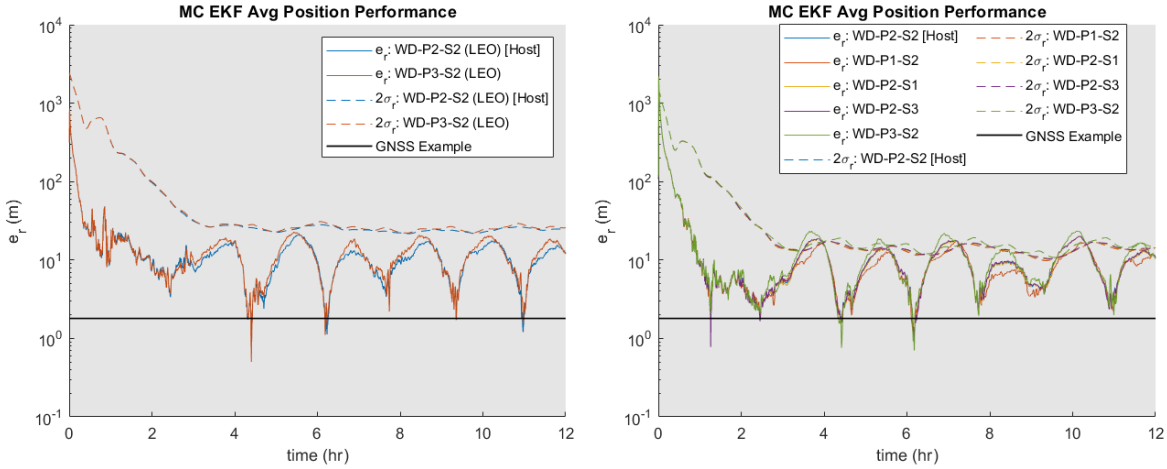


Figure 4-6: Average Monte Carlo (30 runs) EKF position errors with 24 x 24 gravity field force model for (a) Cross-Planar Link and (b) Four-Way Link. The GNSS example error is 1.8 m, which is the on-orbit GPS receiver performance for the TET-1 satellite [27].

The measurement biases are set to zero for this analysis, so the results assume an idealized form of measurement bias parameter knowledge such that the residual uncertainty is negligible. In practice, the filter would need to estimate these biases to achieve this a similar level of accuracy. In some cases, on-orbit calibration may also be needed. Results in the literature for radio ISL navigation indicate that filters that incorporate bias estimation yield similar performance to the same filter simulation but with negligible bias [38]. Hence, we expect the performance results here to not change significantly if biases are estimated within the filtering algorithm. All this being said, the results here are representative of an idealized estimation process, which is intended to compare idealized filter performance for different orbit cases at a high level. Filter performance in practice may be somewhat worse unless it is carefully designed and tested for the particular application. As a final note, there are other nonlinear filtering algorithms like the Unscented Kalman Filter (UKF) and

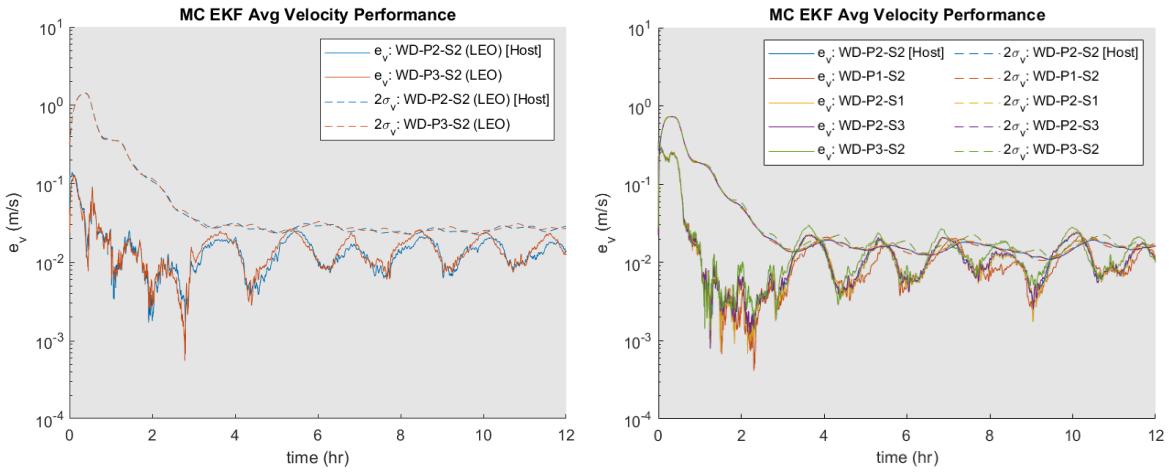


Figure 4-7: Average Monte Carlo (30 runs) EKF velocity errors with 24 x 24 gravity field force model for (a) Cross-Planar Link and (b) Four-Way Link.

particle filter that could be applied to the problem. However, for this problem, these algorithms can be significantly more computationally expensive to evaluate than the EKF, and the improvement in performance is limited by the CRLB, which as we will see ends up being at best only a small degree of improvement over the EKF. Therefore, we did not run additional Monte Carlo simulations with these other algorithms.

The EKF performance with the 24 x 24 gravity field model for the baseline cross-planar link and the four-way link configurations is shown in Figures 4-6 and 4-7. The graphed quantities are $e_r$ (the norm of the position error), $2\sigma_r$ (twice the norm of the position variances), $e_v$ (the norm of the velocity error), $2\sigma_v$ (twice the norm of the velocity variances).

The summary statistics are given in Table 4.6. The RMS position and velocity errors are about 2-3 times the CRLB uncertainties. Note that these statistics are not directly related (the CRLB being a covariance estimate) but a rough guess of 3-sigma of the CRLB uncertainty does yield a good approximation of the EKF RMS error. The additional partners in a four-way link improve the orbit determination slightly relative to the single non-singular configuration. Given these results, a 24 x 24 force model with at least one non-singular configuration link partner can yield orbit determination results on-par with GNSS receivers ($\sim$0.1-10 m, see Figure 1-1).

Table 4.6: LEO constellation results for average of Monte Carlo (30 runs) EKF with 24 x 24 gravity field force model.

| Satellite | $e_r$ (m) | | | $e_v$ (mm/s) | | |
|---|---|---|---|---|---|---|
| | Min | RMS | Max | Min | RMS | Max |
| Cross-Planar Link: $t_s = 4.54$ hr, $l^{99}_{CN(P)} = 9.15$, Avg. NEES = 14.77 (99% Bds. [9.82, 14.43]), $\sigma_{q,\text{rms}} = 3.98 \times 10^{-5}$ m/s$^2$ | | | | | | |
| WD-P2-S2 | 1.12 | 11.46 | 21.00 | 3.86 | 14.55 | 25.25 |
| WD-P3-S2 | 1.11 | 13.04 | 22.74 | 5.93 | 16.17 | 26.49 |
| Four-Way Link: $t_s = 4.77$ hr, $l^{99}_{CN(P)} = 9.87$, Avg. NEES = 34.96 (99% Bds. [26.48, 33.77]), $\sigma_{q,\text{rms}} = 4.42 \times 10^{-5}$ m/s$^2$ | | | | | | |
| WD-P2-S2 | 0.95 | 10.49 | 19.98 | 2.47 | 12.95 | 24.13 |
| WD-P1-S2 | 0.91 | 9.22 | 17.56 | 2.50 | 11.37 | 22.18 |
| WD-P2-S1 | 0.96 | 10.40 | 19.98 | 1.73 | 13.04 | 25.09 |
| WD-P2-S3 | 1.03 | 10.60 | 20.08 | 2.55 | 13.04 | 23.82 |
| WD-P3-S2 | 0.70 | 12.07 | 23.48 | 4.67 | 14.76 | 28.56 |

## 4.2 Case Study: GPS Constellation

There is interest in placing laser communications crosslinks on navigation satellites for intersatellite communications [72]. We are interested in how this would be different than the LEO constellation we have just studied. For this analysis, the GPS constellation is modeled as Walker-Delta 55° : 24/6/2 [139] (although the exact slots of the GPS satellites have been individually optimized so that they don't exactly follow this simple definition). The initial orbit elements are in Table 4.7. We again select a host

Table 4.7: Initial orbit elements for GPS satellites selected for analysis from Walker-Delta Constellation 55° : 24/6/2 [139]. The ($a$,$e$,$i$,$\omega_p$) coordinates are based on TLE data for USA319 from June 2022.

| Satellite | $a$ (km) | $e$ | $i$ (deg) | $\Omega$ (deg) | $\omega_p$ (deg) | $M$ (deg) |
|---|---|---|---|---|---|---|
| WD-P2-S2 (Host) | 26559.6 | $5.41 \times 10^{-3}$ | 55.20 | 60 | 188.27 | 119.46 |
| WD-P1-S2 | 26559.6 | $5.41 \times 10^{-3}$ | 55.20 | 0 | 188.27 | 89.38 |
| WD-P2-S1 | 26559.6 | $5.41 \times 10^{-3}$ | 55.20 | 60 | 188.27 | 29.69 |
| WD-P2-S3 | 26559.6 | $5.41 \times 10^{-3}$ | 55.20 | 60 | 188.27 | 210.31 |
| WD-P3-S2 | 26559.6 | $5.41 \times 10^{-3}$ | 55.20 | 120 | 188.27 | 149.69 |

satellite (WD-P2-S2) in the constellation for study, and we select its partners based on the same communications link principles as the Starlink constellation: the host

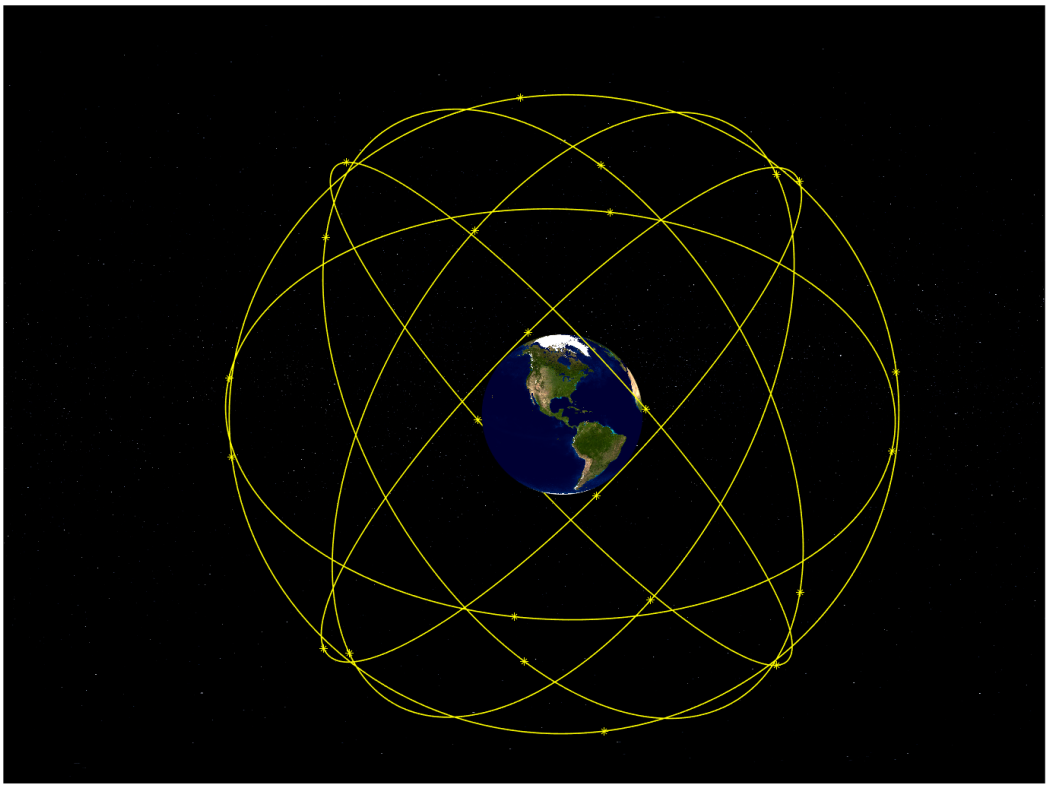

Figure 4-8: GPS Constellation (Walker-Delta 55° : 24/6/2 model [139] rendered using MATLAB R2023b in the local inertial frame)

satellite links to its co-moving neighbors. See Figure 4-9 for a plot of the selected satellites' orbits with the maximum of 4 links shown. We do not consider crossing planes for satellite partners since there are so few total planes. We again assume gimbal-mounted terminals, and since the partners are co-moving, the required terminal slew rates relative to LVLH are very small (about 0.01 deg/sec). The required maximum design range to support the four-way link configuration is 37981 km, which we round up to 38000 km for the terminal maximum range requirement design parameter. Note that the TESAT Laser Communications Terminal (LCT) proposed to be used for the Galileo implementation of this concept would have a link range up to 45000 km [72]. With the same 10 degree sun keep out angle along with these constraints, the host has continuous link access to all four partners for the selected orbital configuration. Again, the impact of sun-keep out will change over time with

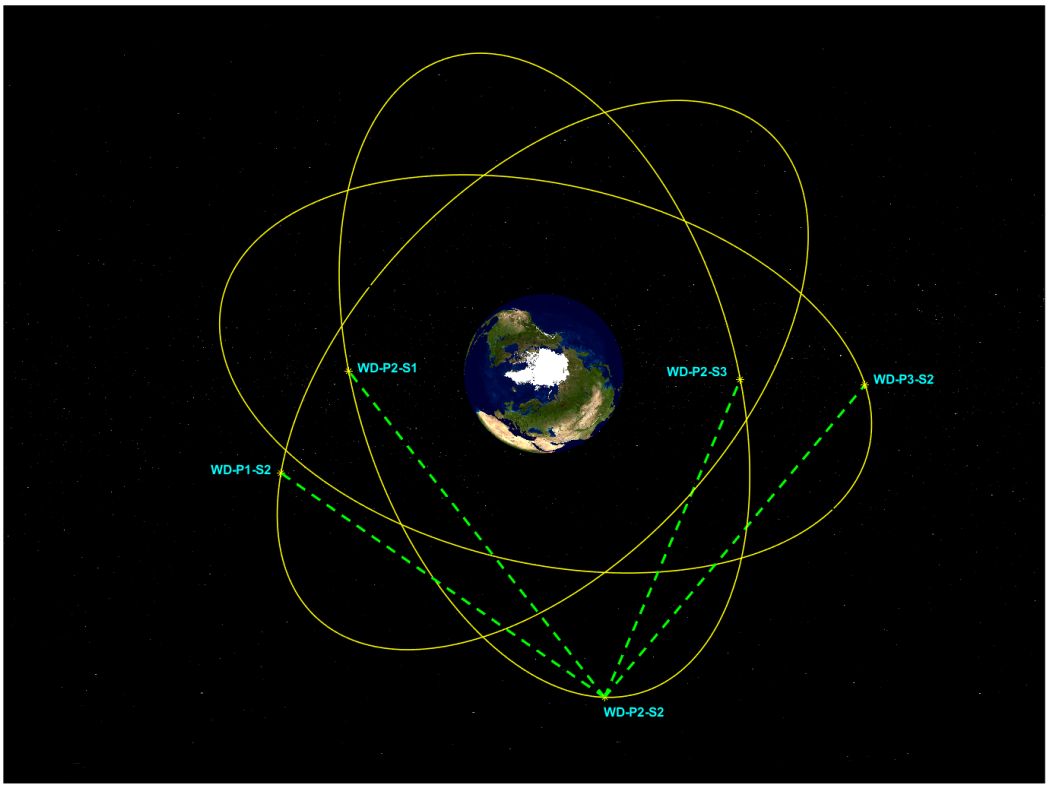


Figure 4-9: Selected satellites for analysis from the GPS constellation.

the precession of the orbit. The measurement noise values with varying link ranges are calculated and shown in Figure 4-10, and the summary statistics are displayed in Table 4.8. The ranging error is slightly higher than the LEO case due to the longer time of flight. The angular errors are similar since the transmit laser parameters are optimized for the new design range to achieve the same SNR at maximum range.

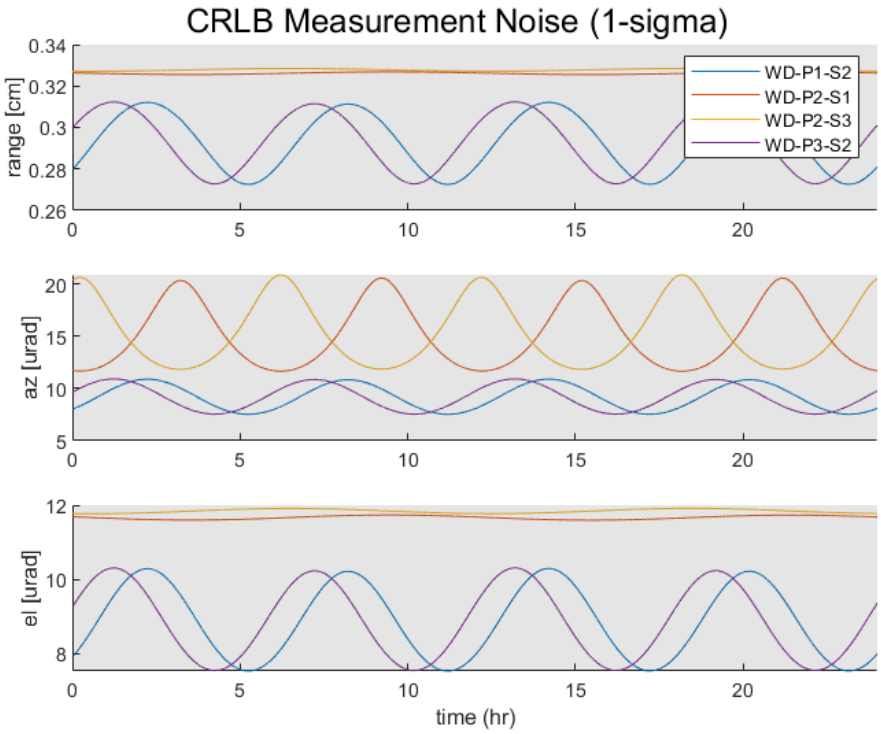


Figure 4-10: Measurement noise standard deviation values for all of the selected satellite links over the simulation duration.

Table 4.8: Measurement noise (1-sigma) model statistics for selected GPS satellites. Host satellite is WD-P2-S2.

| Partner Satellite | Min | RMS | Max |
|---|---|---|---|
| Range [cm] | | | |
| WD-P1-S2 | 0.273 | 0.293 | 0.312 |
| WD-P2-S1 | 0.326 | 0.326 | 0.327 |
| WD-P2-S3 | 0.327 | 0.328 | 0.328 |
| WD-P3-S2 | 0.273 | 0.294 | 0.312 |
| Azimuth ($\theta$) [$\mu$rad] | | | |
| WD-P1-S2 | 7.530 | 9.241 | 10.890 |
| WD-P2-S1 | 11.654 | 15.431 | 20.560 |
| WD-P2-S3 | 11.828 | 15.690 | 20.873 |
| WD-P3-S2 | 7.544 | 9.264 | 10.913 |
| Elevation ($\phi$) [$\mu$rad] | | | |
| WD-P1-S2 | 7.530 | 8.909 | 10.292 |
| WD-P2-S1 | 11.596 | 11.665 | 11.735 |
| WD-P2-S3 | 11.769 | 11.841 | 11.913 |
| WD-P3-S2 | 7.544 | 8.928 | 10.309 |

### 4.2.1 Process Noise: Perturbing Accelerations

The analysis of perturbing accelerations is shown in Table 4.9. They are graphed over time in Figure 4-11. The simulation duration is 24 hours, and the sampling period is 10 seconds. The Earth reference truth force model is the same as the LEO case. The spacecraft parameters are modeled based on estimates from available information: mass of about 3000 kg (average of the satellite wet and dry mass) and solar panel area of about 28.6 $m^2$ [140, 141]. We again assume that the panels are sun-pointed. With the the high altitude orbits, the effects of the higher order terms in the Earth's gravitational aspheric potential are significantly reduced. The dominant perturbation is the 2x0 term ($J_2$) and the next two dominant perturbations are the third body potentials from the Moon and the Sun. The low-order aspheric gravitational potential terms (12x12) follow, and then solar radiation pressure. Note that there is no drag outside of LEO, so the only non-gravitational force is solar radiation pressure. The process noise and preliminary CRLB results for the cross-

Table 4.9: MEO-MEO Perturbing Accelerations

| Acceleration | $a_{\text{rms}}$ ($m/s^2$) |
|---|---|
| Newtonian | 0.565 |
| $J_2$ | $5.74 \times 10^{-5}$ |
| TBP: Moon | $3.42 \times 10^{-6}$ |
| TBP: Sun | $1.38 \times 10^{-6}$ |
| 12 x 12 | $3.73 \times 10^{-7}$ |
| SRP | $4.15 \times 10^{-8}$ |
| Solid Tides | $1.32 \times 10^{-9}$ |
| Relativity | $2.83 \times 10^{-10}$ |
| Ocean Tides | $1.28 \times 10^{-10}$ |
| TBP: Planets | $1.36 \times 10^{-11}$ |
| 24 x 24 | $2.14 \times 10^{-14}$ |
| 70 x 70 | $3.22 \times 10^{-24}$ |

planar link are shown in Table 4.10. Given that the crosslinks are again continuous, the bias effect of SRP is expected to be minimal between measurements. Hence, we select the 12 x 12 and TBP-Sun-Moon gravitational force model for further analysis, which has similar (though slightly higher) expected position uncertainty for the cross-planar link as the LEO case. The expected velocity uncertainty is lower than the LEO

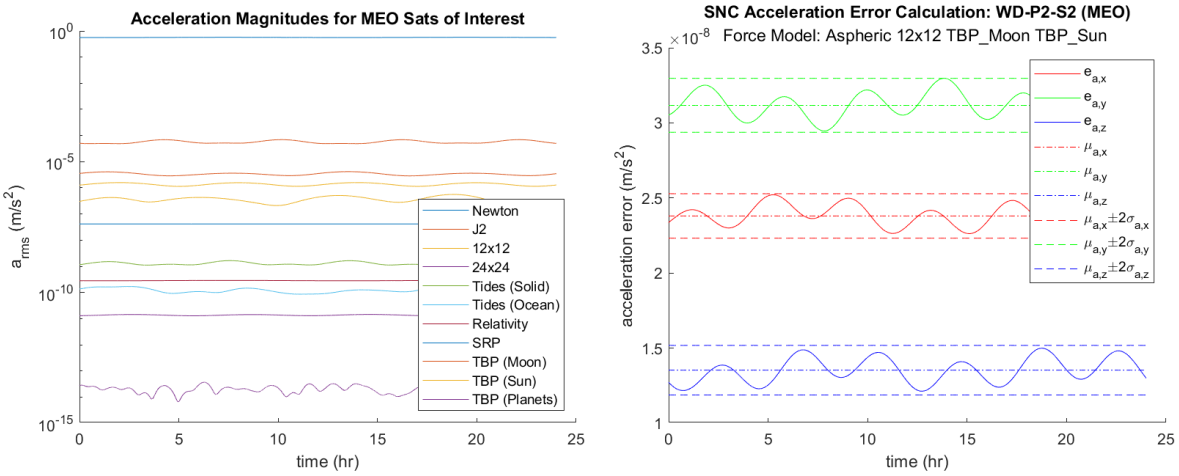


Figure 4-11: (a) RMS acceleration for both MEO satellites due to perturbations over the simulation period. (b) Acceleration error and statistics for host satellite using 12x12 and TBP gravity model.

case, which is a general trend for higher altitude orbits: higher position uncertainty and lower velocity uncertainty. Since it is a gravity-only model, this avoids needing the attitude and mass information for the partner satellites and the solar weather data. If the link has long outage periods (e.g., 30 min), SRP would be needed to accurately propagate the orbit between measurement intervals. For the co-orbital

Table 4.10: MEO Cross-Planar Link (Adjacent Planes) Process Noise Analysis.

| Force Model | WD-P2-S2 | | | | |
|---|---|---|---|---|---|
| | $\sigma_{a,p}$ (m/s$^2$) | $\lvert\frac{\mu_{a,p}}{\sigma_{a,p}}\rvert_{\max}$ | $\sigma_{r,\text{rms}}$ (m) | $\sigma_{v,\text{rms}}$ (mm/s) | $t_s$ (hr) |
| $J_2$ | $2.95 \times 10^{-6}$ | 0.22 | 17.25 | 2.35 | 7.75 |
| $J_2$ & TBP | $1.60 \times 10^{-7}$ | 1.01 | 6.12 | 0.85 | 8.63 |
| 12x12 & TBP | $8.24 \times 10^{-10}$ | 34.65 | 6.15 | 0.87 | 6.37 |
| 12x12 & TBP & SRP | $8.15 \times 10^{-10}$ | 0.03 | 6.15 | 0.87 | 6.37 |
| Force Model | WD-P3-S2 | | | | |
| | $\sigma_{a,p}$ (m/s$^2$) | $\lvert\frac{\mu_{a,p}}{\sigma_{a,p}}\rvert_{\max}$ | $\sigma_{r,\text{rms}}$ (m) | $\sigma_{v,\text{rms}}$ (mm/s) | $t_s$ (hr) |
| $J_2$ | $2.21 \times 10^{-6}$ | 0.22 | 21.47 | 3.19 | 7.75 |
| $J_2$ & TBP | $2.06 \times 10^{-7}$ | 0.84 | 6.23 | 0.93 | 8.63 |
| 12x12 & TBP | $8.10 \times 10^{-10}$ | 35.75 | 5.93 | 0.90 | 6.37 |
| 12x12 & TBP & SRP | $7.78 \times 10^{-10}$ | 0.06 | 5.93 | 0.90 | 6.37 |

link station keeping error, we used the relative RAAN requirement for the Galileo GNSS satellites of $\pm 2^\circ$ as a reference [142]. For a moderate offset of $0.667^\circ$ in RAAN,

the co-orbital case becomes observable with a reasonable CRLB position uncertainty of about 22 m; however, the CRLB uncertainty improves by about four times for the cross-planar link. The CRLB performance level for the single cross-planar link of about 6 m RMS is on par or better than state-of-the-art ground Doppler tracking or radar tracking. Adding the coplanar link slightly improves performance for the host and the cross-planar partner. The uncertainty on the coplanar partner is higher than either the host or cross-planar partner, which makes sense given that it has perfect station keeping so the coplanar partner is in a singular configuration relative to the host. Adding the other two partners to complete the four-way link again slightly improves the estimation performance for all satellites, however it is only about a 3 m and 0.5 mm/s difference compared to the single cross-planar link. As was the case for the LEO satellites, once a continuous link is established to a non-singular configuration partner, the estimation CRLB uncertainty is on par with state-of-the-art (SOA) radio ground tracking techniques, and additional partners only slightly improve performance (though they would be needed for a low-latency communications routing network).

Table 4.11: MEO Constellation Example CRLB Results using 12 x 12 + TBP gravity field model. The orbital elements are exactly as in Table 4.7, except for the station keeping error offset applied to the partner satellite for the co-orbital case.

| Satellite | $\sigma_r$ (m) | | | $\sigma_v$ (mm/s) | | |
|---|---|---|---|---|---|---|
| | Min | RMS | Max | Min | RMS | Max |
| Co-Orbital Link with moderate station keeping error $\delta\Omega = 0.667$deg: $t_s = 13.29$ hrs, $l^{99}_{CN(P)} = 11.08$ | | | | | | |
| WD-P2-S2 (Host) | 14.46 | 21.51 | 28.84 | 1.64 | 2.45 | 3.02 |
| WD-P2-S3 | 15.83 | 22.70 | 29.04 | 1.66 | 2.63 | 3.01 |
| | | Cross-Planar Link (Adjacent Planes): $t_s = 6.37$ hrs, $l^{99}_{CN(P)} = 10.11$ | | | | |
| WD-P2-S2 (Host) | 4.39 | 6.15 | 8.57 | 0.63 | 0.87 | 1.29 |
| WD-P3-S2 | 4.29 | 5.93 | 8.45 | 0.65 | 0.90 | 1.30 |
| | | Cross-Planar & Co-planar Link: $t_s = 5.33$ hrs, $l^{99}_{CN(P)} = 10.82$ | | | | |
| WD-P2-S2 (Host) | 3.92 | 5.69 | 9.58 | 0.56 | 0.80 | 1.22 |
| WD-P2-S3 | 7.78 | 10.97 | 17.93 | 1.12 | 1.60 | 2.36 |
| WD-P3-S2 | 4.15 | 5.76 | 9.48 | 0.58 | 0.87 | 1.42 |
| | | Four-Way Link: $t_s = 4.97$ hrs, $l^{99}_{CN(P)} = 10.90$ | | | | |
| WD-P2-S2 (Host) | 2.71 | 3.89 | 6.46 | 0.38 | 0.57 | 0.88 |
| WD-P1-S2 | 2.80 | 4.11 | 6.74 | 0.42 | 0.60 | 0.94 |
| WD-P2-S1 | 6.37 | 9.28 | 16.50 | 0.94 | 1.36 | 2.13 |
| WD-P2-S3 | 7.24 | 10.29 | 17.48 | 1.05 | 1.51 | 2.21 |
| WD-P3-S2 | 2.91 | 4.11 | 6.71 | 0.40 | 0.60 | 0.93 |

### 4.2.2 Monte Carlo Kalman Filtering Simulations

We run Monte Carlo EKF simulations with the cross-planar baseline case and the four-way link. The average estimation errors over time are shown in Figure 4-12 and 4-13. The Monte Carlo statistics are summarized in Table 4.12. The EKF performs similarly to the CRLB, and the NEES metrics are better optimized than for the LEO case (the rms process noise used is also lower since the model is more accurate). The RMS position and velocity errors for the host are 6.14 m and 0.91 mm/s for the cross-planar case, and they are slightly improved to 4.55 m and 0.74 mm/s for the

four-way link. This confirms the CRLB result that there are diminishing returns for navigation when adding link partners beyond what is needed for a continous-contact, non-singular configuration. Also, the EKF results confirm that even with the single cross-planar link, orbit determination performance is on-par or better than SOA radio tracking of MEO satellites (∼1-10 m, see Figure 1-1).

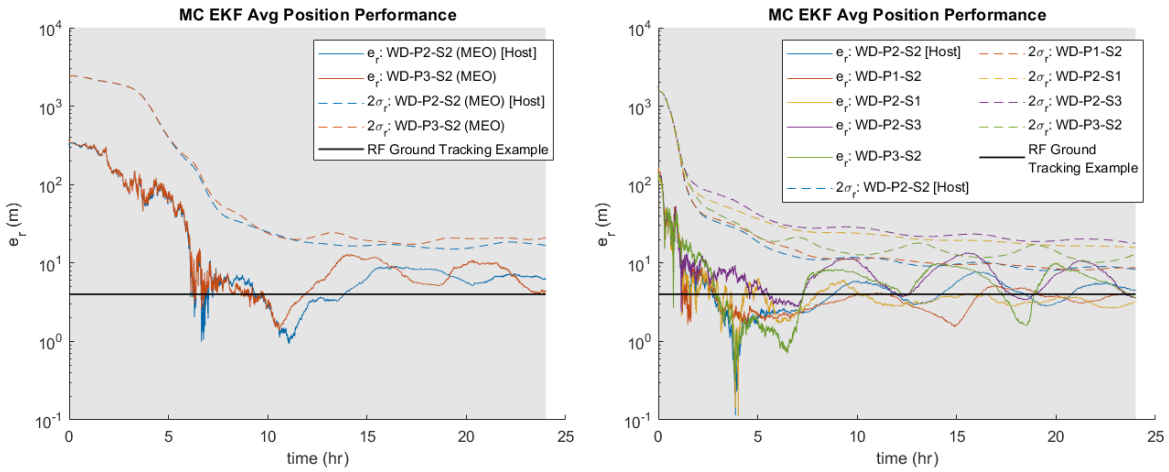


Figure 4-12: Average Monte Carlo (30 runs) position errors for selected GPS satellites for (a) Cross-Planar Link and (b) Four-Way Link. The RF ground tracking example error is 4 m, which is the orbit determination error of GPS satellites based on carrier phase measurements from a network of North American ground stations [20, 19].

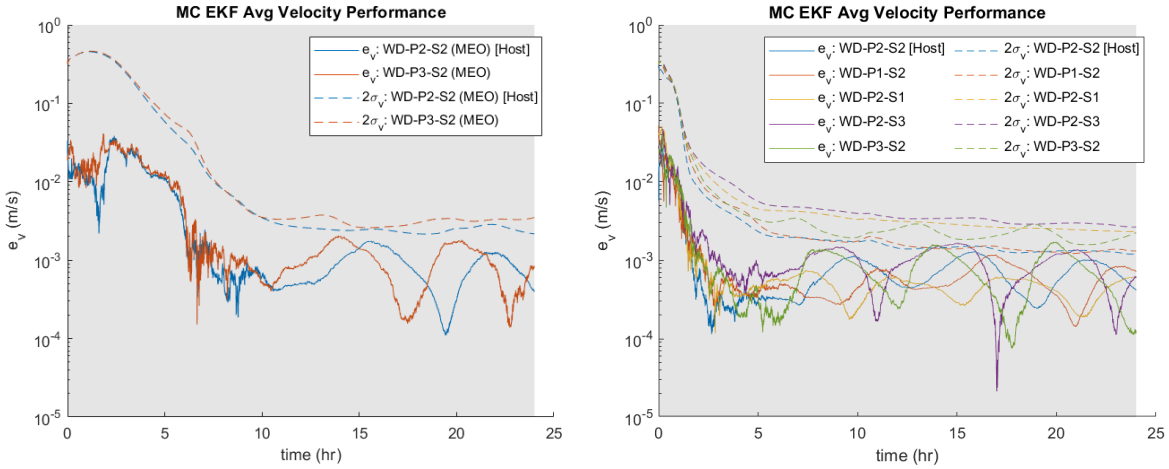


Figure 4-13: Average Monte Carlo (30 runs) velocity errors for selected GPS satellites for (a) Cross-Planar Link and (b) Four-Way Link.

Table 4.12: MEO constellation results for average of Monte Carlo (30 runs) EKF with 12 x 12 and TBP gravity field force model.

| Satellite | $e_r$ (m) | | | $e_v$ (mm/s) | | |
|---|---|---|---|---|---|---|
| | Min | RMS | Max | Min | RMS | Max |
| Cross-Planar Link: $t_s = 9.39$ hr, $l^{99}_{CN(P)} = 8.99$, Avg. NEES = 12.68 (99% Bds. [9.82, 14.43]), $\sigma_{q,\text{rms}} = 1.65 \times 10^{-6}$ m/s$^2$ | | | | | | |
| WD-P2-S2 (Host) | 0.93 | 6.14 | 9.16 | 0.11 | 0.91 | 1.75 |
| WD-P3-S2 | 1.38 | 7.75 | 12.98 | 0.14 | 1.08 | 2.05 |
| Four-Way Link: $t_s = 4.96$ hr, $l^{99}_{CN(P)} = 9.44$, Avg. NEES = 30.51 (99% Bds. [26.48, 33.77]), $\sigma_{q,\text{rms}} = 1.24 \times 10^{-6}$ m/s$^2$ | | | | | | |
| WD-P2-S2 (Host) | 1.70 | 4.55 | 7.74 | 0.24 | 0.74 | 1.30 |
| WD-P1-S2 | 1.53 | 3.44 | 5.26 | 0.14 | 0.60 | 1.18 |
| WD-P2-S1 | 1.71 | 3.50 | 6.45 | 0.17 | 0.48 | 0.75 |
| WD-P2-S3 | 2.74 | 7.63 | 13.56 | 0.02 | 1.01 | 1.67 |
| WD-P3-S2 | 0.70 | 6.34 | 10.06 | 0.08 | 0.88 | 1.72 |

## 4.3 Case Study: LunaNet Constellation

There is interest from NASA and ESA in developing a lunar communications network to support lunar ground and satellite operations by providing relay crosslinks around the Moon and (near-)continuous coverage of lunar surface regions of interest [143]. The network would enable rapid data relays between lunar assets and the Earth. Unlike an Earth constellation, which needs broad coverage of most of the central body, the lunar constellation is tailored for polar and far side regional coverage since those are the regions that would be of most interest for ground activities and low-altitude lunar orbiters. A notional LunaNet constellation configuration was presented by Schier of the NASA SCaN program [143], which we will use for our analysis. The initial orbit elements are in Table 4.13. The satellites in plane 1 provide coverage for the southern pole, the satellites in plane 2 provide coverage for the northern pole, and the satellites in plane 3 provide coverage of the equatorial region, including the far-side (the region facing away from the Earth). These satellites would also be able to network to the Gateway orbiter and other existing lunar relay satellites (e.g. LRO), though we do not consider these additional links here for simplicity, since they are unnecessary

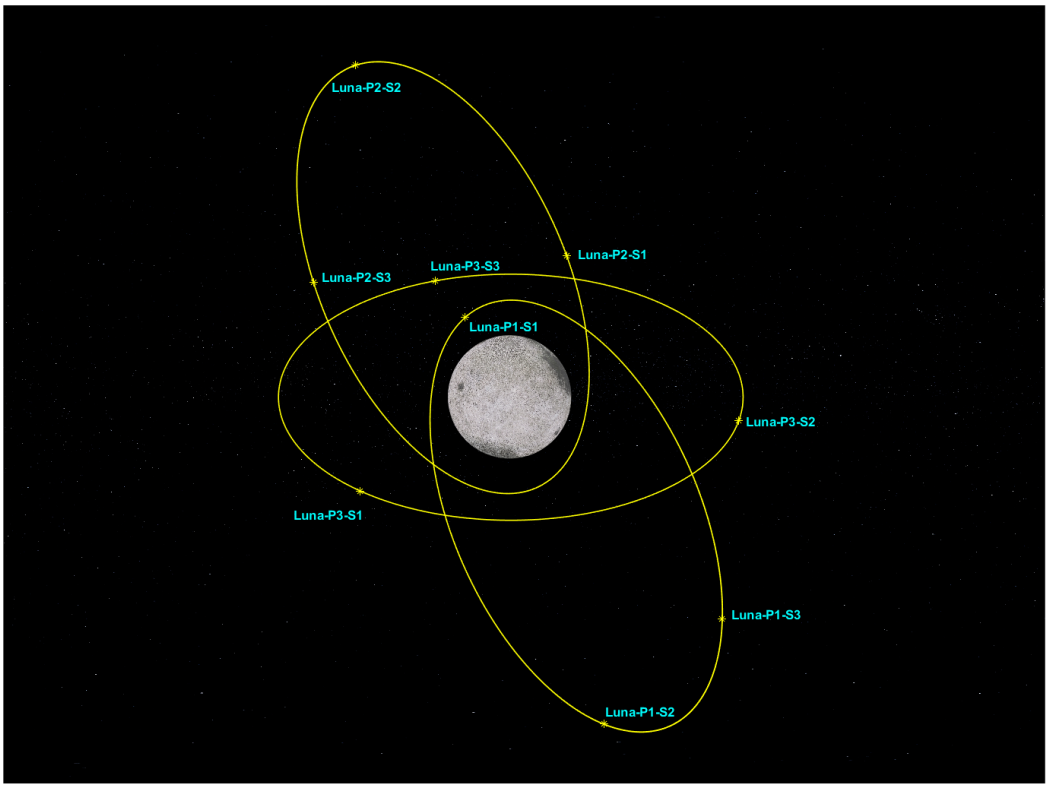


Figure 4-14: Notional LunaNet Constellation (proposed configuration [143] rendered using MATLAB R2023b in the local inertial frame)

for baseline OISL navigation performance. Due to the strong effects of the Earth third body potential perturbations and lunar central body aspheric perturbations at lower altitudes (less than about 750 km altitude), many lunar orbits are unstable [144, 145]. Therefore, the orbits must be selected from classes of stable orbits that do not require significant station keeping for orbit maintenance. The satellites in plane 1 and 2 are from a class of inclined, elliptical lunar frozen (ELF) orbits developed by JPL [144]. Note that for ELF orbits, the argument of perigee can only take values of 90° or 270°. The satellites in plane 3 are in a circular, equatorial orbit. Note that for our configuration, the satellites in plane 1 are taken directly from Ely et al. [144]. The satellites in plane 2 are derived directly from the satellites in plane 1 with a 180° offset to the argument of perigee and an additional offset to the mean anomaly to improve link access. Technically, the semi-major axes of the satellites in

plane 2 should be optimized with additional small offsets to the semi-major axes on the order of a few hundred meters to minimize station keeping requirements, but this is irrelevant for our short term simulations and beyond the scope of this work. For further details on semi-major axis optimization, see Ely et al. [146].

Table 4.13: LunaNet Constellation Initial Orbit Elements [143, 144]

| Satellite | $a$ (km) | $e$ | $i$ (deg) | $\Omega$ (deg) | $\omega_p$ (deg) | $M$ (deg) |
|---|---|---|---|---|---|---|
| Luna-P1-S1 (Host) | 6541.4 | 0.6 | 56.2 | 0 | 90 | 0 |
| Luna-P1-S2 | 6541.623 | 0.6 | 56.2 | 0 | 90 | 120 |
| Luna-P1-S3 | 6539.069 | 0.6 | 56.2 | 0 | 90 | 240 |
| Luna-P2-S1 | 6541.4 | 0.6 | 56.2 | 0 | 270 | 40 |
| Luna-P2-S2 | 6541.623 | 0.6 | 56.2 | 0 | 270 | 160 |
| Luna-P2-S3 | 6539.069 | 0.6 | 56.2 | 0 | 270 | 280 |
| Luna-P3-S1 | 6541.4 | 0.006 | 0 | 0 | 90 | 80 |
| Luna-P3-S2 | 6541.4 | 0.006 | 0 | 0 | 90 | 200 |
| Luna-P3-S3 | 6541.4 | 0.006 | 0 | 0 | 90 | 320 |

The launch costs to deep space are significantly higher than to Earth orbit, so the constellation must have a limited number of satellites. The proposal for this constellation is to initially only include two satellites per ELF orbit and one satellite in the equatorial orbit for partial coverage [143]. Then, the constellation can be further developed over time with an additional satellite in each of the ELF orbits and two additional satellites in the equatorial orbit to provide continous coverage. These additional satellites also enable coplanar crosslink relays, which would significantly reduce data routing latency through the constellation. The required maximum design range to support the four-way link configuration is 15785 km, which we round up to 16000 km for the terminal maximum range requirement design parameter. The corresponding measurement noise is is presented in Table 4.14. The ranging noise is slightly better than the MEO link case due to the smaller time of flight. The maximum azimuth errors are higher than the Earth orbit cases.

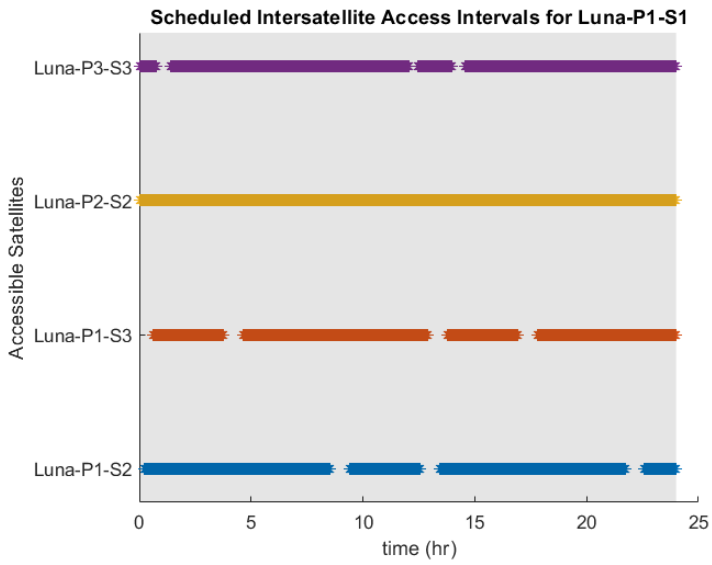


Figure 4-15: Link access for selected satellites with sun keep-out constraint of 10 degrees, maximum range of 16,000 km, and maximum slew rate of 1 deg/sec.

Table 4.14: LunaNet Measurement Noise (1-sigma). Host satellite is Luna-P1-S1.

| Partner Satellite | Min | RMS | Max |
|---|---|---|---|
| Range [cm] | | | |
| P1-S2 | 0.136 | 0.160 | 0.187 |
| P1-S3 | 0.136 | 0.161 | 0.187 |
| P2-S2 | 0.149 | 0.190 | 0.219 |
| P3-S3 | 0.091 | 0.155 | 0.172 |
| Azimuth ($\theta$) [$\mu$rad] | | | |
| P1-S2 | 5.73 | 8.79 | 14.04 |
| P1-S3 | 5.73 | 8.49 | 14.02 |
| P2-S2 | 10.28 | 15.24 | 21.04 |
| P3-S3 | 5.53 | 22.33 | 66.00 |
| Elevation ($\phi$) [$\mu$rad] | | | |
| P1-S2 | 5.73 | 6.57 | 7.99 |
| P1-S3 | 5.73 | 6.62 | 7.97 |
| P2-S2 | 5.99 | 8.79 | 11.73 |
| P3-S3 | 5.47 | 6.37 | 6.95 |

### 4.3.1 Process Noise: Perturbing Accelerations

For this analysis, the satellites in the ELF orbits and the equatorial orbits will have somewhat different perturbing accelerations due to the difference in eccentricity and inclination. The analysis of perturbing accelerations is shown in Table 4.15. Note that

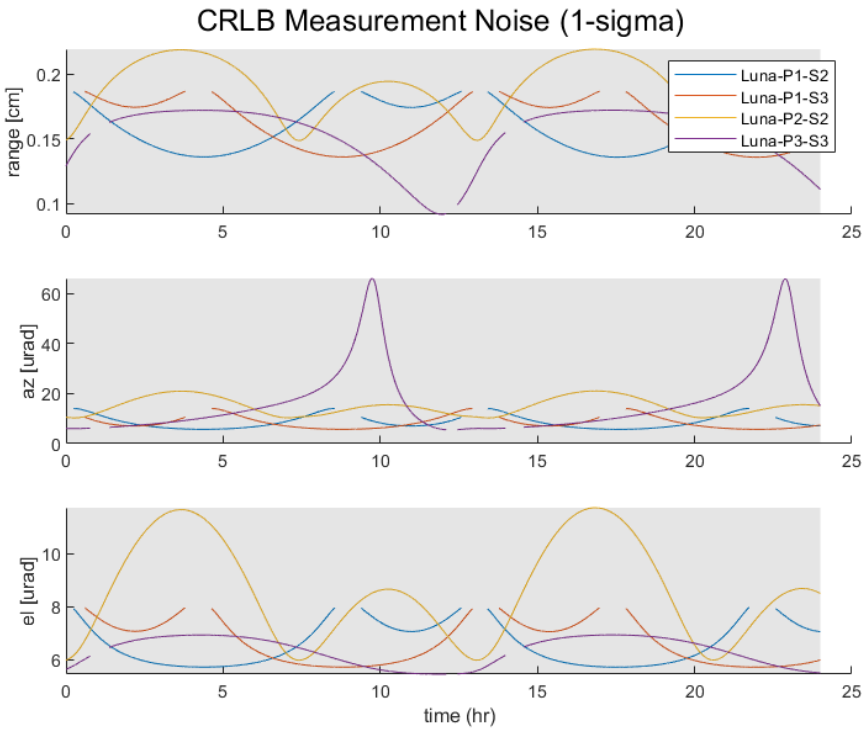


Figure 4-16: Measurement noise standard deviation values for all of the selected satellite links over the simulation duration.

the perturbations are ordered by the P1 and P2 case magnitudes. They are plotted over time in Figure 4-17. The simulation settings and measurement constraints are the same as the MEO case. The Moon's gravity model is based on the AIUB-GRL350B coefficients [94]. The satellite masses and solar panel areas are modeled based on available information for the Lunar Reconnaisance Orbiter (LRO): 1398 kg (average of the satellite wet and dry mass) and 7.35 $m^2$ [147]. The solar panels are assumed sun-pointing, which maximizes the effect of SRP. The dominant perturbing effect for both types of orbits is the third body potential perturbation from the Earth. The low-order (up to 12 x 12) central body aspheric perturbations are next, which are reduced for the equatorial orbit by about an order of magnitude. This is followed by the third-body perturbing potential from the sun for both types of orbits. The ELF orbits are much more strongly affected by higher order central body aspheric potential effects (24 x 24) than the equatorial orbit due to the relatively low perilune altitude of the ELF orbits. This is why the aspheric accelerations periodically spike for the

ELF orbits in Figure 4-17 (a). Hence, solar radiation pressure follows 24 x 24 for ELF and it follows TBP-sun for equatorial. Due to the fairly high average altitudes of both types of orbits, the high order central body aspheric perturbations (higher than 24 x 24) have only a small effect, whereas they have relatively strong effects for low altitude orbits. This is due to the relatively large asymmetries in the Moon's mass distribution, so low altitude orbiters need a full order gravity field potentials to accurately describe the orbit [145]. We analyzed errors for four different force

Table 4.15: LunaNet Perturbing Accelerations (ordered by P1 and P2).

| Acceleration | $a_{\text{rms}}$ (m/s$^2$) | |
|---|---|---|
| | P1 & P2 | P3 |
| Newtonian | 0.214 | 0.115 |
| TBP: Earth | $8.26 \times 10^{-5}$ | $8.17 \times 10^{-5}$ |
| $J_2$ | $2.59 \times 10^{-5}$ | $2.46 \times 10^{-6}$ |
| 12 x 12 | $1.06 \times 10^{-5}$ | $1.44 \times 10^{-6}$ |
| TBP: Sun | $4.03 \times 10^{-7}$ | $3.97 \times 10^{-7}$ |
| 24 x 24 | $5.58 \times 10^{-8}$ | $6.30 \times 10^{-13}$ |
| SRP | $2.36 \times 10^{-8}$ | $2.24 \times 10^{-8}$ |
| 70 x 70 | $4.86 \times 10^{-10}$ | $7.48 \times 10^{-19}$ |
| TBP: Planets | $3.76 \times 10^{-12}$ | $3.35 \times 10^{-12}$ |
| 100 x 100 | $4.26 \times 10^{-18}$ | $\approx 0$ |

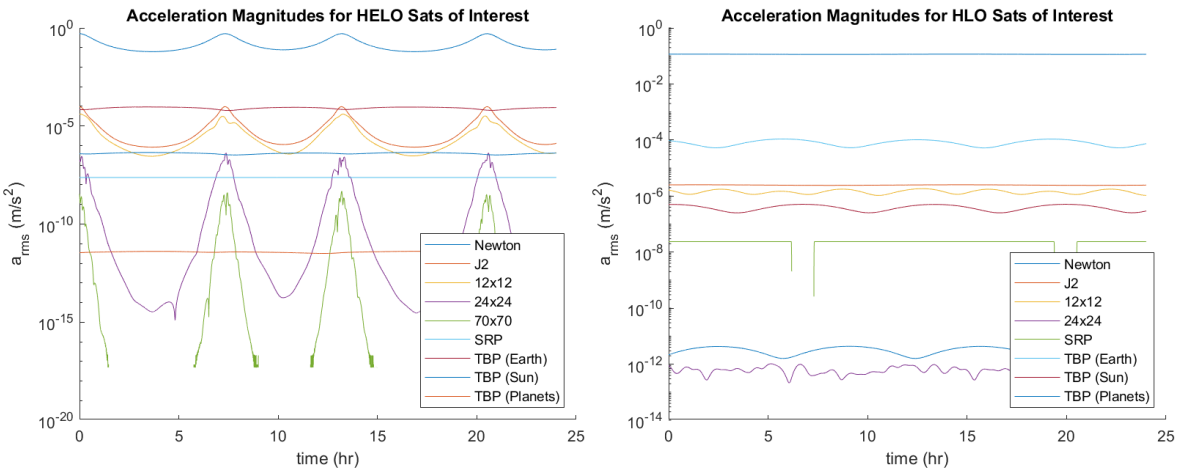


Figure 4-17: RMS acceleration for (a) ELF satellites (P1-S1 & P2-S2) and (b) equatorial satellites (P3-S3) due to perturbations over simulation period.

models for both types of orbits. The CRLB predictions for cases are all on-par or

somewhat better than the LEO and MEO cases we have analyzed in Sections 4.1 and 4.2. The highest accuracy model achieved sub-meter CRLB predictions. We choose the 12 x 12 and TBP-Earth-Sun model to further analyze with the EKF since it has high CRLB accuracy predictions, and it is a purely gravitational model. The co-

Table 4.16: LunaNet Process Noise Analysis. The CRLB configuration is P1-S1 (Host), P2-S2, & P3-S3.

| Force Model | P1-S1 | | | | |
|---|---|---|---|---|---|
| | $\sigma_{a,p}$ (m/s$^2$) | $\lvert\frac{\mu_{a,p}}{\sigma_{a,p}}\rvert_{\max}$ | $\sigma_{r,\text{rms}}$ (m) | $\sigma_{v,\text{rms}}$ (mm/s) | $t_s$ (hr) |
| J2 & TBP-Earth | $6.83 \times 10^{-6}$ | 0.18 | 9.35 | 1.92 | 6.54 |
| 12 x 12 & TBP-Earth | $1.59 \times 10^{-7}$ | 1.67 | 1.38 | 0.17 | 10.18 |
| 12 x 12 & TBP-Earth-Sun | $2.68 \times 10^{-8}$ | 0.79 | 0.98 | 0.12 | 9.11 |
| 24 x 24, TBP-Earth-Sun, & SRP | $2.96 \times 10^{-10}$ | 0.05 | 0.60 | 0.07 | 9.47 |
| Force Model | P2-S2 | | | | |
| | $\sigma_{a,p}$ (m/s$^2$) | $\lvert\frac{\mu_{a,p}}{\sigma_{a,p}}\rvert_{\max}$ | $\sigma_{r,\text{rms}}$ (m) | $\sigma_{v,\text{rms}}$ (mm/s) | $t_s$ (hr) |
| J2 & TBP-Earth | $5.38 \times 10^{-6}$ | 0.22 | 10.91 | 2.42 | 6.54 |
| 12 x 12 & TBP-Earth | $1.66 \times 10^{-7}$ | 1.33 | 2.26 | 0.28 | 10.18 |
| 12 x 12 & TBP-Earth-Sun | $3.91 \times 10^{-8}$ | 0.59 | 2.07 | 0.24 | 9.11 |
| 24 x 24, TBP-Earth-Sun, & SRP | $3.15 \times 10^{-10}$ | 0.09 | 0.88 | 0.10 | 9.47 |
| Force Model | P3-S3 | | | | |
| | $\sigma_{a,p}$ (m/s$^2$) | $\lvert\frac{\mu_{a,p}}{\sigma_{a,p}}\rvert_{\max}$ | $\sigma_{r,\text{rms}}$ (m) | $\sigma_{v,\text{rms}}$ (mm/s) | $t_s$ (hr) |
| J2 & TBP-Earth | $8.42 \times 10^{-7}$ | 0.18 | 8.94 | 1.31 | 6.54 |
| 12 x 12 & TBP-Earth | $2.26 \times 10^{-7}$ | 0.20 | 1.60 | 0.23 | 10.18 |
| 12 x 12 & TBP-Earth-Sun | $3.97 \times 10^{-9}$ | 3.11 | 1.02 | 0.13 | 9.11 |
| 24 x 24, TBP-Earth-Sun, & SRP | $3.08 \times 10^{-12}$ | 0.05 | 0.52 | 0.07 | 9.47 |

planar (ELF-to-ELF) link case is observable because there is already an offset in the semi-major axes of the two spacecraft built into the constellation design. The cross-planar link cases have slightly better performance because they are further from the singular configuration. There are two-cross planar link cases: between planes 1 and 2 (ELF-to-ELF) and between planes 1 (or 2) and 3 (ELF-to-Equatorial). The predicted CRLB RMS uncertainties for the ELF-to-Equatorial case are about half that for the ELF-to-ELF case. Including both link partners gives slightly better performance than

either of the solo-links. And the four way case is again marginally better. This further supports the running trend of diminishing returns for additional link partners beyond the baseline single-partner cases. The CRLB predictions are somewhat lower than for either the LEO or MEO cases, though they are the same order of magnitude. All of the predicted CRLB uncertainties are better than SOA DSN tracking capabilities [12].

Table 4.17: LunaNet Constellation Example Results using 12 x 12 and TBP gravity field model.

| Satellite | $\sigma_r$ (m) | | | $\sigma_v$ (mm/s) | | |
|---|---|---|---|---|---|---|
| | Min | RMS | Max | Min | RMS | Max |
| Co-Planar Link (ELF-to-ELF): $t_s = 12.32$ hrs, $l^{99}_{CN(P)} = 9.13$ | | | | | | |
| Luna-P1-S1 | 0.69 | 3.74 | 5.19 | 0.14 | 0.45 | 1.22 |
| Luna-P1-S2 | 0.58 | 3.81 | 5.42 | 0.15 | 0.43 | 1.04 |
| Cross-Planar Link (ELF-to-ELF): $t_s = 9.89$ hrs, $l^{99}_{CN(P)} = 8.70$ | | | | | | |
| Luna-P1-S1 (Host) | 0.52 | 3.05 | 5.77 | 0.14 | 0.39 | 1.16 |
| Luna-P2-S2 | 0.44 | 2.69 | 3.71 | 0.13 | 0.36 | 0.97 |
| Cross-Planar Link (ELF-to-Equatorial): $t_s = 9.39$ hrs, $l^{99}_{CN(P)} = 8.12$ | | | | | | |
| Luna-P1-S1 (Host) | 0.41 | 1.22 | 1.79 | 0.07 | 0.15 | 0.33 |
| Luna-P3-S3 | 1.02 | 1.21 | 1.72 | 0.13 | 0.16 | 0.22 |
| Two-Way Link: $t_s = 8.48$ hrs, $l^{99}_{CN(P)} = 9.11$ | | | | | | |
| Luna-P1-S1 (Host) | 0.31 | 0.98 | 1.39 | 0.06 | 0.12 | 0.29 |
| Luna-P2-S2 | 0.40 | 2.07 | 2.90 | 0.12 | 0.24 | 0.64 |
| Luna-P3-S3 | 0.84 | 1.02 | 1.38 | 0.11 | 0.13 | 0.19 |
| Four-Way Link: $t_s = 9.05$ hrs, $l^{99}_{CN(P)} = 8.52$ | | | | | | |
| Luna-P1-S1 (Host) | 0.25 | 0.78 | 1.18 | 0.05 | 0.09 | 0.24 |
| Luna-P1-S2 | 0.27 | 1.35 | 1.94 | 0.09 | 0.19 | 0.62 |
| Luna-P1-S3 | 0.35 | 1.38 | 1.98 | 0.09 | 0.16 | 0.41 |
| Luna-P2-S2 | 0.37 | 2.01 | 2.86 | 0.11 | 0.23 | 0.63 |
| Luna-P3-S3 | 0.68 | 0.85 | 1.23 | 0.09 | 0.11 | 0.16 |

### 4.3.2 Monte Carlo Kalman Filtering Simulations

We ran a Monte Carlo simulation for the lowest and highest uncertainty CRLB cases: the four-way link and the single ELF-to-ELF link. The results are shown in Figures 4-18 and 4-19, and the performance statistics are summarized in Table 4.18. The Monte Carlo rms errors are slightly higher than the predicted CRLB uncertainties, although the NEES metrics are a bit high (the filter is overly-optimistic on average), which is due to the periodic spikes in the force model error at the ELF perilune points.

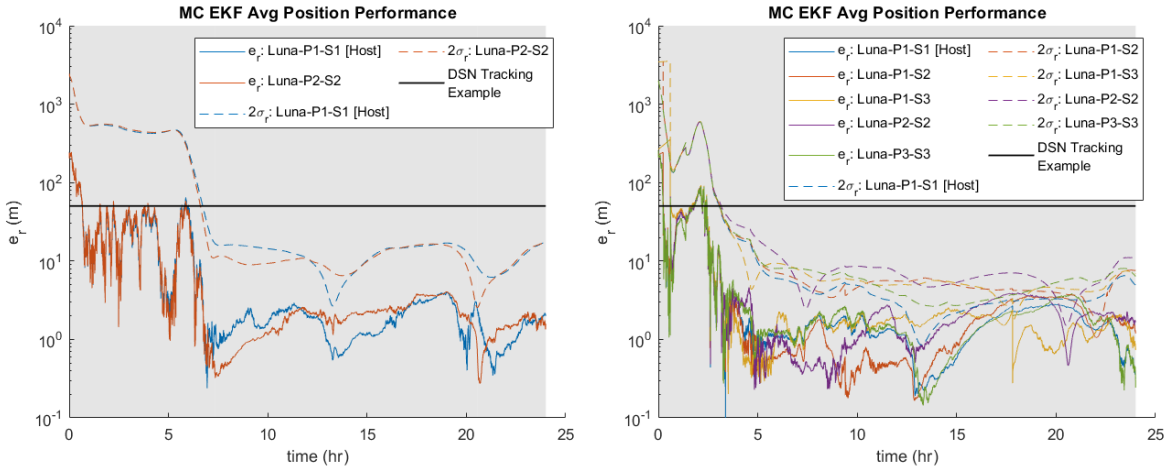


Figure 4-18: Average Monte Carlo (30 runs) EKF position errors for selected LunaNet satellites with 12 x 12 + TBP gravity model for (a) Cross-Planar Link (ELF-to-ELF) and (b) Four-Way Link. The DSN ground tracking example error is 50.3 m, which is the simulated orbit determination error of an equatorial 100 km altitude circular Lunar orbit using 9 DSN ground stations [31].

Overall, the EKF MC simulations confirm the CRLB result that there are diminishing returns for navigation when adding link partners beyond what is needed for a continous-contact, non-singular configuration. Also, the EKF results confirm that even with the single cross-planar link, orbit determination performance is better than SOA radio ground tracking via the DSN (∼1-1000 m, see Figure 1-1).

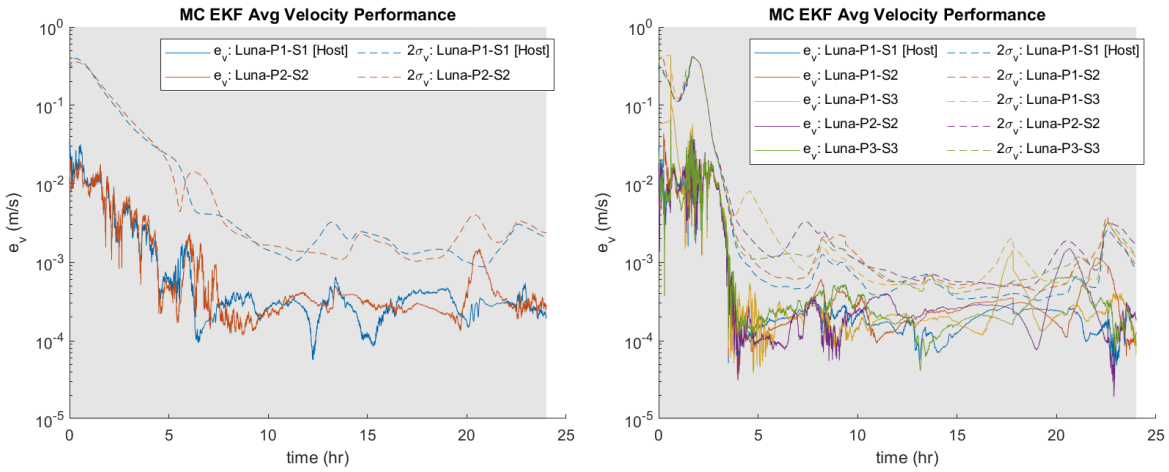


Figure 4-19: Average Monte Carlo (30 runs) velocity errors with 12 x 12 + TBP gravity model for (a) Cross-Planar Link (ELF-to-ELF) and (b) Four-Way Link.

Table 4.18: LunaNet constellation results for average of Monte Carlo (30 runs) EKF with 12 x 12 + TBP gravity model.

| Satellite | $e_r$ (m) | | | $e_v$ (mm/s) | | |
|---|---|---|---|---|---|---|
| | Min | RMS | Max | Min | RMS | Max |
| Cross-Planar Link (ELF-to-ELF): $t_s = 10.92$ hr, $l^{99}_{CN(P)} = 10.03$, Avg. NEES = 43.81 (99% Bds. [9.82, 14.43]), $\sigma_{q,\text{rms}} = 2.51 \times 10^{-6}$ m/s$^2$ | | | | | | |
| Luna-P1-S1 (Host) | 0.35 | 2.00 | 4.05 | 0.06 | 0.31 | 0.66 |
| Luna-P2-S2 | 0.27 | 2.34 | 4.09 | 0.13 | 0.42 | 1.49 |
| Four-Way Link: $t_s = 10.71$ hr, $l^{99}_{CN(P)} = 9.81$, Avg. NEES = 37.54 (99% Bds. [26.48, 33.77]), $\sigma_{q,\text{rms}} = 2.40 \times 10^{-6}$ m/s$^2$ | | | | | | |
| Luna-P1-S1 (Host) | 0.19 | 1.68 | 2.83 | 0.05 | 0.19 | 0.31 |
| Luna-P1-S2 | 0.17 | 2.12 | 3.61 | 0.06 | 0.38 | 1.13 |
| Luna-P1-S3 | 0.28 | 1.65 | 2.54 | 0.07 | 0.33 | 1.41 |
| Luna-P2-S2 | 0.47 | 2.39 | 3.93 | 0.02 | 0.45 | 1.49 |
| Luna-P3-S3 | 0.14 | 1.88 | 3.86 | 0.04 | 0.31 | 0.68 |

## 4.4 Case Study: MarsNet Constellation

Although the current NASA focus is lunar missions, there has also been interest in establishing a constellation around Mars for networking among assets [148, 149]. The existing Mars Relay Network consists of five different orbiters: MRO, MAVEN, MO, MEX, and TGO [68]. An analysis of the theoretical OISL navigation performance

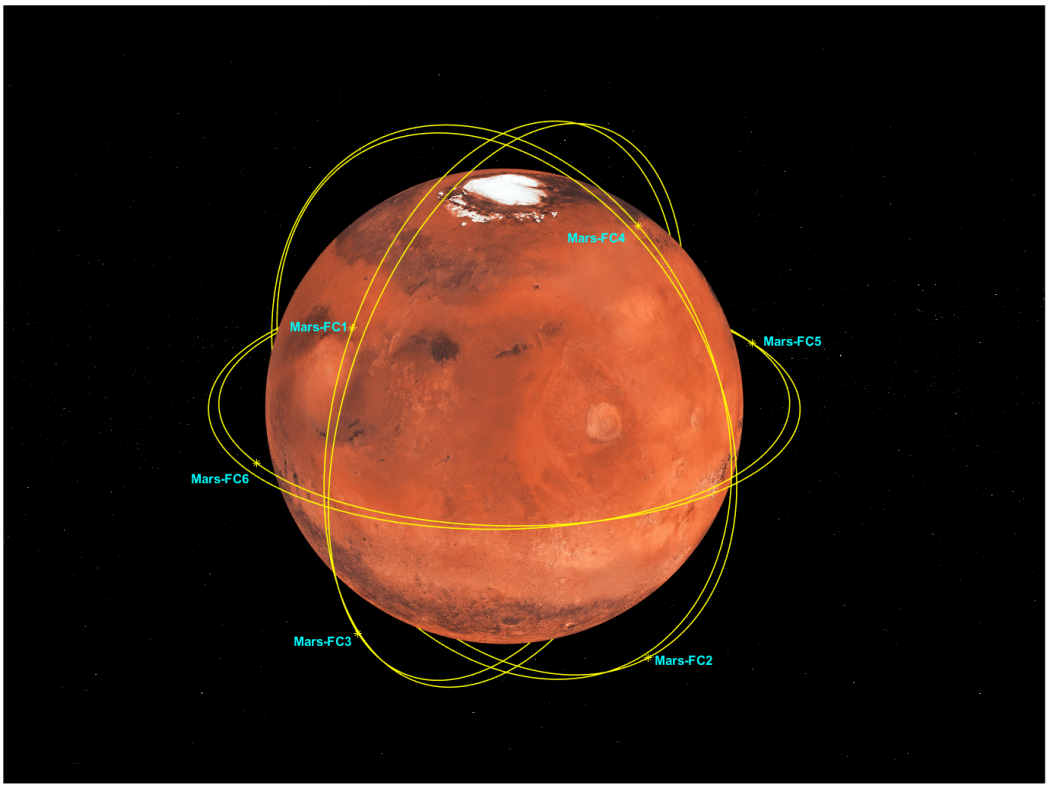


Figure 4-20: MarsNet Scenario (proposed FC-MARS-doubleR configuration [150] rendered using MATLAB R2023b in the local inertial frame)

if these orbiters were replaced with satellites equipped with lasercom terminals was conducted by Dave [68], which showed that the achievable performance was on-par with or better than DSN tracking. For this study, we are interested in a future Mars Network (MarsNet) of new satellites in a constellation that is purpose built for (near-)continuous coverage of the Martian regions of interest, which are the equatorial and polar regions [148, 150, 149]. Once again, the number of satellites in the constellation is relatively small to minimize its development cost. Several constellation designs were proposed by Bell et al., with one called "4retro111" (consisting of 6 satellites in retrograde orbits) being the suggested constellation design with the best coverage [148]. De'Sanctis et al. proposed several flower constellation designs and showed that they offer better coverage than the 4retro111 design [150]. We use their recommended constellation design called "FC-MARS-doubleR". The initial orbit elements are in

Table 4.19. Each satellite is in its own orbital plane, so the intersatellite connectivity is not optimal since there are no coplanar links. Presumably the constellation would

Table 4.19: MarsNet Constellation Initial Orbit Elements [150]

| Satellite | $a$ (km) | $e$ | $i$ (deg) | $\Omega$ (deg) | $\omega_p$ (deg) | $M$ (deg) |
|---|---|---|---|---|---|---|
| Mars-FC1 (Host) | 4130 | 0.017 | 88.1 | 342 | 313.7 | 128.495 |
| Mars-FC2 | 4130 | 0.017 | 88.1 | 72 | 313.7 | 218.184 |
| Mars-FC3 | 4130 | 0.017 | 88.1 | 162 | 313.7 | 307.564 |
| Mars-FC4 | 4130 | 0.017 | 88.1 | 252 | 313.7 | 37.786 |
| Mars-FC5 | 4130 | 0.018 | 0.7 | 235.1 | 49.2 | 331.795 |
| Mars-FC6 | 4130 | 0.018 | 0.7 | 55.1 | 49.2 | 331.795 |

be further built out for low-latency as the needed in the future, but we will analyze the baseline constellation design since that is more realistically achievable in the near-term. The first four satellites (FC1 to FC4) are in polar orbits for coverage of the north and south poles. The other two satellites (FC5 & FC6) are are in equatorial orbits for equatorial coverage. All of the orbits are at a relatively low altitude and are circular. There are spikes in the azimuth errors for Mars-FC3; this is due to

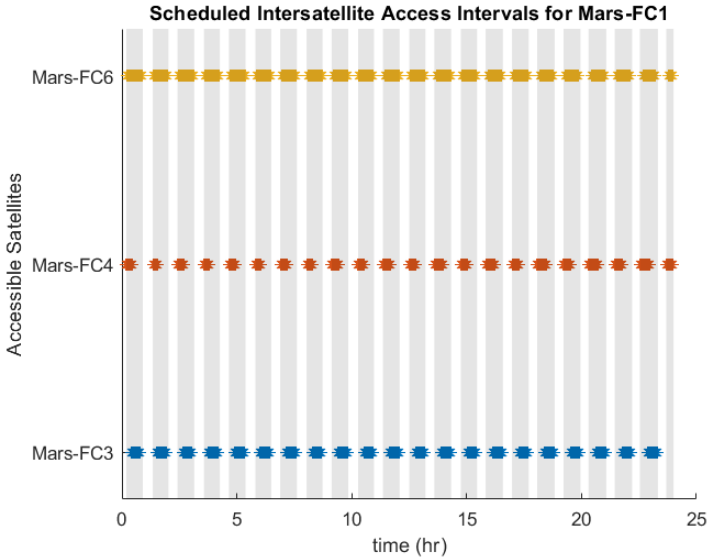


Figure 4-21: Link access for selected satellites with sun keep-out constraint of 10 degrees, maximum range of 16000 km, and maximum slew rate of 1 deg/sec.

the two satellites flying by each other with opposing velocities, which exaggerates the angular errors due to the high relative velocities. The same effect impacts the azimuth

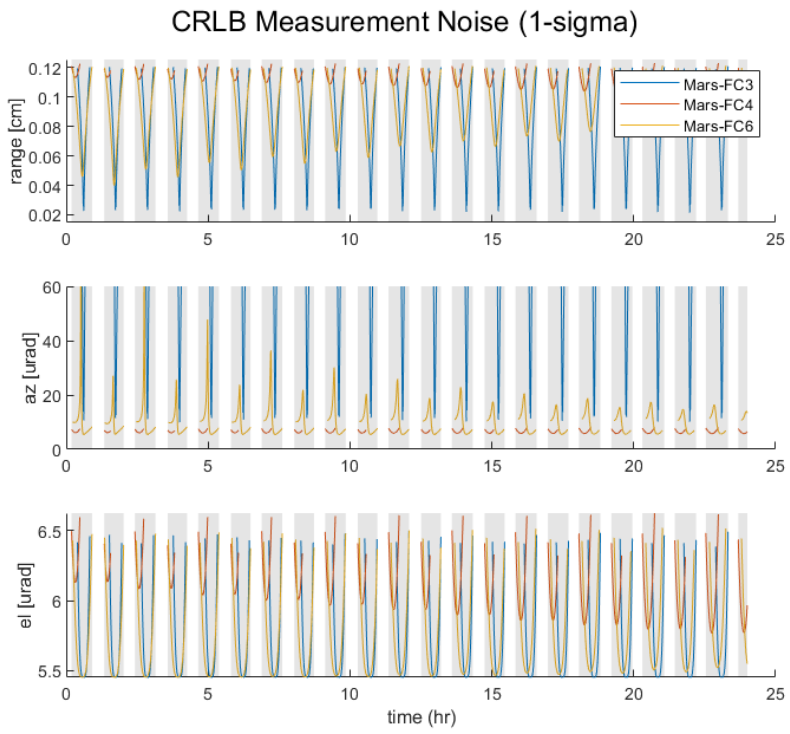


Figure 4-22: Measurement noise standard deviation values for all of the selected satellite links over the simulation duration.

errors for Mars-FC6, since the two satellites fly by each other with roughly orthogonal velocities. The link durations are limited in part by the maximum 1 deg/sec slew rate due to this as well.

Table 4.20: MarsNet Measurement Noise (1-sigma). Host satellite is Mars-FC1.

| Partner Satellite | Min | RMS | Max |
|---|---|---|---|
| Range [cm] | | | |
| Mars-FC3 | 0.022 | 0.086 | 0.121 |
| Mars-FC4 | 0.102 | 0.112 | 0.123 |
| Mars-FC6 | 0.040 | 0.093 | 0.121 |
| Azimuth ($\theta$) [$\mu$rad] | | | |
| Mars-FC3 | 9.96 | 230.05 | 913.02 |
| Mars-FC4 | 5.77 | 6.51 | 7.98 |
| Mars-FC6 | 5.45 | 12.24 | 199.32 |
| Elevation ($\phi$) [$\mu$rad] | | | |
| Mars-FC3 | 5.45 | 5.69 | 6.50 |
| Mars-FC4 | 5.45 | 5.74 | 6.52 |
| Mars-FC6 | 5.45 | 5.74 | 6.52 |

### 4.4.1 Process Noise: Perturbing Accelerations

The analysis of perturbing accelerations is shown in Table 4.21. They are graphed over time in Figure 4-23. The simulation settings and measurement constraints are the same as the Lunar case. The Mars gravity model is based on the GGM1025A coefficients, and the truth reference model has a maximum degree/order of 80. The satellite parameters are based on available information for the Mars Reconnaissance Orbiter (MRO): 1606 kg mass (average of the satellite wet and dry mass) and 12 $m^2$ solar panel area [151]. Again, the solar panels are assumed to be continuously sun pointing. Given that these orbits are fairly low altitude, the dominant perturbations are from the aspheric central body gravitational potential terms up to maximum order. This is similar to the LEO case without drag. Note that for the perturbation degrees studied, each set of included terms has an RMS acceleration of about one order of magnitude less than the previous set. The third body potential perturbations from the Sun follow the highest order aspheric potential terms, followed by the solar radiation pressure effect. The third body potential perturbations from other planets are effectively negligible.

Table 4.21: MarsNet Perturbing Accelerations

| Acceleration | $a_{\text{rms}}$ ($m/s^2$) |
|---|---|
| Newtonian | 2.51 |
| $J_2$ | $6.40 \times 10^{-3}$ |
| 12 x 12 | $7.82 \times 10^{-4}$ |
| 24 x 24 | $2.30 \times 10^{-5}$ |
| 80 x 80 | $2.70 \times 10^{-6}$ |
| TBP: Sun | $6.54 \times 10^{-8}$ |
| SRP | $1.31 \times 10^{-8}$ |
| TBP: Planets | $1.50 \times 10^{-12}$ |

We again selected four force models for process noise analysis. The high accuracy models have sub-meter prediced CRLB performance, which is about an order of magnitude better than the lower accuracy models. We selected the lower accuracy 24 x 24 model for further analysis (as in the LEO case) since it is a purely gravitational model that is fairly inexpensive to evaluate. Like the lunar constellation, there are two dif-

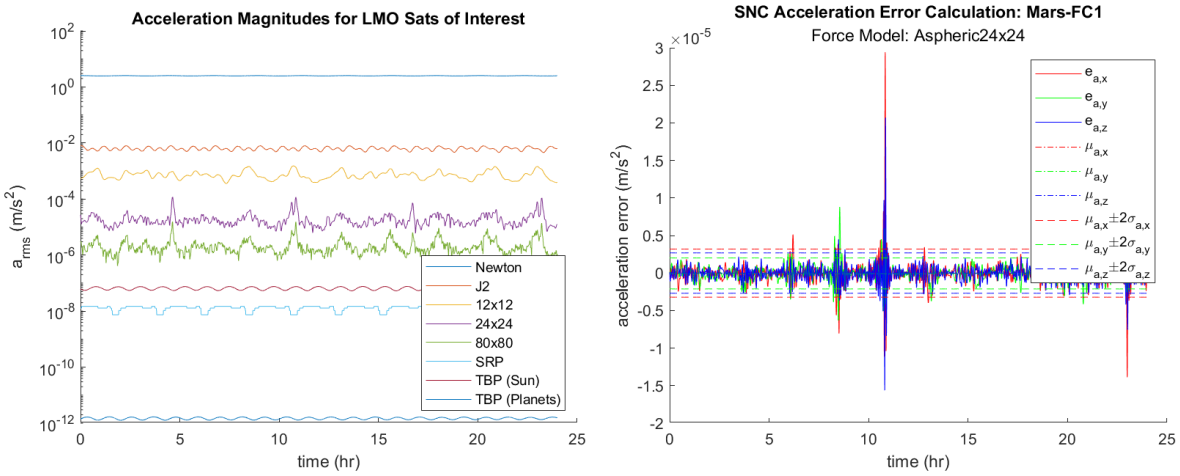


Figure 4-23: (a) RMS acceleration for MarsNet satellites due to perturbations over simulation period. (b) Acceleration error and statistics for host satellite using 24 x 24 gravity model.

Table 4.22: MarsNet Process Noise Analysis. CRLB configuration is Mars-FC1 (host), Mars-FC4, & Mars-FC6.

| Force Model | Mars-FC1 | | | | |
|---|---|---|---|---|---|
| | $\sigma_{a,p}$ (m/s$^2$) | $\lvert\frac{\mu_{a,p}}{\sigma_{a,p}}\rvert_{\max}$ | $\sigma_{r,\text{rms}}$ (m) | $\sigma_{v,\text{rms}}$ (mm/s) | $t_s$ (hr) |
| 12 x 12 | $1.34 \times 10^{-5}$ | 0.04 | 14.68 | 19.61 | 6.33 |
| 24 x 24 | $1.35 \times 10^{-6}$ | 0.05 | 2.83 | 2.93 | 6.47 |
| 80 x 80 & TBP-Sun | $3.22 \times 10^{-9}$ | 2.22 | 0.38 | 0.30 | 4.16 |
| 80 x 80, TBP-Sun, & SRP | $4.98 \times 10^{-10}$ | 0.04 | 0.09 | 0.07 | 9.29 |
| Force Model | Mars-FC4 | | | | |
| | $\sigma_{a,p}$ (m/s$^2$) | $\lvert\frac{\mu_{a,p}}{\sigma_{a,p}}\rvert_{\max}$ | $\sigma_{r,\text{rms}}$ (m) | $\sigma_{v,\text{rms}}$ (mm/s) | $t_s$ (hr) |
| 12 x 12 | $1.36 \times 10^{-5}$ | 0.05 | 20.78 | 23.71 | 6.33 |
| 24 x 24 | $1.42 \times 10^{-6}$ | 0.05 | 3.87 | 3.77 | 6.47 |
| 80 x 80 & TBP-Sun | $3.39 \times 10^{-9}$ | 2.17 | 0.39 | 0.30 | 4.16 |
| 80 x 80, TBP-Sun, & SRP | $5.03 \times 10^{-10}$ | 0.03 | 0.09 | 0.07 | 9.29 |
| Force Model | Mars-FC6 | | | | |
| | $\sigma_{a,p}$ (m/s$^2$) | $\lvert\frac{\mu_{a,p}}{\sigma_{a,p}}\rvert_{\max}$ | $\sigma_{r,\text{rms}}$ (m) | $\sigma_{v,\text{rms}}$ (mm/s) | $t_s$ (hr) |
| 12 x 12 | $1.35 \times 10^{-5}$ | 0.21 | 18.48 | 24.61 | 6.33 |
| 24 x 24 | $2.08 \times 10^{-6}$ | 0.01 | 4.36 | 5.06 | 6.47 |
| 80 x 80 & TBP-Sun | $3.64 \times 10^{-9}$ | 1.68 | 0.48 | 0.38 | 4.16 |
| 80 x 80, TBP-Sun, & SRP | $5.05 \times 10^{-10}$ | 0.02 | 0.12 | 0.10 | 9.29 |

ferent types of links: links between polar inclined planes (Polar-to-Polar) and links between a polar plane and the equatorial plane (Polar-to-Equatorial). Like the lunar

case, the Polar-to-Polar links perform somewhat worse than the Polar-to-Equatorial links. However, due to access limitations because of the limited number of satellites, the predicted CRLB uncertainties are about 10 m and 10 mm/s worse than the lunar case. This still is on-par or better than SOA DSN tracking [12] (see Figure 1-1). Higher accuracy force models would be needed for solo links to accurately propagate the orbits in-between access intervals. Adding a bidirectional link not only enables global data routing, but also improves the navigation performance somewhat (the polar-to-equatorial link is doing the heavy lifting). Note that as the orbits precess; the polar-to-equatorial link partner oscillates between FC5 and FC6 every few days, so both of these partners would be used over time for data routing and navigation. The three-way link is slightly better than the two-way link, but not significantly. This affirms the previous results in this chapter and Chapter 2 on diminishing returns for multiple access.

Table 4.23: MarsNet Constellation Example Results using 24 x 24 gravity field model.

| Satellite | $\sigma_r$ (m) | | | $\sigma_v$ (mm/s) | | |
|---|---|---|---|---|---|---|
| | Min | RMS | Max | Min | RMS | Max |
| Cross-Planar Link (Polar-to-Polar): $t_s = 2.59$ hrs, $l^{99}_{CN(P)} = 9.08$ | | | | | | |
| Mars-FC1 | 2.56 | 18.93 | 74.25 | 4.85 | 17.78 | 64.53 |
| Mars-FC4 | 2.54 | 13.43 | 61.55 | 3.24 | 13.01 | 56.36 |
| Cross-Planar Link (Polar-to-Equatorial): $t_s = 7.35$ hrs, $l^{99}_{CN(P)} = 8.59$ | | | | | | |
| Mars-FC1 | 1.69 | 4.48 | 12.79 | 2.02 | 4.68 | 12.75 |
| Mars-FC6 | 1.89 | 6.35 | 19.43 | 2.55 | 6.70 | 18.86 |
| Two-Way Link: $t_s = 6.47$ hrs, $l^{99}_{CN(P)} = 8.58$ | | | | | | |
| Mars-FC1 | 1.14 | 2.83 | 6.10 | 1.25 | 2.93 | 6.34 |
| Mars-FC4 | 1.50 | 3.87 | 9.76 | 1.46 | 3.77 | 8.89 |
| Mars-FC6 | 1.80 | 4.36 | 10.45 | 2.03 | 5.06 | 10.68 |
| Three-Way Link: $t_s = 2.59$ hrs, $l^{99}_{CN(P)} = 8.46$ | | | | | | |
| Mars-FC1 | 0.98 | 2.06 | 5.63 | 0.66 | 2.36 | 6.09 |
| Mars-FC3 | 1.26 | 2.35 | 5.84 | 0.82 | 2.98 | 5.87 |
| Mars-FC4 | 1.27 | 3.37 | 9.49 | 1.21 | 3.28 | 8.65 |
| Mars-FC6 | 1.67 | 3.12 | 7.75 | 1.52 | 3.97 | 8.76 |

### 4.4.2 Monte Carlo Kalman Filtering Simulations

The Monte Carlo EKF simulation is carried out for the two-way link and the three-way link. We use the two-way link instead of a single partner link because the single links have limited access and would require higher accuracy force models. The results

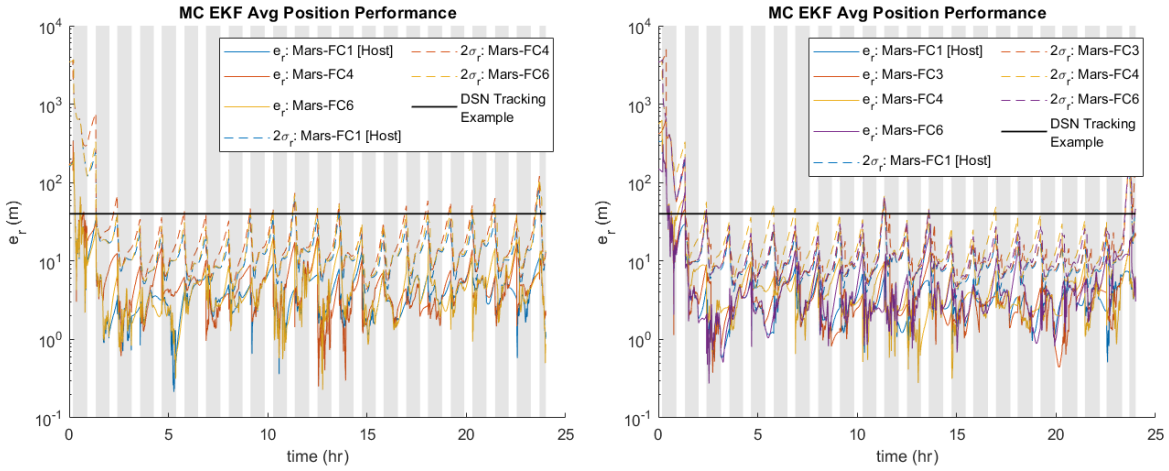


Figure 4-24: Average Monte Carlo (30 runs) position errors for selected MarsNet satellites with 24 x 24 gravity model for (a) Two-way and (b) Three-Way Link. The DSN ground tracking example error is 40 m, which is the simulated orbit determination error for MAVEN during a DSN downlink [12] (in-between DSN downlinks, the simulated DSN tracking error increased up to 150 m).

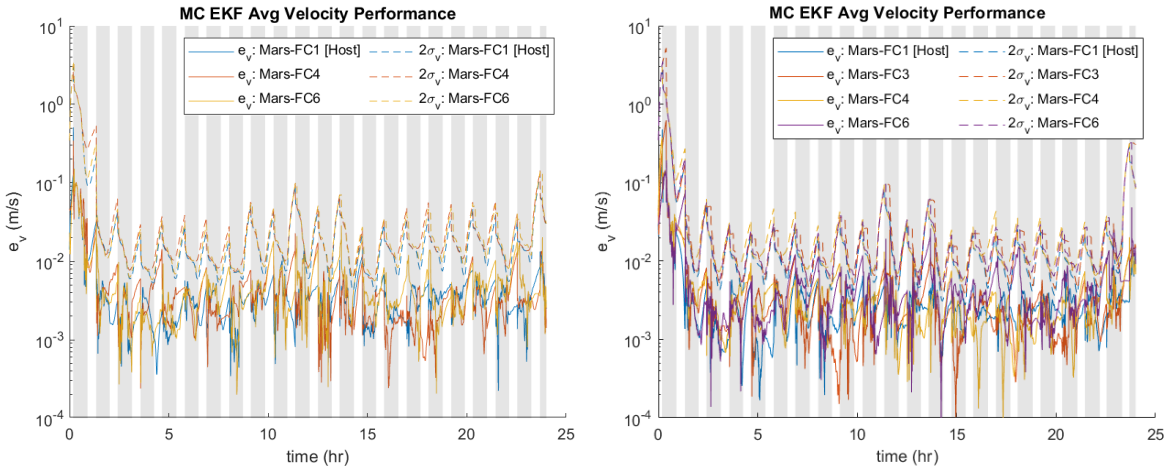


Figure 4-25: Average Monte Carlo (30 runs) velocity errors with 24 x 24 gravity model for (a) Two-way and (b) Three-Way Link.

are shown in Figures 4-24 and 4-25, and the performance statistics are summarized

in Table 4.24. The performance is on-par or better than existing SOA using DSN tracking (∼10-1000 m, see Figure 1-1), and there are once again diminishing returns for multiple access.

Table 4.24: MarsNet constellation results for average of Monte Carlo (30 runs) EKF with 24 x 24 gravity model.

| Satellite | $e_r$ (m) | | | $e_v$ (mm/s) | | |
|---|---|---|---|---|---|---|
| | Min | RMS | Max | Min | RMS | Max |
| Two-Way Link: $t_s = 7.34$ hr, $l^{99}_{CN(P)} = 9.72$, Avg. NEES = 18.79 (99% Bds. [15.30, 20.95]), $\sigma_{q,\text{rms}} = 1.47 \times 10^{-5}$ m/s$^2$ | | | | | | |
| Mars-FC1 (Host) | 0.36 | 4.55 | 13.31 | 0.22 | 4.02 | 13.71 |
| Mars-FC4 | 0.25 | 5.52 | 20.31 | 0.24 | 4.74 | 22.71 |
| Mars-FC6 | 0.23 | 6.56 | 24.78 | 0.20 | 6.02 | 28.58 |
| Three-Way Link: $t_s = 7.34$ hr, $l^{99}_{CN(P)} = 10.73$, Avg. NEES = 24.71 (99% Bds. [20.87, 27.38]), $\sigma_{q,\text{rms}} = 2.26 \times 10^{-5}$ m/s$^2$ | | | | | | |
| Mars-FC1 (Host) | 0.51 | 3.43 | 7.53 | 0.20 | 3.07 | 14.43 |
| Mars-FC3 | 0.44 | 4.80 | 23.04 | 0.10 | 3.75 | 24.90 |
| Mars-FC4 | 0.28 | 4.14 | 14.99 | 0.10 | 3.60 | 20.05 |
| Mars-FC6 | 0.68 | 6.05 | 26.63 | 0.05 | 5.86 | 48.27 |

## 4.5 Chapter Summary

In this chapter we applied the measurement models from Chapter 3 to case studies of OISL-based navigation in satellite constellations around the Earth, the Moon, and Mars. We studied the Starlink LEO constellation, the GPS MEO constellation, a notional lunar constellation called LunaNet, and a notional MarsNet constellation. The LEO constellation and MarsNet constellations were both low-altitude, so they had similar results, though the Mars constellation had somewhat worse performance due to the limited number of satellites and no continous access to any particular satellite. We used the same force model (24 x 24 gravity) for studying the OISL navigation performance for both of these constellations. The MEO and Lunar constellations are both relatively high altitude, and we used the 12 x 12 + TBP-Sun-Earth gravity force model for both of these cases. We purposely did not include non-gravitational forces

(drag and SRP) in the models to avoid the need to transfer satellite attitude and mass data in real-time. The only thing that each of these constellations needs is to be periodically synchronized with the Earth-based time reference (e.g., UTC) in order to accurately calculate their gravitational forces (which are time-based). This would be the case anyways, since the users of these constellations will also need periodic absolute time synchronization with Earth.

Across all of the cases studied, a baseline level OISL navigation performance can be established with (near-)continuous access to only one link partner in a non-singular orbit configuration. If additional partners are needed for (near-)continuous link access, then that number of partners is needed for baseline performance: as in the Mars case, where due to the limited number of satellites, two link partners were needed to help fill in the link access gaps. Adding additional partners beyond the baseline performance case does not significantly improve OISL navigation performance, although these additional partners will typically be needed anyway for low-latency intersatellite data routing. The number of partners for baseline OISL navigation performance is less than that needed for low-latency data routing, so any reasonably well designed constellation with built-in OISL crosslinks will already have the necessary features for baseline OISL navigation performance. Baseline OISL navigation performance is about 0.1-10 m and 0.1-10 mm/s, which is on-par or better than existing SOA day-to-day navigation/tracking: GNSS for LEO ($\sim$0.1-10 m), radio ground tracking for MEO ($\sim$1-10 m), and DSN radio tracking for the Lunar case ($\sim$1-1000 m) and the Mars case ($\sim$10-1000 m) (see Figure 1-1).

THIS PAGE INTENTIONALLY LEFT BLANK

# Chapter 5

# Summary and Future Work

In Chapter 2, we compared the observability of different subsets of the three measurement types: range, doppler, and bearings. The range and Doppler measurements are essentially equivalent in terms of observability, and therefore whichever one has a lower effective measurement error will dominate the estimate. Using both measurements is redundant in most cases. Using only range, Doppler, or bearings is only a partial measurement of the relative position vector, so it is well known that in such a scenario, the absolute orbit is only partially observable in the Newtonian gravity case, and the observability improves with force model perturbations that remove symmetries from the force model; *a priori* knowledge is needed to converge to a solution. A lasercom terminal is able to measure the full relative position vector (range and bearings, or Doppler and bearings), which makes the absolute orbit fully observable for most orbital configurations. The two-satellite problem is known to be unobservable in the Newtonian gravity case if the two satellites have the same shape parameters $(a, e)$ and satisify at least one of: share the same orbital plane, are only offset in inclination, or are only offset in RAAN by 180°. In principle, this would rule out intersatellite links between satellites that share the same orbit, which is the most common of the three cases in practice. However, we have shown that the unobservability criteria behave like singularities, and small offsets from these configurations due to imperfect station keeping and perturbing forces restore observability. Apart from keeping the configuration away from the unobservable cases, the perturbing forces do not other-

wise increase observability (unlike the single measurement cases).

We showed that if the host satellite has multiple link partners, only one pair of satellites in the estimation problem needs to be observable, since once the host satellite's absolute orbit is known, any other satellite's orbit is observable using the relative position measurements provided by the lasercom terminal. We assessed the sensitivity of the the problem observability to measurement parameters. In particular, we showed that decreasing the measurement period improved observability proportional to the square-root of the measurement period. We also showed that either the range/Doppler or the bearings measurement determines lower bound on observability, depending on which one has a lower effective error. In our example, the range had a lower effective noise, so the problem was most sensitive to errors in the angular measurement. At the end of Chapter 2, we analyzed the effects of process noise for both continuous link access and duty-cycled link access cases. We showed that the problem is less sensitive to process noise if continuous links are available, as would be expected. We also showed that the problem has low sensitivity to short outage periods if the process noise is sufficiently low (e.g., $\sigma_q \leq 2 \times 10^{-7}$ m/s$^2$ for a LEO orbit with continuous measurements). We noted that there are diminishing returns to decreasing process noise.

In Chapter 3, we performed systems analysis of the range, Doppler, and bearings measurements that can be generated using a laser communications system. We analyzed both the measurement error from the lasercom terminal design and the physical measurement model. For the ranging and Doppler error models, we focused on a full-duplex, direct-detection PPM laser communications system design with an atomic clock. We performed link analysis to show how there are potentially three regimes of ranging error depending on the operational data rate: detector error dominated, synchronization error dominated, and clock error dominated. For a maximum design link range of 50,000 km, the data rate defined regimes are approximately 10-20 Mbps, 20-100 Mbps, and $>$ 100 Mbps. For the high data rate (e.g. 622 Mbps - 1.244 Gbps), long link range systems that are planned for most future missions, the ranging and Doppler measurements will be clock error limited. In comparison, the RF ranging

noise is mainly limited by phase detection errors. The atomic clock error is negligible for the RF system, but it dominates our reference 622 Mbps lasercom system over all ranging integration times. Shorter range links at high rates will be synchronization error dominated. At 622 Mbps, the transition point is a maximum design link range less than about 2000 km, which would be typical for a large constellation (e.g. Starlink). Given a terminal design for some maximum range, the ranging noise varies in real-time as the link range varies because of variable power received (due to path loss). Shorter-range links will have higher received power and better ranging performance, in addition to higher communications data rate capacity. For the reference 622 Mbps link, the ranging error varies from about 1-5 mm (1-sigma) from 5,000-50,000 km.

The Doppler measurement gives the average range rate over an integration time. Given this model, the Doppler error is also dependent on the data rate. For our reference data rate of 622 Mbps with a Doppler integration time of 1 minute, the error from the detector/sychronization parts of the system dominate the error from the clock. The clock error only becomes the dominant error for short integration times (about 2 seconds in this case). Like the range error, the Doppler error also varies in real-time with the range because of the varying received power. For our reference link, it varies from about 1-20 microns/second (1-sigma) from 5,000-50,000 km. For the bearings error model, we showed how the noise in the calculated inertial bearings angles comes from both the lasercom terminal laser acquisition/tracking sensor (part of its PAT system), which gives angles relative to the sensor frame, and the star tracker that is used to determine the terminal's attitude with respect to the inertial frame. We analyzed a quadcell PAT sensor model and showed how the measurement noise depends on the SNR. For a given SNR requirement at the design max range, the worst case error can be derived. The noise equivalent angle decreases with range as the received power increases. The minimum NEA is limited by the residual effects of vibrational platform jitter (either the residuals from the damping/control system or the direct structural vibrations). Note that the sensor will also saturate at extremely short ranges (on the order of 10 km). The measurement frequency for complete range/Doppler and bearings measurements is limited by the star tracker to

about 1-5 Hz, which is the lowest measurement frequency of all of the sensors (due to longer integration times needed to image stars).

We also analyzed the physical model for light propagation between the terminals, which is the basis for all of the measurements. The measured range for a two-way link is the apparent time of flight of light for the uplink combined with the downlink, along with any hardware delays. For the link configurations and measurement noise levels of interest (i.e. 1,000 to 100,000 km between satellites orbiting the same central body with mm to cm level noise), the TOF model needs to be better than about 1 picosecond. We showed that for this purpose, it is sufficient to model the TOF using special relativity with a single general relativistic correction: the Shapiro delay. The implicit, nonlinear equation that must be solved iteratively for the TOF can be truncated to 3 iterations with negligible error. The Doppler measurement is the integrated Doppler shift, which is mathematically equivalent to the average apparent range-rate over the integration time (plus noise). The average apparent range-rate is the difference of the apparent ranges at the endpoints of the integration interval divided by the integration time. This eliminates the hardware delay contribution. It also differences the relativistic effects; however, for sufficiently high relative velocities (e.g., a LEO-GEO relay), the Shapiro correction must still be taken into account for sufficiently accurate modeling. Again, the iterative solution to the differential TOF equation can be stopped at three iterations with negligible error. The bearings measurement is actually of the apparent angles due to the time of flight of the signal. For typical noise levels, the apparent bearings can be calculated only using special relativity, and the iterative algorithm can be stopped at one iteration, so the time of flight can be approximated as the geometric range divided by the speed of light, where any hardware delays should be taken into account when calculating the geometric range at the measurement time. We derived expressions for the measurement gradients.

In Chapter 4, we applied the measurement models from the Chapter 3 to case studies of OISL-based navigation in satellite constellations around the Earth, the Moon, and Mars. We studied the Starlink LEO constellation, the GPS MEO constellation,

a notional lunar constellation called LunaNet, and a notional MarsNet constellation. The LEO constellation and MarsNet constellations were both low-altitude, so they had similar results, though the Mars constellation had somewhat worse performance due to the limited number of satellites and no continous access to any particular satellite. We used the same force model (24 x 24 gravity) for studying the OISL navigation performance for both of these constellations. The MEO and Lunar constellations are both relatively high altitude, and we used the 12 x 12 and TBP-Sun-Earth gravity force model for both of these cases. We did not include non-gravitational forces (drag and SRP) in the models to avoid the need to transfer satellite attitude and mass data in real-time, since the improvement to performance is not significant. The only thing that each of these constellations needs is to be periodically synchronized with the Earth-based time reference (e.g. UTC) in order to accurately calculate their gravitational forces (which are time-based). This would be the case anyways, since the users of these constellations will also need periodic absolute time synchronization with Earth.

Across all of the cases studied, a baseline level OISL navigation performance can be established with (near-)continuous access to only one link partner in a non-singular orbit configuration. If additional partners are needed for (near-)continous link access, then that number of partners is needed for baseline performance (as in the Mars case where due to the limited number of satellites, two link partners were needed to help fill in the link access gaps). Adding additional partners beyond the baseline performance case does not significantly improve OISL navigation performance, although these additional partners will typically be needed anyway for low-latency intersatellite data routing. The number of partners for baseline OISL navigation performance is less than that needed for low-latency data routing, so any reasonably well designed constellation with built-in OISL crosslinks will already have the necessary features for baseline OISL navigation performance. Baseline OISL navigation performance is about 0.1-10 m and 0.1-10 mm/s, which is on-par or better than existing SOA day-to-day navigation/tracking: GNSS for LEO ($\sim$0.1-10 m), radio ground tracking for MEO ($\sim$1-10 m), and DSN radio tracking for the Lunar case ($\sim$1-1000 m) and the

Mars case (∼10-1000 m).

## 5.1 Summary of Contributions

The main contributions of this work are:

- Chapter 2: We performed systematic observability analysis, using idealized OISL measurement models. We analyzed the sensitivity of orbit determination performance with respect to orbital geometries and to measurement parameters, and assessed the impact of non-observable configurations for satellite constellations.

- Chapter 3: We performed systems analysis to develop higher fidelity OISL measurement models that capture key system parameters and include relevant relativistic effects. We developed the analytical relationships between optical communications system parameters (e.g., data rate) and OISL measurement capabilities. We analyzed the sensitivity of the measurement model to the optical communications system design parameters.

- Chapter 4: We performed OISL navigation performance analysis using high fidelity OISL measurement models, for constellation case studies for the Earth, the Moon, and Mars using Cramer-Rao Lower Bound (CRLB) and Monte Carlo Kalman Filter simulations. We assessed the effects of perturbations on problem performance for realistic force models, with higher fidelity than $J_2$ gravity. We showed how different crosslink configurations in the constellation network impact the system performance.

## 5.2 Future Work

Future work that would be benefit this area of study includes the following:

- Modeling the effects of measurement bias errors for performance analysis.

- Testing algorithms for online bias estimation.
- Analyzing effectiveness of ground and on-orbit calibration procedures for navigation purposes.
- Adding periodic station keeping maneuvers and simulating orbit determination over long time horizons (e.g., several months).
- Assessing the performance of different formulations of adaptive Kalman filters for both the variable measurement noise and the process noise.
- Using on-orbit data from lasercom crosslinks to test the models used herein.
- Analyzing other deep space navigation cases of interest: Earth-Moon and Earth-Sun Lagrange points, navigation during flight between the Earth and Moon, navigation during heliocentric trajectories through the solar system, navigation around other central bodies (besides the Earth, Moon, and Mars), navigation around asteroids and comets.
- Investigating the effects of fusing measurements from other sources with OISLs: RF ISLs, RF ground links, optical ground links, GPS, OpNav.

THIS PAGE INTENTIONALLY LEFT BLANK

# Appendix A

# Measurement Model Gradients

The gradient expressions for the measurement models used in this work are given in this appendix.

## A.1 Idealized Geometric Measurement Gradients

There is a symmetry between the measurement gradients with respect to the host and partner states that can be derived as follows:

$$\frac{\partial \mathbf{y}_i}{\partial \mathbf{x}_i} = \left[\frac{\partial \mathbf{y}_i}{\partial \mathbf{r}_i}, \frac{\partial \mathbf{y}_i}{\partial \mathbf{v}_i}\right] = \left[\frac{\partial \mathbf{y}_i}{\partial \boldsymbol{\rho}}\frac{\partial \boldsymbol{\rho}}{\partial \mathbf{r}_i}, \frac{\partial \mathbf{y}_i}{\partial \dot{\boldsymbol{\rho}}}\frac{\partial \dot{\boldsymbol{\rho}}}{\partial \mathbf{v}_i}\right] = \left[\frac{\partial \mathbf{y}_i}{\partial \boldsymbol{\rho}}, \frac{\partial \mathbf{y}_i}{\partial \dot{\boldsymbol{\rho}}}\right] \tag{A.1a}$$

$$\frac{\partial \mathbf{y}_i}{\partial \mathbf{x}_0} = \left[\frac{\partial \mathbf{y}_i}{\partial \mathbf{r}_0}, \frac{\partial \mathbf{y}_i}{\partial \mathbf{v}_0}\right] = \left[\frac{\partial \mathbf{y}_i}{\partial \boldsymbol{\rho}}\frac{\partial \boldsymbol{\rho}}{\partial \mathbf{r}_0}, \frac{\partial \mathbf{y}_i}{\partial \dot{\boldsymbol{\rho}}}\frac{\partial \dot{\boldsymbol{\rho}}}{\partial \mathbf{v}_0}\right] = \left[-\frac{\partial \mathbf{y}_i}{\partial \boldsymbol{\rho}}, -\frac{\partial \mathbf{y}_i}{\partial \dot{\boldsymbol{\rho}}}\right] = -\frac{\partial \mathbf{y}_i}{\partial \mathbf{x}_i} \tag{A.1b}$$

Hence, the measurement gradients with respect to the host and partner states are equal in magnitude and opposite in sign, and they can be straightforwardly calculated using the measurement gradients with respect to the relative position and velocity vectors as follows:

$$\frac{\partial \mathbf{y}_i}{\partial \mathbf{x}_i} = -\frac{\partial \mathbf{y}_i}{\partial \mathbf{x}_0} = \left[\frac{\partial \mathbf{y}_i}{\partial \boldsymbol{\rho}}, \frac{\partial \mathbf{y}_i}{\partial \dot{\boldsymbol{\rho}}}\right] = \begin{bmatrix} \frac{\partial \rho_i}{\partial \boldsymbol{\rho}}, \mathbf{0}_{1\times 3} \\ \frac{\partial \theta_i}{\partial \boldsymbol{\rho}}, \mathbf{0}_{1\times 3} \\ \frac{\partial \phi_i}{\partial \boldsymbol{\rho}}, \mathbf{0}_{1\times 3} \\ \frac{\partial \dot{\rho}_i}{\partial \boldsymbol{\rho}}, \frac{\partial \dot{\rho}_i}{\partial \dot{\boldsymbol{\rho}}} \end{bmatrix} \tag{A.2a}$$

Some useful, general vector gradient formulae are as follows:

$$\frac{\partial \|\mathbf{a}\|}{\partial \mathbf{a}} = \frac{\mathbf{a}^T}{\|\mathbf{a}\|} = \hat{\mathbf{a}}^T \tag{A.3a}$$

$$\frac{\partial \hat{\mathbf{a}}}{\partial \mathbf{a}} = \frac{1}{\|\mathbf{a}\|} I - \frac{1}{\|\mathbf{a}\|^3} \mathbf{a}\mathbf{a}^T = \frac{1}{\|\mathbf{a}\|} \left( I - \hat{\mathbf{a}}\hat{\mathbf{a}}^T \right) \tag{A.3b}$$

The nonzero measurement component gradients are therefore:

$$\frac{\partial \rho_i}{\partial \boldsymbol{\rho}_i} = \hat{\boldsymbol{\rho}}_i^T = \frac{[x_i - x_0, y_i - y_0, z_i - z_0]}{\rho_i} \tag{A.4a}$$

$$\frac{\partial \theta_i}{\partial \boldsymbol{\rho}_i} = \frac{(\boldsymbol{\rho}_i \cdot \mathbf{E}_x)\mathbf{E}_y^T - (\boldsymbol{\rho}_i \cdot \mathbf{E}_y)\mathbf{E}_x^T}{(\boldsymbol{\rho}_i \cdot \mathbf{E}_x)^2 + (\boldsymbol{\rho}_i \cdot \mathbf{E}_y)^2} = \frac{[-(y_i - y_0), x_i - x_0, 0]}{(x_i - x_0)^2 + (y_i - y_0)^2} \tag{A.4b}$$

$$\frac{\partial \phi_i}{\partial \boldsymbol{\rho}_i} = \frac{\mathbf{E}_z^T - (\hat{\boldsymbol{\rho}}_i \cdot \mathbf{E}_z)\hat{\boldsymbol{\rho}}_i^T}{\rho_i \sqrt{1 - (\hat{\boldsymbol{\rho}}_i \cdot \mathbf{E}_z)^2}} \tag{A.4c}$$

$$= \frac{[-(z_i - z_0)(x_i - x_0), -(z_i - z_0)(y_i - y_0), (x_i - x_0)^2 + (y_i - y_0)^2]}{\rho_i^2 \sqrt{(x_i - x_0)^2 + (y_i - y_0)^2}} \tag{A.4d}$$

$$\frac{\partial \dot{\rho}_i}{\partial \boldsymbol{\rho}_i} = \frac{1}{\rho_i} \left( \dot{\boldsymbol{\rho}}_i^T - \dot{\rho}_i \hat{\boldsymbol{\rho}}_i{}^T \right) \tag{A.4e}$$

$$= \frac{[\dot{x}_i - \dot{x}_0, \dot{y}_i - \dot{y}_0, \dot{z}_i - \dot{z}_0]}{\rho_i} - \frac{\dot{\rho}_i \, [x_i - x_0, y_i - y_0, z_i - z_0]}{\rho_i^2} \tag{A.4f}$$

$$\frac{\partial \dot{\rho}_i}{\partial \dot{\boldsymbol{\rho}}_i} = \hat{\boldsymbol{\rho}}_i^T = \frac{\partial \rho_i}{\partial \boldsymbol{\rho}_i} \tag{A.4g}$$

## A.2 Two-Way Apparent Range Measurement Gradient

To use this model for apparent range in the EKF and CRLB algorithms, expressions for the gradients with respect the spacecraft state vectors at $t_R$ are needed. To facilitate this, it is helpful to explicitly write out the argument dependencies in the

time of flight equations.

$$\rho_{a,ud}(\mathbf{x}_0, \mathbf{x}_i) = \frac{c}{2}\tau_{ud}(\mathbf{x}_0, \mathbf{x}_i) = \frac{1}{2}\left(c\tau_u(\mathbf{x}_0, \mathbf{x}_i) + c\tau_d(\mathbf{x}_0, \mathbf{x}_i)\right) \tag{A.5a}$$

$$c\tau_d(\mathbf{x}_0, \mathbf{x}_i) = c\tilde{f}_\tau^d\left(\mathbf{r}'_0(\mathbf{x}_0), \mathbf{r}'_{i,d}(\mathbf{x}_i, \tau_d(\mathbf{x}_0, \mathbf{x}_i))\right) \tag{A.5b}$$

$$c\tau_u(\mathbf{x}_0, \mathbf{x}_i) = c\tilde{f}_\tau^u\left(\mathbf{r}''_i(\mathbf{x}_i, \tau_d(\mathbf{x}_0, \mathbf{x}_i)), \mathbf{r}''_{0,u}(\mathbf{x}_0, \tau_d(\mathbf{x}_0, \mathbf{x}_i), \tau_u(\mathbf{x}_0, \mathbf{x}_i))\right) \tag{A.5c}$$

$$c\tilde{f}_\tau^d(\mathbf{r}'_0, \mathbf{r}'_{i,d}) = \left\|\boldsymbol{\rho}_{a,d}\right\| + \frac{2\mu}{c^2}\ln\left(\frac{\|\mathbf{r}'_0\| + \left\|\mathbf{r}'_{i,d}\right\| + \left\|\boldsymbol{\rho}_{a,d}\right\|}{\|\mathbf{r}'_0\| + \left\|\mathbf{r}'_{i,d}\right\| - \left\|\boldsymbol{\rho}_{a,d}\right\|}\right) \tag{A.5d}$$

$$c\tilde{f}_\tau^u(\mathbf{r}''_i, \mathbf{r}''_{0,u}) = \left\|\boldsymbol{\rho}_{a,u}\right\| + \frac{2\mu}{c^2}\ln\left(\frac{\|\mathbf{r}''_i\| + \left\|\mathbf{r}''_{0,u}\right\| + \left\|\boldsymbol{\rho}_{a,u}\right\|}{\|\mathbf{r}''_i\| + \left\|\mathbf{r}''_{0,u}\right\| - \left\|\boldsymbol{\rho}_{a,u}\right\|}\right) \tag{A.5e}$$

$$\boldsymbol{\rho}_{a,d} \equiv \mathbf{r}'_{i,d} - \mathbf{r}'_0,\ \boldsymbol{\rho}_{a,u} = \mathbf{r}''_i - \mathbf{r}''_{0,u} \tag{A.5f}$$

$$\mathbf{r}'_0(\mathbf{x}_0) \equiv \mathbf{r}_0(t') = \mathbf{r}_0 - \mathbf{v}_0\tau_d^{\mathrm{rx}} + \frac{1}{2}\mathbf{a}_0(\mathbf{r}_0)(\tau_d^{\mathrm{rx}})^2 \tag{A.5g}$$

$$\mathbf{r}'_{i,d}(\mathbf{x}_i, \tau_d) \equiv \mathbf{r}_i(t' - \tau_d) = \mathbf{r}_i - \mathbf{v}_i(\tau_d^{\mathrm{rx}} + \tau_d) + \frac{1}{2}\mathbf{a}_i(\mathbf{r}_i)(\tau_d^{\mathrm{rx}} + \tau_d)^2 \tag{A.5h}$$

$$\mathbf{r}''_i(\mathbf{x}_i, \tau_d) \equiv \mathbf{r}_i(t'') = \mathbf{r}_i - \mathbf{v}_i(\tau''_c + \tau_d) + \frac{1}{2}\mathbf{a}_i(\mathbf{r}_i)(\tau''_c + \tau_d)^2 \tag{A.5i}$$

$$\mathbf{r}''_{0,u}(\mathbf{x}_0, \tau_d, \tau_u) \equiv \mathbf{r}_0(t'' - \tau_u) = \mathbf{r}_0 - \mathbf{v}_0(\tau''_c + \tau_d + \tau_u) + \frac{1}{2}\mathbf{a}_0(\mathbf{r}_0)(\tau''_c + \tau_d + \tau_u)^2 \tag{A.5j}$$

$$\mathbf{a}_0(\mathbf{r}_0) = -\frac{\mu}{\|\mathbf{r}_0\|^3}\mathbf{r}_0,\ \mathbf{a}_i(\mathbf{r}_i) = -\frac{\mu}{\|\mathbf{r}_i\|^3}\mathbf{r}_i \tag{A.5k}$$

$$\mathbf{x}_0 = [\mathbf{r}_0^T, \mathbf{v}_0^T]^T \equiv [\mathbf{r}_0^T(t_R), \mathbf{v}_0^T(t_R)]^T \tag{A.5l}$$

$$\mathbf{x}_i = [\mathbf{r}_i^T, \mathbf{v}_i^T]^T \equiv [\mathbf{r}_i^T(t_R), \mathbf{v}_i^T(t_R)]^T \tag{A.5m}$$

The gradient expressions can be then be derived by straightforward (and tedious) differentiation.

$$\frac{\partial \rho_{a,ud}}{\partial \mathbf{x}_0} = \frac{1}{2}\left(\frac{\partial c\tau_u}{\partial \mathbf{x}_0} + \frac{\partial c\tau_d}{\partial \mathbf{x}_0}\right),\ \frac{\partial \rho_{a,ud}}{\partial \mathbf{x}_i} = \frac{1}{2}\left(\frac{\partial c\tau_u}{\partial \mathbf{x}_i} + \frac{\partial c\tau_d}{\partial \mathbf{x}_i}\right) \tag{A.6a}$$

$$\frac{\partial c\tau_d}{\partial \mathbf{x}_0} = \left(1 + \frac{\partial c\tilde{f}_\tau^d}{\partial \mathbf{r}'_{i,d}}\frac{\mathbf{v}'_{i,d}}{c}\right)^{-1}\frac{\partial c\tilde{f}_\tau^d}{\partial \mathbf{r}'_0}\frac{\partial \mathbf{r}'_0}{\partial \mathbf{x}_0} \tag{A.6b}$$

$$\frac{\partial c\tau_d}{\partial \mathbf{x}_i} = \left(1 + \frac{\partial c\tilde{f}_\tau^d}{\partial \mathbf{r}'_{i,d}}\frac{\mathbf{v}'_{i,d}}{c}\right)^{-1}\frac{\partial c\tilde{f}_\tau^d}{\partial \mathbf{r}'_{i,d}}\frac{\partial \mathbf{r}'_{i,d}}{\partial \mathbf{x}_i} \tag{A.6c}$$

$$\frac{\partial c\tau_u}{\partial \mathbf{x}_0} = \left(1 + \frac{\partial c\tilde{f}_\tau^u}{\partial \mathbf{r}''_{0,u}}\frac{\mathbf{v}''_{0,u}}{c}\right)^{-1}\left(\frac{\partial c\tilde{f}_\tau^u}{\partial \mathbf{r}''_{0,u}}\frac{\partial \mathbf{r}''_{0,u}}{\partial \mathbf{x}_0} - \left(\frac{\partial c\tilde{f}_\tau^u}{\partial \mathbf{r}''_i}\frac{\mathbf{v}''_i}{c} + \frac{\partial c\tilde{f}_\tau^u}{\partial \mathbf{r}''_{0,u}}\frac{\mathbf{v}''_{0,u}}{c}\right)\frac{\partial c\tau_d}{\partial \mathbf{x}_0}\right) \tag{A.6d}$$

$$\frac{\partial c\tau_u}{\partial \mathbf{x}_i} = \left(1 + \frac{\partial c\tilde{f}_\tau^u}{\partial \mathbf{r}''_{0,u}}\frac{\mathbf{v}''_{0,u}}{c}\right)^{-1}\left(\frac{\partial c\tilde{f}_\tau^u}{\partial \mathbf{r}''_i}\frac{\partial \mathbf{r}''_i}{\partial \mathbf{x}_i} - \left(\frac{\partial c\tilde{f}_\tau^u}{\partial \mathbf{r}''_i}\frac{\mathbf{v}''_i}{c} + \frac{\partial c\tilde{f}_\tau^u}{\partial \mathbf{r}''_{0,u}}\frac{\mathbf{v}''_{0,u}}{c}\right)\frac{\partial c\tau_d}{\partial \mathbf{x}_i}\right) \tag{A.6e}$$

$$\frac{\partial c\tilde{f}_\tau^d}{\partial \mathbf{r}'_{i,d}} = \hat{\boldsymbol{\rho}}_{a,d}^T + \frac{2\mu}{c^2}\left(\frac{\hat{\mathbf{r}}_{i,d}'^T + \hat{\boldsymbol{\rho}}_{a,d}^T}{\|\mathbf{r}'_0\| + \|\mathbf{r}'_{i,d}\| + \|\boldsymbol{\rho}_{a,d}\|} - \frac{\hat{\mathbf{r}}_{i,d}'^T - \hat{\boldsymbol{\rho}}_{a,d}^T}{\|\mathbf{r}'_0\| + \|\mathbf{r}'_{i,d}\| - \|\boldsymbol{\rho}_{a,d}\|}\right) \tag{A.6f}$$

$$\frac{\partial c\tilde{f}_\tau^d}{\partial \mathbf{r}'_0} = -\hat{\boldsymbol{\rho}}_{a,d}^T + \frac{2\mu}{c^2}\left(\frac{\hat{\mathbf{r}}_0'^T - \hat{\boldsymbol{\rho}}_{a,d}^T}{\|\mathbf{r}'_0\| + \|\mathbf{r}'_{i,d}\| + \|\boldsymbol{\rho}_{a,d}\|} - \frac{\hat{\mathbf{r}}_0'^T + \hat{\boldsymbol{\rho}}_{a,d}^T}{\|\mathbf{r}'_0\| + \|\mathbf{r}'_{i,d}\| - \|\boldsymbol{\rho}_{a,d}\|}\right) \tag{A.6g}$$

$$\frac{\partial c\tilde{f}_\tau^u}{\partial \mathbf{r}''_i} = \hat{\boldsymbol{\rho}}_{a,u}^T + \frac{2\mu}{c^2}\left(\frac{\hat{\mathbf{r}}_i''^T + \hat{\boldsymbol{\rho}}_{a,u}^T}{\|\mathbf{r}''_i\| + \|\mathbf{r}''_{0,u}\| + \|\boldsymbol{\rho}_{a,u}\|} - \frac{\hat{\mathbf{r}}_i''^T - \hat{\boldsymbol{\rho}}_{a,u}^T}{\|\mathbf{r}''_i\| + \|\mathbf{r}''_{0,u}\| - \|\boldsymbol{\rho}_{a,u}\|}\right) \tag{A.6h}$$

$$\frac{\partial c\tilde{f}_\tau^u}{\partial \mathbf{r}''_{0,u}} = -\hat{\boldsymbol{\rho}}_{a,u}^T + \frac{2\mu}{c^2}\left(\frac{\hat{\mathbf{r}}_{0,u}''^T - \hat{\boldsymbol{\rho}}_{a,u}^T}{\|\mathbf{r}''_i\| + \|\mathbf{r}''_{0,u}\| + \|\boldsymbol{\rho}_{a,u}\|} - \frac{\hat{\mathbf{r}}_{0,u}''^T + \hat{\boldsymbol{\rho}}_{a,u}^T}{\|\mathbf{r}''_i\| + \|\mathbf{r}''_{0,u}\| - \|\boldsymbol{\rho}_{a,u}\|}\right) \tag{A.6i}$$

$$\mathbf{v}'_{i,d} = -\frac{\partial \mathbf{r}'_{i,d}}{\partial \tau_d} = \mathbf{v}_i - \mathbf{a}_i(\tau_d^{\mathrm{rx}} + \tau_d),\ \mathbf{v}''_i = -\frac{\partial \mathbf{r}''_i}{\partial \tau_d} = \mathbf{v}_i - \mathbf{a}_i(\tau''_c + \tau_d) \tag{A.6j}$$

$$\mathbf{v}''_{0,u} = -\frac{\partial \mathbf{r}''_{0,u}}{\partial \tau_d} = -\frac{\partial \mathbf{r}''_{0,u}}{\partial \tau_u} = \mathbf{v}_0 - \mathbf{a}_0(\tau''_c + \tau_d + \tau_u) \tag{A.6k}$$

$$\frac{\partial \mathbf{r}'_0}{\partial \mathbf{x}_0} = \left[\frac{\partial \mathbf{r}'_0}{\partial \mathbf{r}_0}, \frac{\partial \mathbf{r}'_0}{\partial \mathbf{v}_0}\right] = \left[I + \frac{(\tau_d^{\mathrm{rx}})^2}{2}\frac{\partial \mathbf{a}_0}{\partial \mathbf{r}_0}, -\tau_d^{\mathrm{rx}} I\right] \tag{A.6l}$$

$$\frac{\partial \mathbf{r}'_{i,d}}{\partial \mathbf{x}_i} = \left[\frac{\partial \mathbf{r}'_{i,d}}{\partial \mathbf{r}_i}, \frac{\partial \mathbf{r}'_{i,d}}{\partial \mathbf{v}_i}\right] = \left[I + \frac{(\tau_d^{\mathrm{rx}} + \tau_d)^2}{2}\frac{\partial \mathbf{a}_i}{\partial \mathbf{r}_i}, -(\tau_d^{\mathrm{rx}} + \tau_d) I\right] \tag{A.6m}$$

$$\frac{\partial \mathbf{r}''_i}{\partial \mathbf{x}_i} = \left[\frac{\partial \mathbf{r}''_i}{\partial \mathbf{r}_i}, \frac{\partial \mathbf{r}''_i}{\partial \mathbf{v}_i}\right] = \left[I + \frac{(\tau''_c + \tau_d)^2}{2}\frac{\partial \mathbf{a}_i}{\partial \mathbf{r}_i}, -(\tau''_c + \tau_d) I\right] \tag{A.6n}$$

$$\frac{\partial \mathbf{r}''_{0,u}}{\partial \mathbf{x}_0} = \left[\frac{\partial \mathbf{r}''_{0,u}}{\partial \mathbf{r}_0}, \frac{\partial \mathbf{r}''_{0,u}}{\partial \mathbf{v}_0}\right] = \left[I + \frac{(\tau''_c + \tau_d + \tau_u)^2}{2}\frac{\partial \mathbf{a}_0}{\partial \mathbf{r}_0}, -(\tau''_c + \tau_d + \tau_u) I\right] \tag{A.6o}$$

$$\frac{\partial \mathbf{a}}{\partial \mathbf{r}} = -\frac{\mu}{\|\mathbf{r}\|^3}\left(I - 3\hat{\mathbf{r}}\hat{\mathbf{r}}^T\right) \tag{A.6p}$$

## A.3 Apparent Range-Rate Measurement Gradient

The gradient expressions are straightforward to calculate using the apparent range gradients, the state transition matrix, and system memory:

$$\frac{\partial \bar{\dot{\rho}}_{a,ud}(\mathbf{x}_0(t),\mathbf{x}_i(t),T_I)}{\partial \mathbf{x}_0(t)} = \frac{1}{T_I}\left(\frac{\partial \rho_{a,ud}(\mathbf{x}_0(t),\mathbf{x}_i(t))}{\partial \mathbf{x}_0(t)} - \frac{\partial \rho_{a,ud}(\mathbf{x}_0(t-T_I),\mathbf{x}_i(t-T_I))}{\partial \mathbf{x}_0(t)}\right) \tag{A.7a}$$

$$= \frac{1}{T_I}\left(\frac{\partial \rho_{a,ud}(\mathbf{x}_0(t),\mathbf{x}_i(t))}{\partial \mathbf{x}_0(t)} - \frac{\partial \rho_{a,ud}(\mathbf{x}_0(t-T_I),\mathbf{x}_i(t-T_I))}{\partial \mathbf{x}_0(t-T_I)}\frac{\partial \mathbf{x}_0(t-T_I)}{\partial \mathbf{x}_0(t)}\right) \tag{A.7b}$$

$$= \frac{1}{T_I}\left(\frac{\partial \rho_{a,ud}(\mathbf{x}_0(t),\mathbf{x}_i(t))}{\partial \mathbf{x}_0(t)} - \frac{\partial \rho_{a,ud}(\mathbf{x}_0(t-T_I),\mathbf{x}_i(t-T_I))}{\partial \mathbf{x}_0(t-T_I)}\Phi_0(t-T_I,t)\right) \tag{A.7c}$$

$$\frac{\partial \bar{\dot{\rho}}_{a,ud}}{\partial \mathbf{x}_0}(t,T_I) = \frac{1}{T_I}\left(\frac{\partial \rho_{a,ud}}{\partial \mathbf{x}_0}(t) - \frac{\partial \rho_{a,ud}}{\partial \mathbf{x}_0}(t-T_I)\Phi_0(t-T_I,t)\right) \tag{A.7d}$$

$$\frac{\partial \bar{\dot{\rho}}_{a,ud}}{\partial \mathbf{x}_i}(t,T_I) = \frac{1}{T_I}\left(\frac{\partial \rho_{a,ud}}{\partial \mathbf{x}_i}(t) - \frac{\partial \rho_{a,ud}}{\partial \mathbf{x}_i}(t-T_I)\Phi_i(t-T_I,t)\right) \tag{A.7e}$$

## A.4 Bearing Angles Measurement Gradient - Pinhole Camera

To use this model for apparent range in the EKF and CRLB algorithms, expressions for the gradients with respect the spacecraft state vectors at $t_R$ are needed. Note that for simplicity, the sensor orientation bias error is set to the identity matrix such that

$\hat{R}_B^S = R_B^S$.

$$\begin{bmatrix} \theta_C \\ \phi_C \end{bmatrix} = \mathbf{y}_{\theta_C,\phi_C}(x_c, y_c, \hat{R}_B^S, \hat{R}_I^B) = \mathbf{h}_{\theta_C,\phi_C}(\mathbf{x}_0, \mathbf{x}_i, \mathbf{n}_A, \delta\mathbf{q}_I^B; \delta\mathbf{q}_B^S) \tag{A.8a}$$

$$\theta_C = \tan^{-1}\left(\frac{\hat{\boldsymbol{\rho}}_C \cdot \mathbf{E}_y}{\hat{\boldsymbol{\rho}}_C \cdot \mathbf{E}_x}\right) \in [0, 2\pi) \tag{A.8b}$$

$$\phi_C = \sin^{-1}(\hat{\boldsymbol{\rho}}_C \cdot \mathbf{E}_z) \in [-\pi/2, \pi/2] \tag{A.8c}$$

$$\hat{\boldsymbol{\rho}}_C = (\hat{R}_I^S)^T \frac{\mathbf{u}'_C}{\|\mathbf{u}'_C\|} \tag{A.8d}$$

$$\hat{R}_I^S = R_B^S \hat{R}_I^B = R_B^S R(\delta\mathbf{q}_I^B)^T R_I^B \tag{A.8e}$$

$$\mathbf{u}'_C = \frac{1}{\boldsymbol{\rho}_{a,d}^S \cdot \mathbf{e}_z^S} \boldsymbol{\rho}_{a,d}^S - \begin{bmatrix} \mathbf{n}_A \\ 0 \end{bmatrix} \tag{A.8f}$$

$$\boldsymbol{\rho}_{a,d}^S = R_I^S \boldsymbol{\rho}_{a,d} \tag{A.8g}$$

$$\boldsymbol{\rho}_{a,d} = \boldsymbol{\rho}' - \mathbf{v}_i \frac{\|\boldsymbol{\rho}'\|}{c} = \boldsymbol{\rho} - \dot{\boldsymbol{\rho}}\tau_d^{\mathrm{rx}} - \mathbf{v}_i \frac{\|\boldsymbol{\rho} - \dot{\boldsymbol{\rho}}\tau_d^{\mathrm{rx}}\|}{c} \tag{A.8h}$$

The gradient expressions are derived as follows:

$$H = \frac{\partial \mathbf{h}_{\theta_C,\phi_C}}{\partial \mathbf{x}}(\mathbf{n}_A = \mathbf{0}, \delta\mathbf{q}_I^B = \mathbf{0}) \tag{A.9a}$$

$$\frac{\partial \mathbf{h}_{\theta_C,\phi_C}}{\partial \mathbf{x}} = \frac{\partial \mathbf{h}_{\theta_C,\phi_C}}{\partial \boldsymbol{\rho}_{a,d}} \frac{\boldsymbol{\rho}_{a,d}}{\partial \mathbf{x}} = \frac{\partial \mathbf{h}_{\theta_C,\phi_C}}{\partial \hat{\boldsymbol{\rho}}_C} \frac{\hat{\boldsymbol{\rho}}_C}{\partial \boldsymbol{\rho}_{a,d}} \frac{\boldsymbol{\rho}_{a,d}}{\partial \mathbf{x}} \tag{A.9b}$$

$$\frac{\partial \mathbf{h}_{\theta_C,\phi_C}}{\partial \hat{\boldsymbol{\rho}}_C}(\mathbf{n}_A = \mathbf{0}, \delta\mathbf{q}_I^B = \mathbf{0}) = \begin{bmatrix} \frac{\hat{\rho}_{a,d}^x \mathbf{E}_y^T - \hat{\rho}_{a,d}^y \mathbf{E}_x^T}{(\hat{\rho}_{a,d}^x)^2 + (\hat{\rho}_{a,d}^y)^2} \\ \frac{\mathbf{E}_z^T}{\sqrt{1-(\hat{\rho}_{a,d}^z)^2}} \end{bmatrix} \tag{A.9c}$$

$$= \frac{\partial}{\partial \hat{\boldsymbol{\rho}}_{a,d}} \begin{bmatrix} \tan^{-1}\left(\frac{\hat{\boldsymbol{\rho}}_{a,d}\cdot\mathbf{E}_y}{\hat{\boldsymbol{\rho}}_{a,d}\cdot\mathbf{E}_x}\right) \\ \sin^{-1}(\hat{\boldsymbol{\rho}}_{a,d}\cdot\mathbf{E}_z) \end{bmatrix} \tag{A.9d}$$

$$\frac{\hat{\boldsymbol{\rho}}_C}{\partial \boldsymbol{\rho}_{a,d}}(\mathbf{n}_A = \mathbf{0}, \delta\mathbf{q}_I^B = \mathbf{0}) = \frac{1}{\left\|\boldsymbol{\rho}_{a,d}\right\|}\left(I - \hat{\boldsymbol{\rho}}_{a,d}\hat{\boldsymbol{\rho}}_{a,d}^T\right) = \frac{\partial \hat{\boldsymbol{\rho}}_{a,d}}{\partial \boldsymbol{\rho}_{a,d}} \tag{A.9e}$$

$$\frac{\partial \mathbf{h}_{\theta_C,\phi_C}}{\partial \boldsymbol{\rho}_{a,d}}(\mathbf{n}_A = \mathbf{0}, \delta\mathbf{q}_I^B = \mathbf{0}) = \left(\frac{\partial}{\partial \hat{\boldsymbol{\rho}}_{a,d}} \begin{bmatrix} \tan^{-1}\left(\frac{\hat{\boldsymbol{\rho}}_{a,d}\cdot\mathbf{E}_y}{\hat{\boldsymbol{\rho}}_{a,d}\cdot\mathbf{E}_x}\right) \\ \sin^{-1}(\hat{\boldsymbol{\rho}}_{a,d}\cdot\mathbf{E}_z) \end{bmatrix}\right) \frac{\partial \hat{\boldsymbol{\rho}}_{a,d}}{\partial \boldsymbol{\rho}_{a,d}} \tag{A.9f}$$

$$= \frac{\partial}{\partial \boldsymbol{\rho}_{a,d}} \begin{bmatrix} \tan^{-1}\left(\frac{\boldsymbol{\rho}_{a,d}\cdot\mathbf{E}_y}{\boldsymbol{\rho}_{a,d}\cdot\mathbf{E}_x}\right) \\ \sin^{-1}\left(\frac{\boldsymbol{\rho}_{a,d}\cdot\mathbf{E}_z}{\left\|\boldsymbol{\rho}_{a,d}\right\|}\right) \end{bmatrix} \tag{A.9g}$$

$$\frac{\partial \theta_C}{\partial \boldsymbol{\rho}_{a,d}} = \frac{(\boldsymbol{\rho}_{a,d}\cdot\mathbf{E}_x)\mathbf{E}_y^T - (\boldsymbol{\rho}_{a,d}\cdot\mathbf{E}_y)\mathbf{E}_x^T}{(\boldsymbol{\rho}_{a,d}\cdot\mathbf{E}_x)^2 + (\boldsymbol{\rho}_{a,d}\cdot\mathbf{E}_y)^2} \tag{A.9h}$$

$$\frac{\partial \phi_C}{\partial \boldsymbol{\rho}_{a,d}} = \frac{\mathbf{E}_z^T - (\hat{\boldsymbol{\rho}}_{a,d}\cdot\mathbf{E}_z)\hat{\boldsymbol{\rho}}_{a,d}^T}{\rho_{a,d}\sqrt{1-(\hat{\boldsymbol{\rho}}_{a,d}\cdot\mathbf{E}_z)^2}} \tag{A.9i}$$

$$\frac{\boldsymbol{\rho}_{a,d}}{\partial \mathbf{x}_0} = \left(I - \frac{1}{c}\mathbf{v}_i\hat{\boldsymbol{\rho}}'^T\right)[-I, \tau_d^{\mathrm{rx}} I] \tag{A.9j}$$

$$\frac{\boldsymbol{\rho}_{a,d}}{\partial \mathbf{x}_i} = \left(I - \frac{1}{c}\mathbf{v}_i\hat{\boldsymbol{\rho}}'^T\right)[I, -\tau_d^{\mathrm{rx}} I] + \left[0, -\frac{\left\|\boldsymbol{\rho}'\right\|}{c} I\right] \tag{A.9k}$$

THIS PAGE INTENTIONALLY LEFT BLANK

# Appendix B

# Additional Figures from Observability Analysis

Additional figures generated during the observability analysis of Chapter 2 are found in this appendix.

## B.1 Observability Survey over Orbital Geometries

These are the velocity uncertainties for the orbital geometry survey for the LEO and MEO cases in Figures B-1 and B-2, respectively.

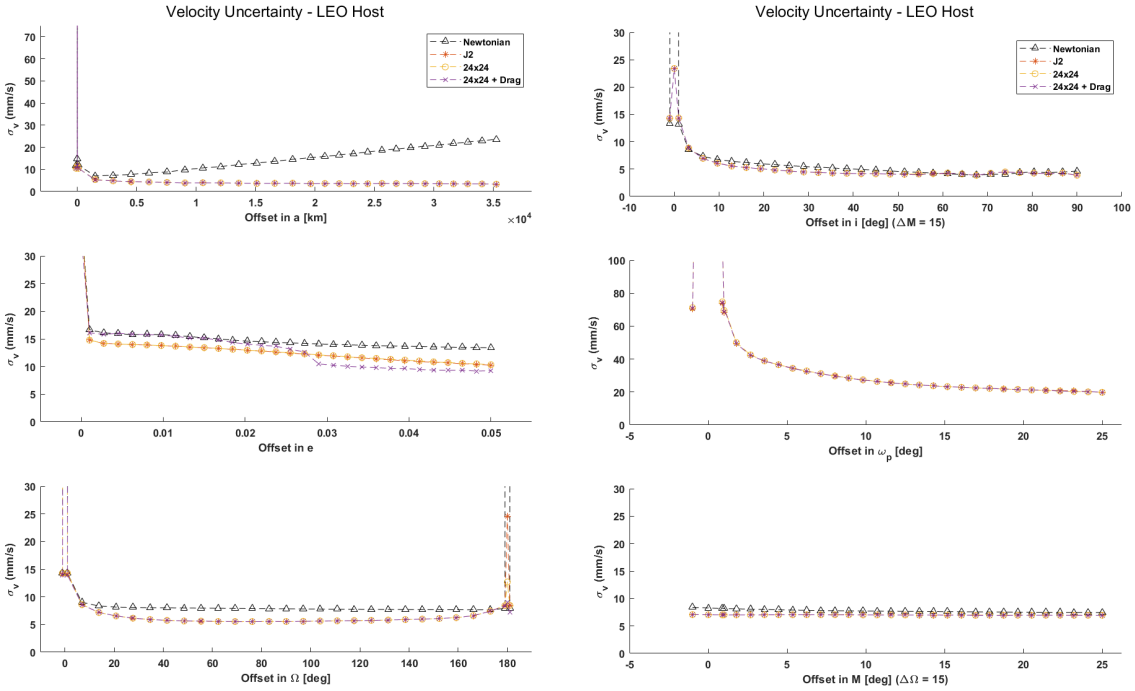


Figure B-1: Velocity uncertainties for varying relative initial orbital elements with various perturbing forces and LEO host satellite.

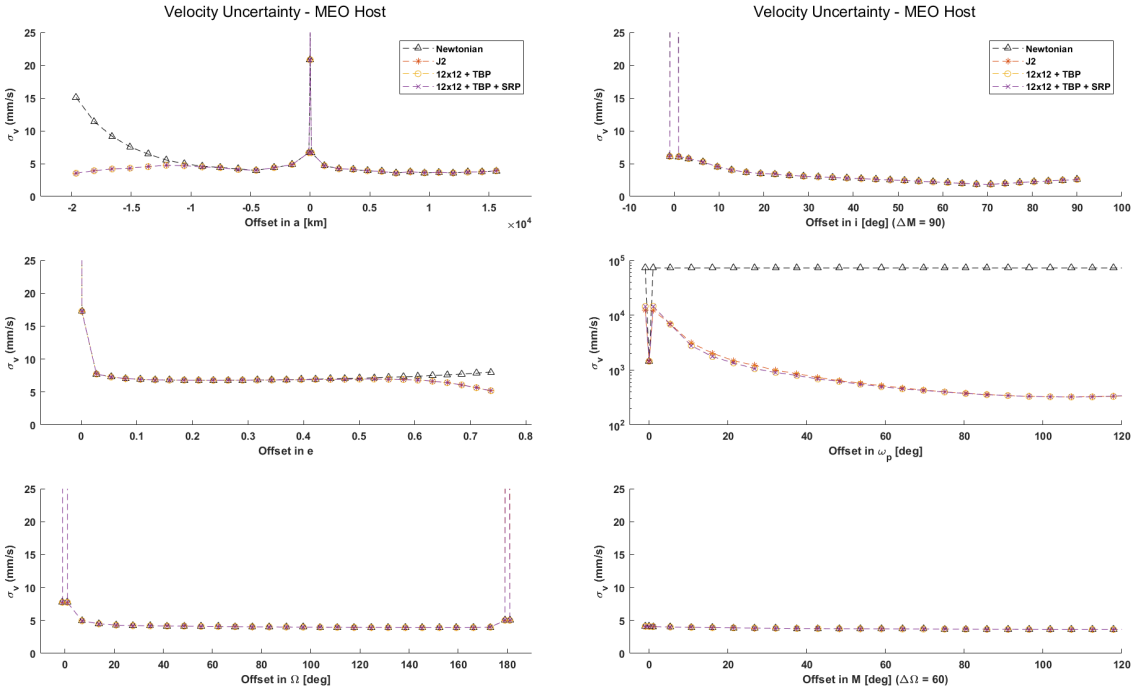


Figure B-2: Velocity uncertainties for varying relative initial orbital elements with various perturbing forces and MEO host satellite.

## B.2 Sensitivity to Measurement Parameters

These are the velocity uncertainties for the measurement parameter sensitivity analyses.

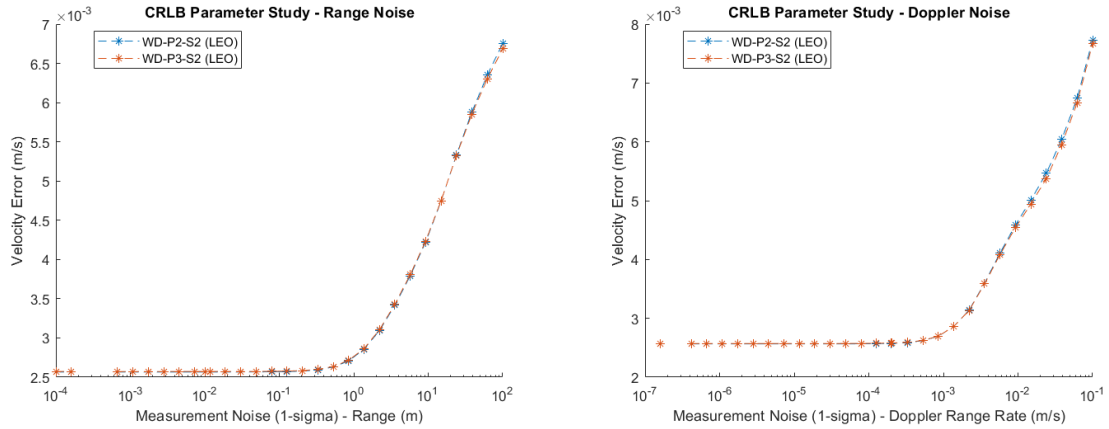


Figure B-3: Variation in RMS velocity uncertainty with range and range-rate noise. Note that since the range and Doppler measurements are redundant, for range noise variation, the measurement configuration is range-bearings; and, for range-rate noise variation, the measurement configuration is Doppler-bearings.

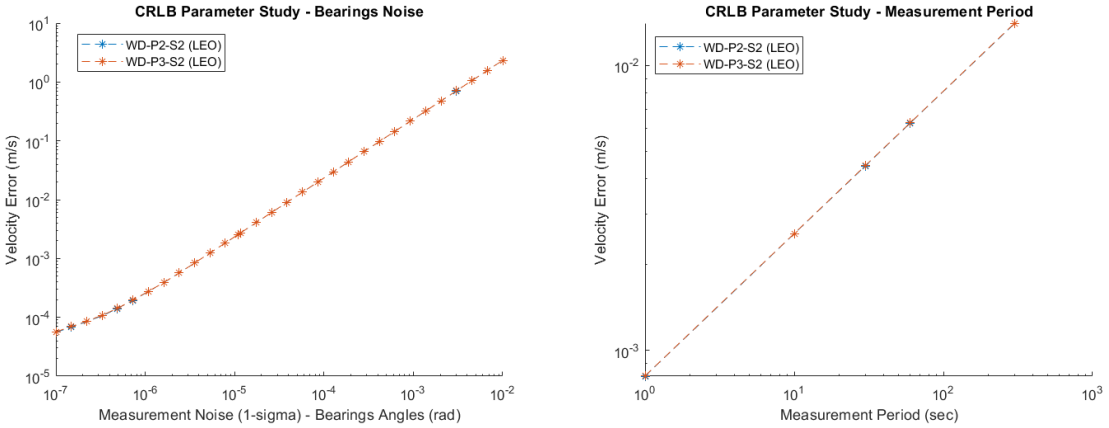


Figure B-4: Variation in RMS velocity uncertainty with (a) bearings noise on both az and el for range-bearings configuration and (b) measurement period for range-bearings configuration.

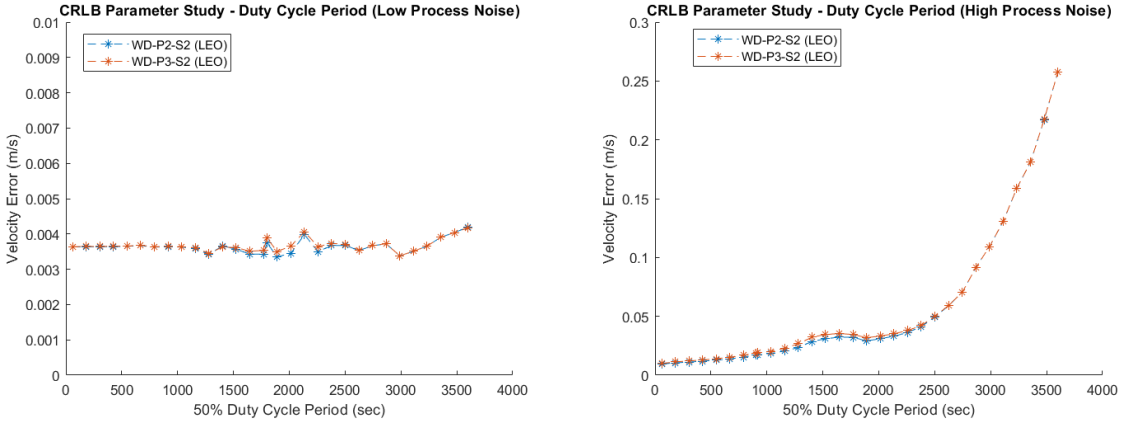


Figure B-5: Variation in RMS velocity uncertainty with period for a 50% on/off link duty cycle with (a) $\sigma_q = 3.16 \times 10^{-8}$ m/s$^2$ and (b) $\sigma_q = 3.99 \times 10^{-6}$ m/s$^2$.

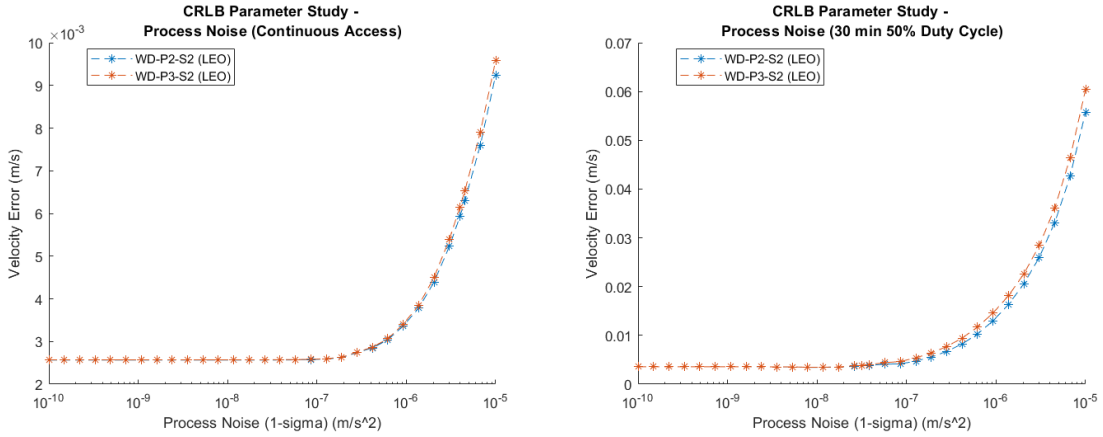


Figure B-6: Variation in RMS velocity uncertainty with process noise for (a) continous link access and (b) a 50% link duty cycle with a 30 minute period.

THIS PAGE INTENTIONALLY LEFT BLANK

# Bibliography


[1] Thomas Schetter, Mark Campbell, and Derek Surka. "Multiple agent-based autonomy for satellite constellations". In: *Artificial Intelligence* 145.1-2 (2003), pp. 147–180. ISSN: 00043702. DOI: 10.1016/S0004-3702(02)00382-X.

[2] Aizaz U Chaudhry and Halim Yanikomeroglu. "Laser Inter-Satellite Links in a Starlink Constellation". In: *IEEE Vehicular Technology Magazine* (2021).

[3] Zhigui Kang et al. "Precise orbit determination for the GRACE mission using only GPS data". In: (2006), pp. 322–331. DOI: 10.1007/s00190-006-0073-5.

[4] Michael E. Hough. "Precise orbit determination using satellite radar ranging". In: *Journal of Guidance, Control, and Dynamics* 35.4 (2012), pp. 1048–1058. ISSN: 15333884. DOI: 10.2514/1.56873.

[5] D.R. Speece. *Orbit Determination Error Analysis*. Tech. rep. Aerospace Corporation, 1963.

[6] N.M. Harwood, M. Rutten, and R.P. Donnelly. "Orbital Error Analysis for Surveillance of Space". In: *AMOS Technical Conference*. 2012.

[7] Erin Kahr, Oliver Montenbruck, and Kyle P.G. O'Keefe. "Estimation and analysis of two-line elements for small satellites". In: *Journal of Spacecraft and Rockets* 50.2 (2013), pp. 433–439. ISSN: 00224650. DOI: 10.2514/1.A32352. URL: https://doi.org/10.2514/1.A32352.

[8] Tim Flohrer, Holger Krag, and Heiner Klinkrad. "Assessment and Categorization of TLE Orbit Errors for the US SSN Catalogue". In: *AMOS Technical Conference*. 2008.

[9] Danielle Racelis and Mathieu Joerger. "High-integrity TLE error models for MEO and GEO satellites". In: *2018 AIAA SPACE and Astronautics Forum and Exposition* (2018), pp. 1–13. DOI: 10.2514/6.2018-5241.

[10] Nathan L. Parrish et al. "Near rectilinear halo orbit determination with simulated DSN observations". In: *AIAA Scitech 2020 Forum* 1 PartF (2020), pp. 1–19. DOI: 10.2514/6.2020-1700.

[11] Lisa Policastri et al. "Orbit Determination and Acquisition for LADEE and LLCD Mission AAS 15-257 Orbit Determination and Acquisition for LADEE and LLCD Mission Operations". In: September 2017 (2015), pp. 2875–2894.

[12] Sarah Elizabeth McCandless and Tomas Martin-Mur. "Navigation using deep-space optical communication systems". In: *AIAA/AAS Astrodynamics Specialist Conference, 2016* September 2016 (2016), pp. 1–17. DOI: 10.2514/6.2016-5567.

[13] Todd A. Ely, Jill Seubert, and Julia Bell. "Advancing navigation, timing, and science with the deep space atomic clock". In: *13th International Conference on Space Operations, SpaceOps 2014* May (2014), pp. 1–19. DOI: 10.2514/5.9781624101991.0105.0138.

[14] Margaret Rybak, Penina Axelrad, and Jill Seubert. "Investigation of CSAC Driven One-Way Ranging Performance for CubeSat Navigation". In: *AIAA/USU Conference on Small Satellites*. 2018. URL: https://digitalcommons.usu.edu/cgi/viewcontent.cgi?article=4129%5C&context=smallsat.

[15] Siamak G. Hesar et al. "Lunar far side surface navigation using Linked Autonomous Interplanetary Satellite Orbit Navigation (LiAISON)". In: *Acta Astronautica* 117 (Dec. 2015), pp. 116–129. ISSN: 00945765. DOI: 10.1016/j.actaastro.2015.07.027.

[16] Oliver Montenbruck and Eberhard Gill. *Satellite Orbits*. 4th ed. Berlin: Springer-Verlag, 2012. ISBN: 978-3-540-67280-7.

[17] Cyrus Foster, Henry Hallam, and James Mason. "Orbit determination and differential-drag control of Planet Labs cubesat constellations". In: *Advances in the Astronautical Sciences*. Vol. 156. 2016. ISBN: 9780877036296. arXiv: 1509.03270.

[18] G. Beutler. "GPS orbit determination using the double difference phase observable". In: *Applied Geodesy: Global Positioning System — Networks — Particle Accelerators — Mathematical Geodesy*. Ed. by Stuart Turner. Springer Berlin, Heidelberg, 1987, pp. 31–46. DOI: 10.1007/BFb0010109.

[19] Stephen Whalley. "Precise Orbit Determination for GPS Satellites". PhD Thesis. University of Nottingham, 1990. DOI: 10.1007/978-981-19-4839-8_10.

[20] V. Ashkenazi et al. "Orbit Determination for GPS Satellites". In: *Global Positioning System: An Overview*. Ed. by Yehuda Bock and Norman Leppard. Edinburgh, Scotland: Springer-Verlag New York Inc., 1990. DOI: 10.1007/978-1-4615-7111-7_18.

[21] J. S. Ulvestad. *Use of the VLBI Delay Observable for Orbit Determination of Earth-Orbiting VLBi Satellites*. Tech. rep. 42-110. 1992, pp. 77–91. URL: https://ntrs.nasa.gov/archive/nasa/casi.ntrs.nasa.gov/19930010230.pdf.

[22] Erin Kahr et al. "GPS tracking on a nanosatellite the CanX-2 flight experience". In: *8th International ESA Conference on Guidance, Navigation & Control Systems*. 2011. URL: http://www.researchgate.net/profile/Kyle_Okeefe3/publication/225024567_GPS_Tracking_of_a_Nanosatellite__The_CanX-2_Flight_Experience/links/00b4951c4c77293e31000000.pdf.

[23] Peter W Grenfell. "GNSS-Based Relative Navigation for LEO Nanosatellite Laser Communications". PhD thesis. Massachusetts Institute of Technology, 2020.

[24] Oliver Montenbruck, Florian Kunzi, and André Hauschild. "Performance assessment of GNSS-based real-time navigation for the Sentinel-6 spacecraft". In: *GPS Solutions* 26.1 (2022), pp. 1–11. ISSN: 15211886. DOI: 10.1007/s10291-021-01198-9. URL: https://doi.org/10.1007/s10291-021-01198-9.

[25] Stephen Winkler et al. "GPS Receiver on-Orbit Performance for the GOES-R Spacecraft". In: *10th International ESA Conference on Guidance, Navigation, and Control Systems*. 2017.

[26] Takuji Ebinuma and Martin Unwin. "GPS Receiver Demonstration On A Galileo Test Bed Satellite". In: *Journal of Navigation* 60.3 (2007), pp. 349–362. ISSN: 03734633. DOI: 10.1017/S0373463307004365.

[27] André Hauschild, Markus Markgraf, and Oliver Montenbruck. "GPS Receiver Performance On Board a LEO Satellite". In: *InsideGNSS* 9.July/August (2014), pp. 47–57. URL: http://www.insidegnss.com/node/4093.

[28] C Jayles and M Costes. "Ten centimeter orbits in real-time on-board of a satellite : DORIS-DIODE current status". In: 54 (2004), pp. 315–323. DOI: 10.1016/S0094-5765(03)00048-1.

[29] Christian Jayles, Jean Pierre Chauveau, and Albert Auriol. "DORIS/DIODE: Real-Time Orbit Determination Performance on Board SARAL/AltiKa". In: *Marine Geodesy* 38.June 2014 (2015), pp. 233–248. ISSN: 1521060X. DOI: 10.1080/01490419.2015.1015695.

[30] Thierry Tournier and Pascal Cauquil. "Orbit and Time On-Board Computation: From the Current SPOT4 Solution To GNSS2 Needs". In: *International Symposium on Space Flight Dynamics*. 1999.

[31] Bradley C. Collicott and David C. Woffinden. "Lunar navigation performance using the deep space network and alternate solutions to support precision landing". In: *AIAA Scitech 2021 Forum* January (2021), pp. 1–17. DOI: 10.2514/6.2021-0375.

[32] F.L. Markley. "Autonomous Navigation Using Landmark and Intersatellite Data". In: *AIAA/AAS Astrodynamics Conference*. 1984. DOI: 10.2514/6.1984-1987. URL: http://arc.aiaa.org.

[33] Mark L. Psiaki and Arthur Earl Bryson. "Autonomous orbit and magnetic field determination using magnetometer and star sensor data". In: *Journal of Guidance, Control, and Dynamics* 18.3 (1995), pp. 584–592. ISSN: 07315090. DOI: 10.2514/3.21427.

[34] Kerry D Hicks, William E Wiesel, and True Star. "Autonomous Orbit Determination System for Earth Satellites". In: 15.3 (1992), pp. 562–566. DOI: 10.2514/3.20876.

[35] Keidai Iiyama, Justin Kruger, and Simone D'Amico. "Autonomous Distributed Angles-Only Navigation and Timekeeping in Lunar Orbit". In: *Proceedings of the ION International Technical Meeting*. 2022.

[36] Justin Kruger and Simone D'Amico. "Observability analysis and optimization for angles-only navigation of distributed space systems". In: *11th International Workshop on Satellite Constellations  Formation Flying*. 2022.

[37] Suneel I Sheikh et al. "Spacecraft Navigation Using X-Ray Pulsars". In: *Journal of Guidance Control and Dynamics* 29.1 (2006). DOI: 10.2514/1.13331.

[38] Erdem Turan, Stefano Speretta, and Eberhard Gill. "Performance analysis of crosslink radiometric measurement based autonomous orbit determination for cislunar small satellite formations". In: *Advances in Space Research* (2022). ISSN: 18791948. DOI: 10.1016/j.asr.2022.11.032. arXiv: 2204.14152.

[39] Erdem Turan, Stefano Speretta, and Eberhard Gill. "Autonomous navigation for deep space small satellites: Scientific and technological advances". In: *Acta Astronautica* 193.July 2021 (2022), pp. 56–74. ISSN: 00945765. DOI: 10.1016/j.actaastro.2021.12.030. URL: https://doi.org/10.1016/j.actaastro.2021.12.030.

[40] Keric Hill, Martin W Lo, and George H Born. "Linked, Autonomous, Interplanetary Satellite Orbit Navigation (LiAISON)". In: *AAS/AIAA Astrodynamics Specialists Conference*. 2005.

[41] Keric Hill and George H. Born. "Autonomous interplanetary orbit determination using satellite-to-satellite tracking". In: *Journal of Guidance, Control, and Dynamics* 30.3 (2007), pp. 679–686. ISSN: 15333884. DOI: 10.2514/1.24574.

[42] Morris Katzman, ed. *Laser Satellite Communications*. Prentice-Hall, Inc., 1987. ISBN: 0135238048.

[43] William L. Casey and Stephen G. Lambert. *Laser Communications in Space*. Norwood: Artech House Inc, 1995. ISBN: 0890067228.

[44] Hamid Hemmati. *Near-Earth Laser Communications*. Ed. by H. Hemmati. H. Hemmati. CRC Press, 2009, p. 418. ISBN: 9781420015447. DOI: 10.1201/9781420015447.

[45] David J. Israel, Bernard L. Edwards, and John W. Staren. "Laser communications relay demonstration (LCRD) update and the path towards optical relay operations". In: *IEEE Aerospace Conference Proceedings* (2017), pp. 1–6. ISSN: 1095323X. DOI: 10.1109/AERO.2017.7943819.

[46] Don Cornwell. "NASA's Optical Communications Program for 2017 and Beyond". In: *IEEE International Conference on Space Optical Systems and Applications (ICSOS)*. 2017, pp. 10–14. ISBN: 9781509065110.

[47] David J Israel et al. "LunaNet: A flexible and extensible lunar exploration communications and navigation infrastructure". In: *Small Satellite Conference*. 2020.

[48] Bhavya Lal et al. "Global Trends in Space Situational Awareness (SSA) and Space Traffic Management (STM)". In: *Institute for Defense Analysis* (2018). URL: https://www.ida.org/idamedia/Corporate/Files/Publications/STPIPubs/2018/D-9074.pdf.

[49] *Technology Horizons: A Vision for Air Force Science and Technology 2010-30*. Tech. rep. Maxwell AFB: Office of the US Air Force Chief Scientist, 2011. DOI: 10.1017/CBO9781107415324.004. arXiv: arXiv:1011.1669v3.

[50] Mark Dmytryszyn, Matthew Crook, and Timothy Sands. "Lasers for Satellite Uplinks and Downlinks". In: *Sci* 2.2 (2020), p. 44. DOI: 10.3390/sci2020044.

[51] Guangning Yang et al. "Innovative free space optical communication and navigation system with high data rate communication, precision ranging, range rate measurements, and accurate spacecraft pointing". In: *Free-Space Laser Communication and Atmospheric Propagation XXVIII*. 2016. ISBN: 9781628419740. DOI: 10.1117/12.2197923.

[52] Alexa C. Aguilar. "Multiple Simultaneous Optical Links for Space-Based Platforms". Doctor of Philosophy. Massachusetts Institute of Technology, 2022. URL: https://dspace.mit.edu/handle/1721.1/145093.

[53] Bryan S. Robinson et al. "The lunar laser communications demonstration". In: *2011 International Conference on Space Optical Systems and Applications, ICSOS'11* Llcd (2011), pp. 54–57. ISSN: 0277786X. DOI: 10.1109/ICSOS.2011.5783709.

[54] Alberto Carrasco-Casado et al. "LEO-to-ground optical communications using SOTA (Small Optical TrAnsponder): Payload verification results and experiments on space quantum communications". In: *Acta Astronautica* 139 (2017), pp. 377–384. ISSN: 00945765. DOI: 10.1016/j.actaastro.2017.07.030. URL: http://dx.doi.org/10.1016/j.actaastro.2017.07.030.

[55] C Schmidt, M Brechtelsbauer, and F Rein. "OSIRIS Payload for DLR's BiROS Satellite". In: *Conference on Space Optical Systems* (2014). URL: http://elib.dlr.de/89346/.

[56] Siegfried Janson et al. "The NASA Optical Communications and Sensor Demonstration Program : Initial Flight Results". In: *29th Annual AIAA/USU Conference on Small Satellities* (2015), SSC16–III–03.

[57] *Web Page. RISESat (Rapid International Scientific Experiment Satellite) / Hodoyoshi-2*. Accessed 2019. URL: https://directory.eoportal.org/web/eoportal/satellite-missions/r/risesat.

[58] Bryan S. Robinson et al. "TeraByte InfraRed Delivery (TBIRD): a demonstration of large-volume direct-to-Earth data transfer from low-Earth orbit". In: *SPIE LASE*. San Francisco, 2018. DOI: 10.1117/12.2295023.

[59] Jessica Chang et al. "Body pointing, acquisition and tracking for small satellite laser communication". In: *Free-Space Laser Communications XXXI* March (2019). DOI: 10.1117/12.2511159.

[60] Kerri Cahoy et al. "The CubeSat Laser Infrared CrosslinK Mission (CLICK)". In: *International Conference on Space Optics*. Vol. 11180. 2018. DOI: 10.1117/12.2535953.

[61] Marc Casanovas Ventura. "Study: An Assessment on the Requirements for Deep Space Optical Communications". PhD thesis. Universitat Politecnica De Catalunya, 2021.

[62] James Dailey et al. "High output power laser transmitter for high-efficiency deep-space optical communications". In: *Proc. SPIE 10910, Free-Space Laser Communications XXXI*. 2019. ISBN: 9781510624627. DOI: 10.1117/12.2511193.

[63] E. Perez, M. Bailly, and J. M. Pairot. "Pointing Acquisition And Tracking System For Silex Inter Satellite Optical Link". In: *SPIE 1989 Technical Symposium on Aerospace Sensing*. Vol. 1111. 1989. DOI: 10.1117/12.977988.

[64] Zoran Sodnik, Bernhard Furch, and Hanspeter Lutz. "Optical Intersatellite Communication". In: *IEEE Journal of Selected Topics in Quantum Electronics* 16.5 (2010). ISSN: 03540596. DOI: 10.1109/MILCOM.2010.5680175.

[65] F. Heine et al. "Optical Intersatellite Communication". In: *Proceedings - IEEE Military Communications Conference MILCOM* 16.5 (2010), pp. 1583–1587. ISSN: 03540596. DOI: 10.1109/MILCOM.2010.5680175.

[66] Antonios Seas, Zachary Gonnsen, and Timothy Yarnall. *ILLUMA-T : Integrated LCRD LEO User Modem and Amplifier Terminal Payload*. Tech. rep. NASA, 2018. URL: https://ntrs.nasa.gov/search.jsp?R=20180002846.

[67] Gregory W. Heckler et al. "Metric Tracking Services in the Era of Optical Communications". In: *70th International Astronautical Congress*. 2019.

[68] Pratik K Dave. "Autonomous Navigation of Distributed Spacecraft using Intersatellite Laser Communications". PhD thesis. Massachusetts Institute of Technology, 2020.

[69] Mark L Psiaki. "Autonomous Orbit Determination for Two Spacecraft from Relative Position Measurements". In: *Journal of Guidance Control and Dynamics* 22.2 (1999).

[70] Jozef C. Van Der Ha. *Mission Design & Implementation of Satellite Constellations*. Springer Science and Business Media, 1998. ISBN: 9789401061377.

[71] Manuele Dassié and Gabriele Giorgi. "Relativistic Modelling for Accurate Time Transfer via Optical Inter-Satellite Links". In: *Aerotecnica Missili & Spazio* 100.3 (2021), pp. 277–288. ISSN: 0365-7442. DOI: 10.1007/s42496-021-00087-1. URL: https://doi.org/10.1007/s42496-021-00087-1.

[72] Herwig Zech et al. "Optical intersatellite links for navigation constellations". In: SPIE-Intl Soc Optical Eng, July 2019, p. 34. ISBN: 9781510630772. DOI: 10.1117/12.2535954.

[73] Kay Yong, C. C. Chao, and Anthony S. Liu. "Autonomous Navigation for Satellites using Lasercom Systems". In: *Proceedings of the American Control Conference*. Vol. 1982-June. Institute of Electrical and Electronics Engineers Inc., 1982, pp. 636–642. DOI: 10.23919/acc.1982.4787930.

[74] *The Doppler Equation in Range and Range Rate Measurement*. Tech. rep. Goddard Space Flight Center, 1965.

[75] Robert L. Herklotz. "Incorporation of Cross-link Range Measurements in the Orbit Determination Process to Increase Satellite Constellation Autonomy". PhD thesis. Massachusetts Institute of Technology, 1987.

[76] Xiaofang Zhao, Shenggang Liu, and Chao Han. "Performance analysis of autonomous navigation of constellation based on inter satellite range measurement". In: *Procedia Engineering* 15 (2011), pp. 4094–4098. ISSN: 18777058. DOI: 10.1016/j.proeng.2011.08.768. URL: http://dx.doi.org/10.1016/j.proeng.2011.08.768.

[77] Liuqing Xu, Xiaoxu Zhao, and Lili Guo. "An autonomous navigation study of Walker constellation based on reference satellite and inter-satellite distance measurement". In: *2014 IEEE Chinese Guidance, Navigation and Control Conference, CGNCC 2014*. IEEE, 2014, pp. 2553–2557. ISBN: 9781479946990. DOI: 10.1109/CGNCC.2014.7007568.

[78] Jo Ryeong Yim, John L. Crassidis, and John L. Junkins. "Autonomous orbit navigation of two spacecraft system using relative line of sight vector measurements". In: *Advances in the Astronautical Sciences* (2004). ISSN: 00653438.

[79] G. Gaias, S. D'Amico, and J.-S. Ardaens. "Angles-Only Navigation to a Noncooperative Satellite Using Relative Orbital Elements". In: *Journal of Guidance, Control, and Dynamics* 37.2 (2014), pp. 439–451. ISSN: 0731-5090. DOI: 10.2514/1.61494. URL: http://arc.aiaa.org/doi/10.2514/1.61494.

[80] Mark L. Psiaki. "Absolute orbit and gravity determination using relative position measurements between two satellites". In: *Journal of Guidance, Control, and Dynamics* 34.5 (2011), pp. 1285–1297. ISSN: 15333884. DOI: 10.2514/1.47560.

[81] Kai Xiong, Chunling Wei, and Liangdong Liu. "Autonomous navigation for a group of satellites with star sensors and inter-satellite links". In: *Acta Astronautica* 86 (2013), pp. 10–23. ISSN: 00945765. DOI: 10.1016/j.actaastro.2012.12.001. URL: http://dx.doi.org/10.1016/j.actaastro.2012.12.001.

[82] Youtao Gao, Bo Xu, and Lei Zhang. "Feasibility study of autonomous orbit determination using only the crosslink range measurement for a combined navigation constellation". In: *Chinese Journal of Aeronautics* 27.5 (2014), pp. 1199–1210. ISSN: 10009361. DOI: 10.1016/j.cja.2014.09.005.

[83] Yangwei Ou, Hongbo Zhang, and Jianjun Xing. "Autonomous orbit determination and observability analysis for formation satellites". In: *Chinese Control Conference, CCC* 2016-Augus (2016), pp. 5294–5300. ISSN: 21612927. DOI: 10.1109/ChiCC.2016.7554179.

[84] Ruipeng Li, Hongzhuan Qiu, and Kai Xiong. "Autonomous navigation for constellation based on inter-satellite ranging and directions". In: *Proceedings IECON 2017 - 43rd Annual Conference of the IEEE Industrial Electronics Society* 2017-Janua (2017), pp. 2985–2990. DOI: 10.1109/IECON.2017.8216504.

[85] Yangwei Ou, Hongbo Zhang, and Bin Li. "Absolute orbit determination using line-of-sight vector measurements between formation flying spacecraft". In: *Astrophysics and Space Science* 363.4 (2018). ISSN: 1572946X. DOI: 10.1007/s10509-018-3293-2. URL: http://dx.doi.org/10.1007/s10509-018-3293-2.

[86] John L. Crassidis and John L. Junkins. *Optimal Estimation of Dynamic Systems*. 2nd. CRC Press, 2004. ISBN: 158488391X.

[87] Byron D. Tapley, Bob E. Schutz, and George H. Born. *Statistical Orbit Determination*. Burlington: Elsevier Inc, 2004. ISBN: 0-12-683630-2.

[88] Eric A. Butcher, Jingwei Wang, and T. Alan Lovell. "On Kalman filtering and observability in nonlinear sequential relative orbit estimation". In: *Journal of Guidance, Control, and Dynamics* 40.9 (2017), pp. 2167–2182. ISSN: 07315090. DOI: 10.2514/1.G002702.

[89] James H Taylor. "The Cramer-Rao Estimation Error Lower Bound Computation for Deterministic Nonlinear Systems". In: 2 (1979), pp. 343–344.

[90] Andrew O'Dea et al. *202 Doppler Tracking*. Tech. rep. Jet Propulsion Laboratory, 2021.

[91] Quan Chen et al. "Analysis of Inter-Satellite Link Paths for LEO Mega-Constellation Networks". In: *IEEE Transactions on Vehicular Technology* 70.3 (2021), pp. 2743–2755. ISSN: 19399359. DOI: 10.1109/TVT.2021.3058126.

[92] Jintao Liang, Aizaz U. Chaudhry, and Halim Yanikomeroglu. "Phasing Parameter Analysis for Satellite Collision Avoidance in Starlink and Kuiper Constellations". In: *Proceedings - 2021 IEEE 4th 5G World Forum, 5GWF 2021* (2021), pp. 493–498. DOI: 10.1109/5GWF52925.2021.00093.

[93] MathWorks. *MATLAB*. 2023. URL: https://www.mathworks.com/products/matlab.html.

[94] CS GROUP. *Orekit*. 2023. URL: https://www.orekit.org/.

[95] Bo Su and Qingrui Zhou. "Analysis of Dynamic Evolution and Station-Keeping of Starlink". In: *Proceeding - 2021 China Automation Congress, CAC 2021*. Vol. 2. 0. 2021, pp. 8229–8234. ISBN: 9781665426473. DOI: 10.1109/CAC53003.2021.9728207.

[96] Chance Johnson, Lauchie Scott, and Stefan Thorsteinson. *Space-Based Photometric Observations of the Spacex Starlink Constellation Satellites-Preliminary Findings*. Tech. rep. Defence R&D Canada Ottawa, 2020.

[97] *Starlink Satellite Constellation*. 2019. URL: https://www.eoportal.org/satellite-missions/starlink#spacecraft.

[98] Scott Palo, George Stafford, and Alan Hoskins. "An Agile Multi-Use Nano Star Camera for Constellation Applications". In: *Small Satellite Conference* (2013).

[99] Marc Sanchez Net and Jon Hamkins. *Optical Telemetry Ranging*. Tech. rep. IPN, 2020.

[100] Peter W. Kinman and Robert M. Gagliardi. "Doppler and range determination for deep space vehicles using active optical transponders". In: *Applied Optics* 27.21 (1988), p. 4487. ISSN: 0003-6935. DOI: 10.1364/ao.27.004487.

[101] Jon Hamkins et al. *Telemetry Ranging: Concepts*. Tech. rep. 2015, pp. 1–20.

[102] Paul C. Serra. "Integrated, Low-Power Sub-Nanosecond Timing Systems for Space Navigation and Communication". PhD thesis. University of Florida, 2018.

[103] *Optical High Data Rate (HDR) Communication - 1550nm*. Tech. rep. CCSDS, 2022.

[104] Bruce Moision and Baris I. Erkmen. "Bounds on parameter estimation precision for optical ranging systems". In: *SPIE Optical Engineering + Applications*. 2012. ISBN: 9780819492357. DOI: 10.1117/12.930096.

[105] Victor Vilnrotter and Jon Hamkins. "Telecommand / Telemetry Ranging for Deep-Space Applications". In: *2019 IEEE Aerospace Conference*. IEEE, 2019, pp. 1–10. ISBN: 9781538668542.

[106] Walt Kester. *Converting Oscillator Phase Noise to Time Jitter*. Tech. rep. Analog Devices, 2008.

[107] *Time & Frequency Synchronization Solutions Product Catalog*. Tech. rep. Symmetricom, 2012.

[108] Baris I. Erkmen and Bruce Moision. "Maximum likelihood time-of-arrival estimation of optical pulses via photon-counting photodetectors". In: *IEEE International Symposium on Information Theory - Proceedings*. IEEE, 2009. ISBN: 9781424443130. DOI: 10.1109/ISIT.2009.5205546.

[109] Bruce Moision, Sami Asmar, and Kamal Oudrhiri. "Radio science from an optical communications signal". In: *IEEE Aerospace Conference Proceedings*. IEEE, 2013. ISBN: 9781467318112. DOI: 10.1109/AERO.2013.6497168.

[110] *Optical Communications Coding and Synchronization*. Tech. rep. CCSDS, 2019.

[111] Kenneth Andrews et al. "Telemetry-based ranging". In: *IEEE Aerospace Conference Proceedings*. IEEE, 2010. ISBN: 9781424438884. DOI: 10.1109/AERO.2010.5446926.

[112] C. C. Chen and C. S. Gardner. *Comparison of direct and heterodyne detection optical intersatellite communication links*. Tech. rep. 1987. URL: http://adsabs.harvard.edu/abs/1987STIN...8718694C.

[113] Catherine L. Thornton and James S. Border. *Radiometric Tracking Techniques for Deep Space Navigation*. Tech. rep. Jet Propulsion Lab, 2000. DOI: 10.1002/0471728454.

[114] Lorenzo Galleani. "A tutorial on the two-state model of the atomic clock noise". In: *Metrologia* 45.6 (2008). ISSN: 00261394. DOI: 10.1088/0026-1394/45/6/S23.

[115] Bruce Moision, Janet Wu, and Shervin Shambayati. "An optical communications link design tool for long-term mission planning for deep-space missions". In: *IEEE Aerospace Conference Proceedings* (2012), pp. 1–12. ISSN: 1095323X. DOI: 10.1109/AERO.2012.6187102.

[116] Bruce Moision and Hua Xie. *An Approximate Link Equation for the Direct-Detected Optical PPM Link*. Tech. rep. Jet Propulsion Laboratory, California Institute of Technology, 2014, pp. 1–14.

[117] Abhijit Biswas et al. *Deep-space Optical Terminals (DOT) Systems Engineering*. Tech. rep. 183. 2010.

[118] Bernard Edwards et al. *Overview of the Laser Communications Relay Demonstration Project*. Tech. rep. MIT Lincoln Laboratory, 2012.

[119] Joseph J. Scozzafava et al. "Design of a very small inertially stabilized optical space terminal". In: *Free-Space Laser Communications VII* (2007). ISSN: 0277786X. DOI: 10.1117/12.738384.

[120] Dirk Giggenbach. "Free-Space Optical Data Receivers with Avalanche Detectors for Satellite Downlinks Regarding Background Light". In: *Sensors* (2022).

[121] Microchip Technology Incorporated. *MAC-SA5X*. Tech. rep. 2021. URL: https://ww1.microchip.com/downloads/en/DeviceDoc/00003348.pdf%20%0A.

[122] Yihao Yan et al. “Revisiting the light time correction in gravimetric missions like GRACE and GRACE follow-on”. In: *Journal of Geodesy* 95.48 (2021). ISSN: 14321394. DOI: 10.1007/s00190-021-01498-5. arXiv: 2005.13614. URL: https://doi.org/10.1007/s00190-021-01498-5.

[123] Antonio Genova and Flavio Petricca. “Deep-space navigation with intersatellite radio tracking”. In: *Journal of Guidance, Control, and Dynamics* 44.5 (2021), pp. 1068–1079. ISSN: 15333884. DOI: 10.2514/1.G005610.

[124] D. W. Allan, N. Ashby, and C. C. Hodge. *The Science of Timekeeping*. Tech. rep. 1997, pp. 1–88. URL: http://www.allanstime.com/Publications/DWA/Science_Timekeeping/TheScienceOfTimekeeping.pdf%5Cnhttp://literature.agilent.com/litweb/pdf/5965-7984E.pdf.

[125] W J Riley. *Handbook of Frequency Stability Analysis*. U. S. GOVERNMENT PRINTING OFFICE, 2008. ISBN: 3019753058.

[126] *Industrial camera mvBlueFOX-MLC*. URL: https://www.directindustry.com/prod/matrix-vision-gmbh/product-29519-550149.html.

[127] *QD50-0 Quadrant Photodiodes*. URL: https://www.osioptoelectronics.com/products/photodetectors/quadrant-and-bi-cell-photodiodes-spot-series/qd50-0.

[128] Z Zhengyou. “A Flexible New Technique for Camera Calibration”. In: *IEEE transactions on pattern analysis and machine intelligence* 22.11 (2000), pp. 1330–1334. URL: https://www.microsoft.com/en-us/research/publication/a-flexible-new-technique-for-camera-calibration/.

[129] OpenCV. *Camera Calibration and 3D Reconstruction*. 2019. URL: https://docs.opencv.org/2.4/modules/calib3d/doc/camera_calibration_and_3d_reconstruction.html.

[130] D. M. Boroson et al. “The Lunar Laser Communications Demonstration (LLCD)”. In: *Proceedings - 2009 3rd IEEE International Conference on Space Mission*

*Challenges for Information Technology, SMC-IT 2009* Llcd (2009), pp. 23–28. DOI: 10.1109/SMC-IT.2009.57.

[131] Paul Serra et al. "Optical Communications Crosslink Payload Prototype Development for the Cubesat Laser Infrared CrosslinK (CLICK) Mission". In: *AIAA/USU Conference on Small Satellites*. 2019.

[132] *Red Enhanced Quad Cell Silicon Photodiode SD 085-23-21-021*. Tech. rep. Luna Optoelectronics, 2016. URL: https://www.lasercomponents.com/de/?embedded=1%5C&file=fileadmin/user_upload/home/Datasheets/luna/si-pin/quads/sd085-23-21-021.pdf%5C&no_cache=1.

[133] F. Landis Markley and John L Crassidis. *Fundamentals of Spacecraft Attitude Determination and Control*. New York: Springer Science+Business Media, 2014. ISBN: 9781493908011.

[134] Tina Shih et al. "A modular, agile, scalable optical terminal architecture for space communications". In: *2017 IEEE International Conference on Space Optical Systems and Applications, ICSOS 2017* (2018), pp. 203–207. DOI: 10.1109/ICSOS.2017.8357236.

[135] M. Faup, G. Planche, and T. Tolke. "Experience gained in the frame of Silex programme development and future trends". In: *AIAA International Communications Satellite Systems Conference* Technical (1996), pp. 779–792. DOI: 10.2514/6.1996-1078.

[136] David A Vallado. "An Analysis of State Vector Propagation Using Differing Flight Dynamics Programs". In: *AAS/AIAA Space Flight Mechanics Conference*. 2005.

[137] Nathan Stacey and Simone D'Amico. "Adaptive and Dynamically Constrained Process Noise Estimation for Orbit Determination". In: *IEEE Transactions on Aerospace and Electronic Systems* 57.5 (2021), pp. 2920–2937. ISSN: 15579603. DOI: 10.1109/TAES.2021.3074205. arXiv: 1909.07921.

[138] Yaakov Bar-Shalom, X. Rong Li, and Thiagalingam Kirubarajan. *Estimation with Applications to Tracking and Navigation*. John Wiley  Sons,Inc., 2001. ISBN: 047141655X.

[139] Jeremy J. Davis and Daniele Mortari. "Reducing Walker, Flower, and streets-of-coverage constellations to a single constellation design framework". In: *Advances in the Astronautical Sciences* 143.January 2012 (2012), pp. 697–712. ISSN: 00653438.

[140] *GPS Block III*. 2023. URL: https://en.wikipedia.org/wiki/GPS_Block_III.

[141] *Lockheed Martin A2100*. 2023. URL: https://en.wikipedia.org/wiki/Lockheed_Martin_A2100.

[142] Daniel Navarro-Reyes, Anna Notarantonio, and Giacomo Taini. "Galileo Constellation: Evaluation of Station Keeping Strategies". In: *Proceedings 21st International Symposium on Space Flight Dynamics*. Toulouse, France, 2009.

[143] James Schier. "LunaNet Overview". In: *NESC Unique Science from the Moon in the Artemis Era Workshop*. 2022.

[144] Todd A. Ely. "Stable constellations of frozen elliptical inclined lunar orbits". In: *Journal of the Astronautical Sciences* 53.3 (2005), pp. 301–316. ISSN: 00219142. DOI: 10.1007/bf03546355.

[145] Martin Lara, Bernard De Saedeleer, and Sebastian Ferrer. "PRELIMINARY DESIGN OF LOW LUNAR ORBITS". In: *Proceedings of the 21st International Symposium on Space Flight Dynamics*. 2009, pp. 1–15.

[146] Todd A. Ely and Erica Lieb. "Constellations of elliptical inclined lunar orbits providing polar and global coverage". In: *Journal of the Astronautical Sciences* 54.1 (2006), pp. 53–67. ISSN: 00219142. DOI: 10.1007/BF03256476.

[147] *LRO (Lunar Reconnaissance Orbiter)*. 2013. URL: https://www.eoportal.org/satellite-missions/lro#launch.

[148] D. J. Bell et al. “Mars network: A Mars orbiting communications & navigation satellite constellation”. In: *IEEE Aerospace Conference Proceedings* 7 (2000), pp. 75–88. ISSN: 1095323X. DOI: 10.1109/aero.2000.879277.

[149] Enes Koktas and Ertugrul Basar. “Communications for the Planet Mars: Past, Present, and Future”. In: (2022), pp. 1–35. arXiv: 2211.14245. URL: http://arxiv.org/abs/2211.14245.

[150] Mauro De Sanctis et al. “Flower constellation of orbiters for martian communication”. In: *IEEE Aerospace Conference Proceedings* 3.1 (2007). ISSN: 1095323X. DOI: 10.1109/AERO.2007.352713.

[151] *Mars Reconnaissance Orbiter*. 2023. URL: https://en.wikipedia.org/wiki/Mars_Reconnaissance_Orbiter.